UNIVERSITE
BRETAGNE
LOIRE

Le Mans
Université

Thèse de Doctorat

Tymur PARPIIEV

Mémoire présenté en vue de l'obtention du
grade de Docteur de Le Mans Université
sous le sceau de l'Université Bretagne Loire

École doctorale : Matière, Molécules et Matériaux (3M)

Discipline : Physique
Spécialité : Ondes et Matériaux
Unité de recherche : IMMM UMR 6283 CNRS

Soutenue le 18/12/2017
Thèse N° : 2017LEMA1044

Ultrafast magneto-acoustics in magnetostrictive materials

JURY

Rapporteurs :	**Jean-Yves BIGOT**, Directeur de Recherche CNRS, IPCMS Strasbourg
	Christine BOEGLIN, Directeur de Recherche CNRS, IPCMS Strasbourg
Examinateurs :	**Matias BARGHEER,** Professeur, IPA, Potsdam
	Laura THEVENARD Chargé de recherche CNRS, INSP, Paris VI**,** Paris
	Florent CALVAYRAC Professeur, IMMM, Le Mans
Directeur de Thèse :	**Thomas PEZERIL**, Chargé de recherche CNRS, IMMM, Le Mans
Co-encadrant de Thèse :	**Vasily TEMNOV**, Chargé de recherche CNRS, IMMM, Le Mans

Ultrafast Magnetoacoustics in Magnetostrictive Materials

By

Tymur PARPIIEV

PhD Thesis

Submitted in partial fulfillment of the requirements
for the Degree of Doctor of Philosophy in Physics
at Le Mans Université in the Doctoral School
"Matière, Molécules et Matériaux"

Le Mans, France, 2017

"I like the scientific spirit - the holding off, the being sure but not too sure, the willingness to surrender ideas when the evidence is against them: this is ultimately fine - it always keeps the way beyond open - always gives life, thought, affection, the whole man, a chance to try over again after a mistake - after a wrong guess."

Walt Whitman,
Walt Whitman's Camden Conversations

Acknowledgments

Despite the fact that Ph.D project is a solo task, this work would never have been completed without all the support and encouragement that I have had from many different people. Unfortunately, it is impossible to list all of them, whom I am grateful so much.

I sincerely thank my supervisor Dr. Thomas Pezeril, who welcomed me to his team. I really appreciate his guidance, that was leading me step by step further in comprehension of physics. Without his help with experiments and advises, I could not attained this level and completed this thesis. His passionate and enthusiastic attitude to science encouraged me during all this time.

I also would like to thank my co-supervisor Dr. Vasily Temnov for his scientific advises, invaluable help with new directions in research, personal qualities and extremely motivating discussions about science and life.

A special thanks go to all current and former members of the scientific group "NOVA". I enjoyed working together with you all, it brought me the precious knowledges and new experience.

I have met a lot of new friends during my Ph.D time. I am glad to express my acknowledgments of gratitude to all of them and especially to my lab co-workers: Yevheniia Chernukha, Ievgeniia Chaban, Dr. Viktor Shalagatski and Dr. Alexandr Alekhin, who was helping me and taught me a lot about physics.

This research become possible due the financial support of the French National Research Agency under the grant ANR-14-CE26-0008.

I sincerely thank my parents and family to whom I tender my gratitude. Your deepest love guide me all my live. Mom and Dad, you are always dividing with me all my successes and failures and you are always there to help. I am incredibly happy to have parents like you by my side. Thank you for everything.

Abstract

English

The advent of femtosecond lasers has been at the origin of many discoveries in solid state physics. In particular, in the field of magnetism it became possible to measure how femtosecond optical demagnetization can probe the exchange interaction in ferromagnetic metals. Laser-induced demagnetization of materials with strong magneto-elastic coupling should lead to the release of its build-in strains, thus to the generation of both longitudinal and shear acoustic waves. The physical mechanism is known as direct magnetostriction, which is the property of ferromagnetic materials to change their shape or dimensions during the process of magnetization/demagnetization. The inverse phenomenon appears when an applied external stress modifies statically or dynamically the magnetization configuration of a ferromagnet. A number of new physical phenomena are expected to arise when an ultrafast acoustic pulse, exited by absorption of a femtosecond laser pulse in photoacoustic transducer, is injected to a ferromagnetic sample.

In this thesis, generation of shear picosecond acoustic pulses in strongly magnetostrictive materials such as Terfenol is processed analytically and shown experimentally. In case of Terfenol with strong magneto-crystalline anisotropy, laser-induced *demagnetostriction* is responsible for shear waves excitation.

First, the phenomenological model of direct magnetostriction in a Terfenol monocrystalline film is developed. Transversal strain generation efficiency strongly depends on the orientation of the film magnetization. Time-resolved linear MOKE pump-probe experiments show that transient laser-induced release of the magnetoelastic strains in the films lead to the excitation of GHz longitudinal and shear acoustic waves. These results are the first experimental observation of picosecond shear acoustic wave excitation by laser-induced demagnetostriction mechanism.

Second, the interaction of an optically generated longitudinal acoustic wave with the magnetization of a Terfenol thin film is reported. Arrival of the ps strain wave alters a change of its magnetization and leads to the acoustic mode conversion. Which is another pathway of shear acoustic wave generation. This effect highlight a strong coupling

of elastic and spin subsystems in Terfenol. Hence, there are two laser-induced mechanisms of the shear wave excitation in materials with strong magneto-elastic coupling: (i) transient demagnetostriction and (ii) acoustic mode conversion. The Frequency bandwidth of the generated acoustic pulses matches the demagnetization timescale and lies in the range of several hundreds of GHz, close to 1 THz.

These experimental and theoretical results could have large impacts in several fields of applications: Brillouin spectroscopy at GHz-THz frequencies with both longitudinal and shear acoustic polarizations, magnetic recording with ultrafast longitudinal and shear acoustic waves.

Résumé

Français

L'avènement du laser femtoseconde a été à l'origine de nombreuses découvertes dans le domaine de la physique du solide. Par exemple, dans le domaine du magnétisme, il est devenu possible de mesurer comment la démagnétisation femtoseconde peut permettre de sonder l'interaction d'échange dans les métaux ferromagnétiques. La démagnétisation induite par le laser d'un matériau avec un fort couplage magnéto-élastique amène à la relaxation de ses contraintes, générant ainsi des ondes acoustiques longitudinales et transversales. Le méchanisme physique est connu sous le nom de magnétostriction directe, qui est une propriété des matériaux ferromagnétiques de changer leur forme ou leurs dimensions lors du processus de magnétisation/démagnétisation. Le phénomène inverse apparaît lorsqu'une contraine externe appliquée modifie statiquement ou dynamiquement la configuration de magnétisation du matériau ferromagnétique. Il est attendu de la sorte qu'une impulsion acoustique ultra-rapide, generée par absorption d'une impulsion laser femtoseconde dans un transducteur photoacoustique, puisse modifier l'aimantation d'un échantillon ferromagnétique magnéstroctif.

Dans ce travail de thèse, la génération d'impulsions acoustiques picosecondes transversales dans des matériaux fortement magnétostrictifs est traitée analytiquement et montrée expérimentalement dans le cas d'un alliage de Terfenol. Dans le cas de ce matériau à fort couplage magnéto-cristallin, *le mécanisme de démagnétostriction* induit par laser est responsable de l'excitation d'ondes acoustiques transversales.

En premier lieu, nous avons développé un modèle phénoménologique de magnétostriction directe dans un film monocristallin de Terfenol. L'efficacité de génération de déformation transversale dépend fortement de l'orientation de l'aimantation du film. Les expériences pompe-sonde linéaire MOKE résolues en temps montrent que la relaxation transitoire des contraintes magnéto-élastiques du film amène à l'excitation d'ondes GHz acoustiques longitudinales et transversales. Ces résultats sont la première observation expérimentale de l'excitation d'ondes acoustiques transversales picoseconde par mécanisme de démagnétostriction induit par laser.

En second lieu, nous avons analysé le processus d'interaction d'ondes acoustiques

longitudinales générées optiquement avec l'aimantation d'un film mince de Terfenol. L'onde acoustique picoseconde produit un changement de magnétisation du film et induit la conversion de modes acoustiques. C'est une autre voie de génération d'ondes acoustiques transversales que nous avons mis en évidence. Cet effet est une conséquence du fort couplage des sous-systèmes élastiques et magnt́iques dans le Terfenol. Par conséquent, il existe deux mécanismes de l'excitation des ondes transversales dans des matériaux à fort couplage magnéto-élastique: (i) démagnétostriction induite par laser et (ii) conversion de modes acoustiques. La gamme de fréquence des impulsions générées est liée à l'échelle de temps de démagnétisation, qui corresponds à quelques centaines de GHz - 1 THz.

Les résultats expérimentaux et théoriques obtenus dans le cadre de cette thèse pourraient amener à des retombées applicatives importantes: spectroscopie Brillouin de materiaux à des fréquences GHz-THz impliquant des ondes acoustiques longitudianles mais aussi transverses, enregistrement magnetique à partir d'ondes acoustiques ultrarapides longitudinales et transverses.

Contents

Introduction

Recent developments in the field of electronics have led to a drastic decrease in the size of electronic devices. Following empiric Moore's law [1] the number of transistors on a single silicon chip doubles every 24 months with simultaneous chip size decrease. Indeed, in 1971 the production standards in electronic industry were 10 μm, in 1978 - 3 μm, in 1989 - 1 μm, in 1997 - 0,25 μm, in 2005 - 65 nm, 2014 - 14 nm, finally, 10 nm [2] in 2017. At the same time a transfer of many services and commerce online, development of social networks and big data analytics demand higher data storage capacities. Usually digitally stored data is represented by two stable states of a media, considered as numerical 0 or 1, determined by some physical effect. Modern hard disc drives contain about Tbit/in^2. They record data by magnetizing a thin film of a ferromagnetic material, eventually, different state of magnetization represents binary data bits. Consequently, manipulation of big amounts of data requires an increase in writing/reading speed. There is a competition among companies and scientists in the elaboration of new approaches in data recording. From the point of view of the performance and non-volatily the most perspective technologies are Magnetic Random-Access Memory (MRAM) and Spin-Transfer-Torque Magnetic Random Access Memory (STT-MRAM). Results presented in this thesis can be utilized as an alternative approach for the ultrafast magnetic data recording.

Advanced materials elaboration and characterization is one of the key elements in the production of data storage devices. In particular, thin films, superlattices, nanoclusters, which play a crucial role in the enhancement of material's properties: thermal and electric conductivity, resistance to aggressive environment influences, etc. Consequently, the role of their characterization methods is extremely important. Morphology, chemical composition, electric properties of thin films can be measured by ordinary techniques, however, generally it is difficult to test their mechanical properties. Besides, small film thickness prohibits utilization of contact methods. On the contrary, photoacoustic techniques based on transient laser pulses is a convenient tool to investigate their mechanic properties. Use of all-optical methods provides an accurate, non-contact and non-destructive testing of samples.

Development of coherent light sources has led to new discoveries. For example, femtosecond *fs* laser systems are used to generate coherent acoustic phonons, to decrease magnetization modulus of magnetic materials at subpicosecond timescale [3] or to switch their magnetization [4], etc. Work of Thomsen et all [5] in 1984 started picosecond ultrasonic spectroscopy, which is an all-optical method to monitor mechanic properties of thin films, multilayer samples or nano objects. Short laser pulses, called pump pulses, excite the media. Consequently, acoustic waves in the ∼10-800 GHz frequency and ∼4-100 nm wavelength ranges are generated after energy redistribution through different channels. Subsequent time delayed laser pulse (probe) is used to monitor non-equilibrium dynamics in the medium. It gathers information about the time dependent optical reflectivity, which can be used to examine the evolution of the sample's mechanical properties. Thus, a set of stroboscopic images, taken with a time step of tens of femtoseconds, forms a dynamical picture. Pump-probe techniques provide direct, time domain measurement of the generated acoustics, or of other processes excited by pump pulses. In the most general case it is limited by generation of only longitudinal acoustic waves (LW) that propagates into the depth of the structure and reveals diagonal elements of elastic constants tensor. In contrast, the excitation of shear acoustic waves (SW) is prohibited because of symmetry reasons in most cases. On the contrary to longitudinal acoustic waves, the generation of transversal or shear acoustic waves is a non trivial task and sometimes demands complicated experimental approaches. Thus, picosecond shear acoustic waves transducers, that don't require sophisticated experimental configurations, would shed the light on the entire Brillouin zone of materials together with longitudinal ones, that are already widely investigated. They could be utilized to study elastic properties of different materials. At the moment, there are several techniques to optically generate SW: thermoelasticity, inverse piezoelectricity, deformation potential mechanisms in off-axis crystals, transient gratings excitation, electrostriction, direct piezoelectricity, ultrafast demagnetostriction [6]. Due to the nature of the particles oscillations in the lattice, all of these mechanisms are related to the breaking of the crystal symmetry. Nonetheless an accessible frequency range is below 1 THz.

This work is focused on the ultrafast laser-mediated *magneto-elastic* mechanism for longitudinal and shear acoustic waves generation in GHz-THz frequency range. The conventional way to reverse the magnetization is to apply a magnetic field. However, change of magnetization doesn't occur if the magnetic field pulse is shorter than 2 ps. Since the first observation of subpicosecond optical demagnetization of a ferromagnetic Ni film [3], manipulation of magnetization at faster timescale became possible. Laser induced demagnetization of samples with strong magneto-elastic coupling, is expected to lead to the release of the build-in stresses and generation of both longitudinal and shear acoustic waves in presence of a certain anisotropy of the properties of the media. Comprehensive research of the magnetic and magneto-elastic properties of rare-earth elements was carried out in 1960's [7], [8], [9]. Particular interest was paid to the heavy lanthanide metals with huge magnetic anisotropy, it resulted in the discovery of $REFe_2$ (RE = Sm, Tb, Dy, Er, Tm) binary compounds with the strongest exchange interaction and highest magneto-elastic coupling [10], [11]. For example, ferromagnetic $SmFe_2$ and $TbFe_2$ (Terfenol) are the alloys that possess highest magneto-crystalline anisotropy and so-called "giant" magnetostriction coefficients $\lambda_s(SmFe_2) = -1560 \cdot 10^{-6}$, $\lambda_s(TbFe_2) = 1750 \cdot 10^{-6}$ (negative and positive signs correspond to the contraction or dilation of the lattice upon an applied magnetic field). The reason of such strong magnetostriction is the presence of rare-earth ions with highly anisotropic 4f electrons cloud (most extended in case of Sm and most flattened in Tb). Moreover, a strong $Fe - Fe$ and $Fe - RE$ exchange coupling preserves the rare-earth sublattice magnetization stable at room temperature, resulting in higher, than pure Sm or Tb, Curie temperatures. Properties of Terfenol make it an ideal choice for the study of spin-lattice coupling via the direct magnetostriction for GHz-THz acoustic pulses generation. Moreover, reversed mechanism of the inverse magnetostriction after an injection of acoustic pulses into such highly magnetostrictive compound is expected to reveal number of new physical effects. Synthesis of rare-earth elements with high purity has been an issue because of the similarity of their chemical properties, however, the solution was found using ion exchange methods [12]. Now Terfenol alloy is a commercially available material with average price that varies around 10$ per 1 g. Manufacturing of $REFe_2$ thin monocrystalline films by molecular beam epitaxy was reported in [13], $TbFe_2$ films with surface quality suitable for picosecond ultrasonic experiments was fabricated in the scope of the thesis of Mougin [14].

The major fundamental challenges, that constitute the motivation of this work are:

1. Does laser-mediated direct magnetostriction in Terfenol lead to the generation of longitudinal and shear acoustic pulses and, if so, in what frequency range?

2. How spin-ordered Terfenol compound behaves after an injection of laser-induced ultrasonic pulses?

Scope of the thesis

The present thesis addresses all mentioned fundamental challenges. After a general introduction, laser induced magnetization dynamics in metals, generation and detection of coherent acoustic phonons and ultrafast magnetoacoustics will be overlooked in Chapter 1. The proposed experimental approach is given at the end of this chapter. It is based on the emission of strain waves after the transient change of the magnetization of Terfenol films with strong spin-lattice coupling.

Chapter 2 starts with a description of the direct magnetostriction effect. Linear magneto-optical pump-probe technique for the investigation of ultrafast magnetization dynamics of Terfenol alloys is introduced. The demagnetization of Terfenol films occurs on a two steps time scale of $\tau_1 \sim 1.5$ ps and $\tau_2 \sim 15$ ps due to strong spin-lattice coupling. Laser excitation and subsequent demagnetization of Terfenol lead to the release of its build-in strains, that propagate in the attached dielectric layer, which is described by the dynamics of an elementary volume element subjected to a stress gradient in the continuous medium. Laser-induced magneto-elastic response of the ferromagnetic thin film is interpreted in the frame of the mechanistic approach, based on the instantaneous change of its free energy density by the pump pulse. Experimental results obtained on a monocrystalline $TbFe_2/SiO_2$ hybrid samples emphasize the generation of the approximately 8 ps shear acoustic pulses via transient demagnetostriction mechanism. Injection of GHz longitudinal strain pulse into the Terfenol film leads to the acoustic mode conversion with efficiency of about 10 %. Landau-Lifshitz equation has been utilized to numerically simulate an optimal experimental geometry for acoustic mode conversion in monocrystalline Terfenol films. The out-of-plane tilt of $TbFe_2$ magnetization is considered to be a crucial parameter for the generation of shear acoustic waves via demagnetostriction and mode conversion mechanisms.

Chapter 3 sums up all experimental results concerning Terfenol films presented in this thesis. Laser-induced generation of picosecond shear strain waves and their subsequent propagation in an attached SiO_2 lens demonstrates that magnetostrictive material can be a source of GHz shear acoustic waves in a simple picosecond ultrasonics geometry. Last section is devoted to the overview of other magnetostrictive materials, that can be the alternative source of the GHz coherent longitudinal and shear acoustic strain waves.

Chapter 1

Magnetization dynamics and acoustic phonons

This chapter introduces the fundamental concepts of femtomagnetism, picosecond ultrasonics and ultrafast magneto-acoustics. In the first section, we focus on the domain of femtomagnetism research that considers the dynamics of the magnetization of magnetic materials induced by femtosecond laser pulses. Typical time scales vary from several tens of femtoseconds to few picoseconds. The first experimental observation of spin dynamics occurring on sub-picosecond timescale was made on 22 nm polycrystalline Ni film after its excitation by 60 fs laser pulses. This result was interpreted in terms of the phenomenological three temperatures model (3TM). Despite the fact that laser-induced demagnetization have been under investigation for two decades, there is still no consensus about the common model which describes this phenomenon in all variety of magnetic materials. Coherent magnetization dynamics follows the ultrafast demagnetization at longer timescale and is described by the Landau-Lifshitz equation. In addition to the common probe wavelength in the visible light range, ultraviolet, far-infrared and x-ray probe provide information about the dynamic state of magnetization of a magnetic material.

Coherent laser-induced lattice dynamics and mechanisms of its generation and detection are reviewed in the second section. The main attention is focused on the non-trivial mechanisms of generation and detection of shear acoustic pulses.

The third section is devoted to the manipulation of magnetization of magnetic materials by GHz acoustic pulses. The possibility of an inverse interaction is considered, i.e. excitation of the strain waves after transient laser-induced demagnetization of magnetic materials. The experimental approach proposed in this thesis is based on the laser-induced demagnetization of highly magnetostrictive materials and subsequent excitation of GHz longitudinal and shear acoustic pulses due to their strong spin-lattice coupling. Physical frameworks of femtomagnetism, picosecond ultrasonics and ultrafast magneto-acoustics will be utilized in the interpretation of the experimental results presented in Ch. 2 and Ch. 3.

1.1 Laser-induced magnetization dynamics

The aim of this section is to introduce laser-induced magnetization dynamics, which, in fact, consist of vast variety of effects occurring at different time and space scales [15]. Action of femtosecond laser pulses on magnetic materials is at the core of femtomagnetism. The ultrafast laser modification of magnetization is named femtosecond *demagnetization* and can be divided into an incoherent and coherent contributions. Incoherent dynamics is represented by the ultrafast drop of the remanent magnetization from its original value. It occurs during the first ps after excitation, depending on the materials. Out-of-equilibrium coherent precession of magnetization around the effective field follows the incoherent dynamics during the next hundreds of ps. The demagnetization effect has an important impact on the ultrafast response of Terfenol films upon laser excitation. In particular from the point of view of the lattice dynamics during the demagnetization/remagnetization process. A short overview of the first relevant study implying magnetization and acoustics is given at the beginning of this section.

First observation

The first observation of the spin dynamics after laser excitation of ferromagnetic thin films with femtosecond temporal resolution was made by Beaurepaire et al. in 1996 (see [3]). They reported the transient decrease of the remanent magnetization of Ni films at about 50% upon fs-laser excitation (see Fig. 1.1).

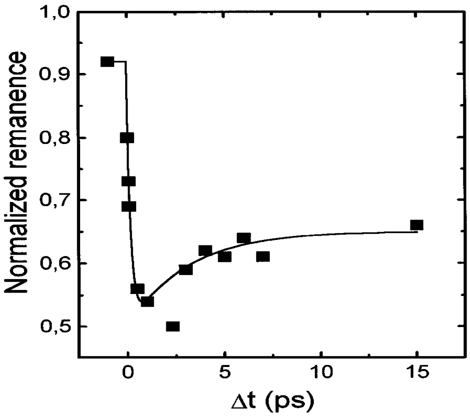

Fig. 1.1: Ultrafast release of magnetization of a 22 nm Ni film under fs laser excitation.

Fig. 1.1 shows the variation of magneto-optical Kerr rotation measured on a 22 nm polycrystalline Ni film after its excitation by 60 fs laser pulses. It indicates a sudden drop of the signal amplitude, which is proportional to the magnetization, at ~ 1 ps time scale. This work attracted big interest in the community and triggered a vast number of studies. A new domain called femtomagnetism emerged, which considers the influence of femtosecond laser pulses on magnetic materials. Up to now, 1 ps demagnetization timescale has been confirmed for all transition metals and some alloys [16]. However, the typical timescale of laser-induced demagnetization varies with the pump fluence [17] or temperature [18], as observed in rare-earth Tb and Gd and other types of materials. Koopmans et al [17] reported two types of magnetization dynamics, which occurs at different time scale: (i) the first-type is inherent to Fe, Co and Ni and their alloys, depending on pump fluence and sample temperature. It occurs at sub-picosecond time scale. (ii) The second-type is ascribed to the materials with weak interaction between electron and spin subsystems. It is characterized by longer (more than 1 ps) demagnetization and was reported in rare-earth Gd, TbFe alloy [19], several oxides and magnetic semiconductors (InMnAs [20]).

1.1.1 Laser-induced demagnetization

Laser-induced dynamics in a metallic material can be described by the two- temperature model (2TM) [21], where the energy distributes between the electrons T_e and the lattice T_l subsystems. The presence of magnetic ordering in the material introduces another subsystem - *spin*, that should also be taken into account during the energy distribution. The excitation of the magnetic medium by fs-laser pulses takes it away from its internal equilibrium state at subpicosecond timescale, so the use of thermodynamics for the description of magnetism is not relevant. The development of a theoretical model, which can describe ultrafast demagnetization became a challenge. Spin is conserved in the optical transitions, hence, the pump pulse excites only the electron sub-system, which is heated instantly to the thermalized distribution. The phenomenological three-temperature model (3TM) was proposed (see [3] and [22]), to describe the experimental observation of laser-induced demagnetization of ferromagnetic materials. It suggests the energy flux between three subsystems: electrons, spins and the lattice, proportional to the temperature differences between them and described by the following rate equations of the electrons T_e, lattice T_p and spins T_s temperatures

$$C_e\frac{dT_e}{dt} = P(t) - g_{ep}(T_e - T_p) - g_{es}(T_e - T_s),$$

$$C_s\frac{dT_s}{dt} = -g_{es}(T_s - T_e) - g_{sp}(T_s - T_p), \tag{1.1}$$

$$C_p \frac{dT_p}{dt} = -g_{ep}(T_p - T_e) - g_{sp}(T_p - T_s),$$

where C_e is the electronic specific heat, C_s, C_p are the magnetic and lattice contributions to the specific heat, g_{ep}, g_{es}, and g_{sp} are the electron-lattice, electron-spin, and spin-lattice coupling constants. Typical timescale of the electron-electron and electron-lattice coupling varies from several femtoseconds to some picoseconds, respectively. Direct energy transfer from the electrons to the magnetic sub-system takes place via *e.g.* quasi-elastic spin-flip scattering and/or can excite the spin system *i.e.* magnons. Indirect interplay originates via phonon-mediated spin-flip mechanism. The characteristic time scales of both effects are 100 fs and 100 ps [23] respectively. During the indirect interaction hot electrons thermalize with the lattice to attain thermal equilibrium and then via orbit-lattice coupling, which affects spin states of the material, see Fig 1.2.

3TM is a simple description of the energy equilibration processes. Nevertheless, it doesn't take into account transfer of the angular momentum, thus, omits some microscopic mechanisms, that also govern magnetization dynamics. Excitation of magnetic materials with fs laser pulses, that are shorter than the time scale of the spin-orbit interaction (0.1-1 ps), takes it out of the equilibrium state, where thermodynamics and static macrospin considerations can not be applied to explain the magnetization dynamics. At short timescale, the magnetic anisotropy and exchange interaction should be considered as time-dependent parameters [24]. Underlying physical mechanisms remain under debate. Koopmans et al [17] proposed an alternative microscopic three temperature model (M3TM) to describe the magnetization dynamics. Unlike to the 3TM, it suggests the

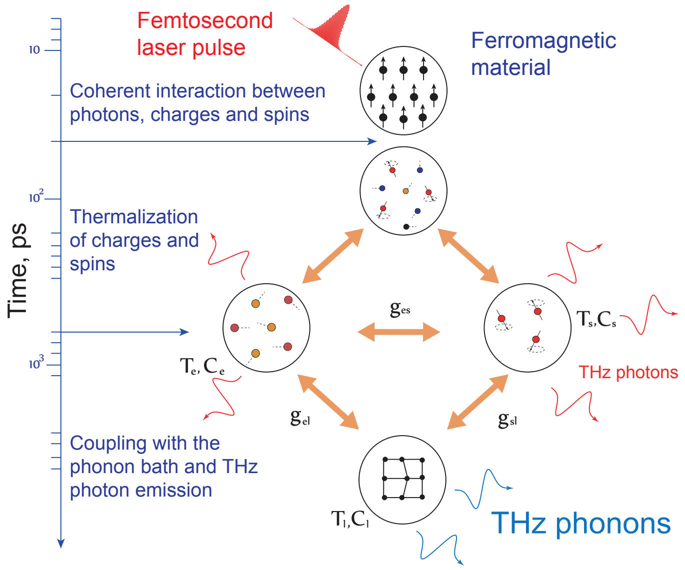

Fig. 1.2: Scheme of the interaction of a laser pulse and the spin state of a magnetic material [23].

transfer of angular momentum to the lattice during energy distribution between hot electrons and spins. After neglecting the spin specific heat and assuming instantaneous thermalization of the electron gas, three coupled differential equations were obtained

$$\begin{gathered}C_e|T_e|\frac{dT_e}{dt} = \nabla_z(k\nabla_z T_e) + g_{ep}(T_p - T_e),\\ C_p\frac{dT_p}{dt} = g_{ep}(T_e - T_p),\\ \frac{dm}{dt} = Rm\frac{T_p}{T_c}(1 - m\coth(\frac{mT_c}{T_e})),\end{gathered} \tag{1.2}$$

where ∇_z indicate derivation with respect to z coordinate, which is normal to the surface, k is the thermal conductivity.

1.1.2 Coherent magnetization dynamics

Time-domain measurements of the photoexcited periodic precession of magnetization give a quantitative information about demagnetization, anisotropy and damping effects occurring in the excited materials. Fig. 1.3 [24] shows a schematic of the excitation of the precessional motion of magnetization. Initially (a) at time zero $\Delta t = 0$, the magnetization is aligned along the effective field, given by the sum of the anisotropy (H_a), demagnetizing, and external fields. After (b) action of a laser pump pulse the magnitude M and/or the anisotropy change due to heating, thereby altering the equilibrium orientation. (c) The magnetization precesses around the new equilibrium direction that is slowly restored due to the heat diffusion. The precession of a magnetic moment $\overrightarrow{M}$ of the spin-ordered material in the external field $\overrightarrow{H}$ is described by *Landau-Lifshitz* equation

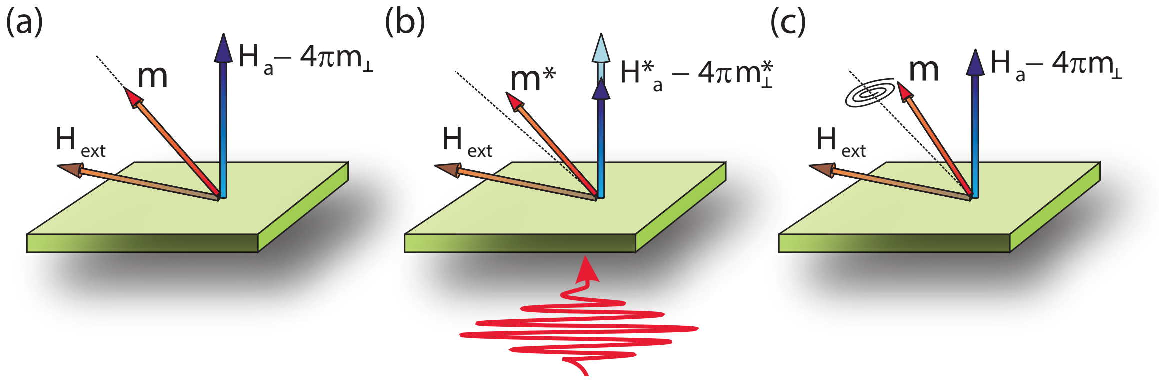

Fig. 1.3: Optical excitation of coherent precession. $H_d = -4\pi m_\perp$ is the shape anisotropy.

$$\frac{d\overrightarrow{M}}{dt} = -\gamma\mu_0[\overrightarrow{M} \times \overrightarrow{H}_{eff}], \tag{1.3}$$

where γ is the gyromagnetic ratio, μ_0 - the magnetic permeability of vacuum, $\overrightarrow{H}_{eff}$ - the effective magnetic field. The gyromagnetic ratio of a single electron with only the spin magnetic moment is equal to

$$\frac{\gamma_e}{2\pi} = g_s\mu_B/h \approx 28\frac{GHz}{T}, \tag{1.4}$$

where μ_B is the Bohr magneton. The expression of the magnetization precession in the case of magnetically homogeneous ferromagnet has the form of Eq. (1.3). In 1955 Gilbert suggested to add the damping term in the Landau-Lifshitz equation (1.3), which is proportional to the time derivative of the magnetization M

$$\frac{d\overrightarrow{M}}{dt} = -\gamma\mu_0[\overrightarrow{M} \times \overrightarrow{H}_{eff}] + \frac{\eta}{|\overrightarrow{M}|}[\overrightarrow{M} \times \frac{d\overrightarrow{M}}{dt}], \tag{1.5}$$

where η is the damping parameter depending on the material. Equation (1.5) is named Landau-Lifshitz-Gilbert equation. It is valid in a temperature window, where $|\overrightarrow{M}| = const$. The Landau-Lifshitz-Bloch (LLB) equation [25] takes into account the change of the magnitude of the magnetization vector $\overrightarrow{M}$ at high temperatures

$$\frac{d\overrightarrow{M}}{dt} = -\gamma\mu_0[\overrightarrow{M} \times \overrightarrow{H}_{eff}] + \gamma\alpha_1\frac{[\overrightarrow{M} \cdot \overrightarrow{H}_{eff}] \cdot \overrightarrow{M}}{|\overrightarrow{M}|^2} - \gamma\alpha_2\frac{[\overrightarrow{M} \times \overrightarrow{H}_{eff}] \times \overrightarrow{M}}{|\overrightarrow{M}|^2}, \tag{1.6}$$

where α_1 and α_2 are the longitudinal and transversal damping parameters [24].

1.1.3 Detection of magnetization dynamics

In practice, the study of the ultrafast magnetization dynamics is realized by the employment of the laser pump-probe technique with a subpicosecond temporal resolution. Generally, ultrafast excitation of magnetic materials doesn't vary much with modification of the pump wavelength. On the contrary, depending on the probe spectral range, different informations about the state of magnetization can be provided. Ultraviolet, far-infrared and x-ray spectral ranges can be used as an additional tool to the common probe in the visible range to monitor ultrafast magnetization dynamics.

In contrast to the indirect magneto-optical methods, where the polarization rotation is measured, the utilization of *ultraviolet probes* in combination with spin-sensitive detectors provides a direct access to the spin distribution of the electron gas in metals. Hence, the interpretation of time-resolved photoemission results is much more straightforward than in the case of TR magneto-optical experiments. The excitation of the magnetic material by photons with an energy larger than the work function, may result in an emission of the electrons from the surface. The spectroscopy of the emitted spin-polarized electrons gives access to the static electronic structure of the sample, the energy and momentum distribution of the electrons in [26], [27]. The disadvantage of this method is the requirement of the high quality and electronic conductivity of the sample surface.

To obtain information about the conductivity of materials it can be possible to use a *terahertz probe* in the far-infrared spectral range. It is an indirect technique, which can be sensitive to the magnetic phase transitions if the conductance of the free-electron gas is sensitive to the magnetic order. In the case of some particular materials (most of the antiferromagnets, some rare-earth elements [28]) it can potentially provide a direct access to the spin state of the system.

X-ray probe too can be utilized in order to study the orientation of the magnetization and antiferromagnetic vector of the materials by analogy to the magneto-optical phenomena in the visible spectral range. However, the main advantage of the x-ray absorption techniques is that there are relatively narrow transitions at well-defined energies of the magnetic materials so this is an elemental selectivity method. Based on its advantages, time-resolved x-ray probe contributes to the deeper comprehension of ultrafast laser-induced magnetization dynamics. The first x-ray absorption results with 100 fs temporal resolution were reported in [29].

Non-linear magneto-optical techniques, e.g. the magnetization-induced Second Harmonic Generation (mSHG) is sensitive to ultrafast magnetization dynamics at surfaces and interfaces [30], [31]. Linear magneto-optical response, which is sensitive to the bulk or skin-depth magnetization of spin-ordered materials is more commonly measured. Magneto-optic Faraday effect [32] causes the rotation of the polarization of light propagating through a magnetized medium, which is proportional to the angle of the applied magnetic field. The same effect occurring at the near-surface region of several tens of nm of a magnetic medium was called the magneto-optical Kerr effect (MOKE) [33]. The phenomenological description of the MOKE is based on the analysis of the dielectric tensor of the magnetic medium [34]

$$\widetilde{\varepsilon} = \varepsilon \cdot \begin{bmatrix} 1 & i \cdot Q_z & -i \cdot Q_y \\ -i \cdot Q_z & 1 & i \cdot Q_x \\ i \cdot Q_y & -i \cdot Q_x & 1 \end{bmatrix}.$$

where $\overrightarrow{Q} = (Q_x, Q_y, Q_z)$ is the Voigt vector, proportional to the magnetization $\overrightarrow{M}$. It can be expressed as a product of the Voigt constant q and the magnetization:

$$\overrightarrow{Q} = q \cdot \overrightarrow{M}.$$

Three magneto-optical geometries are distinguished depending on the orientation of the magnetization vector M with respect to the plane of incidence of the probe beam:

1. In *the polar* MOKE configuration, the magnetization of the film lies perpendicularly to the film surface and lies in the plane of incidence of the probe. The change of probe polarization is proportional to the out-of-plane component of magnetization.
2. *The longitudinal* MOKE is measured at oblique incidence when the magnetization lies on the film and is contained in the plane of incidence of the probe beam. Linearly polarized light incident on the surface undergoes a change of its polarization, that is directly proportional to the in-plane component of magnetization.
3. *The transversal* MOKE is measured at oblique incidence if the magnetization of the film is perpendicular to the plane of incidence and along the sample surface. The T-MOKE depends on the second order terms in Q and results in a change of reflectivity.

There is another important difference between polar (P) and longitudinal (L) MOKE : a relation between the polarization changes of the initially p- and s-polarized waves as [34]:

$$r_{ps}(P) = r_{sp}(P) \qquad r_{ps}(L) = -r_{sp}(L).$$

Therefore, by utilizing initially p- and s-polarized probe pulses, it is possible to disentangle P and L contributions to the measured MOKE signal.

To conclude the section, the role of acoustic waves on the fs timescale processes of demagnetization is usually neglected. It is suggested that phonons are involved in this process at longer time scales of 10-100 ps during the energy exchange between hot electrons and lattice. For materials with weak spin-lattice coupling (transition metals, e.g.), this assumption is correct if the magnetostriction is weak and does not play significant role in the energy distribution. On the contrary, in highly magnetostrictive materials (rare-earth based alloys, for example) it is expected to influence the demagnetization process. Recent works [35, 36], demonstrated the ultrafast demagnetization and all-optical switching for a broad range of rare-earth-transition metals compounds with high magnetostriction. Owing to strong spin-orbit coupling in RE materials, the spin-lattice relaxation channel should be taken into account for the description of ultrafast laser-induced demagnetization events.

1.2 Coherent lattice dynamics

This section is focused on the high frequency acoustic waves in a solid medium. An optical pump can excite different types of strain waves: longitudinal, shear, Rayleigh, etc. In the most general case, the generation of shear or transversal waves doesn't occur due to symmetry reasons.

Acoustic waves in solids are periodic oscillations of the lattice, which propagate in the material at a given velocity due to the action of elastic forces. This velocity is often called speed of sound and depends on the material. Unlike liquid or gaseous media where in the general case only longitudinal waves can propagate, in solids several types of oscillations are possible: longitudinal, shear, Rayleigh waves etc. Longitudinal phonons are periodic particle movements that does not change the shape of the elementary unit cell, only the distance between neighbor atoms, i.e the displacement of the particles coincide with the direction of the wave propagation Fig. 1.4. It is also called compressional waves because it produces a contraction of the media on its rise front and a dilation after it. Transversal or shear waves also emerge along the propagation direction, but unlike the longitudinal ones, they modify the shape of the lattice unit cell and not the volume. Particles oscillations occur in the plane, which is perpendicular to the direction of wave propagation. Normally both acoustic modes travel in the bulk but have different velocities: speed of the longitudinal phonons is linked to the bulk elasticity modulus of the material, while in the case of shear phonons it is related to the shear elasticity modulus. An ability of the medium to maintain both longitudinal and shear lattice oscillations permits to generate Rayleigh waves, that occur at the near surface region of the sample, it is an ellipsoidal in-plane particle motion near the surface of a solid. They combine both longitudinal and shear motions but have a lower frequency (lower speed) and higher wavelength. All of them can be used in different sample characterization techniques for ultrasound testing which is applied in a variety of domains. In solids three different modes (one longitudinal and two transversals) with mutually orthogonal displacements are possible along any propagation direction. This work is focused on the generation of GHz longitudinal and, in particular, shear acoustic pulses in thin ferromagnetic films and molecular crystals by means of the *picosecond* *ultrasonics* technique [37].

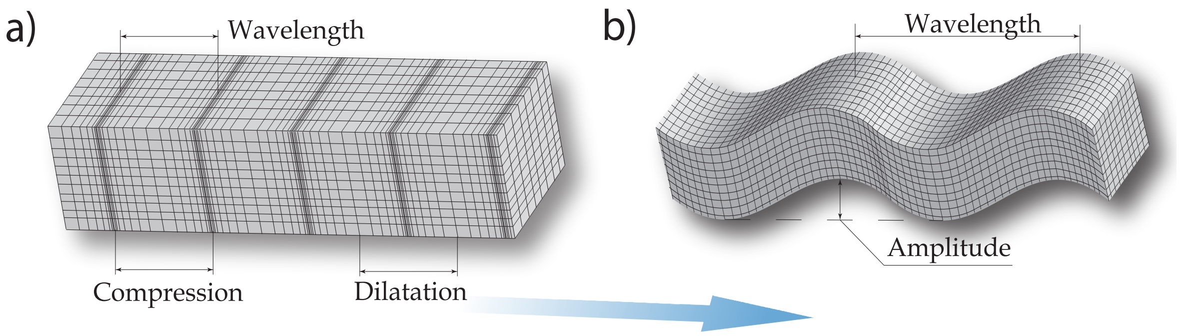

Fig. 1.4: a) Longitudinal and b) shear acoustic waves propagating in the same direction.

1.2.1 Optical generation of coherent acoustic phonons

Among different mechanisms of acoustic wave generation, we consider only the photoexcitation processes, which allow to generate coherent strain waves with the frequency bandwidth of hundreds of GHz. Laser excitation of the sample leads to the energy exchange between hot electrons and lattice, which occurs during the next few picoseconds. Hence, the phonons emerge until temperatures T_e and T_p are equilibrated, the energy distribution occurs via the electron-phonon coupling. Since the first observation in 1984 [5], the generation of acoustic waves by ultrashort laser pulses has been widely studied. There are several types of photoexcitation mechanisms for strain waves with different acoustic polarizations, that are briefly reviewed elsewhere [38], [39], [40].

In the most general case, in a mechanically isotropic material, the *thermoelastic effect* is responsible for the generation of longitudinal waves (LW), which are driven by the homogeneous thermal expansion of the lattice after laser excitation [37]. No collimated shear waves (SW)are excited in this case at all. It is a consequence of the isotropy of thermal gradient propagating uniformly in the hemisphere away from the heated point while transverse displacements orthogonal to this symmetrical excitation are forbidden. In materials with broken axial symmetry, the thermoelastic mechanism is an efficient tool for picosecond SW excitation [41]. LW and SW are coupled at the boundaries of the medium [42], thus thermo-elastically generated plane LW under some conditions can be converted into SW through *acoustic mode conversion* mechanism [43]. The break of the axial symmetry permits to overcome the symmetry restriction [39] for the excitation of shear acoustic frequencies above few GHz.

Inverse piezoelectricity(IPE) and *deformation potential*(DP) are other possible mechanisms of generation of GHz acoustic waves. IPE and DP are observed in piezoelectric semiconductors or insulators laser-excited above their band-gap. In these types of materials there is a competition between these two photo-excitation mechanisms: the inverse piezoelectric effect, linked to the screening of the built-in sample electric fields, and the electron-hole-phonon deformation potential mechanism, related to the modification of the interatomic electrostatic forces by the laser excitation of charges. Laser-induced modification of the electronic distribution impacts the perturbation of the local electrostatic equilibrium of electrons and cations. It leads to the modification of the lattice equilibrium position and subsequent excitation of acoustic waves. Like in thermoelasticity, in highly symmetric samples there is no SW excitation through IPE and DP mechanisms due to symmetry considerations mentioned earlier. Laser-induced shear acoustic waves do not emerge via any of these mechanisms, unless the samples axial symmetry is broken [41].

Hence, the break of the axial symmetry is required to generate GHz shear acoustic waves through thermoelastic mechanism, common for all types of materials, or inverse piezoelectric and deformation potential mechanism, typical to the piezoelectric samples.

The *transient grating* (TG) excitation technique was proposed as an alternative approach to excite GHz shear acoustic waves [44], [45]. Due to the periodic distribution of heat deposition, laser-induced thermoelastic effect leads to the excitation of longitudinal acoustic gratings that are the superposition of two coupled longitudinal plane acoustic waves that propagates obliquely to the sample surface. Consequently, upon reflection at an interface, they undergo partial mode conversion into shear acoustic gratings (SAG). Longitudinal acoustic gratings can be considered as the superposition of two plane longitudinal acoustic waves with non-zero in-plane components of their wavevectors k_x. These plane longitudinal waves propagate obliquely and originates a partial mode conversion into SAG after the reflection at an interface. However, there is no experimental evidences so far for the picosecond shear acoustic waves excitation via this technique, because of the complexity of the experimental geometry [45].

Shear wave excitation through *electrostriction* mechanism has been demonstrated in the MHz frequency range in dielectrics via TG excitation by intense pulsed electric fields. This technique is based on impulsive stimulated brillouin scattering (ISBS) detected in ellipsometric scheme [46]. Optical frequency of the laser pulse is much higher than the acoustic frequency bandwidth of any material, hence, the envelope of the laser pulse drives the lattice motion through the electrostriction mechanism. This technique remains poorly developed because of the low excitation efficiency which results in low signal levels. To overcome this obstacle, excitation by far-infrared light with THz frequency was suggested to match the frequency of the light source and the acoustic frequency spectrum of the samples [6].

Magnetic counterpart of electrostriction - *magnetostriction* occurs in materials with high magneto-elastic coupling. Low frequency (below ∼ 100 kHz) strains generation by modulated magnetic field is already wide used in ultrasonic devises [47]. Theoretically, laser-induced demagnetisation of magnetostrictive materials at picosecond timescale could permit to overcome this limit and excite acoustic pulses in the GHz-THz frequency range. It will allow to study the spin-lattice relaxation channel by probing generated acoustic echoes. The variation of the magnetization state of the magnetostrictive material leads to the simultaneous change of its shape. As far as the demagnetostriction process is expected to match the subpicosecond demagnetization timescale of ferromagnets, laser-induced release of the magnetostrictive stresses is expected to excite picosecond acoustic pulses with GHz frequency spectrum.

Transient laser-induced demagnetization of highly magnetostrictive materials (Terfenol alloy for example) should directly enable the generation of shear waves even in elastically isotropic medium. Thus, *demagnetostriction*(= demagnetization of magnetostrictive materials) can be an efficient alternative to all the methods listed above for GHz shear acoustic wave generation. *One of the main challenges of this thesis is to confirm this assumption experimentally.*

1.2.2 Optical detection of coherent acoustic phonons

Ultrafast lattice dynamics are generally monitored by measuring the transient change of optical transmission ΔT or reflectivity ΔR of the photoexcited medium by time-delayed probe pulses [5], [38]. In the case of a semi-infinite medium, the change of the complex transient optical reflectivity $\Delta r/r$ of the probe beam caused by longitudinal wave can be expressed as

$$\frac{\Delta r}{r} = -2iku(0) + \frac{4ik_0 n}{1-n^2}\frac{\partial n}{\partial \eta}\int_0^\infty \eta_{zz}(z,t)e^{2ink_z}dz, \tag{1.7}$$

where k is the probe beam wavevector in vacuum, $u(0)$ is the displacement of the free surface , n is a complex refractive index of the medium, z, $\partial n/\partial \eta$, $\partial \eta$ are the direction of propagation, the photoelastic coefficient and the strain deformation, respectively. In reflectometry the modulus of Eq. (1.7) stands for the magnitude of the intensity of the

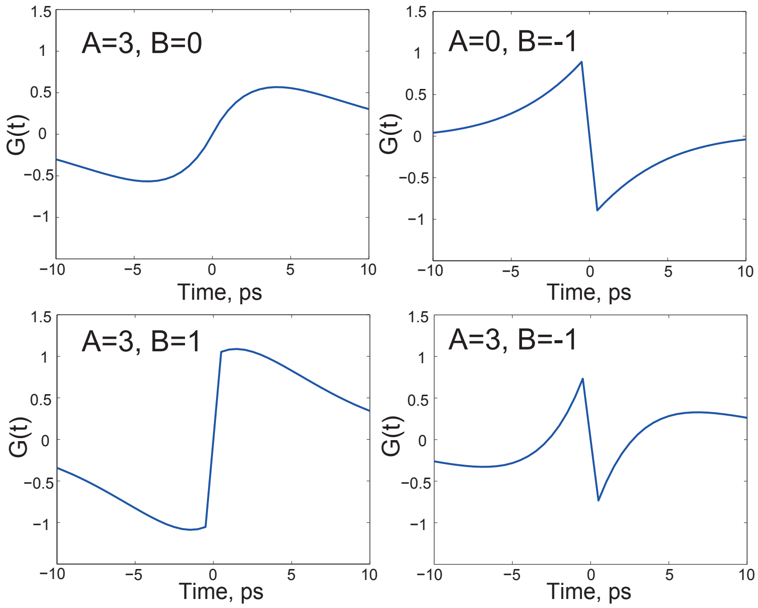

Fig. 1.5: The transient reflectivity response function G(t) with different combinations of the sensitivity coefficients A and B.

reflected beam. This technique is suitable for detection of longitudinal and, with some additional selection rules [6], [39], shear acoustic waves. Thomsen [48] has shown that in fact $\Delta R(t)$ can be expressed in the form

$$\Delta R(t) = \int_0^\infty f(z)\eta(z,t)dz, \tag{1.8}$$

where $f(z)$ is a sensitivity function, defined in [48], that determines how strain changes the reflectivity response at different depth below the surface

$$f(z) = f_0[\frac{\partial n}{\partial \eta_{33}} sin(\frac{4\pi nz}{\lambda} - \phi)] + \frac{\partial k}{\partial \eta_{33}} cos(\frac{4\pi nz}{\lambda} - \phi)]e^{-z/\xi}, \tag{1.9}$$

where ξ is the optical skin depth of a probe beam at a wavelength λ, $0 \leq \phi \leq \pi/2$.

Generally $f(z)$ is an exponentially decaying function of two terms: (i) first sine-term A is a smooth function and (ii) the second cosine-term B which is characterized by a sharp shape. When a short strain pulse convolutes with the first term of Eq. (1.9), which is determined by the speed of sound in the medium and its optical constants, it outputs a smooth shape that does not contain information about the strain profile. However, the convolution of the second term with a sharp profile provides an integral of the pulse shape. Hence, the sensitivity function can preserve and output the shape of the reflectivity signal detected by a probe pulse. This shape will be different depending on the ratio between the first A and the second B term of the Eq. (1.9).

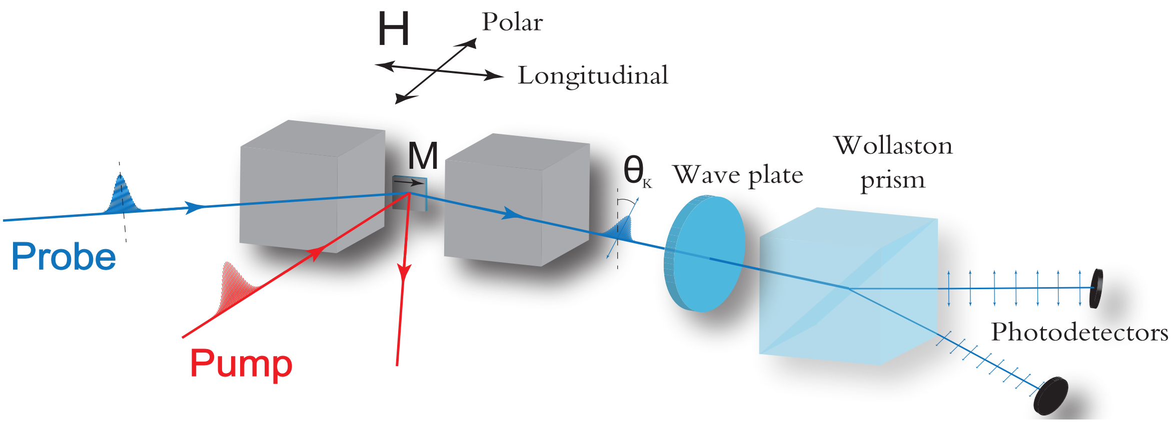

Fig. 1.6: Optical scheme for the detection of magneto-optical Kerr effect, identical to the optical scheme for the detection of shear acoustic waves.

Fig. 1.5 presents both terms A and B of the sensitivity function expressed in Eq. (1.9) for Terfenol (curves on the top row), considering different detection scenarios. Since there is a lack of data about the complex refractive index of Terfenol alloy, we used the data n = 2.9174, k = 3.3545 for Fe at λ = 800 nm [49]. The skin depth of the probe pulse is $\delta = \lambda/4\pi k =$ 19 nm. The sensitivity response corresponding to a detection scenario of B/A = 1/3 and B/A =-1/3, to the B term approaching to zero or the A term being very small are displayed in Fig. 1.5. The sensitivity function can lead to many different detected shapes of the acoustic strain pulse. It is straightforward from Eq. (1.9) that the shape of the transient reflectivity response can be defined and determined by the ratio of two terms, and can be expressed as [50]

$$B/A = \frac{\beta - \chi}{\beta\chi + 1}, \qquad \chi = \frac{\partial n}{\partial \eta_{33}} / \frac{\partial k}{\partial \eta_{33}}, \qquad \beta = (\frac{n}{k})\frac{n^2 + k^2 - 1}{n^2 + k^2 + 1}. \tag{1.10}$$

In the short-pulse limit, the second term B is dominant and the time derivative of the reflectivity response determines the acoustic strain profile. The first term A plays an important role with the time broadening of the pulse.

From the beginning of picosecond ultrasonics, longitudinal waves have been easily detected via interferometric, deflectometric or reflectometric techniques. However, in the case of shear acoustic waves, the detection is not always as straightforward. In 1976 Bauer et al. [51] proposed to measure the rotation of the probe polarization θ rather than ΔR induced by a shear acoustic wave. This detection method was called *depolarized Brillouin scattering* technique. It is also referred as an ellipsometric scheme [52] or MOKE detection, because of the identical experimental setups with MOKE detection in femtomagnetism, see Fig 1.6.

In such detection scheme, the polarization of the laser probe beam is analyzed upon reflection from the surface of a sample. Hence, depolarized Brillouin or MOKE detection scheme is a polarization dependent measurement. It consists of a half- or a quarter- waveplate, a Wollaston polariser, which is made of two prisms cemented together that splits an incident beam into two orthogonally polarized outputs separated by a separation angle. A pair of photodetectors mounted on the exit of the Wollaston prism detect the rotation or ellipticity change of the probe beam polarization. Initially balanced to 0, the optical bridge allows to detect the differential intensity obtained from two photodiodes, which is proportional to the rotation of polarization angle θ_K

$$I = I_{PD1} - I_{PD2}.$$

Sometimes a Glan-Taylor prism is used to separate s and p polarized light. It reflects s-component on the air-gap between two prisms and transmits purely p-polarized one. In current experiments we used the set-up based on a Wollaston polarizer and two-channel balanced photodiodes. In the case of an opaque substrate coated with a transparent isotropic film the photoelastic detection analysis in the film is simplified due to the fact that such film supports only pure shear or longitudinal polarizations. Strain propagating along the normal of the film (z-axis) has nonzero shear components $\eta_4 = 2\eta_{yz}$ or $\eta_5 = 2\eta_{xz}$ and a longitudinal component $\eta_3 = \eta_{zz}$. These modulate the permittivity tensor ε of the isotropic film [41]

$$\Delta\varepsilon = \begin{bmatrix} P_{12}\eta_3 & 0 & P_{44}\eta_5 \\ 0 & P_{12}\eta_3 & P_{44}\eta_4 \\ P_{44}\eta_5 & P_{44}\eta_4 & P_{11}\eta_3 \end{bmatrix}.$$

where P_{11}, P_{12} and $P_{44} = (P_{11} - P_{12})/2$ are photoelastic tensor components [53]. The coupling of $\Delta\varepsilon$ to shear strain is off diagonal and involves the suffix z, the corresponding induced change in probe polarization depends only on the z component of the probe light electric field. Thus, it is important to emphasize proper selectivity rules that must be utilized for the detection of shear acoustic waves [6]:

1. Oblique optical incidence of the probe beam is mandatory for detection of the SW. Hence, the detection efficiency is higher at greater angles of probe incidence and reaches its maxima at 90 degrees. This condition derives from proportionality of the shear photo-elastic term and in-plane projection of the probe wavevector.

2. Direction of the SW acoustic polarization must be perpendicular to the plane of

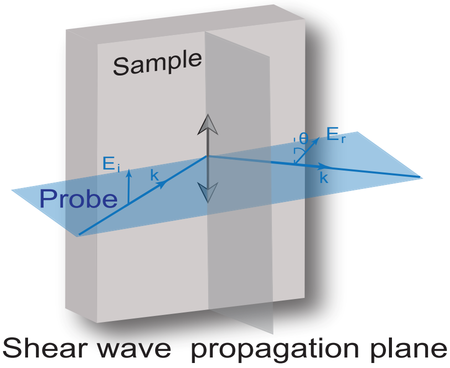

Fig. 1.7: Illustration of shear acoustic waves detection conditions.

incidence of the probe beam Fig. 1.7.

3. S polarized incident light is scattered to P polarized light and vice versa. SW rotate the probe polarization, they do not induce any ellipticity at the contrary to magnetized samples.

In summary, depolarized Brillouin scattering technique is a reliable tool to detect shear strain waves by measuring the rotation of the probe beam polarization. Together with the selection rules it has been utilized for the detection of shear acoustic waves in the experimental part of the thesis.

1.3 Ultrafast magnetoacoustics

In femtomagnetism laser-generated photons are used to control the magnetization state of a magnetic material. Another way to manipulate the magnetization at ultrafast timescale was reported in [54] by Sherbakov et al. Injection of GHz acoustic pulses into thin films of a ferromagnetic semiconductor at 1.6 K induces a tilt of its magnetization $\overrightarrow{M}$, that triggered coherent precession Fig. 1.8 (a). Picosecond strain pulses were generated in a 100-nm thick Al film deposited on the back side of a GaAs substrate. Time-resolved evolution of the Kerr rotation angle $\Delta\varphi(t)$ have been measured at different applied magnetic fields, where t=0 corresponds to the time of arrival of the strain pulse into the GaAs layer. Oscillations with a frequency of about 10 GHz are clearly distinguished after t>150 ps, when the strain pulse has already traversed the ferromagnetic layer. These oscillations are damped at about 1 ns, their frequency and amplitude depend on the applied magnetic field. Kerr signal obtained at H=0.8 kOe, where the low-frequency oscillations have the highest amplitude, is shown in Fig. 1.8 (b). Low frequency oscillations are present only if a magnetic field is applied, and they vanish at

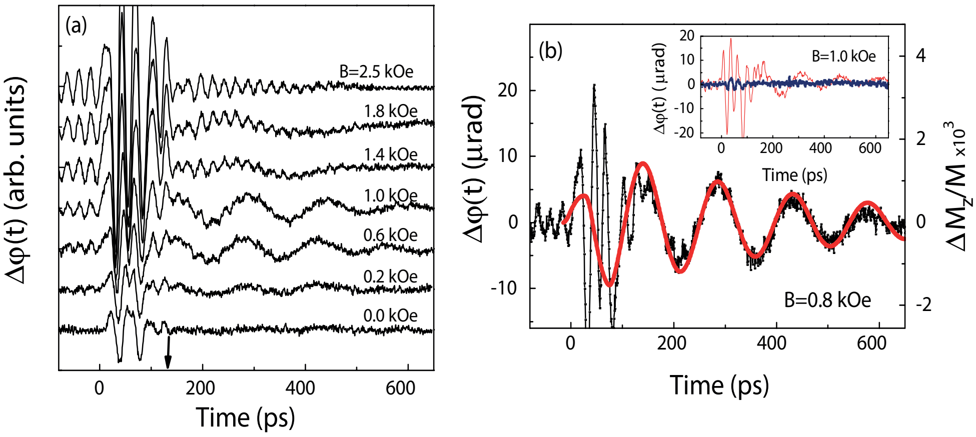

Fig. 1.8: Key results of [54] showing strain pulse-induced Kerr angle measured at various magnetic fields.

magnetic fields above 2.5 kOe. High frequency oscillations have an acoustic origin while low-frequency oscillations of $\Delta\varphi(t)$ are the feature of the modulation of M_z in the GaAs layer. These oscillations appear due to the strain-induced tilt of the magnetization $\overrightarrow{M}$, followed by a coherent precession of $\overrightarrow{M}$ around its equilibrium direction. The oscillation frequency in the GHz range is typical for such precession, as it was further confirmed by the ferromagnetic resonance FMR experiments.

In the last years this topic has attracted more attention in the community [55], [56]. In [57] it was shown that quasilongitudinal and quasitransverse ultrasonic pulses injected into a ferromagnetic (311) (Ga,Mn)As film induce dynamical shear strain in the film, thereby modulating the magnetic anisotropy and inducing resonant precession of the magnetization at a frequency ∼10 GHz. Kim et al. [58] have shown the transient reorientation and precession of the magnetization of ferromagnetic Ni films at room temperature by acoustic pulses. This effect is explained in terms of the three temperature model. The equation of the strain wave propagation and magnetization dynamics are quantitatively described by the magnetoacoustic Landau-Liftshitz-Gilbert equation [59]. Theoretical modeling of Terfenol-D thin film in [60] shows the out-of-plane deviation of magnetization vector followed by its precession after action of ultrafast acoustic pulses [61]. Terfenol-D free energy density possesses biaxial anisotropy, thus four in-plane energy minimum. If an out-of-plane "kick" exceeds the ∼ 20-degree threshold value, the magnetization decays into another minimum, i.e. switching occurs. Manipulation of the magnetization by periodic excitation patterns (transient grating spectroscopy) is another example of ultrafast spin-lattice coupling [62],[63].

In the recent decade clear evidence of interaction of acoustic pulses with the magnetization state of different materials at picosecond time scale was introduced. However, emission of the acoustic pulses after ultrafast release of the magnetization upon excitation of a magnetic sample by a femtosecond laser pulse was not studied. For materials with low spin-lattice coupling, this inverse effect is relatively small and is often not considered. However, generation of up to several THz longitudinal coherent acoustic phonons during demagnetization of Fe/MgO films was reported [64], what is more important is that the lifetime of the detected acoustic pulses is comparable with the electron and spin termalization timescale. In the case of rare-earth-iron alloys due to strong bulk magneto-elastic coupling and magneto-crystalline anisotropy, generation of high frequency longitudinal and shear strain waves is expected. Terfenol ($TbFe_2$) is known as one of the most magnetostrictive materials, besides, it exhibits particularly large magneto-elastic anisotropy. Its magnetostrictive coefficients are $\lambda_{100} = +300 \times 10^{-6}$, $\lambda_{111} = +2460 \times 10^{-6}$ [10], it is clear that $\lambda_{100} \ll \lambda_{111}$. Due to these properties, Terfenol alloy is an ideal prototype to study laser-induced generation of picosecond shear acoustic pulses. Longitudinal phonons, generated by demagnetization of the sample as well, will act on top of the thermo-elastically generated ones. Thermo-elastic emission of the shear strains is not expected due to symmetry reasons in such samples. Only magnetostriction can lead to shear acoustic excitation. Moreover, the efficiency of generation of both modes is anisotropic and should depend on the initial experimental geometry.

Hence, the study of ultrafast magnetoacoustics in materials with strong magneto-elastic coupling such as Terfenol alloys is proposed in the present thesis. So called *"demagnetostriction"* is a process of generation of the shear and longitudinal picosecond acoustic pulses as a result of the laser-induced transient demagnetization of the magnetostrictive material. Fig. 1.9 gives the scope of the experimental approach utilized in the thesis.

Thin films of non-magnetic dielectric layers with well known optical and mechanical properties are deposited on top of the studied ferromagnetic Terfenol films and plays a role as an "acoustic delay line" to study the generated strain pulses. The Laser pump-probe experiment starts with (i) optical pumping of the $TbFe_2$ film within the optical skin depth by an intense femtosecond laser pump pulse, which leads to (ii) the transient demagnetization of the monocrystalline Terfenol film. It results in the release of the build-in static strains at picosecond timescale, thus longitudinal and shear acoustic pulses emerge. Direct emission of the shear phonons with a well defined acoustic polarization is a consequence of the high magneto-crystalline anisotropy of Terfenol films. (iii)

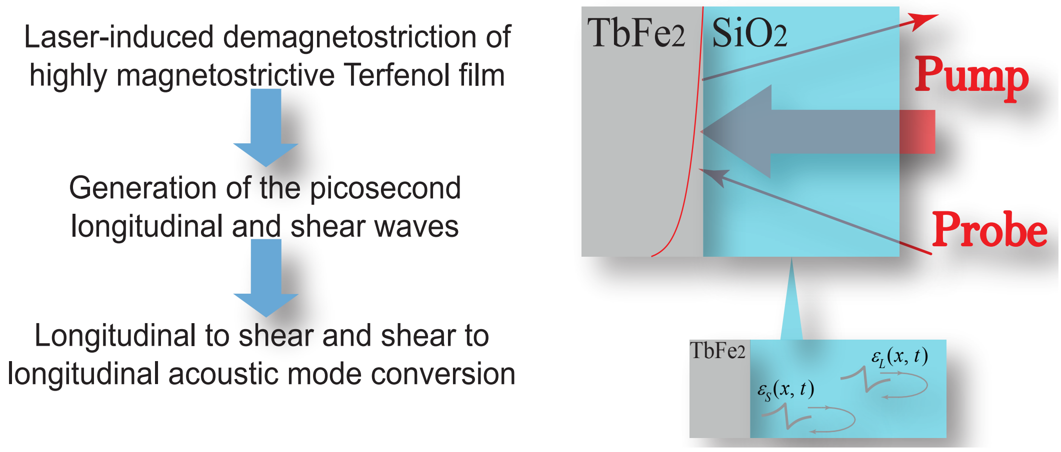

Fig. 1.9: Experimental approach proposed in the thesis.

Next, picosecond acoustic pulses are injected into the attached dielectric layer, where they propagate with different velocities υ_S and υ_L towards the free interface. They get reflected at the free surface and they arrive back to the interface, where they were initially generated, and get detected by time-delayed laser probe pulses. Thus, acoustic waves traverse a dielectric layer twice. (iv) Unexpected longitudinal to shear and shear to longitudinal acoustic mode conversion occurs at the interface of Terfenol upon reflection of the first acoustic wave packet into the ferromagnetic layer. Hence, the second picosecond shear strain pulse is generated and propagates through the acoustic delay line and so on. Since the velocities of both acoustic modes are precisely defined, the thickness of the dielectric layer is chosen so that longitudinal and shear echoes do not overlap in time.

In summary, ultrafast magnetoacoustics became a topic of high scientific interest during the last decade due to the unique potential in fundamental science and industrial applications, in the field of data storage and time resolved magnetic imaging. Notably, the modulation of the magnetization by GHz-THz acoustic pulses or emission of picosecond strain waves after laser-induced demagnetization of strongly correlated systems.

1.4 Conclusion

The physical frameworks of femtomagnetism, picosecond acoustics and ultrafast magneto-acoustics were overviewed in the context of this work. Laser-induced magnetization dynamics of magnetic materials consist of two contributions: incoherent, which occurs at sub-picosecond time scale and the following coherent precession of magnetization. Phenomenological 3TM and M3TM intuitively describe the optically-induced magnetization dynamics, however, a common basic model, which can be applied to all magnetic materials is still under debates. While the precession of magnetization can be excited by a visible pump pulse, detection in different spectral ranges by direct or indirect techniques provide additional information about the state of magnetization.

Laser-induced generation of coherent picosecond acoustic phonons were briefly reviewed. Excitation of longitudinal waves occurs in the general case of laser-matter interaction in solid medium. In this chapter main attention was focused on the non-trivial generation and detection of shear acoustic phonons. It has been shown that depolarized Brillouin scattering technique is a reliable tool for the detection of shear strain waves by measuring the rotation of polarization of the probe beam. Additional selectivity rules define our experimental geometry, which will be utilized during the experiments in the next Chapters.

Manipulation of the magnetization state of magnetic materials is possible not only by laser pulses, but also by GHz acoustic waves. The experimental approach proposed in this thesis is based on the inverse effect i.e. direct magnetostriction. The laser-induced demagnetization of the strongly magnetostrictive Terfenol alloy leads to the excitation of picosecond longitudinal and shear acoustic pulses. Study of the inverse magnetostriction effect will be possible after the subsequent injection of ultrasonic pulses into the ferromagnetic film.

The role of the acoustical phonons at ultrafast timescale is most of the time neglected. However, it is expected to influence the demagnetization process in highly magnetostrictive materials (e.g. rare-earth based alloys). Regarding the strong spin-orbit coupling of RE ions, the spin-lattice relaxation channel should be taken into account for the description of ultrafast laser-induced demagnetization events in RE-based compounds. In this scope, a study of the spin-lattice coupling in a Terfenol alloy via demagnetostriction process at picosecond timescale is of particular interest. A phenomenological model and the experimental results obtained on Terfenol/dielectric hybrid samples will be presented in the next Chapter.

CHAPTER 2

Ultrafast magnetoacoustics in Terfenol

The main goal of this thesis is to study the laser-induced generation of picosecond shear acoustic waves in materials with strong magneto-elastic coupling such as Terfenol alloys. The following chapter introduces the phenomenological description of the direct and inverse magnetostriction effects and gives a comparison of the magnetostriction coefficients of different ferromagnetic materials and alloys. Laser pump-probe experiments have been performed on $TbFe_2/SiO_2$ bi-layered structures deposited on Sapphire or CaF_2 substrates. We have experimentally demonstrated picosecond laser-induced demagnetization of monocrystalline $TbFe_2$ thin films, simultaneous generation of strain waves, which propagate through an attached dielectric silica dioxide layer and undergo intermode conversion from longitudinal to shear and vice versa in the skin-depth of Terfenol.

In the first section, the electron structure and magnetism of Terbium and Iron elements are reviewed. Large magnetostriction of Terfenol is caused by the strong anisotropy of the bound $4f$ electrons of Terbium. Next, the phenomenon of direct magnetostriction is reviewed through semi-quantitative phenomenological and mechanistic approaches. The observed magneto-elastic response of Terfenol thin films is interpreted within the framework of the mechanistic formalism. Laser-induced demagnetization of Terfenol and subsequent coherent magnetization dynamics are monitored by measuring transient Kerr rotation $\Delta\theta(t)$ and ellipticity $\Delta\phi(t)$. It is shown that the demagnetization timescale of Terfenol is influenced by the strong spin-lattice coupling of Terbium. Laser excitation of monocrystalline Terfenol films leads to the release of the build-in static strains, which then are injected into the attached dielectric layer. Lattice dynamics are monitored by the depolarized Brillouin scattering technique, which reveals a direct generation of the GHz shear and longitudinal acoustic modes. Efficiency of the shear acoustic wave excitation strongly depends on the experimental geometry, i.e. orientation of the Terfenol magnetization. Moreover, the laser excitation of the ferromagnetic film with strong magneto-elastic coupling leads to the generation of GHz circularly polarized acoustic waves. In addition, we have performed numerical simulation of the shear strain waves excitation in polycrystalline Terfenol films.

The effect of inverse magnetostriction in Terfenol is examined in the last section of this chapter. When the acoustic wave packet, generated by the demagnetostriction mechanism, reaches the ferromagnetic layer after its round trip in the dielectric, it provokes the reorientation of $\overrightarrow{M}$ and modifies the magnetic anisotropy field. Hence, it tilts $\overrightarrow{H}_{eff}$, which is directly coupled to the modification of the build-in static strains via the magneto-elastic energy. It causes excitation of a secondary wave packet with longitudinal to shear (L-S) or shear to longitudinal (S-L) modes, i.e. acoustic mode conversion after the injection of picosecond ultrasonic pulse in highly magnetostrictive film.

2.1 Direct magnetostriction of Terfenol thin films

Magnetostriction is a magneto-elastic phenomenon which causes a ferromagnetic materials to change its shape or dimensions upon magnetization/demagnetization process, i.e. it couples changes of the magnetization and mechanical deformations of a magnetic material. Elastic degree of freedom is introduced in the system upon a change of magnetization and vice versa - mechanical deformation induces modification of its magnetic properties. It is a result of the interaction of the magnetic anisotropy, elastic and exchange energies of the material. Two types of magnetostrictive phenomenon should be distinguished: (i) *spontaneous* and (ii) *Joule magnetostriction*. In its turn, there are direct and inverse Joule magnetostriction. A particular case of a ferromagnetic Terfenol film of cubic symmetry is considered in this section.

The intrinsic spontaneous magnetostriction occurs in each domain of a magnetic material at the temperature that is below its Curie temperature even in the absence of an external magnetic field. It is still not well understood and often described as Invar anomalies [65]. It has been observed in various intermetallic compounds, rare-earth metals and rare-earth compounds. In ferromagnetic cubic materials, this distortion is of the order of 10^{-5} for transition metals and about 10^{-3} for rare-earth compounds. The difference of two orders of magnitude is explained by the strong anisotropy energies of rare-earth metals. Hence, every domain is distorted in a spontaneous way along different directions that results in zero total deformation. Forced or Joule magnetostriction occurs in materials in the presence of an external magnetic field that aligns all magnetic domains in one particular direction, so they form one single domain. This effect can be observed at the macroscopic scale.

Magnetoelasticity can be described by two approaches: (i) a *semi quantitative phenomenological*, based on the Heisenberg-Weiss theory [66] and *mechanistic* approaches. In [67] Heisenberg used quantum mechanics to improve and quantify the model for the ferromagnetic system taking into account the previous work of Weiss [68]. It was demonstrated that the "molecular field" of Weiss theory was not actually a magnetic field, but represents the exchange energy stabilizing the parallel spin orientation. An analogous interaction can be applied to the Terfenol system, where the spin moment can be envisioned as rigidly attached by strong spin-orbit coupling to the anisotropically shaped 4f electron charge cloud. A consequence of this "crystal field energy" is the tendency of the magnetic moment to be stabilized along a particular crystalline direction due to the electrostatic attraction or repulsion between its attached electronic charge distribution and the neighbouring charged ions [69]. (ii) The second mechanistic approach describes another point of view on the model of the composites macroscopic behaviour. Magnetostrictive materials exhibit a coupled response between their elastic and magnetic behaviours, which occurs through a modification of the free energy density F_t of the crystal in the form,

$$F_t = F_k + F_e + F_z + F_{ex}. \tag{2.1}$$

It is described by the sum of several components: magneto-crystalline anisotropy F_k, elastic F_e, Zeeman F_z and exchange energies F_{ex}. In the case of ferromagnetic materials, some contributions can be omitted: dipole-dipole energy is much lower than exchange energy, thus its contribution to the total free energy density is neglected. Exchange coupling between *Tb* and *Fe* moments is about 300 T [70], so we presume that the moments keep their original ferromagnetic configuration. The film thickness is assumed to be large enough (minimum 50 nm in this work) for exhibiting the spherical symmetry, thus surface effects can be neglected. The expression of the magneto-crystalline anisotropy energy can be written using Taylor series expansion

$$F_k(m, \varepsilon_{ij}) = F_a + F_{me}(m, \varepsilon_{ij}), \tag{2.2}$$

where F_a is an anisotropy energy which represents energy required to flip magnetization between different crystalline axes. In the case of cubic symmetry its lower order term is expressed as

$$F_a = K_1(m_1^2 m_2^2 + m_2^2 m_3^2 + m_3^2 m_1^2), \tag{2.3}$$

where K_1 is an anisotropy constant ($K_1 = -7.6$ MPa for $TbFe_2$ [10]), m_i is a direction cosines of the unit vector m, that lies along the magnetization $\overrightarrow{M}$. F_{me} is the magneto-elastic energy and ε_{ij} is the deformation tensor in Cartesian system of coordinates. The magneto-elastic energy is expressed, utilizing only the second order terms of m, as

$$F_{me} = \sum_{ij}\sum_{\nu\mu}(b_{ij})_{\nu\mu}m_\nu m_\mu \varepsilon_{ij}, \tag{2.4}$$

where b is the tensor of magnetoelastic interaction constants (magnetoelastic constants). The lowest term of the elastic energy has the form

$$F_e = \frac{1}{2}\sum_{ijkl} c_{ijkl}\varepsilon_{ij}\varepsilon_{kl}, \tag{2.5}$$

where c_{ijkl} are the elastic constants. The Zeeman energy which describes the potential energy of a magnetic material in presence of an external magnetic field is

$$F_z = -M_s(mH_i), \tag{2.6}$$

where M_s and H_i are the saturation magnetization and demagnetizing fields, respectively. In case of a cubic symmetry, the exchange energy has the form

$$F_{ex} = \frac{1}{2}H_{ex}a^2M_s((\nabla m_x)^2 + (\nabla m_y)^2 + (\nabla m_z)^2), \tag{2.7}$$

where a is the lattice constant, H_{ex} is the phenomenological exchange field. Terfenol crystal possesses a cubic symmetry. If its crystallographic axes [100], [010], [001] coincide with the right handed x, y, z axes of the Cartesian coordinate system, Eq. (2.4) and Eq. (2.5) can be simplified to

$$\begin{aligned} F_{me} &= b_0(\varepsilon_{xx} + \varepsilon_{yy} + \varepsilon_{zz}) + b_1(m_x^2\varepsilon_{xx} + m_y^2\varepsilon_{yy} + m_z^2\varepsilon_{zz}) \\ &+ b_2(m_xm_y\varepsilon_{xy} + m_xm_z\varepsilon_{xz} + m_ym_z\varepsilon_{yz}), \end{aligned} \tag{2.8}$$

where b_0, b_1, b_2 represent isotropic, tetragonal and rhomboidal magneto-elastic constants, respectively.

$$F_e = \frac{1}{2}c_{11}(\varepsilon_{xx}^2 + \varepsilon_{yy}^2 + \varepsilon_{zz}^2) + c_{12}(\varepsilon_{xx}\varepsilon_{yy} + \varepsilon_{xx}\varepsilon_{zz} + \varepsilon_{yy}\varepsilon_{zz}) + \frac{1}{2}c_{44}(\varepsilon_{xy} + \varepsilon_{xz} + \varepsilon_{yz}), \tag{2.9}$$

where c_{11}, c_{12}, c_{44} are the elastic constants of the cubic crystal, ε_{ij} is the elastic strain tensor. Unlike the magneto-elastic energy, see Eq. (2.8), the elastic energy is independent on the magnetization and introduces a positive contribution to the total free energy density.

The relative length change Δl along an arbitrary axis at some orientation of magnetization (direction cosines m_i) is given by

$$\frac{\Delta l}{l} = \sum_{ij} \varepsilon_{ij} m_i \beta_j. \tag{2.10}$$

Eq. (2.10) shows the relation between the static strain components ε_{ij} and the magnetization directions cosines m_i. These equilibrium strains minimize the sum of magneto-elastic Eq. (2.8) and elastic Eq. (2.9) energies with respect to the strains ε_{ij}. They can be written in the form,

$$\varepsilon_{ii} = \frac{-b_0}{c_{11}+2c_{12}} + \frac{-b_1 m_i^2}{c_{11}-c_{12}} + \frac{c_{12}b_1}{(c_{11}+2c_{12})(c_{11}-c_{12})}, \tag{2.11}$$

$$\varepsilon_{ij} = \frac{-b_2 m_i m_j}{c_{44}}. \tag{2.12}$$

The substitution of the longitudinal and shear strains of Eq. (2.11) and Eq. (2.12) into the expression of the magnetically-induced relative length change of Eq. (2.10) results in

$$\begin{aligned} \frac{\Delta l}{l} &= \lambda_\alpha + \frac{3}{2}\lambda_{100}(m_x^2\beta_x^2 + m_y^2\beta_y^2 + m_z^2\beta_z^2 - \frac{1}{3}) \\ &+ 3\lambda_{111}(m_x\beta_x m_y\beta_y + m_x\beta_x m_z\beta_z + m_y\beta_y m_z\beta_z), \end{aligned} \tag{2.13}$$

where λ_α, λ_{100}, λ_{111} are the magnetostriction constants which represents relative changes in the material shape upon the applied external magnetic field.

Fig. 2.1 schematically depicts the forced magnetostrictive distortions of the cubic unit cell. The constant $\lambda_\alpha = -(b_0 + b_1/3)/(c_{11} + 2c_{12})$ in Fig. 2.1 (a) describes the pure volume magnetostriction that is isotropic and independent of the magnetization direction. This term is often omitted in the expression 2.13. The constant λ_{100} (λ_γ) in Fig. 2.1 (b) is the relative deformation along [100] axis, when the magnetization lies

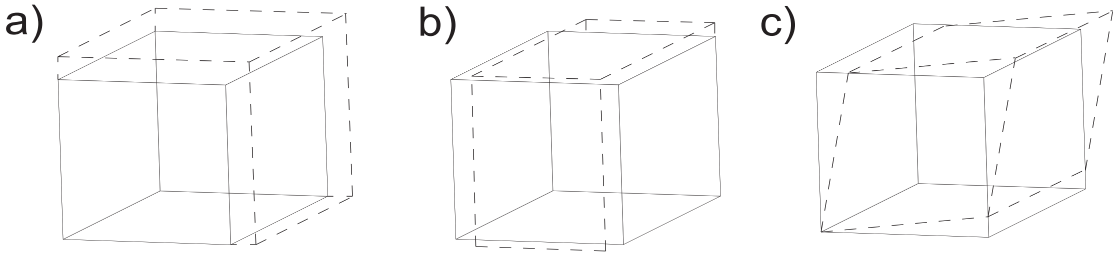

Fig. 2.1: Magnetostrictive distortions of the cubic unit cell a) λ_α, b) λ_γ, c) λ_ε. Dashed line represents the material shape after application of the magnetic field.

along this direction. The constant λ_{111} (λ_{ε}) in Fig. 2.1 (c) represents the rhomboidal distortion that stands for the fractional change in length $\Delta l/l$ along the [111] direction, when the magnetic field is applied along the same crystallographic direction.

$$\lambda_{[100]} = \frac{-2b_1}{3(c_{11} - c_{12})}, \tag{2.14}$$

$$\lambda_{[111]} = \frac{-b_2}{3c_{44}}. \tag{2.15}$$

The phenomenological model, which assumes an atomic origin of the anisotropic magnetostrictive distortion of the cubic *Laves C15* compounds, was proposed by Clark [10]. According to it, the main origin of the strong magnetocrystalline anisotropy of Terfenol alloy is an asymmetry of the Terbium 4f electron cloud.

An existence of two inequivalent tetrahedral sites of the C15 structure allows internal deformation along [111] direction. Since [111] is a diagonal of the cube, this distortion lowers the symmetry and drives an external rhombohedral deformation ($\lambda_{[111]}$), see Fig. 2.1 (c). The distortion along [111] axis is described on Fig. 2.2 (a): two inequivalent tetrahedral sites, situated at $0, 0, 0$ and $\frac{1}{4}, \frac{1}{4}, \frac{1}{4}$, are denoted by $A(A')$ and $B(B')$, respectively. The material is magnetized along [111], an oblate $4f$ electron cloud $(-e)$ lies perpendicular to the magnetization axis. Considering only the electrostatic interaction, the closer location of the $4f$ electron cloud on A to atoms B' than to B causes an extension of the $A - B$ bound. Its magnitude depends on the internal $A - B$ modulus. As a result, an increase of the distance a exceeds a small decrease in the length b, yielding positive external magnetostriction. Potentially high $\lambda_{[100]}$ arises from

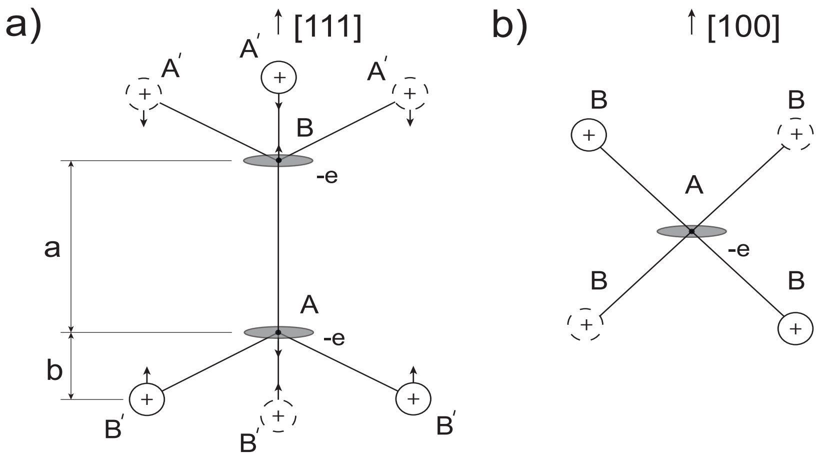

Fig. 2.2: Model of magnetostriction in rare-earth iron Terfenol [10] with the magnetization M aligned along its a) [111] and b) [100] crystallographic axes. Open and broken circles denote atoms above and below the plane of figure, respectively. The iron atoms are not shown.

the asymmetry of the rare-earth $4f$ electron shell, which is significantly shorted out due to the high tetrahedral ($\bar{4}3m$) symmetry at the lanthanide sites. When the magnetic field is applied along the [100] direction, $4f$ electron cloud becomes equidistant to all rare earth nearest neighbors and do not allow magnetostrictively-driven internal deformation via point charge electrostatic interactions. $A - B$ bounds are equivalent, thus symmetry remains high, see Fig. 2.2 (b), consequently the magnetostriction constant $\lambda_{[100]}$ is low.

The magnetostrictive materials can be classified in two types according to their microstructure: (i) crystalline and (ii) amorphous. Unlike amorphous media, crystalline magnetostrictive materials possess large saturation strains. They are represented mainly by the metallic and rare-earth based compounds. 3d transition metals and their alloys were among the first studied materials. They don't exibit big magnetostriction coefficients by themselves. On the contrary, so-called giant magnetostrictive materials have extremely large magnetostriction coefficients (in order of 10^{-2} for Terbium and Dysprosium at cryogenic temperatures). Hence, highly magnetostrictive compounds (the magnetostrictive ferrites [71] and the RE-iron alloys [11]) have been developed on this basis. Values of the magnetostrictive constants of 3d metals Fe, Ni; Terfenol and Terfenol-D at room temperature are shown in Tab. 2.1 [72].

Terfenol possesses large magneto-elastic anisotropy $\lambda_{111} \gg \lambda_{100}$. In a single crystal of Terfenol, the magnetostriction strongly depends on the direction in which it is measured or in which lies the magnetization. Therefore, its behavior will be different, depending on the initial state of magnetization and the chosen direction (easy or difficult axis of the magnetization). There are other parameters which characterize the magneto-elastic coupling in the magnetic medium: saturation magnetostriction coefficient λ_s, magneto-mechanical coupling coefficient k_{33}, which represents the conversion efficiency between the magnetic and elastic energies, Curie temperature T_c. They are presented in Tab. 2.2. All of them depend on the manufacturing process and on the direction of the polarizing magnetic field.

Material	$\lambda_{100}(10^{-6})$	$\lambda_{111}(10^{-6})$
Fe	+19	-18.8
Ni	-46	-25
$TbFe_2$	+300	+2460
$Tb_{0,27}Dy_{0,73}Fe_2$	~ 100	+1620

Table 2.1: Magnetocrystalline anisotropy of cubic ferromagnetic crystals.

Material	$\lambda_s(10^{-6})$	k_{33}	T_c, $°C$
Fe	-9	0.3	770
Ni	-35	0.3	358
Co	-62	0.3	1130
$TbFe_2$	+1753	0.35	438
$Tb_{0,27}Dy_{0,73}Fe_2$	+1100	0.75	380

Table 2.2: Saturation magnetostriction λ_s, magneto-mechanical coupling coefficient k_{33} and Curie temperature T_c of some polycrystalline ferromagnetic materials [10].

Terfenol alloy possesses the strongest positive magnetostriction coefficient. Hence, it is expected that laser-induced demagnetization of thin monocrystalline films of $TbFe_2$ will excite acoustic waves the most efficiently among other magnetostrictive materials.

2.1.1 Terfenol hybrid sample

The typical hybrid sample, studied in this thesis, is composed of a monocrystalline Terfenol film coated with a fused silica dielectric layer. In-plane and out-of-plane magnetized ferromagnetic films were deposited with the molecular beam epitaxy technique at Institut Jean Lamour (IJL) in the group of K. Dumesnil, see Fig. 2.3 (a) and (b). The fabrication process of the in-plane magnetized films consists of several steps. $(11\bar{2}0)$ sapphire (Al_2O_3) wafer was chosen as a substrate. It was preliminary outgazed for several hours at 1070 K, then covered by 500 Å of Nb (110) buffer layer at 1070 K. A single atomic layer of Fe was then deposited at the top at 820 K, followed by the deposition of single crystals (110) $TbFe_2$ thin films. CaF_2 substrates were utilized in the case of (111) out-of-plane magnetized films in Fig. 2.3 (b). It was heated to 873 K and annealed at the same temperature. Then 200 Å of Mo buffer layer was deposited at 973 K. The substrate was cooled to 933 K, and (111) $TbFe_2$ films were grown at this temperature [73]. Afterwards, a capping layer of several nm thick Ti or Au was deposited on top of the Terfenol film to prevent oxidation. Later on, in both cases, the structure was coated with a transparent dielectric layer of SiO_2, which plays a role of an "acoustic delay line". SiO_2 was favored because of its well defined optical and mechanical properties [74], [75], [76]. Detailed samples fabrication process is described elsewhere [14].

The generation of the acoustic phonons occurs in the skin depth of the Terfenol layer, in the vicinity of the Terfenol/fused silica interface. Hence, it is important to understand how the acoustic pulses excited in Terfenol will be transmitted into fused silica. The acoustic impedances Z of our sample layers has been calculated to estimate

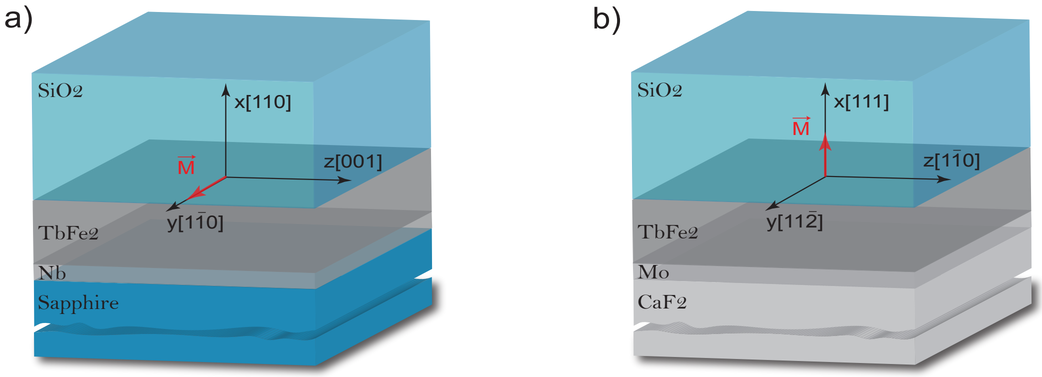

Fig. 2.3: Hybrid sample structure of a) in-plane and b) out-of-plane magnetized Terfenol thin films.

the acoustic reflection and transmission coefficients at different interfaces. Z is equal to the product of the material density ρ and the speed of sound υ

$$Z = \rho\upsilon. \tag{2.16}$$

Conditions of the continuity of the stress and of the acoustic displacement across the interface can be expressed as

$$1 + R = T, \tag{2.17}$$

$$(1 - R)/Z_1 = T/Z_2, \tag{2.18}$$

where R and T are the acoustic reflection and transmission coefficients, respectively. Z_1, Z_2 are the acoustic impedances of the attached materials, a negative sign of R in Eq. (2.18) means a reversal of the reflected acoustic wave polarity (compressive or tensile), with respect to the initial one. Now reflection and transmission coefficients of the acoustic stress at normal incidence can be expressed as

$$R = \frac{Z_2 - Z_1}{Z_2 + Z_1}, \tag{2.19}$$

$$T = \frac{2Z_2}{Z_2 + Z_1}. \tag{2.20}$$

Material	$\rho, kg/m^3$	$\upsilon_l, m/s$	$\upsilon_s, m/s$	Z_l	Z_s
$TbFe_2$ [10], [77], [78]	9170	4170	1980	38	18.15
SiO_2 [74]	2196	5970	3760	13,1	8,256
Nb [79]	8570	5068	2092	43,43	17,93
Al_2O_3 [80]	3980	10000	3988	39,8	15.87

Table 2.3: Mechanical properties of *Terfenol*, SiO_2, Nb, Al_2O_3 layers.

Since the conservation law should be satisfied (the integral of the strain should remain the same), the transmission of strain waves through the interface depend not only on the acoustic impedances, but also on the preserving factor equal to the ratio between the sound velocities in the adjacent layers υ_1/υ_2. This ratio increases or decreases the strain amplitude and shrinks or broadens its spatial profile, depending on υ_1 ans υ_2 values. The reflection and transmission coefficients of the longitudinal and shear acoustic strains at $TbFe_2/SiO_2$ interface were calculated using the data, listed in Tab. 2.3, and the expression

$$\eta_2(t) = [\frac{2Z_2}{Z_2 + Z_1}]\frac{\upsilon_1}{\upsilon_2}\eta_1(t), \tag{2.21}$$

where $\eta_2(t) = 0.73 \cdot \eta_1(t)$ and $\eta_2(t) = 0.4 \cdot \eta_1(t)$ for longitudinal and shear waves, respectively[1]. Hence, this simple analysis shows that strain pulses transmitted to the SiO_2 will be attenuated at the interface, but they preserve their sign and shape, while reflected waves will change their polarity upon reflection. The acoustic waves generated in the skin-depth of the Terfenol layer and propagating into the bulk will be initially transmitted to the buffer Niobium layer and then to the substrate without any significant reflection (reflection coefficients at $TbFe_2/Nb$ and $Nb/Sapphire$ interfaces are about 0.06 for longitudinal and shear waves). So, Terbium-Niobium and Niobium-Sapphire have almost perfect acoustic impedance matching because of the small values of strain amplitude upon the acoustic reflection at their boundaries. Thus, acoustic pulses reflected backwards from the $Nb/TbFe_2$ interface will not perturb the measurements. Moreover, the thickness of the substrate is much bigger (few mm) than the thickness of the $TbFe_2/SiO_2$ structure (about $1 - 1.5\ \mu m$), so the reflection of the strain at the free interface of sapphire can be also neglected due to the big temporal mismatch of the acoustic waves propagation in the substrate and SiO_2.

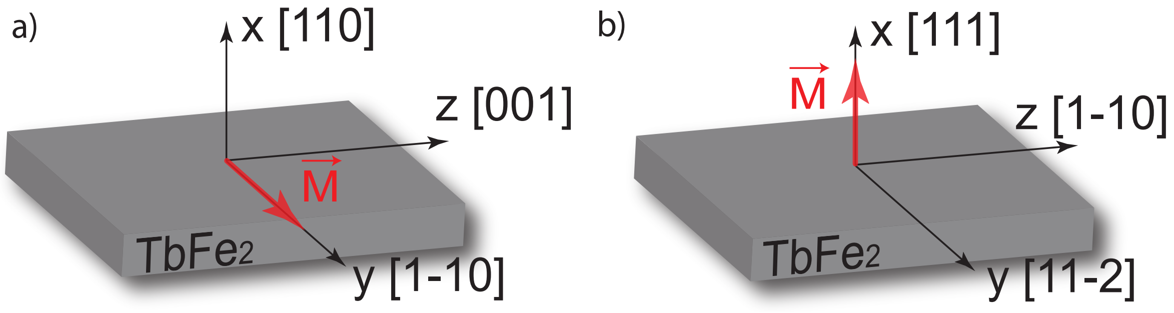

Fig. 2.4: Different crystallographic orientations of a) in-plane and b) out-of-plane magnetized single crystal Terfenol thin films.

---

[1] Mechanical properties of Terfenol-D were used to estimate the acoustic impedance of $TbFe_2$ due to the lack of data about Terfenol in the literature.

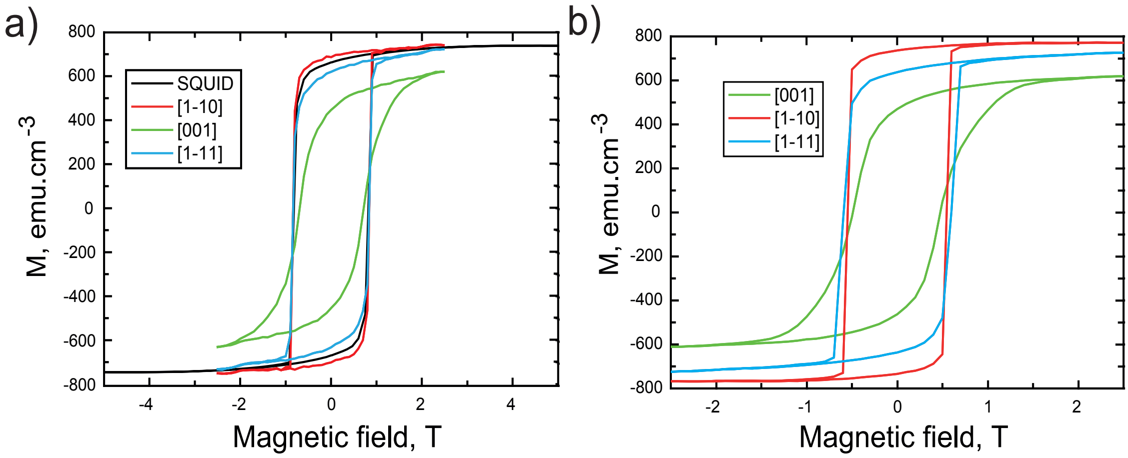

Fig. 2.5: Hysteresis loops of a) 50 nm, b) 300 nm thick in-plane magnetized Terfenol films. Measurements were performed at room temperature. Red, blue and green curves were measured by static MOKE.

The magnetization direction of the Terfenol film is selected by choosing a proper substrate/buffer cut. As a consequence, the in-plane and out-of-plane magnetized Terfenol films have different crystallographic orientations, see Fig. 2.4. (a) In the first case, the magnetization lies in the yz plane of the film, while in the second one (b), it is aligned along the normal to its surface (x axis).

In this scope, static magnetic properties of Terfenol films were studied[2]. These measurements give information about the magnetic hysteresis loops, magnetic anisotropy, orientation of magnetization, etc. The hysteresis loops of a 50 nm (see Fig. 2.5 (a)) and a 300 nm (b) in-plane magnetized Terfenol films were measured by the static MOKE and SQUID techniques. Measurements were performed in the longitudinal and transversal geometries, where the external magnetic field was applied parallel to the sample plane (along [001], $[1-10]$ in-plane axes and their diagonal $[1-11]$). Rectangular shape of the loops indicates an in-plane orientation of the magnetization vector. The coercive field varies depending on the orientation of the magnetic field. Fig. 2.5 reveals the magnetocrystalline anisotropy of the films. [001] and $[1\bar{1}0]$ are the hard and easy axes, respectively. The hysteresis loops show that the saturation magnetization for the $[1\bar{1}0]$ direction requires significantly lower field than for [001] one: ∼0.65 T and ∼2 T, respectively.

Static magnetic properties of a 150 nm thick out-of-plane magnetized Terfenol film were studied by the static MOKE, see Fig. 2.6. Hysteresis loops reveal [111] and $[1\bar{1}0]$ directions as an easy and hard axis, respectively. A coercive field of 1.5 T was found for out-of-plane [111] axis, similar values were found in [81], [82]. Hence, in-plane

---

[2] Static magnetic measurements were performed at IJL after deposition of the ferromagnetic Terfenol films.

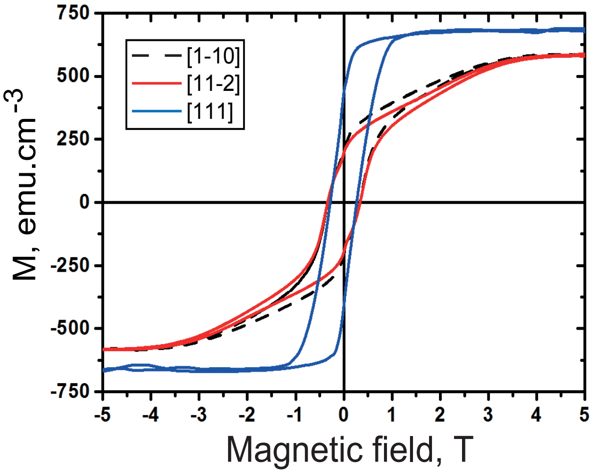

Fig. 2.6: Hysteresis loops of a 150 nm thick out-of-plane magnetized Terfenol film. Measurements were performed by static MOKE at the room temperature.

magnetized films are more appropriate for the study of magneto-acoustic effects due to lower saturation fields.

Incoherent magnetization dynamics

Study of laser-induced dynamics can be facilitated knowing the static properties of Terfenol films from the previous subsection. Photo-induced magnetization dynamics consists of incoherent and coherent contributions. First, laser excitation of a ferromagnetic Terfenol film on a non-conducting substrate is considered. The main goal is to disentangle spin-scattering processes responsible for the transient decrease of the Terfenol magnetization (demagnetization dynamics) and consequently determine their timescale.

Photo-induced magnetization dynamics were studied by *pump-probe technique*. In-plane magnetized sample of 300 nm $TbFe_2$/50 nm Nb/Al_2O_3(11$\bar{2}$0) has been excited at the free interface by an intense linearly polarized pump pulse (160 fs) at $\lambda_p = 800$ nm wavelength. The pump-induced magnetization dynamics is monitored by a ten times less intense time-delayed probe pulse of SHG frequency at $\lambda_p = 400$ nm wavelength. Pump and probe beams are focused on the sample surface at 45 and 5 degrees with respect to its normal. Measurements of the linear MOKE allow to monitor the laser-induced electron-phonon scattering and evolution of the magnetic properties. The laser-induced relative changes of the MOKE rotation $\Delta\theta$, ellipticity $\Delta\varphi$ and the linear reflectivity $\Delta R/R$ are presented in Fig. 2.7.

The magnetization dynamics during the first several picoseconds are governed by

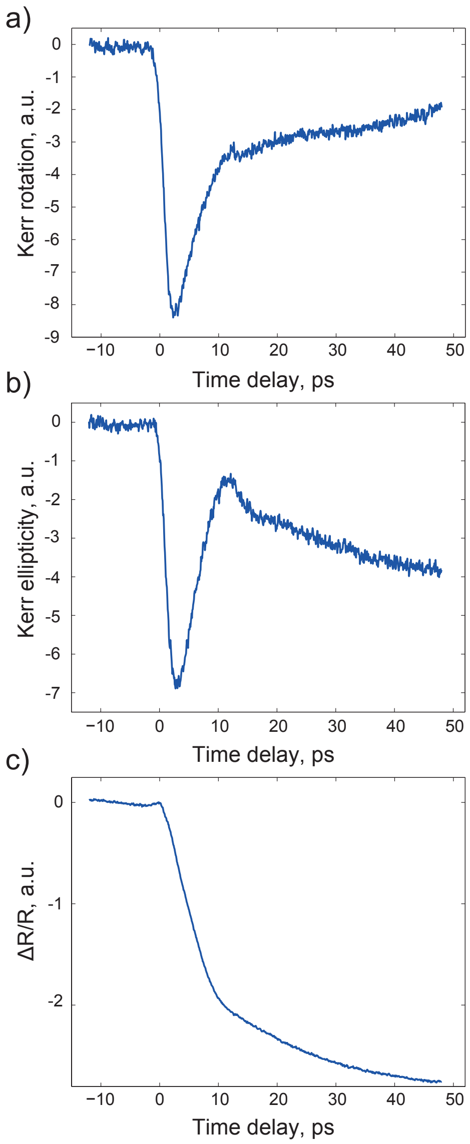

Fig. 2.7: Absolute variations of the a) MOKE rotation $\Delta\theta$, b) ellipticity $\Delta\varphi$ and c) reflectivity $\Delta R/R$ measured on a 300 nm $TbFe_2$ sample with H=7 kOe. Pump fluence was set at 5 mJ/cm^2.

the spin-flip processes. Subsequent relaxation of the magnetization occurs due to the slow heat diffusion from the excitation region into the bulk. The first 50 ps after sample excitation are shown in Fig. 2.7 with about 200 fs resolution. It reveals two step demagnetization process of the Terfenol film, containing ultrafast loss of the remanent magnetization within τ_1 =1.5 ps timescale, observed either in MOKE rotation or ellipticity. It reaches a minimum at Δt = 1.2 ps and relaxes towards its initial state within next τ_2 =40 ps. In comparison to pure transition metals with demagnetization timescales of several hundreds of femtoseconds, relatively long demagnetization time of 1.5 ps is, however, in a good agreement with the previous observation of 3d metals-rare-earth alloys [17], [83]. Such a long timescale is associated with the scattering events between electron, spin and lattice subsystems and their coupling in Terfenol. Two steps demagnetization process is typical for the pure rare-earth metals [84] and RE based compounds [17], [85]. An initial demagnetization occurs at τ_1=1.5 ps. The characteristic time constant of the second step strongly depends on the material. It is related to the coupling strength of the 4f magnetic moments and the lattice [85]: faster demagnetization occurs in materials with stronger coupling. Terbium possesses an orbital moment of L=3 with an anisotropic $4f^8$ orbital configuration (see Appendix B), which determines the strong spin-lattice coupling and efficiency of an angular momentum transfer to the lattice, therefore speeding up the demagnetization. The magnetization dynamics of $TbFe_2$ alloy, which consists of two sublattices, are described by two different microscopic mechanisms at different timescales. The phenomenological M3TM, which suggests Elliot-Yafet type spin-flip scattering in the laser mediated demagnetization, can explain this type of behavior. Though it doesn't take into account direct spin-lattice coupling of 4f magnetic moments, thus, it has to be expanded to include spin-lattice coupling and spin-orbit interaction.

Photoexcited electrons are expected to thermally equilibrate during the first 500 fs via electron-electron scattering. According to the characteristics of the transient reflectivity shown on Fig. 2.7 (c), this process is blurred by the electron and lattice subsystems energy transfer, which occurs within first 8 ps picoseconds. Transient reflectivity $\Delta R/R$ decays exponentially after the excitation and recovers to a constant value in several hundreds of picoseconds. Subsequently, energy flows from lattice to spin subsystem in a few picoseconds, as it is shown in Fig. 2.7 (a). Change of the electron T_e and lattice T_l temperatures at picosecond timescale alters the magneto-optical constants of the film [58], that explains the difference between the MOKE rotation $\Delta\theta$ and ellipticity $\Delta\varphi$ signals.

This experimental observation, along with the previous works in [85], [86], emphasizes the role of the spin-lattice coupling in ultrafast demagnetization of Terfenol. Its demagnetization timescale is much slower than that of pure transition metals (several hundreds of femtoseconds for Fe). Unlike pure iron, which magnetic moment has a delocalized character, the demagnetization timescale of $TbFe_2$ is dominated by the anisotropy of $4f$ orbital of the half-filled 4f shell of Tb and exceeds 1 ps. Several spin flips in the conduction band are required to obtain the same relative decrease of the magnetization as in 3d Fe during the transfer of angular momentum from the spin to the lattice subsystem [3], [29]. Hence, $TbFe_2$ is not suitable magnetic material to control its spin state in the subpicosecond regime due to significant contribution of spin-lattice relaxation of Tb in the demagnetization process. In the case of materials with strong

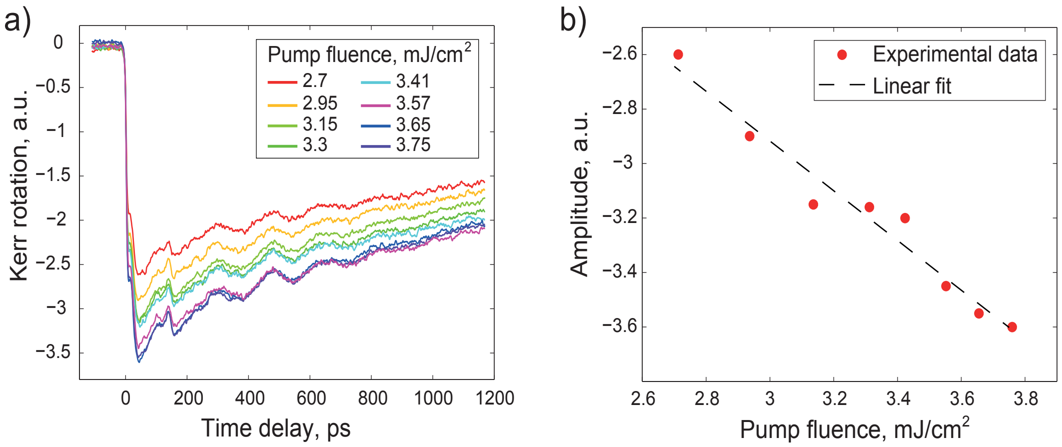

Fig. 2.8: a) Fluence dependent demagnetization of 300 nm Terfenol film measured at H=7 kOe. b) Demagnetization amplitude as a function of pump fluence.

magneto-elastic coupling it cannot be neglected .

Pump fluence dependent measurements were performed in order to check whether there is a threshold in the transient drop of the remanent magnetization of Terfenol films. Fig. 2.8 (b) presents the demagnetization amplitude as a function of the pump fluence, extracted at 5 ps time delay after the excitation. The linear distribution of the Kerr amplitudes shows that the saturation of demagnetization is probably not reached. The possible reason is a spatially inhomogeneous optical excitation of the thick (several hundreds of nm) ferromagnetic film. The periodic oscillations that appear after the first 50 ps are a weak signature of the coherent magnetization precession following the laser excitation. The pump pulse changes the magnitude of $\overrightarrow{M}$ and/or the film anisotropy due to heating, and alters the equilibrium orientation. The magnetization start to precess around a new equilibrium direction that is slowly restored due to heat diffusion.

Hence, the demagnetization timescale of Terfenol films is a two-step process involving energy equilibration and angular momentum transfer between *e*-*p*, *s*-*p* subsystems. Transient demagnetization of Terfenol is a starting point for the generation of acoustic strain waves. Build-in strains are released right after the change of magnetization, as a result of the magnetostrictive stresses in the material. An expected frequency bandwidth of the acoustic pulses will be associated with the demagnetization timescale of the ferromagnetic layer $\tau_1 \sim 1.5$ ps (~ 600 GHz). The incoherent demagnetization of Terfenol is followed by the coherent precession of its magnetization.

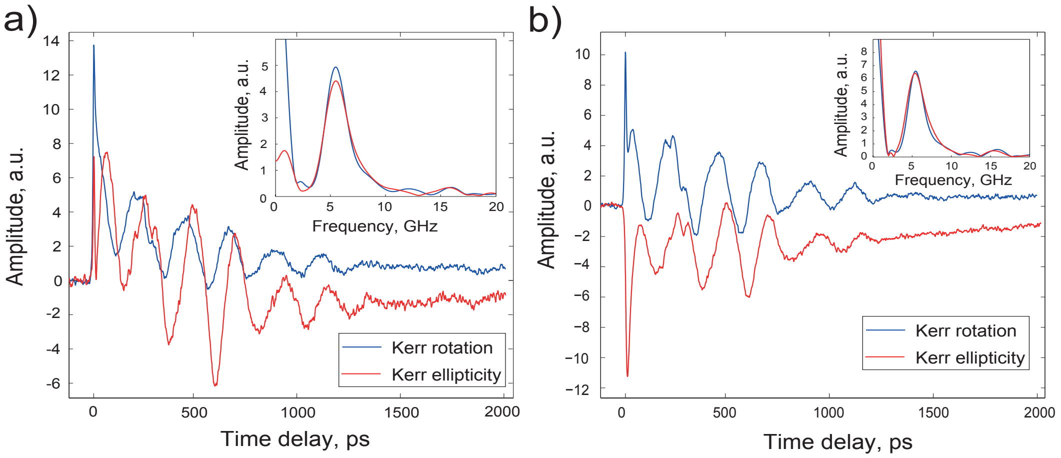

Fig. 2.9: Absolute variations of the MOKE rotation $\Delta\theta$ and ellipticity $\Delta\phi$ measured on a 300 nm $TbFe_2$ for opposite magnetic configurations a) $H_{out-of-plane}(H \rightleftarrows)$ b) $H_{in-plane}(H \uparrow\downarrow)$.

Coherent magnetization dynamics

Coherent photo-induced magnetization dynamics were monitored by measuring the linear MOKE. Experimental geometry is similar to the one used for the measurements of the incoherent dynamics. An in-plane magnetized sample of 300 nm $TbFe_2$ has been excited at the free interface by an intense linearly polarized pump pulse at $\lambda_p = 800$ nm wavelength. The precession of the magnetization was monitored by a tenfold weaker time-delayed probe pulse at $\lambda_p = 400$ nm wavelength. The angle of incidence of the pump and probe beam was 45 and 5 degrees, respectively, with respect to the surface normal.

The linear MOKE signal includes several contributions: ultrafast demagnetization induced by the pump pulse, coherent dynamics (precession) of magnetization and non-magnetic effects. In our experiments, the Kerr rotation and ellipticity are defined as a difference in rotation or ellipticity change of initially linearly polarized light for opposite orientations of the applied field H. Detection of the probe beam polarization rotation $\Delta\theta$ and change of its ellipticity $\Delta\varphi$ for two orthogonal magnetic field configurations $\pm H$ allows to disentangle purely magnetic contributions on the recorded Kerr signals, see Fig. 2.9. Arrows depict the orthogonal direction of the magnetization vector with respect to the plane of incidence of the probe beam. $H \uparrow\downarrow$, $H \rightleftarrows$ signifies the perpendicular and parallel applied external magnetic fields of 0.7 T with respect to the film surface. A homogeneous precession of the film magnetization is observed. It means that all magnetic moments in the probed region precess in-phase and the exchange interaction between them can be omitted. The complex Fourier transform of the observed oscillations has been performed in order to determine their frequency spectrum. Multiplication by a discrete Hann window function is then used for aliasing the spectrum, which emphasizes a 6 GHz precession frequency of the magnetization as shown in the insets of Fig. 2.9 (a) and (b). Hence, the laser-induced periodic magnetization precession of Terfenol can be laser excited in the GHz frequency range. This conclusion will be utilized in the discussions of the lattice dynamics in Terfenol.

Elastic energy for arbitrary direction of the crystallographic axes

Since the experimental crystallographic axes don't correspond to [100], [010], [001], see Fig 2.4, the modification of the elastic energy expressions for both in-plane and out-of-plane magnetized films is required (see Appendix C).

The (x', y', z') coordinate system is adapted for the $TbFe_2$ thin film as in Fig. 2.4. The counter-clockwise rotation around z axis by an angle ξ is required for the in-plane magnetized sample. The rotation matrix for transformation from (x, y, z) to the (x', y', z') coordinate system of the thin film have the form

$$R_z(\xi) = \begin{bmatrix} \cos\xi & \sin\xi & 0 \\ -\sin\xi & \cos\xi & 0 \\ 0 & 0 & 1 \end{bmatrix}.$$

The contracted matrix notations of the strain tensor components ε_{ij} is given by

$$\begin{bmatrix} \varepsilon_{xx} & \varepsilon_{xy} & \varepsilon_{xz} \\ \varepsilon_{yx} & \varepsilon_{yy} & \varepsilon_{yz} \\ \varepsilon_{zx} & \varepsilon_{zy} & \varepsilon_{zz} \end{bmatrix} = \begin{bmatrix} \varepsilon_1 & \frac{1}{2}\varepsilon_6 & \frac{1}{2}\varepsilon_5 \\ \frac{1}{2}\varepsilon_6 & \varepsilon_2 & \frac{1}{2}\varepsilon_4 \\ \frac{1}{2}\varepsilon_5 & \frac{1}{2}\varepsilon_4 & \varepsilon_3 \end{bmatrix}.$$

The transformation law of the elastic constants can be written as [87]

$$c'_{ij} = [M][c_{ij}][M]^T,$$

where $[c_{ij}]$ is the untransformed stiffness matrix, $[M]$, $[M]^T$ are the transformation and transposed transformation matrices, respectively. The cubic symmetry in Terfenol reduce the number of independent components of the matrix $[c_{ij}]$ to 3, and the transformed matrix of the elastic constants c'_{ij} of the in-plane magnetized film will follows [87]

$$c'_{ij} = \begin{bmatrix} c'_{11} & c'_{12} & c'_{13} & 0 & 0 & c'_{16} \\ c'_{12} & c'_{11} & c'_{13} & 0 & 0 & -c'_{16} \\ c'_{13} & c'_{13} & c'_{33} & 0 & 0 & 0 \\ 0 & 0 & 0 & c'_{44} & 0 & 0 \\ 0 & 0 & 0 & 0 & c'_{44} & 0 \\ c'_{16} & -c'_{16} & 0 & 0 & 0 & c'_{66} \end{bmatrix}.$$

where

$$c'_{11} = c_{11} - (\frac{c_{11} - c_{12}}{2} - c_{44}) \sin^2 2\xi,$$

$$c'_{12} = c_{12} - (\frac{c_{11} - c_{12}}{2} - c_{44}) \sin^2 2\xi,$$

$$c'_{13} = c_{12},$$

$$c'_{16} = -(\frac{c_{11} - c_{12}}{2} - c_{44}) \sin 2\xi \cos 2\xi,$$

$$c'_{33} = c_{11},$$

$$c'_{44} = c_{44},$$

$$c'_{66} = c_{44} + (\frac{c_{11} - c_{12}}{2} - c_{44}) \sin^2 2\xi.$$

In the case of counter-clockwise rotation around the z axis by an angle $\xi = -\frac{\pi}{4}$, the elements of the stiffness matrix $[c_{ij}]$ are

$$c'_{11} = \frac{c_{11} + c_{12}}{2} + c_{44}, \qquad c'_{12} = \frac{c_{11} + c_{12}}{2} + c_{44},$$

$$c'_{13} = c_{12}, \qquad c'_{16} = 0, \qquad c'_{33} = c_{11}, \qquad c'_{44} = c_{44},$$

$$c'_{66} = \frac{c_{11} - c_{12}}{2}.$$

Finally, the c'_{ij} in the thin film coordinates

$$c'_{ij} = \begin{bmatrix} c'_{11} & c'_{12} & c_{12} & 0 & 0 & 0 \\ c'_{12} & c'_{11} & c_{12} & 0 & 0 & 0 \\ c_{12} & c_{12} & c_{11} & 0 & 0 & 0 \\ 0 & 0 & 0 & c_{44} & 0 & 0 \\ 0 & 0 & 0 & 0 & c_{44} & 0 \\ 0 & 0 & 0 & 0 & 0 & \frac{c_{11}-c_{12}}{2} \end{bmatrix},$$

and the elastic energy written in the (x', y', z') coordinate system using Eq. (2.5) will have the form

$$\begin{aligned} F_e &= \frac{1}{2}[c_{11}(\frac{1}{2}\varepsilon^2_{x'x'} + \frac{1}{2}\varepsilon^2_{y'y'} + \varepsilon_{x'x'}\varepsilon_{y'y'} + 2\varepsilon^2_{y'x'}) \\ &+ c_{12}(\frac{1}{2}\varepsilon^2_{x'x'} + \frac{1}{2}\varepsilon^2_{y'y'} + \varepsilon_{x'x'}\varepsilon_{y'y'} + 2\varepsilon_{x'x'}\varepsilon_{z'z'} + 2\varepsilon_{y'y'}\varepsilon_{z'z'} - 2\varepsilon^2_{y'x'}) \\ &+ c_{44}(\varepsilon^2_{x'x'} + \varepsilon^2_{y'y'} - 2\varepsilon_{x'x'}\varepsilon_{y'y'} + 4\varepsilon^2_{y'z'} + 4\varepsilon^2_{z'x'})]. \end{aligned} \quad (2.22)$$

The x' axis was chosen as being normal to the surface. Only the strain waves, which are propagating along the x' direction are considered, hence, $\varepsilon_{y'y'} = \varepsilon_{z'z'} = \varepsilon_{y'z'} = 0$ and the Eq. (2.22) can be simplified to

$$F_e = \frac{1}{2}[c_{11}(\frac{1}{2}\varepsilon^2_{x'x'} + 2\varepsilon^2_{y'x'}) + c_{12}(\frac{1}{2}\varepsilon^2_{x'x'} + 2\varepsilon^2_{y'x'}) + c_{44}(\varepsilon^2_{x'x'} + 4\varepsilon^2_{z'x'})]. \quad (2.23)$$

Eq. (2.23) describes the elastic energy density of the in-plane magnetized Terfenol film. In the case of out-of-plane magnetized sample, analogous transformation of the crystallographic axes is required. First, a clockwise rotation of $\xi = \pi/4$ angle around the z axis is performed, so the rotation matrix will have a form similar to the previous case. Taking into account a positive direction of rotation it can be expressed as

$$R_z(\xi) = \begin{bmatrix} \cos\xi & -\sin\xi & 0 \\ \sin\xi & \cos\xi & 0 \\ 0 & 0 & 1 \end{bmatrix}.$$

The transformed matrix of the elastic constants c'_{ij} becomes

$$c'_{ij} = \begin{bmatrix} c'_{11} & c'_{12} & c_{12} & 0 & 0 & 0 \\ c'_{12} & c'_{11} & c_{12} & 0 & 0 & 0 \\ c_{12} & c_{12} & c_{11} & 0 & 0 & 0 \\ 0 & 0 & 0 & c_{44} & 0 & 0 \\ 0 & 0 & 0 & 0 & c_{44} & 0 \\ 0 & 0 & 0 & 0 & 0 & \frac{c_{11}-c_{12}}{2} \end{bmatrix}$$

where

$$c'_{11} = \frac{c_{11} + c_{12} + 2c_{44}}{2},$$

$$c'_{12} = \frac{c_{11} + c_{12} - 2c_{44}}{2}.$$

Second, a clockwise rotation about the y' axis by an angle η is required in order to bring

z' axis along the diagonal of the cube, wherein $\eta = \cos^{-1}(1/\sqrt{3})$ and the rotation matrix equals to

$$R_{y'}(\eta) = \begin{bmatrix} \cos\eta & 0 & -\sin\eta \\ 0 & 1 & 0 \\ \sin\eta & 0 & \cos\eta \end{bmatrix}.$$

Utilization of the transformation matrix of the Bond stress for clockwise rotation about y' axis with $\cos\eta = 1/\sqrt{3}$, $\sin\eta = \sqrt{2/3}$ allows to find the new form of the matrix of the elastic constants c''_{ij}

$$c''_{ij} = \begin{bmatrix} c''_{11} & c''_{12} & c''_{13} & 0 & c''_{15} & 0 \\ c''_{12} & c''_{11} & c''_{13} & 0 & -c''_{15} & 0 \\ c''_{13} & c''_{13} & c''_{33} & 0 & 0 & 0 \\ 0 & 0 & 0 & c''_{44} & 0 & -c''_{15} \\ c''_{15} & -c''_{15} & 0 & 0 & c''_{44} & 0 \\ 0 & 0 & 0 & -c''_{15} & 0 & c''_{66} \end{bmatrix}$$

where

$$c''_{11} = \frac{c_{11} + c_{12} + 2c_{44}}{2}, \qquad c''_{12} = \frac{c_{11} + 5c_{12} - 2c_{44}}{6},$$
$$c''_{13} = \frac{c_{11} + 2c_{12} - 2c_{44}}{3}, \qquad c''_{33} = \frac{c_{11} + 2c_{12} + 4c_{44}}{2},$$
$$c''_{15} = \frac{c_{12} - c_{11} + 2c_{44}}{3\sqrt{2}}, \qquad c''_{44} = \frac{c_{11} - c_{12} + c_{44}}{3},$$
$$c''_{66} = \frac{c_{11} - c_{12} + 4c_{44}}{6}.$$

The x axis is normal to the sample surface and it coincides with the direction of propagation of the acoustic waves. Thus, rotation about y'' axis on $\xi' = 90$ deg is required to bring the expression of the elastic energy in line with the case of in-plane magnetized sample. Bond transformation matrix for a rotation about y'' is given by

$$R_{y''}(\xi') = \begin{bmatrix} \cos\xi' & 0 & \sin\xi' \\ 0 & 1 & 0 \\ -\sin\xi' & 0 & \cos\xi' \end{bmatrix}.$$

The final expression of the elastic modulus tensor c_{ij}[3], reads

---

[3] Here and in the following c_{ij} will be used instead of c'''_{ij} for simplicity.

$$c_{ij} = \begin{bmatrix} c_{13} & c_{12} & c_{13} & 0 & -c_{15} & 0 \\ c_{12} & c_{11} & c_{13} & 0 & -c_{15} & 0 \\ c_{13} & c_{13} & c_{33} & 0 & 0 & 0 \\ 0 & 0 & 0 & c_{44} & 0 & -c_{15} \\ -c_{15} & c_{15} & 0 & 0 & -c_{44} & 0 \\ 0 & 0 & 0 & -c_{15} & 0 & c_{66} \end{bmatrix}.$$

The expression of the elastic energy density F_e for the out-of-plane magnetized films, written in the transformed coordinate system, is

$$\begin{aligned} F_e &= \frac{1}{2}[c_{13}\varepsilon^2_{x'x'} + c_{12}\varepsilon_{x'x'}\varepsilon_{y'y'} + c_{13}\varepsilon_{x'x'}\varepsilon_{z'z'} - c_{15}\varepsilon_{x'x'}\varepsilon_{x'z'} + c_{12}\varepsilon_{x'x'}\varepsilon_{y'y'} \\ &+ c_{11}\varepsilon^2_{y'y'} + c_{13}\varepsilon_{y'y'}\varepsilon_{z'z'} - c_{15}\varepsilon_{y'y'}\varepsilon_{x'z'} + c_{13}\varepsilon_{z'z'}\varepsilon_{x'x'} + c_{13}\varepsilon_{z'z'}\varepsilon_{y'y'} \\ &+ c_{33}\varepsilon^2_{z'z'} + c_{44}\varepsilon^2_{y'z'} - c_{15}\varepsilon_{y'z'}\varepsilon_{x'y'} - c_{15}\varepsilon_{x'z'}\varepsilon_{x'x'} + c_{15}\varepsilon_{x'z'}\varepsilon_{x'y'} - c_{44}\varepsilon^2_{x'z'} \\ &- c_{15}\varepsilon_{x'y'}\varepsilon_{y'z'} + c_{66}\varepsilon^2_{x'y'}]. \end{aligned} \tag{2.24}$$

The direction of the acoustic waves propagation coincides with the x' axis, so only three strains $\varepsilon_{x'x'}$, $\varepsilon_{x'y'}$, $\varepsilon_{x'z'}$ are considered. Now, Eq. (2.24) can be simplified taking to account $\varepsilon_{y'y'} = \varepsilon_{z'z'} = \varepsilon_{y'z'} = 0$, we obtain

$$\begin{aligned} F_e &= \frac{1}{2}[c_{13}\varepsilon^2_{x'x'} - \frac{1}{2}c_{15}(\varepsilon_{x'x'}\varepsilon_{x'z'} + \varepsilon_{x'z'}\varepsilon_{x'x'} - \varepsilon_{x'z'}\varepsilon_{x'y'}) - \frac{1}{2}c_{44}\varepsilon^2_{x'z'} + \frac{1}{2}c_{66}\varepsilon^2_{x'y'}] \\ &= \frac{1}{2}[(\frac{c_{11} + 2c_{12} - 2c_{44}}{3})\varepsilon^2_{x'x'} - (\frac{c_{11} - c_{12} + 2c_{44}}{6\sqrt{2}})(2\varepsilon_{x'x'}\varepsilon_{x'z'} - \varepsilon_{x'z'}\varepsilon_{x'y'}) \\ &- (\frac{c_{11} - c_{12} + c_{44}}{6})\varepsilon^2_{x'z'} + (\frac{c_{11} - c_{12} + 4c_{44}}{12})\varepsilon^2_{x'y'}] \\ &= \frac{1}{2}[\frac{1}{3}c_{11}\varepsilon^2_{x'x'} + \frac{2}{3}c_{12}\varepsilon^2_{x'x'} - \frac{2}{3}c_{44}\varepsilon^2_{x'x'} - \frac{1}{3\sqrt{2}}c_{12}\varepsilon_{x'x'}\varepsilon_{x'z'} + \frac{1}{3\sqrt{2}}c_{11}\varepsilon_{x'x'}\varepsilon_{x'z'} \\ &- \frac{2}{3\sqrt{2}}c_{44}\varepsilon_{x'x'}\varepsilon_{x'z'} + \frac{1}{3\sqrt{2}}c_{12}\varepsilon_{x'z'}\varepsilon_{x'y'} - \frac{1}{6\sqrt{2}}c_{11}\varepsilon_{x'z'}\varepsilon_{x'y'} + \frac{1}{3\sqrt{2}}c_{44}\varepsilon_{x'z'}\varepsilon_{x'y'} \\ &- \frac{1}{6}c_{11}\varepsilon^2_{x'z'} + \frac{1}{6}c_{12}\varepsilon^2_{x'z'} - \frac{1}{6}c_{44}\varepsilon^2_{x'z'} + \frac{1}{12}c_{11}\varepsilon^2_{x'y'} - \frac{1}{12}c_{12}\varepsilon^2_{x'z'} + \frac{1}{3}c_{44}\varepsilon^2_{x'y'}]. \end{aligned} \tag{2.25}$$

Regrouping of the strains and the elastic constants allows to write the final expression of the elastic energy density for the out-of-plane magnetized Terfenol films,

$$\begin{aligned} F_e &= \frac{1}{6}[c_{11}(\varepsilon^2_{x'x'} + \frac{1}{\sqrt{2}}\varepsilon_{x'x'}\varepsilon_{x'z'} - \frac{1}{2\sqrt{2}}\varepsilon_{x'z'}\varepsilon_{x'y'} - \frac{1}{2}\varepsilon^2_{x'z'} + \frac{1}{4}\varepsilon^2_{x'y'}) \\ &- c_{12}(\frac{1}{3}\varepsilon^2_{x'x'} - \frac{1}{\sqrt{2}}\varepsilon_{x'x'}\varepsilon_{x'z'} + \frac{1}{\sqrt{2}}\varepsilon_{x'z'}\varepsilon_{x'y'} + \frac{1}{2}\varepsilon^2_{x'z'} - \frac{1}{4}\varepsilon^2_{x'y'}) \\ &- c_{44}(\frac{1}{3}\varepsilon^2_{x'x'} + \frac{1}{3\sqrt{2}}\varepsilon_{x'x'}\varepsilon_{x'z'} + \frac{1}{\sqrt{2}}\varepsilon_{x'z'}\varepsilon_{x'y'} + \frac{1}{2}\varepsilon^2_{x'z'} - \varepsilon^2_{x'y'})], \end{aligned} \tag{2.26}$$

where ε_{ij} are the strains in conventional cubic coordinate system. The elastic constants of the $TbFe_2$ are unknown, however, $Tb_{0.3}Dy_{0.7}Fe_2$ (Terfenol-D) possesses similar lattice parameters, so its elastic constants probably do not differ a lot $c_{11} = 14.1 \times 10^{10}$ N/m^2, $c_{12} = 6.48 \times 10^{10}$ N/m^2, $c_{44} = 4.87 \times 10^{10}$ N/m^2 [88].

The expressions of the elastic energies for the in-plane Eq. (2.23) and out-of-plane Eq. (2.26) magnetized Terfenol films were derived. The arbitrary direction of acoustic waves propagation along the normal to the surface and the cubic symmetry of Terfenol crystal allow to do some simplifications of the final expressions. Together with the expressions of magneto-elastic energy densities they will be used in the determination of the static build-in strains in the Terfenol films, which are essential for the numerical simulations of the laser-induced strain waves amplitudes.

Magnetoelastic energy for arbitrary direction of magnetization and crystallographic axes

Following the previous paragraph, the general expression for the magneto-elastic energy density of Terfenol films with an arbitrary pointing magnetization can be obtained in a same manner. Modification of the [100], [010], [001] cubic crystal crystallographic axes into experimental (in-plane [001], $[1-10]$, [110] and out-of-plane $[1-10]$, $[11-2]$, [111] magnetized) ones leads to the transformation of the F_{me} expressions[4].

If the piezo-magnetic effect is absent or negligible in the sample, the magneto-elastic energy of the cubic crystal is governed only by magnetostriction. Following [89] in the case of arbitrary pointing magnetization vector, which does not coincide with the edge of ferromagnetic cubic unit cell, expression in Eq. (2.4) should be modified. For that the transformation coefficients $a_{i\nu}$ are introduced

$$e_i = \sum a_{i\nu} e_\nu, \tag{2.27}$$

where e_i, e_ν are the orthogonal unit vectors, oriented along the cube edges in the new coordinate system. The strains ε_{ij} and the magnetization direction cosines m_i will have the form

$$\begin{aligned} \varepsilon_{ii} &= \sum_{\nu\mu} a_{i\nu} a_{i\mu} e_\nu, \\ \varepsilon_{ij} &= \sum_{\nu\mu} (a_{i\nu} a_{j\mu} + a_{j\nu} a_{i\mu}) e_{\nu\mu}, \end{aligned} \tag{2.28}$$

---

[4] Coordinate system modification is identical to the one made for elastic energy density modification.

$$m_i = \sum_{\nu} a_{i\nu} a_{\nu},$$

where $\nu\mu$ is any possible combination of xx, yy, zz, xy, xz, yz. Then the magneto-elastic energy density will be expressed as

$$F_{me} = b_2[\sum_{i} m_i^2 \varepsilon_{ii} + \sum_{ij} m_i m_j \varepsilon_{ij}] + (b_1 - b_2) \sum_{i} m_i^2 \varepsilon_{ii}, \tag{2.29}$$

where $ij = xy, yz, xz$. The first term in Eq. (2.29) is invariant for all directions of the magnetization, while the second can be transformed as

$$\sum_{i} m_i^2 \varepsilon_{ii} = \sum_{\nu'\mu'} \sum_{\nu\mu} T_{\nu'\mu'}^{\nu\mu} m_\nu m_\mu \varepsilon_{\nu\mu}, \tag{2.30}$$

$$T_{\nu'\mu'}^{\nu\mu} = \sum_{i} m_{i\nu'} m_{i\mu'} m_{i\nu} m_{i\mu}.$$

The magneto-elastic constants b_1, b_2 of a crystal with cubic symmetry are usually expressed as

$$b_1 = b_{11} - b_{12}, \quad b_2 = b_{44}, \tag{2.31}$$

where b_{44}, b_{11} and b_{12} represent isotropic, tetragonal and rhomboidal magneto-elastic stresses, respectively. In the general case, the number of independent components of the b_{ijkl} tensor is equal to 36. However, taking into account the dependence of the magnetoelastic energy of Eq. (2.4) only on the direction of magnetization but not its magnitude, this number is reduced to 30. b_{11}, b_{12}, b_{44} are the matrix expressions of the magnetoelastic constants. The relation between matrix and tensor notations for b is as following

$$b_{ijkl} = b_{pq}, \text{ if } p = 1..6, q = 1..3,$$

$$2b_{ijkl} = b_{pq}, \text{ if } p = 1..6, q = 4..6.$$

The matrix b_{pq} for particular crystal symmetry allows to express the magneto-elastic energy density for any crystallographic orientation. Using Eq. (2.15) and the elastic constants of Terfenol-D (see [88]), the magnetoelastic constants of Terfenol films can be calculated: $b_1 = -34.29$ MPa, $b_2 = -359.4$ MPa. It is clear that the main contribution to the magnetostriction of Terfenol films comes from b_2, which is ten times bigger than b_1.

In the case of in-plane magnetized films, when its proper magnetization lies along

[110] crystallographic axis, the magnetoelastic energy is given

$$\begin{aligned}F_{me} = b_1(\frac{1}{2}\varepsilon_{x'x'}(m^2_{x'} + m^2_{y'}) + \frac{1}{2}\varepsilon_{y'y'}(m^2_{x'} + m^2_{y'}) + \varepsilon_{z'z'}m^2_{z'} + 2m_{x'}m_{y'}\varepsilon_{x'y'}) \\ + b_2(\frac{1}{2}\varepsilon_{x'x'}(m^2_{x'} - m^2_{y'}) + \frac{1}{2}\varepsilon_{y'y'}(m^2_{y'} - m^2_{x'}) + 2m_{y'}m_{z'}\varepsilon_{y'z'} + 2m_{x'}m_{z'}\varepsilon_{z'x'}).\end{aligned} \quad (2.32)$$

After all modifications the magneto-elastic energy density for the out-of-plane [111] magnetized sample will be expressed as

$$\begin{aligned}F_{me} = (b_1 - b_2)[\frac{1}{3}m^2_{z'}\varepsilon_{z'z'} + \frac{1}{2}(m^2_{x'}\varepsilon_{x'x'} + m^2_{y'}\varepsilon_{y'y'}) + \frac{1}{6}(m^2_{x'}\varepsilon_{y'y'} + m^2_{y'}\varepsilon_{x'x'} + 2m_{x'}\alpha_{y'}\varepsilon_{x'y'}) \\ + \frac{1}{3\sqrt{2}}(m^2_{x'}\varepsilon_{x'z'} + 2m_{x'}m_{z'}\varepsilon_{x'x'} - (m^2_{y'}\varepsilon_{x'z'} + 2m_{x'}m_{y'}\varepsilon_{y'z'} + 2m_{x'}m_{z'}\varepsilon_{y'y'} + 2m_{y'}m_{z'}\varepsilon_{x'y'})) \\ + \frac{1}{3}(m^2_{x'}\varepsilon_{z'z'} + m^2_{z'}\varepsilon_{x'x'} + 2m_{x'}m_{z'}\varepsilon_{x'z'} + m^2_{y'}\varepsilon_{z'z'} + m^2_{z'}\varepsilon_{y'y'} + 2m_{y'}m_{z'}\varepsilon_{y'z'})],\end{aligned} \quad (2.33)$$

where b_1, b_2 are the magneto-elastic constants of $TbFe_2$, m_i are the direction cosines of the magnetization vector, ε_{ij} are the strains in the cubic coordinate system. An invariant term similar to the one in Eq. (2.29) is omitted. In the new coordinate system the z' axis coincide with [111] direction of the external magnetic field, new x' and old z axes lie in the plane. To bring the new coordinate system into line with the previous case of in-plane magnetized sample, x' is considered as out-of-plane [1$\bar{1}$0] axis, z' and y' coincide with [111] and [11$\bar{2}$] directions, respectively. For that 90 degrees rotation of the coordinate system was performed. Since the acoustic waves propagate along the out of plane x' axis of the sample, $\varepsilon_{y'y'} = \varepsilon_{z'z'} = \varepsilon_{y'z'} = 0$ and Eq. (2.33) can be simplified to

$$\begin{aligned}F_{me} &= (b_1 - b_2)[\frac{1}{6}\varepsilon_{x'x'}(3m^2_{x'} + m^2_{y'} + 2m^2_{z'} + 2\sqrt{2}m_{x'}m_{z'}) + \\ &+ \frac{1}{3}\varepsilon_{x'y'}(m_{x'}m_{y'} - \frac{2}{\sqrt{2}}m_{y'}m_{z'}) + \frac{1}{3\sqrt{2}}\varepsilon_{x'z'}(m^2_{x'} - m^2_{y'} + 2\sqrt{2}m_{x'}m_{z'})].\end{aligned} \quad (2.34)$$

For cubic crystals of $\bar{4}$3m, 432, m$\bar{3}$m point groups matrix b_{pq} in Hermann-Mauguin notation are expressed as [90]

$$b_{pq} = \begin{bmatrix} b_{11} & b_{12} & b_{12} & 0 & 0 & 0 \\ b_{12} & b_{11} & b_{12} & 0 & 0 & 0 \\ b_{12} & b_{12} & b_{11} & 0 & 0 & 0 \\ 0 & 0 & 0 & b_{44} & 0 & 0 \\ 0 & 0 & 0 & 0 & b_{44} & 0 \\ 0 & 0 & 0 & 0 & 0 & b_{44} \end{bmatrix}.$$

The transformation of the b_{pq} matrix for *in-plane* magnetized sample, taking into account its coordinate system, results in

$$b'_{pq} = \begin{bmatrix} b'_{11} & b'_{12} & b_{12} & 0 & 0 & 0 \\ b'_{12} & b'_{11} & b_{12} & 0 & 0 & 0 \\ b_{12} & b_{12} & b_{11} & 0 & 0 & 0 \\ 0 & 0 & 0 & b_{44} & 0 & 0 \\ 0 & 0 & 0 & 0 & b_{44} & 0 \\ 0 & 0 & 0 & 0 & 0 & \frac{(b_{11}-b_{12})}{2} \end{bmatrix}$$

where

$$b'_{11} = \frac{b_{11}+b_{12}+2b_{44}}{2},$$
$$b'_{12} = \frac{b_{11}+b_{12}-2b_{44}}{2}.$$

Subsequently, after utilization of Eq. (2.31), the magnetoelastic coefficients for the *in-plane magnetized film* are $b_1 = 2b_{44}$, $b_2 = b_{44}$. Following the same algorithm, the matrix b_{pq} for *out-plane-magnetized* samples, taking into account its coordinate system, will have the form

$$b_{pq} = \begin{bmatrix} b'_{13} & b'_{12} & b'_{13} & 0 & -b_{15'} & 0 \\ b'_{12} & b'_{11} & b'_{13} & 0 & -b'_{15} & 0 \\ b'_{13} & b'_{13} & b'_{33} & 0 & 0 & 0 \\ 0 & 0 & 0 & b'_{44} & 0 & -b'_{15} \\ -b'_{15} & b'_{15} & 0 & 0 & -b'_{44} & 0 \\ 0 & 0 & 0 & -b'_{15} & 0 & b'_{66} \end{bmatrix}$$

where

$$b'_{11} = \frac{b_{11}+b_{12}+2b_{44}}{2}, \quad b'_{12} = \frac{b_{11}+5b_{12}-2b_{44}}{6},$$
$$b'_{13} = \frac{b_{11}+2b_{12}-2b_{44}}{3}, \quad b'_{33} = \frac{b_{11}+2b_{12}+4b_{44}}{2},$$

$$b'_{15} = \frac{b_{12} - b_{11} + 2b_{44}}{3\sqrt{2}}, \qquad b'_{44} = \frac{b_{11} - b_{12} + b_{44}}{3},$$
$$b'_{66} = \frac{b_{11} - b_{12} + 4b_{44}}{6}.$$

The relationship, given in Eq. (2.31), yields to

$$b_1 = \frac{b_{11} - 3b_{12} + 6b_{44}}{6}, \qquad b_2 = \frac{b_{11} - b_{12} + b_{44}}{3}.$$

The general expression of the magneto-elastic energy density for crystals with cubic symmetry and arbitrary pointing magnetization (see Eq. (2.29)) allows to find the F_{me} for the investigated Terfenol films. These expressions along with the expressions of the elastic energy densities will be used for the determination of the static build-in strains of the experimentally studied films in the next paragraph.

2.1.2 Demagnetostriction of Terfenol

One longitudinal and two shear build-in strains of monocrystalline $TbFe_2$ films are derived by minimizing the free energy density of the ferromagnetic film. The numerical simulations of two particular sample geometries have been performed in order to find an optimal experimental geometry for the efficient generation of picosecond shear acoustic waves (SW). Efficiency of the SW excitation in a polycrystalline Terfenol film will be numerically simulated in the approximation of two crystals as well.

Fig. 2.10 shows the (x', y', z') and (x^*, y^*, z^*) coordinate systems coupled with the

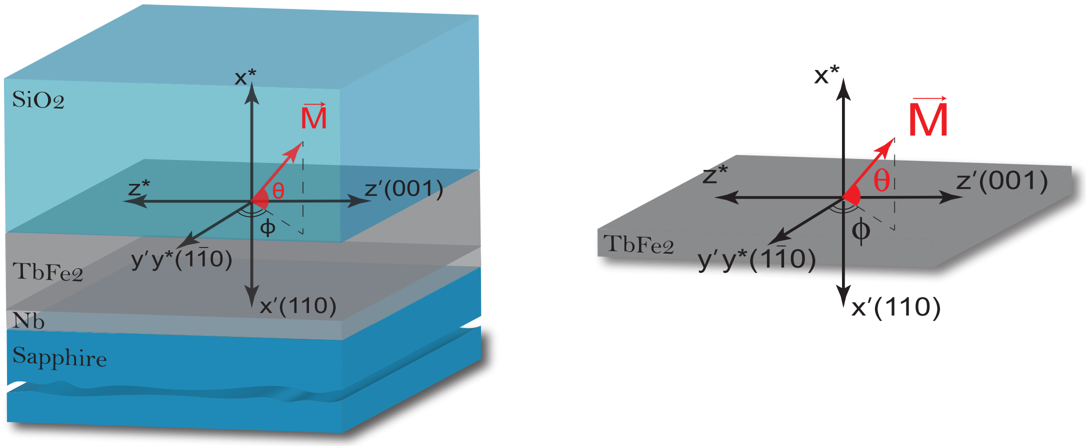

Fig. 2.10: Crystallographic directions and coupled coordinate systems of $TbFe_2$ and SiO_2 layers. The x', y', z' axes coincides with (110), $(1\bar{1}0)$, (001) crystallographic axes of Terfenol, (x^*, y^*, z^*) is used for the SiO_2 layer.

$TbFe_2$ and SiO_2 layers, respectively. The k-vector of the pump and probe beams lies in the plane perpendicular to the yz plane. Following [60], [91] the x' axis is chosen as normal to the magnetic layer, while the y', z' axes lie in the plane of the film. x', y', z' axes coincide with the [110], $[1\bar{1}]0$, [001] crystallographic axes of Terfenol. The (x, y, z) coordinate system can be obtained from the experimental one (x', y', z') by the clock-wise rotation around z axis on angle ξ. θ denotes the out-of-plane tilt angle of the magnetisation $\overrightarrow{M}$, ϕ is an azimuthal angle of the $\overrightarrow{M}$ projection on the $y'z'$ plane.

Static build-in strains in Terfenol films can be obtained by minimizing the free energy density (see Eq. (2.1)). In our approach, it is a sum of the elastic and the magneto-elastic energies, which were estimated earlier. It is assumed that an attached SiO_2 layer don't change the free energy density of $TbFe_2$. The necessary condition for the existence of an extrema is

$$\frac{\partial F}{\partial \varepsilon_{x'x'}} = 0, \quad \frac{\partial F}{\partial \varepsilon_{y'x'}} = 0, \quad \frac{\partial F}{\partial \varepsilon_{z'x'}} = 0, \tag{2.35}$$

where $F = F_e + F_{me}$, F_e is the elastic and F_{me} is the magneto-elastic energies for a particular crystal orientation. Expressions of the magneto-elastic static strains in the case of in-plane magnetized sample can be found by solving three equations in Eq. (2.35), we obtain

$$\boxed{\varepsilon_{x'x'} = -\frac{b_1(m_{x'}^2 + m_{y'}^2) + b_2(m_{x'}^2 - m_{y'}^2)}{(c_{11} + c_{12})/2 + c_{44}},} \tag{2.36}$$

$$\boxed{\varepsilon_{x'y'} = -\frac{b_1(m_{x'}m_{y'})}{c_{11} - c_{12}},} \tag{2.37}$$

$$\boxed{\varepsilon_{x'z'} = -\frac{b_2(m_{x'}m_{z'})}{2c_{44}},} \tag{2.38}$$

where $\varepsilon_{x'x'}$ is the longitudinal and $\varepsilon_{y'x'}$, $\varepsilon_{z'x'}$ are the shear static strains of Terfenol films, b_1, b_2 are the magneto-elastic and c_{11}, c_{12}, c_{44} the elastic constants of Terfenol, $m_{x'}$, $m_{y'}$, $m_{z'}$ are the direction cosines of magnetization $\overrightarrow{M}$. Despite of the fact that there are two $\varepsilon_{y'x'}$, $\varepsilon_{z'x'}$ shear strain components, after the excitation they will propagate with the same velocity and coincide on the experimental signal. Note that since $b_1 \ll b_2$ it is mainly the shear strain $\varepsilon_{z'x'}$ that will drive the excitation of shear strains with an acoustic polarization along z'.

It is straightforward to notice that for the efficient shear waves generation in the case of in-plane magnetized films, their magnetization should be tilted out-of-plane of the sample (see Eq. (2.37) - Eq. (2.38)). If $\overrightarrow{M}$ remains totally in plane one of $m_{x'}$, $m_{y'}$,

$m_{z'}$ is equal to 0 and, consequently, there will be no excitation of the shear phonons.

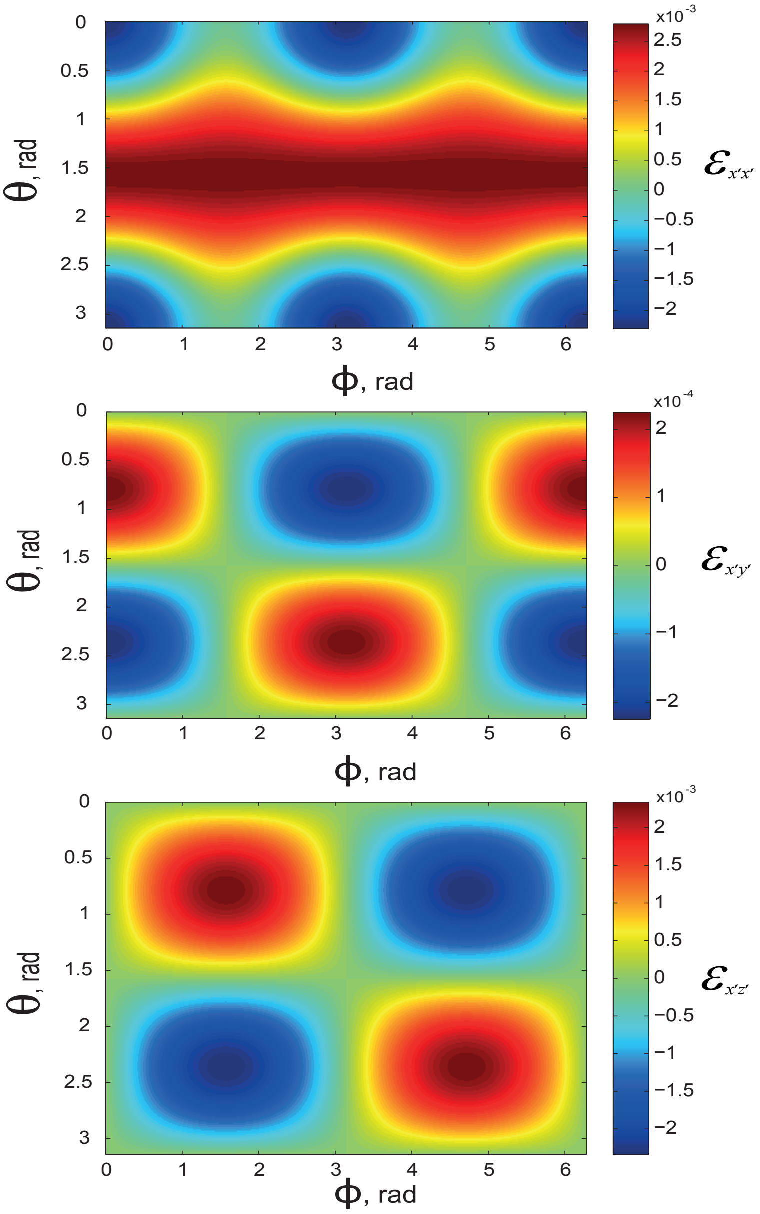

Fig. 2.11: Angular dependence of the longitudinal $\varepsilon_{x'x'}$ and shear $\varepsilon_{x'y'}$, $\varepsilon_{x'z'}$ strain amplitudes on θ out-of-plane magnetization tilt angle and ϕ - azimuthal angle of $\overline{M}$ projection on $y'z'$ plane of the in-plane magnetized films.

Dependencies of the static strain amplitudes on the polar θ and azimuthal ϕ angles of $\overrightarrow{M}$, see Fig. 2.10, were numerically simulated in order to estimate influence of the $\overrightarrow{M}$ orientation on the shear strain waves generation efficiency (see Fig. 2.11). The amplitude of the longitudinal $\varepsilon_{x'x'}$ magneto-elastic strain is minimal if $\theta = 0, \pi$ and $\phi = \pm\pi/2$ and maximal at $\theta = 0, \pi$ and $\phi = 0, \pi$ and at $\theta = \pi/2$ ($\overrightarrow{M}$ is aligned parallel to the normal of the film). On the contrary, shear strain amplitudes show different angular dependencies. First of all, since $\varepsilon_{x'z'}$ shear strain is defined by the b_2 magnetostrictive coefficient, it

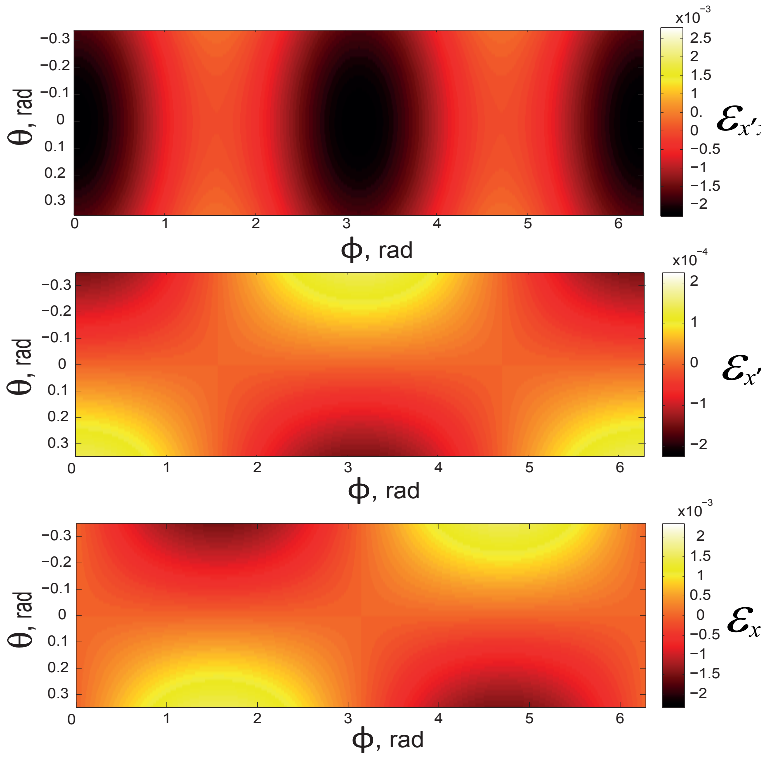

Fig. 2.12: Angular dependence of the longitudinal $\varepsilon_{x'x'}$ and shear $\varepsilon_{x'y'}$, $\varepsilon_{x'z'}$ strain amplitudes on $\theta = \pm 20$ degrees out-of-plane magnetization tilt angle and ϕ - azimuthal angle of $\overline{M}$ projection on $y'z'$ plane of the in-plane magnetized films.

possesses 5 times higher amplitude compared to the $\varepsilon_{x'y'}$, defined by b_1. Any deflection of the magnetization from its initial orientation towards the normal causes non-zero shear strain amplitude. Maximum for the $\varepsilon_{x'y'}$ component is reached if $\overrightarrow{M}$ is aligned along the diagonal between [110] and [1-10] $\theta = \pm\pi/4$ $\phi = 0$. If $\theta = \pm\pi/4$ and $\phi = \pm\pi/4$ i.e. the magnetization points at the 45 degrees with respect to the surface, amplitude of the $\varepsilon_{x'z'}$ strain is maximal. Tilt of the magnetization at 10 degrees with respect to the film surface leads to the non-zero amplitude of the both shear strains, moreover, amplitude of the $\varepsilon_{x'z'}$ component will be 10 times bigger than that of the $\varepsilon_{x'y'}$. Hence, out-of-plane tilt of $\overrightarrow{M}$ of the initially in-plane magnetized Terfenol film is a compulsory condition for the efficient laser-induced magneto-elastic shear waves excitation. Tilt of the magnetization from its initial in-plane position $\theta = \pm 20$ degrees is shown on Fig. 2.14.

It is worth to mention here that following the dependencies of the strain amplitude on the magnetization directions (see Eq. (2.36) - Eq. (2.38)), coherent precession of the magnetization of Terfenol film leads to the continuous change of its static strains, which in fact is a coupling of pure spin and pure elastic waves. This coupling manifest itself as a coupled magneto-elastic wave propagating in the ferromagnetic medium. In ferromagnet with cubic symmetry and magnetized to saturation along the [100] axis, there are three normal waves: right-handed circularly polarized magneto-elastic wave, left-handed circularly polarized magneto-elastic and longitudinal pure elastic wave [92]. Regarding a non-homogeneous shear wave excitation efficiency with the θ and ϕ angles in the in-plane magnetized Terfenol films, excited magneto-elastic waves most probably will have elliptical acoustic polarization. Since the frequency bandwidth of the magnetization precession of Terfenol films lies in the GHz range, potentially it can be a source of picosecond circularly (elliptically) polarized acoustic waves, which are of great interest for applications in picosecond ultrasonics and femtomagnetism. For example, the excitation of the magnetization precession of a ferromagnetic film could be highly efficient with circularly polarized acoustic waves laser-induced in a Terfenol layer.

The static strains for the out-of-plane magnetized films can be found in a similar way by minimizing their free energy density. They can be expressed as

$$\varepsilon_{x'x'} = \frac{(b_1 - b_2)(3m_{x'}^2 + m_{y'}^2 + 2m_{z'}^2 + 2\sqrt{2}\cdot m_{x'}m_{z'})}{c_{11} - (c_{12} + c_{44})/3}, \tag{2.39}$$

$$\varepsilon_{y'x'} = \frac{2(b_1 - b_2)(1/3\cdot m_{x'}m_{y'} - 2/3\sqrt{2}\cdot m_{y'}m_{z'})}{(c_{11} + c_{12})/4 + c_{44}}, \tag{2.40}$$

$$\varepsilon_{z'x'} = -\frac{4(b_1 - b_2)(1/\sqrt{2}\cdot m_{y'}^2 + 1/3\cdot m_{x'}m_{z'})}{c_{11} + c_{12} + c_{44}}. \tag{2.41}$$

The numerical simulations of the angular dependence of static strain amplitudes Eq. (2.39) - Eq. (2.41) on the magnetization direction in case of the out-of-plane magnetized Terfenol film are presented on Fig. 2.13. Unlike the in-plane magnetized film (see Fig. 2.11), two shear components $\varepsilon_{x'y'}$, $\varepsilon_{x'z'}$ show more complex angular dependence of their amplitudes on the angles θ and ϕ. If $\overrightarrow{M}$ remains in its original out-of-plane position ($\theta = \pi/2$ and $\phi = 0$), trains will have opposite sign, which can result in reduction of the total shear strain detection efficiency. This unfavorable situation can be excluded by tuning the azimuthal angle of the magnetization to $\phi = \pi$. Moreover, the value of the SW amplitude will be $\sim$2 times higher than in case of the maximal shear amplitude in the in-plane magnetized film. Asymmetry of the strain amplitudes with respect to the axis $\theta = \pi/2$ can be explained by the more complex crystal orientation during the deposition process and the magneto-crystalline anisotropy of Terfenol. The amplitude of the longitudinal strain $\varepsilon_{x'x'}$ (top sketch) reaches its maximum if $\theta = \pi/4$ deg and significantly modulated with a change of the angle ϕ. Tilt of the magnetization from its initial out-of-plane position $\theta = 90 \pm 20$ degrees is shown on Fig. 2.14. Unlike in-plane magnetized films (see Fig. 2.14), tilt at $\theta = 90 \pm 20$ degrees doesn't result into the equal shear strain amplitude.

According to the simulations, several conclusions about the experimental geometry should be made before proceeding to the time-resolved measurements of the acoustic waves excitation. (i) In the case of the *in-plane* magnetized films, efficiency of the shear waves excitation increases with a simultaneous tilt of its magnetization towards the normal to the surface. The maximum is reached if $\theta = \pm\pi/4$ with respect to the normal of the film and $\pm\phi = \pi/4$. (ii) Due to the strong difference in magnetoelastic constants of Terfenol ($b_2 \gg b_1$), amplitude of the $\varepsilon_{x'y'}$ is 5 times lower than that of the

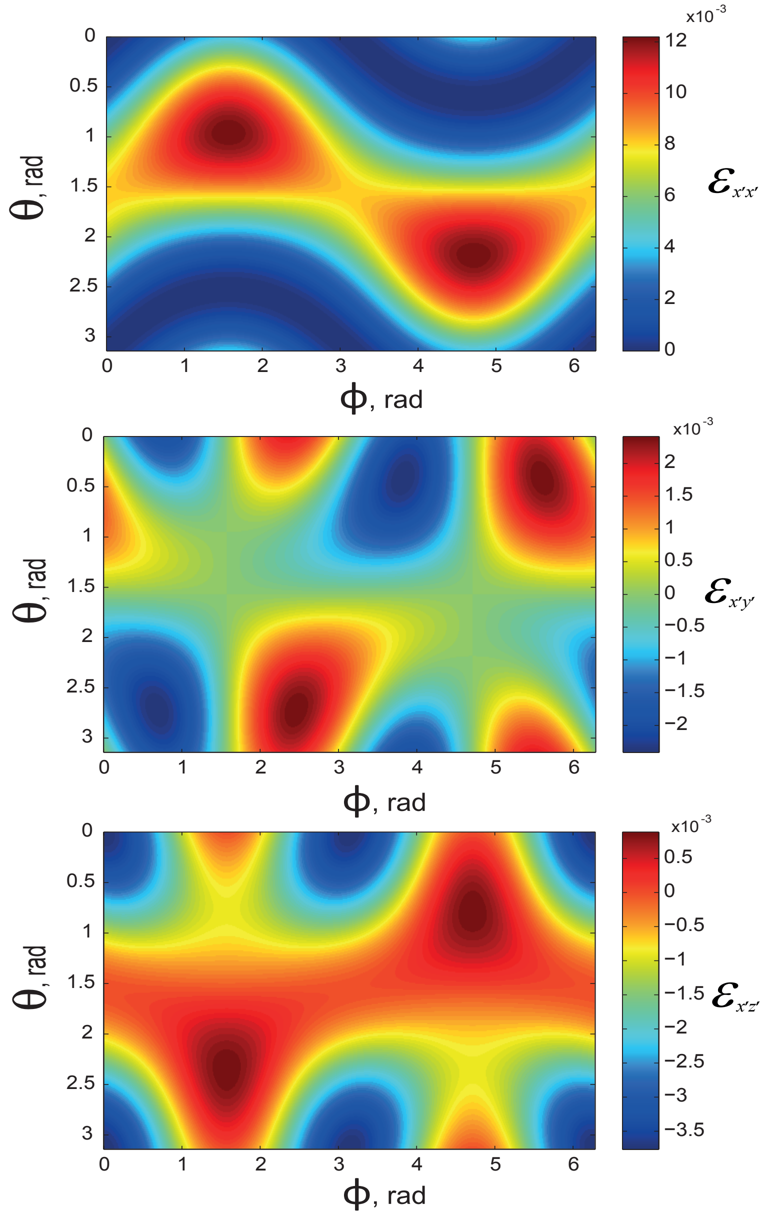

Fig. 2.13: Angular dependence of longitudinal $\varepsilon_{x'x'}$ and shear $\varepsilon_{x'y'}$, $\varepsilon_{x'z'}$ strain amplitudes on θ out-of-plane tilt angle in polycrystalline Terfenol film.

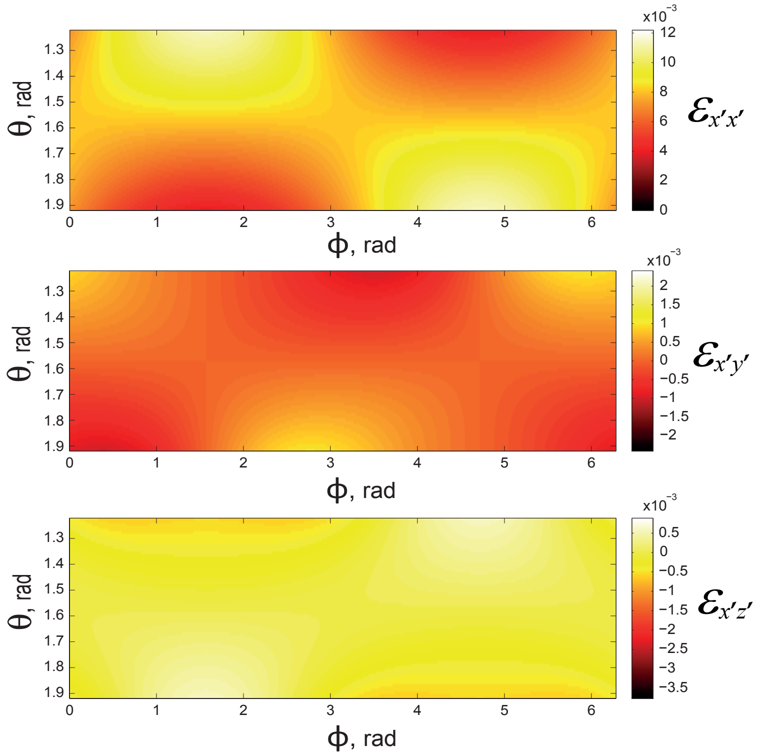

Fig. 2.14: Angular dependence of the longitudinal $\varepsilon_{x'x'}$ and shear $\varepsilon_{x'y'}$, $\varepsilon_{x'z'}$ strain amplitudes on $\theta = \pi/2 \pm 20$ degrees out-of-normal magnetization tilt angle and ϕ - azimuthal angle of $\overline{M}$ projection on $y'z'$ plane of the out-of-plane magnetized films.

$\varepsilon_{x'z'}$ strain. Hence, detection of the SW with acoustic polarization along z' direction is favored. (iii) In the case of the *out-of-plane* magnetized films, the amplitudes of the S strain components shows complex angular dependence. Amplitude of the $\varepsilon_{x'y'}$ and $\varepsilon_{x'z'}$ strains is strongly modulated by orientation of $\overrightarrow{M}$ i.e. polar θ, and azimuthal ϕ angles. Moreover, a tilt of the magnetization towards the easy $[11\bar{2}]$ axis induces the higher shear wave amplitude than the tilt towards $[1\bar{1}0]$. Unlike the out-of plane magnetized film, where the laser-induced longitudinal strain will be always excited if the magnetization remains in its initial position, in the case of the in-plane magnetized film amplitude of the longitudinal strain is strongly depend on tilt of $\overrightarrow{M}$ from its original orientation. Hence, shear waves can be laser-excited in the out-of-plane magnetized Terfenol films with slight in-plane reorientation of their magnetization. However, a full control over $\overrightarrow{M}$ of the in-plane magnetized films is required in order to effectively generate the shear waves by the laser-induced demagnetostriction mechanism.

Polycrystalline Terfenol film

The efficiency of shear strain waves excitation in a polycrystalline Terfenol film is expected to be lower than in monocrystalline samples due to their significantly lower magnetocrystalline anisotropy [93]. It is a result of the random crystals orientation after deposition. Joule magnetostriction of polycrystalline materials is often characterized by λ_s coefficient ($\lambda_s(TbFe_2) = +1.75 \cdot 10^{-3}$). It is based on the estimation of average magnetostriction coefficient in homogeneously distributed monocrystalline crystals. From the point of view of picosecond ultrasonics it is not the best choice. Sound velocity is anisotropic in the majority of metals, thus propagation of the acoustic pulse will be disturbed due to the random orientation of the grains and grain-boundary scattering [94]. Furthermore, it should result in significant time-broadening of the acoustic pulse. If the grain size is comparable to the film thickness, the sound velocity will be different depending on the regions of the film and will be defined by the dominant orientation of the grains in a particular region.

It is problematic to estimate the efficiency of the acoustic strain wave generation in polycrystalline films. Considering a polycrystalline film a set of simple monocrystals with random orientations, the determination of the strains can be established in an extreme case, consisting only of two crystals with defined orientation. Laser generation of the shear wave depends on a total amplitude of the static strain. Let's assume two crystal orientations, which correspond to the in-plane [001], [1$\bar{1}$0], [110] and [1$\bar{1}$0], [11$\bar{2}$], [111] and out-of-plane magnetized crystals, described before. In this simplified case the total build-in strains will have form

$$\varepsilon_{x'x'} = -\frac{b_1(m_{x'}^2 + m_{y'}^2) + b_2(m_{x'}^2 - m_{y'}^2)}{(c_{11}+c_{12})/2 + c_{44}} + \frac{(b_1 - b_2)(3m_{x'}^2 + m_{y'}^2 + 2m_{z'}^2 + 2\sqrt{2} \cdot m_{x'}m_{z'})}{c_{11} - (c_{12} + c_{44})/3}, \tag{2.42}$$

$$\varepsilon_{y'x'} = -\frac{b_1(m_{x'}m_{y'})}{c_{11} - c_{12}} + \frac{2(b_1 - b_2)(1/3 \cdot m_{x'}m_{y'} - 2/3\sqrt{2} \cdot m_{y'}m_{z'})}{((c_{11} + c_{12})/4 + c_{44})}, \tag{2.43}$$

$$\varepsilon_{z'x'} = -\frac{b_2(m_{x'}m_{z'})}{2c_{44}} - \frac{4(b_1 - b_2)(1/\sqrt{2} \cdot m_{y'}^2 + 1/3 \cdot m_{x'}m_{z'})}{c_{11} + c_{12} + c_{44}}. \tag{2.44}$$

The numerical simulation of the angular dependence of the static shear strain amplitudes in a polycrystalline model of Terfenol film (see Eq. (2.43) - Eq. (2.44)) on the angles θ and ϕ, i.e. tilt of its magnetization from an initial orientation (polar θ and azimuthal ϕ angles) is presented on Fig. 2.15. Two shear components $\varepsilon_{x'y'}$, $\varepsilon_{x'z'}$ show different angular dependence of their amplitude on θ and ϕ. It is straightforward that the generation of the shear strain occurs if the magnetization of the film is tilted at some degree out-of-plane or out-of-normal of the sample. Moreover, if $\overrightarrow{M}$ is tilted at $\theta = \pi/2$ with $\phi = 0$ ($\overrightarrow{M}$ is aligned with [11$\bar{2}$] crystallographic axis) from its initial

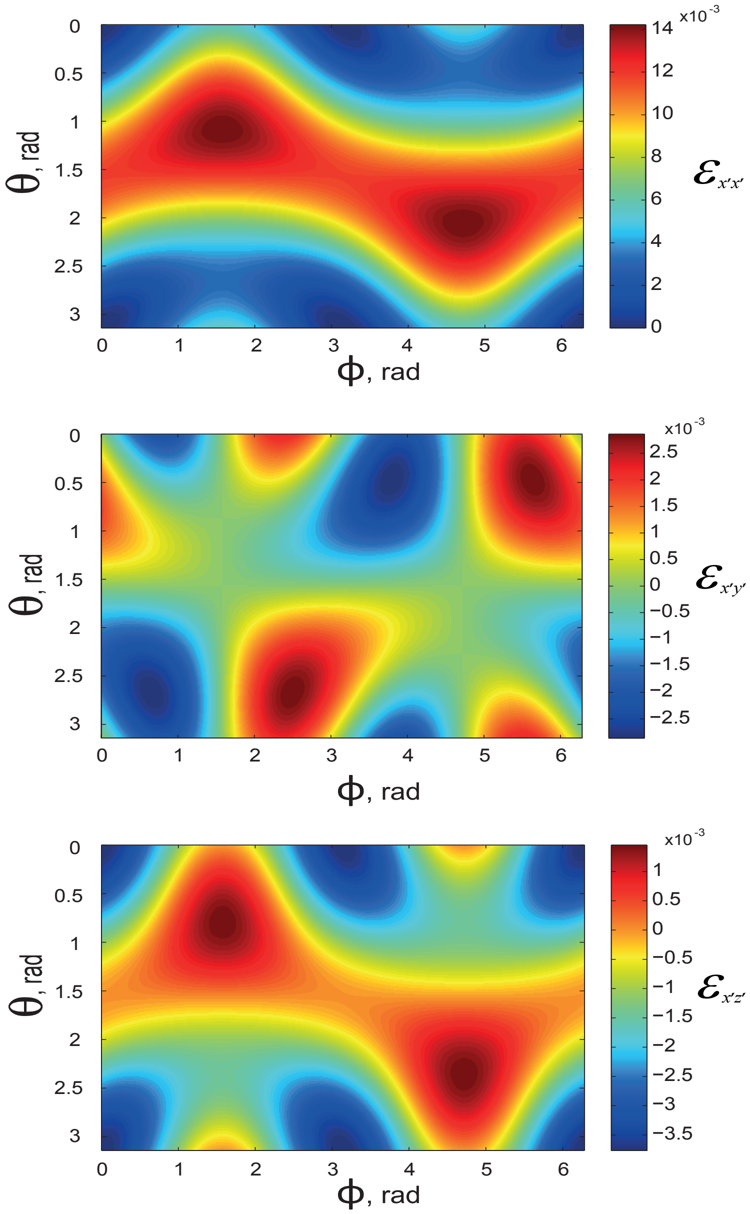

Fig. 2.15: Angular dependence of longitudinal $\varepsilon_{x'x'}$ and shear $\varepsilon_{x'y'}$, $\varepsilon_{x'z'}$ strain amplitudes on θ out-of-plane tilt angle in polycrystalline Terfenol film.

orientation, amplitudes of two shear strain will have 0 amplitude which results in non-efficient excitation of shear strains. However, tilt at $\theta = \pi/4$ with $\phi = \pi$ ($\overrightarrow{M}$ is aligned with $[1\bar{1}0]$ crystallographic axis) results in maximal shear wave amplitude, which reaches 50 % of the longitudinal wave amplitude. Ultimately, excitation efficiency of the shear strain wave packet increases if magnetization of polycrystalline film is tilted towards its normal. Moreover, in-plane projection of the magnetization vector also has a significant impact in the total shear strain generation efficiency.

Polycrystalline Terfenol film has been modeled in the approximation of two crystals with different crystallographic orientations. The efficiency of the shear acoustic waves generation was estimated based on the numerical simulation of its static strain amplitudes. In our simple model the optical excitation of the shear acoustic waves is efficient if the magnetization of the film isn't aligned in plane or along the normal of the film. With omitted boundary effects their amplitudes will be comparable with strain amplitudes in case of a monocrystalline sample. However real polycrystalline Terfenol film will be an unfavorable prototype to study generation of the picosecond SW. Propagation of the strain waves in the attached semi-infinite fused silica layer is discussed in the following paragraph.

2.1.3 Lattice dynamics

An analytical study of the acoustic waves propagation in the attached fused silica layer is performed using the expressions of the static build-in strains of Terfenol films and knowing its demagnetization timescale. Due to the acoustic impedance of the sample layers (see Sec. 2.1.1), acoustic phonons excited in the skin depth of Terfenol and reflected from the $TbFe_2/Nb$ interface are not considered. An analytical processing involves a solution of the acoustic wave propagation equation in the semi-infinite isotropic layer, using Sommerfeld boundary conditions. It allows to find a set of equations, which are determined by the transforms $\widetilde{u_i}(0, \omega)$ of the acoustically-driven surface displacements. Next, the resolution of the thermal diffusion equation allows to find the surface displacement $u_i(0, t)$. Finally, the dynamical strains $\varepsilon_i(x, t)$ are derived from the surface displacement following [39].

The analytical development starts with the fundamental principle of the dynamics of an elementary volume subjected to a stress gradient in a continuous medium. In agreement with Einstein summation indices, Newton's second law can be written as

$$\rho \frac{\partial^2 u_i}{\partial t^2} = \frac{\partial \sigma_{ij}}{\partial x_j}, \tag{2.45}$$

where u_i is a particle displacement vector, ρ is the density of the medium and σ_{ij} is the stress tensor.

$$u_i = u_M + u_T \tag{2.46}$$

where u_M, u_T are the displacements induced by the magnetostriction and thermal expansion, respectively. Propagation of plane acoustic wave is considered along the x direction, consequently all partial derivatives propagating along y and z are omitted.

Thus, only the terms $j = x$ remains in Eq. (2.45).

$$\rho\frac{\partial^2 u_i}{\partial t^2} = \frac{\partial \sigma_{ix'}}{\partial x'}, \tag{2.47}$$

where $\sigma_{ix'}$ are components of the elastic stress tensor and the coordinate axes of the ferromagnetic layer $i = x', y', z'$ and of the dielectric layer $i = x^*, y^*, z^*$. Thermal expansion of the material induced by a thermoelastic process introduces an additional term in the expression of the stress tensor. In the first order of the perturbation, it is proportional to the variation of energy density induced by the laser heating. The expression of elastic stress tensor is given

$$\sigma_{ij} = \frac{1+\delta_{ij}}{2}\frac{\partial(F_e + F_{me})}{\partial \varepsilon_{ij}} - \beta_{kl}c_{ijkl}T = c_{ijkl}\varepsilon_{kl} + \frac{1+\delta_{ij}}{2}\frac{\partial F_{me}}{\partial \varepsilon_{ij}} - \beta_{kl}c_{ijkl}T, \tag{2.48}$$

where c_{ijkl} is a tensor of the elastic constants, β_{kl} is a tensor of the thermal dilatation and T is a change of the temperature, associated with the laser heating. In the following, we will use the thermoelastic tensor B_{ij}, which is equal to

$$B_{ij} = c_{ijkl}\beta_{kl}. \tag{2.49}$$

The last two terms in the expression Eq. (2.48) present a source of the elastic waves excitation: (i) laser-induced modification of the magneto-elastic energy density and (ii) the optical heating. Expression of the magneto-elastic energy density of the in-plane magnetized Terfenol films, when its proper magnetization lies along [110] crystallographic axis is given

$$F_{me} = b_1(\frac{1}{2}\varepsilon_{x'x'}(m_{x'}^2 + m_{y'}^2) + 2m_{x'}m_{y'}\varepsilon_{x'y'}) + b_2(\frac{1}{2}\varepsilon_{x'x'}(m_{x'}^2 - m_{y'}^2) + 2m_{x'}m_{z'}\varepsilon_{z'x'}). \tag{2.50}$$

Change of the temperature causes the stresses, which propagate towards positive and negative directions of x. Longitudinal $\sigma_1(x', t)$ and shear magneto-elastic stresses $\sigma_2(x', t)$, $\sigma_3(x', t)$ of the ferromagnetic layer are equal to

$$\sigma_{x'x'} = \frac{\partial F_{me}}{\partial \varepsilon_{x'x'}}, \qquad \sigma_{y'x'} = \frac{\partial F_{me}}{\partial \varepsilon_{y'x'}}, \qquad \sigma_{z'x'} = \frac{\partial F_{me}}{\partial \varepsilon_{z'x'}}. \tag{2.51}$$

Now, total source magnetoelastic stresses can be expressed as

$$\boxed{\sigma_{x'x'} = \partial\frac{F_{me}}{\partial\varepsilon_{x'x'}} - B_{11}T = \frac{b_1}{2}(m_{x'}^2 + m_{y'}^2) + \frac{b_2}{2}(m_{x'}^2 - m_{y'}^2) - c_{11}\beta_{11}T,}$$

$$\boxed{\sigma_{y'x'} = \frac{1}{2}\partial\frac{F_{me}}{\partial\varepsilon_{y'x'}} - 0 = b_1 m_{x'}m_{y'},} \tag{2.52}$$

$$\boxed{\sigma_{z'x'} = \frac{1}{2}\partial\frac{F_{me}}{\partial\varepsilon_{z'x'}} - 0 = b_2 m_{x'}m_{z'}.}$$

It is important to notice that only longitudinal stress σ_{11} has a thermo-elastic contribution, therefore it will be excited upon both laser-induced demagnetostriction and thermal expansion of the lattice. On the contrary, σ_{21} and σ_{31} can be excited only by the ultrafast release of the magnetoelastic strains. Laser-induced direct magnetostriction is assumed as the main mechanism of the shear elastic waves excitation in Terfenol. In this simplified model a linear character of magneto-elastic constants b_i evolution upon the laser heating is adopted.

$$b_i = b_{i0} - A_i\Delta T, \tag{2.53}$$

where $i = 1, 2$, A_i are the linearising coefficients, ΔT is a film temperature gradient. Temperature-induced change of Terfenol magnetostriction coefficient $\lambda_{[111]}$, which defines the b_2 (see Eq. (2.15)[5]) follows the lowest order single-ion expression $\lambda_{[111]}(T) = \lambda_{[111]}(0)\hat{\mathrm{I}}_{5/2}[\alpha^{-1}(\mathrm{m})]$, see [95].

We assume that laser-induced demagnetization only decreases magnetization modulus of Terfenol film, but not its orientation. The A_i coefficient defines the slope of the b_i change with the laser heating. A_2 can be found from the Fig. 2.16 and it is equal to -2.6 MPa/K. A_1 is assumed to have ten times smaller value -0.24 MPa/K.

At the picosecond timescale the thermal diffusion can be neglected in the absorbing medium itself and in the isotropic dielectric material where the thermal diffusion rates are lower. Boundary conditions, which take into account the continuity of the normal components of mechanical stress on the boundaries, can be expressed as

$$\sigma_{x^*x^*}(x^* = 0, t) = \sigma_{x'x'}(x' = 0, t), \tag{2.54}$$

---

[5] Temperature dependence of the c_{44} elastic constant is neglected.

$$\sigma_{z^*x^*}(x^*=0,t)=\sigma_{z'x'}(x'=0,t), \tag{2.55}$$

$$\sigma_{y^*x^*}(x^*=0,t)=-\sigma_{y'x'}(x'=0,t), \tag{2.56}$$

$$u_{x^*}(x^*=0,t)=-u_{x'}(x'=0,t), \tag{2.57}$$

$$u_{y^*}(x^*=0,t)=u_{y'}(x'=0,t), \tag{2.58}$$

$$u_{z^*}(x^*=0,t)=-u_{z'}(x'=0,t), \tag{2.59}$$

Negative sign in Eq. (2.56) - Eq. (2.59) arise from the convention of propagation direction, see Fig. 2.10. It is straightforward to calculate $\varepsilon_{ix'}(x^*,t)$ following the [39]. The magnetoelastic dynamical strains for $t-x/\upsilon\geq 0$ can be found by solving the equations of motion of the stress in the isotropic medium with boundary conditions Eq. (2.54) - Eq. (2.59):

$$\boxed{\varepsilon_{x'x'}(x^*,t)=\frac{\alpha F\beta_{x'x'}\gamma_1}{2\rho c_p}\frac{\upsilon_l}{\upsilon_l^*}exp(-\upsilon_l\alpha(t-x^*/\upsilon_l^*)),} \tag{2.60}$$

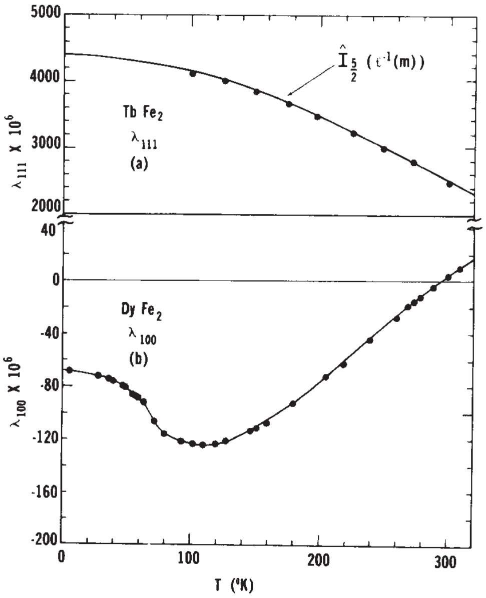

Fig. 2.16: Temperature dependence of a) $TbFe_2$ and b)$DyFe_2$ magnetostriction coefficients $\lambda_{[111]}$, $\lambda_{[100]}$, respectively [95].

$$\boxed{\varepsilon_{x'y'}(x^*,t)=\frac{\alpha F\beta_{x'y'}\gamma_2}{2\rho c_p}\frac{\upsilon_{t1}}{\upsilon_t^*}exp(-\upsilon_{t1}\alpha(t-x^*/\upsilon_t^*)),} \tag{2.61}$$

$$\boxed{\varepsilon_{x'z'}(x^*,t)=\frac{\alpha F\beta_{x'z'}\gamma_3}{2\rho c_p}\frac{\upsilon_{t2}}{\upsilon_t^*}exp(-\upsilon_{t2}\alpha(t-x^*/\upsilon_t^*)),} \tag{2.62}$$

where the sound velocities in Terfenol and fused silica layers are $\upsilon_i=\sqrt{c_i/\rho}$, $\upsilon_i^*=\sqrt{c_i/\rho^*}$, respectively. F is the laser fluence, α is the coefficient of optical absorption of Terfenol at 800 nm. The $REFe_2$ compounds are nearly elastically isotropic ($c_{t1}\backsimeq c_{t2}$), thus in case of Terfenol $\upsilon_{t1}\simeq\upsilon_{t2}$.

$$\boxed{\beta_{x'x'}=-(\rho\upsilon_l^2+\rho^*\upsilon_l\upsilon_l^*)^{-1},} \tag{2.63}$$

$$\boxed{\beta_{x'y'}=-(\rho\upsilon_{t1}^2+\rho^*\upsilon_{t1}\upsilon_t^*)^{-1},} \tag{2.64}$$

$$\boxed{\beta_{x'z'}=-(\rho\upsilon_{t2}^2+\rho^*\upsilon_{t2}\upsilon_t^*)^{-1},} \tag{2.65}$$

$$\boxed{\gamma_1=-\frac{1}{2}[A_1(m_{x'}^2+m_{y'}^2)+A_2(m_{x'}^2-m_{y'}^2)]-[B_{11}],} \tag{2.66}$$

$$\boxed{\gamma_2=-A_1m_{x'}m_{y'},} \tag{2.67}$$

$$\boxed{\gamma_3=-A_2m_{x'}m_{z'}.} \tag{2.68}$$

Eq. (2.60) - Eq. (2.62) present the expressions of the longitudinal and shear strains propagating in the dielectric fused silica. The first term of Eq. (2.60) - Eq. (2.62) ($\frac{\alpha F\beta_{x'i}\gamma_j}{2\rho c_p}$) shows the strain amplitude, while the last one depends on the time delay and represents the propagation of the strain. The preserving factor υ_i/υ_i^* increases or decreases the strain amplitude in case of shrinking or broadening of its spatial profile. Two terms of Eq. (2.66) are related to the magneto-elastic and thermo-elastic strain waves generation. Thermo-elastic term is absent in case of γ_2 and γ_3 because of the magneto-elastic origin of the shear waves excitation in Terfenol films.

Due to the thermo-elastic contribution total longitudinal $\varepsilon_{x'x'}(x^*,t)$ strain, see Fig. 2.17 (a), has ∼10 times bigger amplitude than the purely magneto-elastic longitudinal strain induced by demagnetostriction (b). Fig. 2.18 presents the spatial profile of magneto-elastic $\varepsilon_{x'y'}(x^*,t)$ and $\varepsilon_{x'z'}(x^*,t)$ shear strains after propagation in 400 nm ($\tau_S\sim 110$ ps) of SiO_2 with magnetization tilted at 45 deg (a), 10 deg (b), 5 deg (c) out-of-plane of the in-plane magnetized film. The amplitude of the $\varepsilon_{x'y'}(x^*,t)$ increases with the increase of the $\overrightarrow{M}$ tilt angle. The strain profiles show transient jump of the amplitude on their rising front (travel time of longitudinal and shear strains is set at

Parameter, units	**Value**
Optical absorption coefficient of $TbFe_2$ α, m^{-1}	$5.26{\cdot}10^7$
Density of Terfenol ρ, kg/m^3	9170
Density of the fused silica ρ^*, kg/m^3	2196
Specific heat of Terfenol c_p, J/kgK	350
Thermal dilatation coefficient of Terfenol β, K^{-1}	$1.18{\cdot}10^{-5}$
Elastic constant of Terfenol c_{11}, N/m^2	$117{\cdot}10^9$
Shear wave velocity in Terfenol, υ_{t1}, nm/ps	1.87
Shear wave velocity in fused silica, υ_2^*, nm/ps	3.7
Longitudinal wave velocity in Terfenol, υ_l, nm/ps	4.17
Longitudinal wave velocity in fused silica, υ_1^*, nm/ps	5.9

Table 2.4: Terfenol hybrid sample mechanical parameters.

$\tau \sim 70$ ps), and exponential decay on the back front. Frequency spectrum of the longitudinal (see the inset of Fig. 2.17 (a) and shear pulses (see the inset of Fig. 2.18) (a) is similar.

Spatial profiles of longitudinal $\varepsilon_{x'x'}(x^*,t)$ and shear $\varepsilon_{x'z'}(x^*,t)$ strains at $\theta = 45$ deg and $\theta = 5$ deg are presented on the Fig. 2.19 (a) and (b), respectively. Ratio of the longitudinal $\varepsilon_{x'x'}(x^*,t)$ A_L and shear $\varepsilon_{x'z'}(x^*,t)$ A_S strain amplitudes is defined as A_L/A_S. It is equal to ~3 if magnetization of the film is tilted at 5 degrees out of its plane, see Fig. 2.17 (d). However, it can be reduced down to ~0.6 in case of the $\theta = 45$ degrees, see Fig. 2.17 (c). Parameters utilized in simulations are listed in Tab. 2.1.3

Thereby, the laser-induced demagnetization of the Terfenol films on the timescale of several picoseconds leads to the excitation of the wave packet of two strain waves with different acoustic polarization but similar frequency content, which is in order of

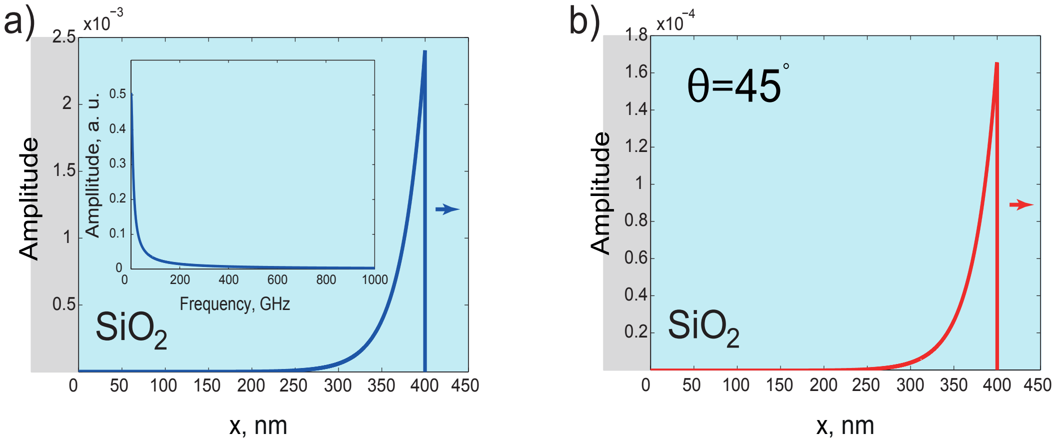

Fig. 2.17: Spatial profile of a) total $c_{11}\beta_{11} \neq 0$ longitudinal $\varepsilon_{x'x'}(x^*,t)$ strain and b) purely magneto-elastic $c_{11}\beta_{11} = 0$, see Eq. (2.66) at $\Delta t \sim 65$ ps. Laser pump fluence is set on F=5mJ/cm^2.

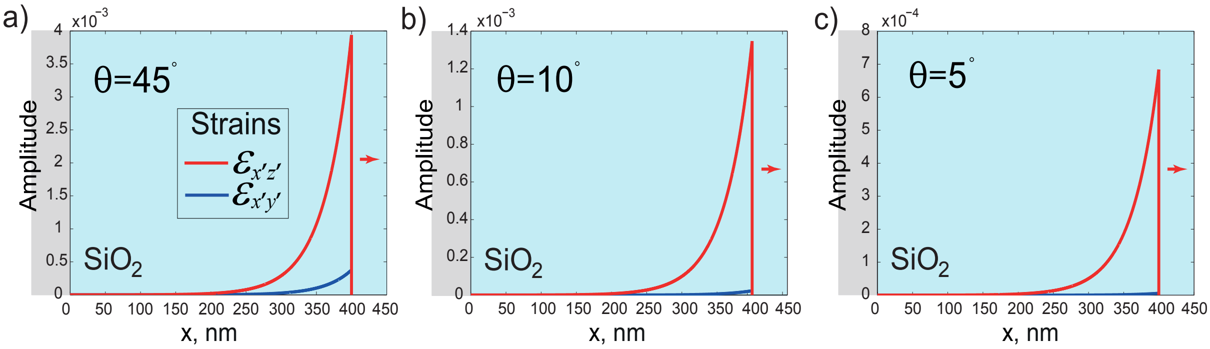

Fig. 2.18: Spatial profile of magneto-elastic $\varepsilon_{x'y'}(x^*,t)$ and $\varepsilon_{x'z'}(x^*,t)$ shear strains (blue and red curves, respectively) at $\Delta t \sim 110$ ps and a) $\theta = 45$ deg, $\phi = 45$ deg, b) $\theta = 5$ deg, $\phi = 45$ deg, b) $\theta = 10$ deg, $\phi = 45$ deg. Laser pump fluence is set on F=5mJ/cm^2.

hundreds of GHz. Amplitudes of the longitudinal and shear strain waves are strongly modulated depending on out-of-plane tilt of the film magnetization, which is an essential condition for the efficient generation of the GHz shear acoustic pulses.

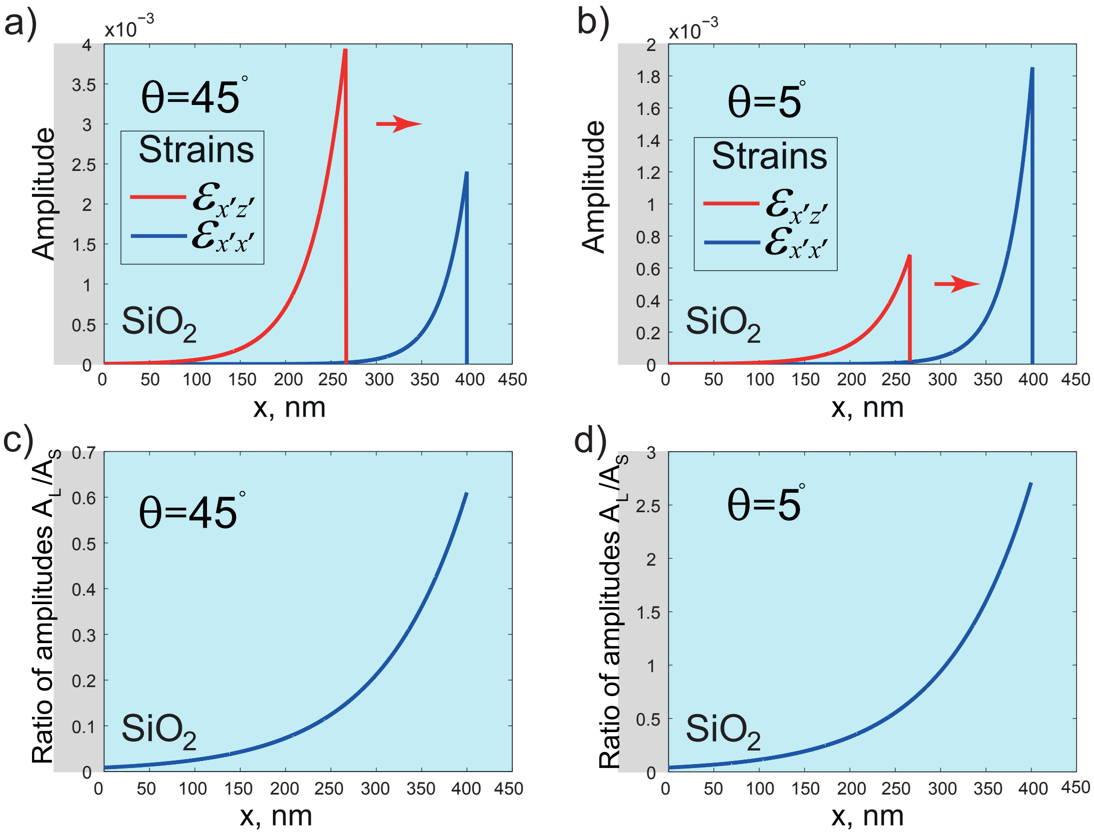

Fig. 2.19: Spatial profiles of longitudinal $\varepsilon_{x'x'}(x^*,t)$ and shear $\varepsilon_{x'z'}(x^*,t)$ strains at a) $\theta = 45$ deg and b) $\theta = 5$ deg. Ratio of the longitudinal A_L and shear A_S strain amplitudes at c) $\theta = 45$ deg and d) $\theta = 5$ deg.

2.2 Experimental study of laser-induced dynamics in Terfenol hybrid samples

Laser-induced dynamics of the Terfenol thin films were investigated by employing a time-resolved laser pump-probe spectroscopy techniques. Fig. 2.20 presents the experimental geometry. A sample is mounted on a non-magnetic stage under a static magnetic field of H∼ 7-8 kOe, which is pointing along the normal of the sample. It is laser excited by a 160 fs intense pump pulse at $\lambda = 800$ nm, focused onto the ferromagnetic film with a spot size of $\sim$ 100 μm, which is two times larger than the spot size of the probe beam. Ten times less intense time-delayed probe pulses at $\lambda = 800(400)$ nm wavelength were focused at the surface at an incident angle of several tens of degrees with respect to its normal, and monitored the time-resolved response of the material after its excitation. The time resolution is limited by the duration of the laser pulse. An example of transient reflectivity signal $\Delta R/R$ is presented in Fig. 2.21.

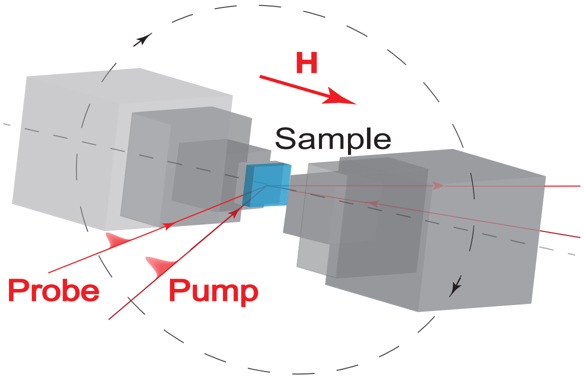

Fig. 2.20: Experimental geometry of the time-resolved laser pump-probe spectroscopy of Terfenol thin films.

Laser pump pulses excite a 300 nm thick $TbFe_2$ film at $\Delta t = 0$. Upon both thermoelastic transient heating and ultrafast release of the magnetostrictive strains, acoustic waves are excited in the surrounding SiO_2 layer of thickness d = 775 nm. These strain waves are detected while propagating back and forth in the SiO_2 layer by a time-delayed probe pulse at 800 nm in Fig. 2.21 (a) or at 400 nm Fig. 2.21 (b) wavelengths at an incident angle of 30 degrees, with respect to the normal of the surface. Since 400 nm compared to 800 nm probe wavelength favors the detection of the longitudinal Brillouin scattering oscillations in SiO_2 (that has been observed earlier in [96]) that disturb the measurement of the acoustic echoes, the probe light at 800 nm wavelength is preferable for further measurements of the acoustic pulses.

Fig. 2.21 depicts a two steps response at different time scales. The rapid increase of the relative amplitude ΔR at $\Delta t = 0$, which is proportional to the pump fluence, it corresponds to the laser heating of the electrons and lattice, and the following slow relaxation during the next ~1 ns. Coherent oscillations on the top of thermal dynamics are associated with inelastic Brillouin scattering of the probe light from the propagating acoustic waves. In fact it is a result of the multiple interferences between the probe beam reflected from the $TbFe_2/SiO_2$ interface and the secondary beams, reflected from the strain pulse, propagating in the dielectric. This effect is often referred as Brillouin scattering [97]. Features centered at 350 ps and 650 ps after the excitation correspond to the time of longitudinal pulse round trip in the dielectric layer. The frequency spectrum in the inset of Fig. 2.21, obtained by numerical Fourier transform, reveals the presence of coherent longitudinal phonons, their frequencies are related to the probe wavelength λ, the SiO_2 refractive index n, to the SiO_2 longitudinal speed of sound υ_L and to the back-scattering angle θ through the relationship $\nu = (2\ n\ \upsilon_L \cos\theta)/\lambda$. The sudden change of the Brillouin scattering oscillations, that appears at 180 ps and 530 ps after excitation comes from the Fabry-Perot cavity effect, that occurs as a result of the free SiO_2 interface displacement at the arrival of the longitudinal pulse. The presence of the shear pulses is hidden by the strong longitudinal Brillouin oscillations, caused by the longitudinal acoustic waves and can't be distinguished. Hence, utilization of the transient reflectivity detection scheme is not an appropriate way to detect propagating shear acoustic waves.

Fig. 2.22 (a) shows the time resolved signals obtained by detection via the MOKE /depolarized Brillouin scattering technique at two out-of-plane magnetic field orienta-

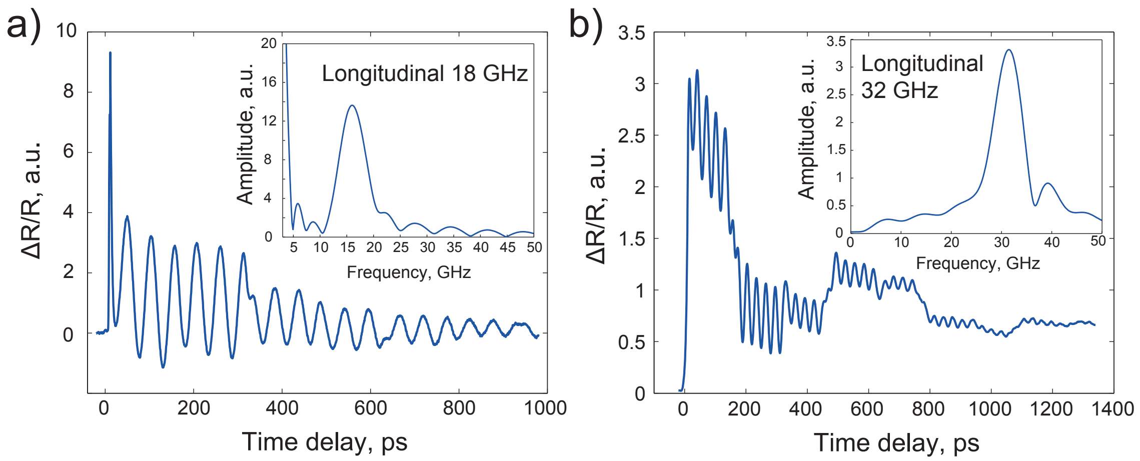

Fig. 2.21: Time-resolved Brillouin scattering of the probe light at a) $\lambda = 800$ nm, b) $\lambda = 400$ nm probe wavelength of a 300 nm thick $TbFe_2$ with in-plane static magnetization coated with a 775 nm thick SiO_2 layer. The inset shows the frequency spectrum of the signal.

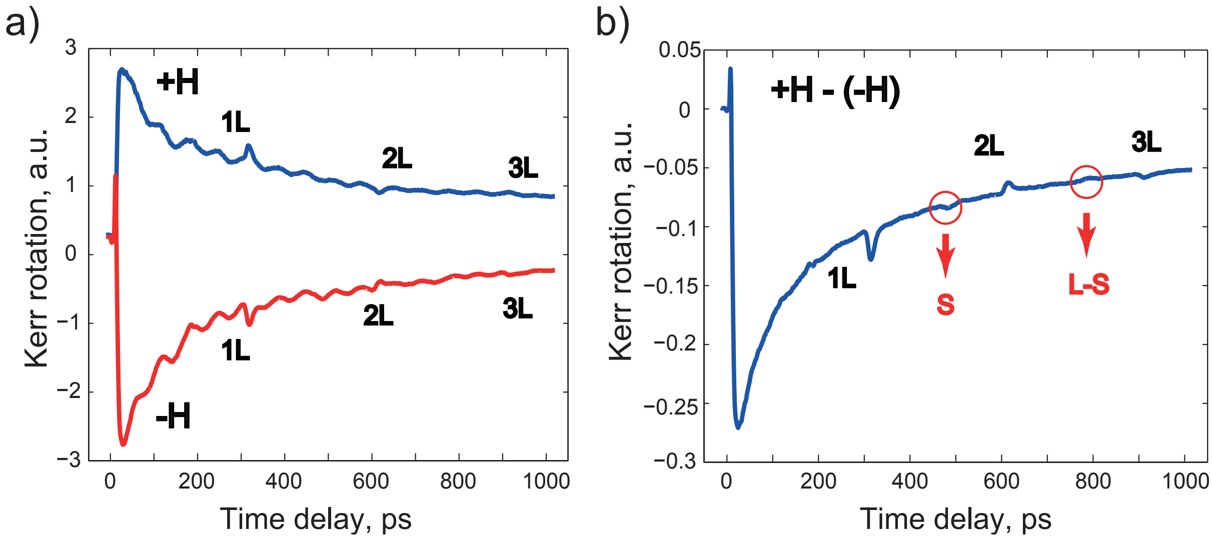

Fig. 2.22: a) Transient time resolved pump-probe MOKE signals recorded in a 300 nm $TbFe_2$/775 nm SiO_2 multi-layer sample of in-plane static magnetization at two out-of-plane DC magnetic field orientations ±H=7 kOe. b) Differential signal $+H-(-H)$ reveals the presence of longitudinal (L) and shear (S) acoustic echoes.

tions $\pm H$. The differential signal calculated by subtracting both signals at $\pm H$ allows to filter out the non-magnetic part. The magneto-optical Kerr response in Fig. 2.22 (b) reveals several acoustic echoes with L longitudinal or S shear acoustic polarizations on top of the demagnetization background. Their arrival time can be estimated knowing the thickness of 775 nm and velocities $v_l = 5.9$ nm/ps and $v_s = 3.7$ nm/ps of the acoustic waves in the SiO_2 film. Moreover, the acoustic waves are partially reflected at the free interface of silica and the subsequent propagation of the pulse back and forth in SiO_2 layer provides observation of corresponding echoes at increasing travel time after excitation. The amplitudes of the echoes decrease as the result of acoustic attenuation and partial transmission through the sample interfaces. Three longitudinal echoes (centered at 350 ps, 650 ps, 950 ps after generation and separated by $2d/\vartheta_l \sim 300$ ps) are clearly distinguished, showing expected π phase difference from one to another. It is explained considering the acoustic impedances and the sign upon reflection at each interface, described in the beginning of this section. The echoes centered at ~ 450 ps and at ~ 800 ps can be clearly distinguished and attributed after estimation of their arrival time to shear acoustic pulses, that agrees with the expected time of shear acoustic waves propagation in the silica layer. The first one of ~ 10 ps duration evidences the ultrafast release of magnetostriction which is the only possible mechanism of shear generation in the present sample [39]. However, the time of arrival of the second pulse doesn't correspond to the double round-trip of the first shear echo in the silica acoustic delay line. Its time arrival corresponds to a longitudinal round trip time plus a shear

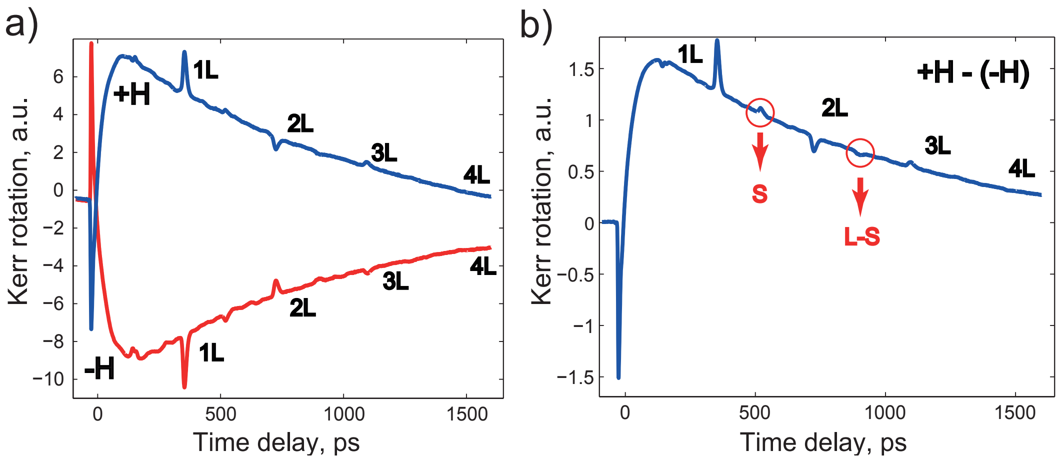

Fig. 2.23: a) Transient time resolved MOKE signals recorded in a 300 nm $TbFe_2$/1000 nm SiO_2 multilayer sample of in-plane static magnetization at two out-of-plane magnetic field orientations ±H=7 kOe. b) Differential signal $+H-(-H)$ shows the presence of longitudinal (L) and shear (S) acoustic echoes.

round trip time in the silica layer. It reveals that acoustic mode conversion of the first longitudinal pulse at 350 ps into a shear pulse happens upon the acoustic reflection at the $TbFe_2/SiO_2$ interface. The ratio of amplitudes of the first longitudinal and the first shear echoes is approximately $A_{1L}/A_{1S} \sim 5$. Since the first shear echo is 5 times weaker than the longitudinal echo, we can neglect the shear to longitudinal mode conversion. Since the ratio of the laser spot size at the sample surface to the film thickness is significantly greater than 1, the so called acoustic diffraction effect which can excite GHz shear acoustic waves at interfaces does not contribute to the first echoes profile. The first shear echo proves the efficient demagnetostriction effect. The different ratio of $\sim$ 5 times between first L and S acoustic echoes can also arise from the different photoelastic constants or magneto-optic coefficients involved in the generation in each case. The slight asymmetry in the measured pulse shapes is explained by a detection process and by mixed electron and thermal diffusion events during the ultrafast laser generation process. The attenuation of the L and S waves are different as well.

The same experiment was performed in order to double-check this result, but this time on a sample with a thicker dielectric layer. Fig. 2.23 (a) presents the measured laser-induced dynamics of a 300 nm $TbFe_2$ film attached to a thicker 1000 nm layer of SiO_2. The time response is detected via the depolarized Brillouin scattering technique at two out-of-plane magnetic field orientations $\pm H$. The differential magneto-optical Kerr response in Fig. 2.22 (b) reveals L longitudinal and S shear acoustic echoes on top of the demagnetization background. Their arrival time correspond to the velocities of L and S strain waves in the 1000 nm fused silica layer. We observe longer acoustic delay time of the measured echoes that agrees with the thicker SiO_2 thickness.

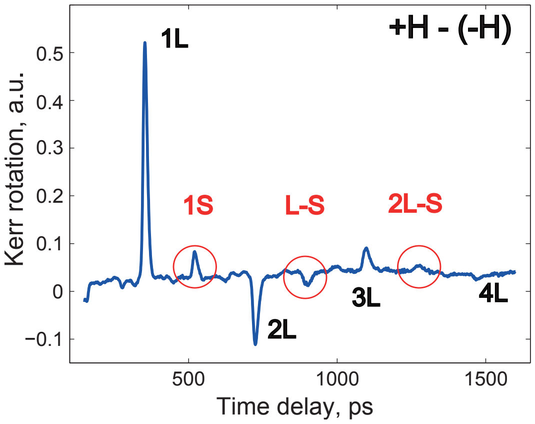

Fig. 2.24: Differential signal $+H - (-H)$ of Fig. 2.23with subtracted background highlighting the excitation of shear acoustic echoes (S) and (L-S) in a 300 nm $TbFe_2$/1000 nm SiO_2 sample.

Features, centered at $\sim$ 380 ps, $\sim$ 760 ps, $\sim$ 1130 ps, $\sim$ 1550 ps and separated by $2d/\vartheta_l \sim 370$ ps are the echoes of the longitudinal pulses traveling back and forth in the dielectric layer, they show alternating π phase shifts as a result of acoustic reflections at the interfaces. Echoes centered at $\sim$ 555 ps, $\sim$ 935 ps, $\sim$ 1310 ps can be distinguished as shear acoustic pulses from the estimation of their arrival time, which fits the expected time of for shear waves propagation in the fused silica layer. Acoustic echoes arrival time is used to estimate the actual thickness of the SiO_2 layer, in fact it is equal to 1110 nm. The generation mechanisms of the first 1S and two subsequent L-S, 2L-S pulses are different, as in the previous sample: (i) demagnetostriction and (ii) mode conversion, respectively. The arrival time of the third shear echo (2L-S) corresponds to the round trip of the shear acoustic pulse, generated by a mode conversion of the 2L strain. Since the generation mechanism of the 1S pulse in case of two samples is the same and the only difference between them is the thickness of the dielectric layer, we observe a longer duration of the pulse $\sim$ 13 ps in the 1000 nm sample in comparison with $\sim$ 10 ps in the 775 nm sample that evidences the acoustic broadening of the GHz transversal waves in SiO_2. The propagation of an ultrasonic pulse through a medium results in its broadening due to the homogeneous acoustic attenuation and other inhomogeneous pulse broadening mechanisms. The measured time duration of the longitudinal (1L, 2L) and shear (1S, 2S) acoustic echoes detected after propagation in SiO_2 layers of different thicknesses confirms this effect, see Tab. 2.5 where the thickness of the dielectric layer is displayed in the first column.

The duration of an echo that propagated through a thinner acoustic delay line is shorter and, thus closer to its initial duration governed by the excitation process. Hence, the thickness of the acoustic delay line should be as thin as possible. However, due to the ratio of the longitudinal and shear sound velocities in the silica dioxide, which is equal to $\upsilon_L/\upsilon_S = 1.5865$ there can be time overlapping of the 1S and 2L echoes in thinner films. The sample covered with a 350 nm thick layer of SiO_2, studied in the scope of the present thesis, still allows to distinguish several echoes of different acoustic polarizations on the experimental signals but the time separation of the longitudinal and shear echoes is more efficient for thicker films with the disadvantage of higher acoustic attenuation. Utilization of different types of acoustic delay lines is possible by deposition of other dielectric materials with different ratio of longitudinal and shear sound velocities (for example, ZnO $\upsilon_L/\upsilon_S = 2.228$).

The quite thick 300 nm Terfenol film prevents uniform laser demagnetization, since the optical skin depth in the metal of about $\sim$ 20 nm is way more thinner than the total thickness. Hence, we have studied thinner magnetostrictive films were studied. Laser-induced dynamics of a 50 nm $TbFe_2$/ 700 nm SiO_2 sample were measured in order to check if the efficiency of generation is improved with a decrease of the magnetostrictive layer thickness. Unfortunately only longitudinal echoes were detected in thin Terfenol layers with no indication of shear waves, see Fig. 2.25. A possible explanation for that is the poor quality of the ferromagnetic layer with internal structural inhomogeneities and high roughness in the case of thinner films.

The same type of time-resolved pump-probe experiments were performed on a 300 nm $TbFe_2$/ 20 nm Mo/CaF_2 structure with an out-of-plane static magnetization, covered by 700 nm of dielectric silica layer. A magnetic field of H=7 kOe was applied along the sample surface in order to tilt the magnetization towards in plane. Fig. 2.26 shows the differential $\pm H$ time resolved Kerr signal. By analogy to Fig. 2.22 (b) it reveals several L longitudinal and S shear acoustic echoes on top of a demagnetization background in the transient Kerr signal. The echoes centered at 300 ps and at 450 ps can be assigned as longitudinal and shear acoustic pulses after estimation of their arrival time which fits the expected time of flight for shear acoustic waves propagating in 1400 nm of silica. Due to the strong saturation field ($\sim$ 1.5 T), which exceeds our available applied static field of 7 kOe, the tilt of $\overrightarrow{M}$ is not efficient. Therefore the efficiency of the shear

	1L, ps	**1S, ps**	**2L, ps**	**2S, ps**
500 nm	11	9	14	18
775 nm	12	9	18	20
1000 nm	13	12	20	24

Table 2.5: Time broadening of the acoustic echoes as a function of SiO_2 thickness.

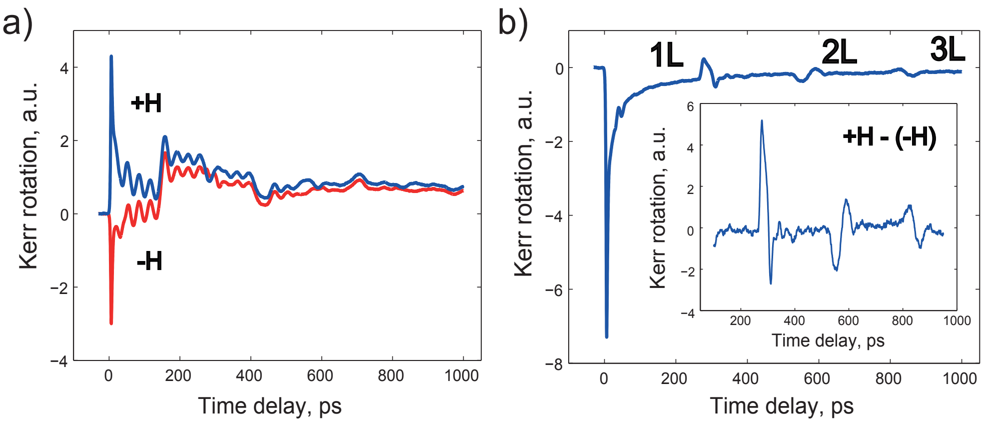

Fig. 2.25: a) Transient time resolved pump-probe MOKE signals recorded in a 50 nm $TbFe_2$/700 nm SiO_2 multi-layer sample of in-plane static magnetization at two out-of-plane magnetic field orientations $\pm H$. b) Differential signal $+H - (-H)$ with subtracted background reveals only the presence of longitudinal acoustic waves generated in the 50 nm Terfenol layer.

strain excitation is low. Hence, further experiments will be performed on the in-plane magnetized samples.

Despite the transient demagnetization of the film, there are no signatures of laser-induced magnetization precession on the experimental curves in Fig. 2.22. On the other hand, the samples uncovered by SiO_2 shows strong coherent magnetization dynamics at about 6 GHz, see Fig. 2.9. We believe that the lack of signal can be explained by the detection of a much smaller polar contribution to TR-MOKE.

The demagnetization timescale of Terfenol films is of paramount interest for further understanding of time duration of the laser generated strain pulses. It was already measured in the previous section with uncovered Terfenol films. Fluence-resolved measurements were performed on 300 nm in-plane magnetized $TbFe_2$ films, covered with 1000 nm of fused silica, to determine its characteristic demagnetization timescale as a

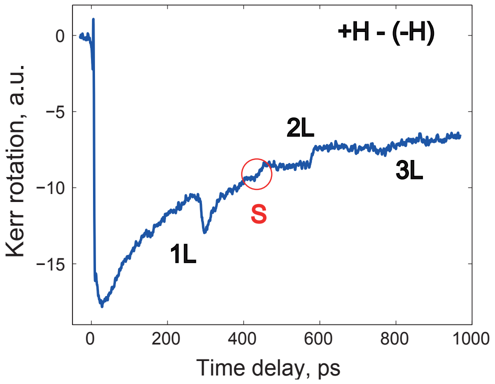

Fig. 2.26: Time resolved Kerr signal recorded for a 300 nm $TbFe_2$/700 nm SiO_2 sample structure with out-of-plane static magnetization, at two in-plane magnetic field orientations $\pm H$.

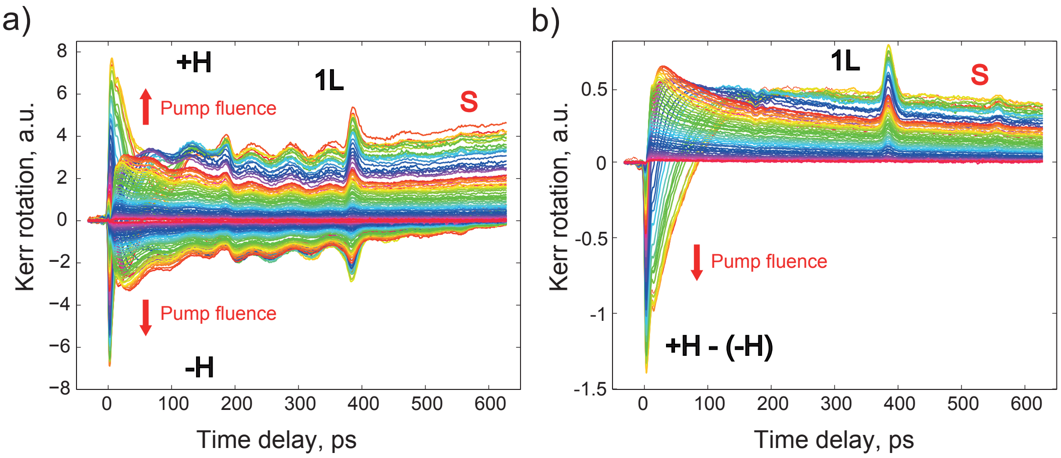

Fig. 2.27: a) Laser-induced variation of time resolved Kerr signals recorded in a 300 nm $TbFe_2$/1000 nm SiO_2 multi-layer sample of in-plane static magnetization at two out-of-plane magnetic field orientations $\pm H$, as a function of pump fluence. b) Differential signals $+H-(-H)$ obtained at different pump fluences.

function of laser pump fluence. Fig. 2.27 (a) presents time- and fluence-resolved MOKE rotation signals detected with two orthogonal orientations of the magnetic field ± H applied along the normal to the sample. Differential signals $+H-(-H)$ reveal the presence of a first longitudinal and shear echoes centered at 380 ps and 555 ps, respectively, see Fig. 2.27 (b), as well as their pump fluence dependence in the 0-8 mJ/cm^2 range. Presence of low-frequency longitudinal Brillouin oscillations on Fig. 2.27 (a) indicate the depolarization of the probe light upon reflection at the Terfenol surface. Differential signals $+H-(-H)$, which are sensitive only to the effects of magnetic origin confirms non-magnetic nature of the longitudinal Brillouin oscillations.

The first 40 ps following the laser excitation at $\Delta t = 0$ ps are depicted on Fig. 2.28 (a). It reveals two steps of the film demagnetization at different time scales:

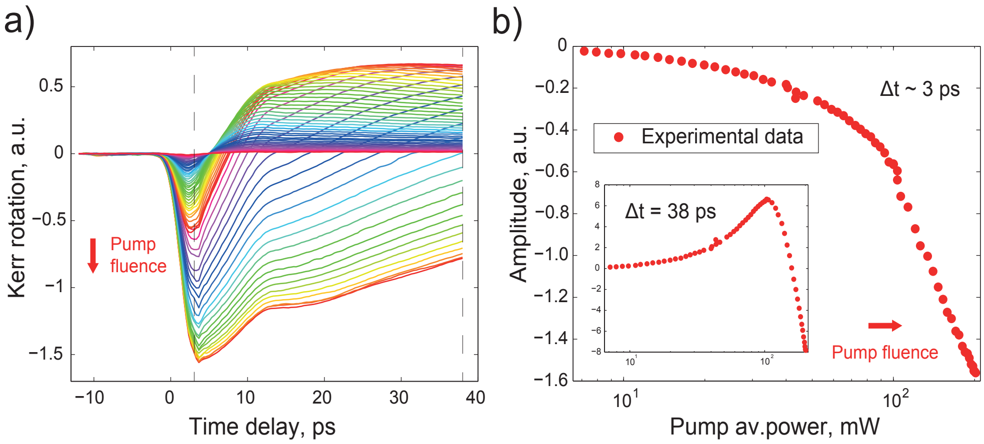

Fig. 2.28: a) Zoom of the ultrafast laser demagnetization of Fig. 2.26 b) during the first 30 ps after laser excitation. b) Demagnetization peak amplitude as a function of pump fluence.

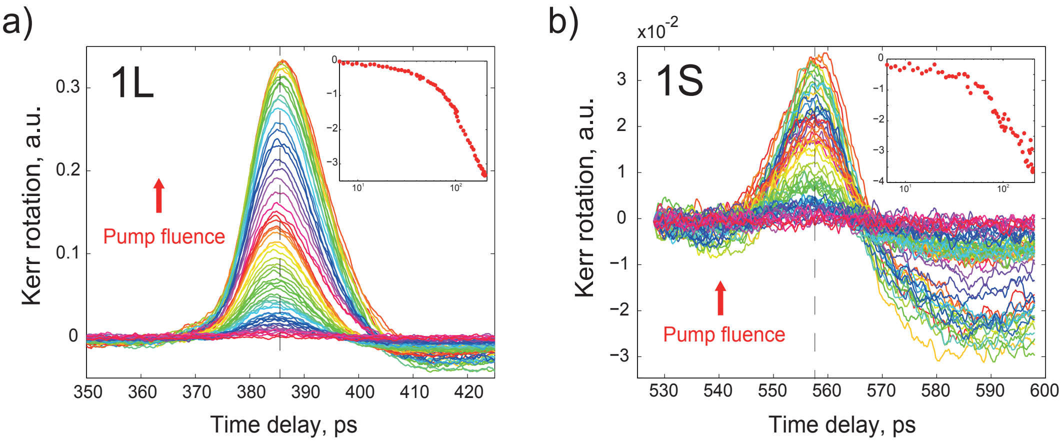

Fig. 2.29: Time-profiles of the a) longitudinal and b) shear acoustic echoes of Fig. 2.26 as a function of pump fluence. The insets show a maximal relative amplitudes change as a function of pump fluence.

(i) ultrafast loss of the remanent magnetization of Terfenol $\tau_1 \sim 1.5$ ps and (ii) the second longer step, which was also observed on the uncovered sample and reported for other rare-earth-based alloys in [17]. It confirms that the deposition of the dielectric layer doesn't influence the demagnetization time scale of the ferromagnetic film. Besides that, the release of Terfenol static strains, occurring simultaneously with its demagnetization generates acoustic waves of several picoseconds time duration. Fig. 2.28 (b) shows the maximum of demagnetization amplitude as a function of pump fluence, extracted around 3 ps time delay (the position of the peak slightly shifts with fluence). Note, that the pump power is given in logarithmic scale. The inset depicts the signal amplitude evolution as a function of pump fluence at $\Delta t = 38$ ps. A linear distribution of the demagnetization amplitudes evidences linear dependence of dynamics at fluences in the 0 - 8 mJ/cm^2 range.

Fig. 2.29 shows the temporal profiles of the a) longitudinal and b) shear acoustic echoes as a function of laser pump fluence. The evolution of longitudinal echo amplitudes at its maximal value follows the same law as the demagnetization at early time delay, see Fig. 2.28 (b). It means that the contribution of the thermoelastic mechanism, which is linear with laser fluence, to the total L strain amplitude is dominant as compared to the magneto-elastic contribution. This result is relevant with our numerical simulations presented on Fig. 2.17. The ratio of the amplitudes A_{1S}/A_{1L} is about 1/10. The evolution of the shear echo amplitudes also obeys the same rule. Echoes duration of $\tau \sim 12$ ps were measured at their FWHM. It is important to have in mind that the timescale τ_{1L} and τ_{1S} of the detected echoes doesn't represent the time duration of the acoustic pulses excited by laser-induced demagnetization of Terfenol. There are several reasons for that: (i) the pulses propagate through 2 μm (round trip in 1000 nm) thick SiO_2 layer and get damped and broaden; (ii) in fact, measured signal represents a convolution of the sensitivity function [48] with the acoustic strain profile, which is initially assumed to have a unipolar shape. Thus, it is mostly the sensitivity function that determines the final shape of the detected echo, i.e. how strain, propagating into the depth of the material contributes to the rotation of the probe polarization.

Optical detection of the magneto-acoustic pulse

Detection of the acoustic strain after its double propagation in the dielectric layer occurs in the skin depth of the Terfenol film, which is described by an exponentially decaying function. Consequently, the duration of the detected acoustic echo is a convolution of the acoustic strain spatial profile ($\sim \exp(-\alpha v_i(t - x/v_i))$) with the spatial profile of the optical detection function ($\sim \exp(-2j\omega(n_k/c)x)$). The unipolar strain pulse propagates in SiO_2 towards the interface, see Fig. 2.30 (1). The optical signal is the convolution of the strain profile with the spatial profile of the optical detection function. (2) The detected dynamics do not carry an accurate and straightforward measure of the strain profile, because of the spatial limitation of the optical detection area. The measured signals accurately describes the true temporal strain profile only if the detection zone is represented by a Dirac function $\delta(x)$. Otherwise, the real duration of the acoustic pulses generated by demagnetostriction can be found by performing the deconvolution of the detection zone profile with the strain spatial profile.

A simplified approximation for the description of the optical detection of the strain pulses consist of assuming that time-resolved measured signals can be described by the

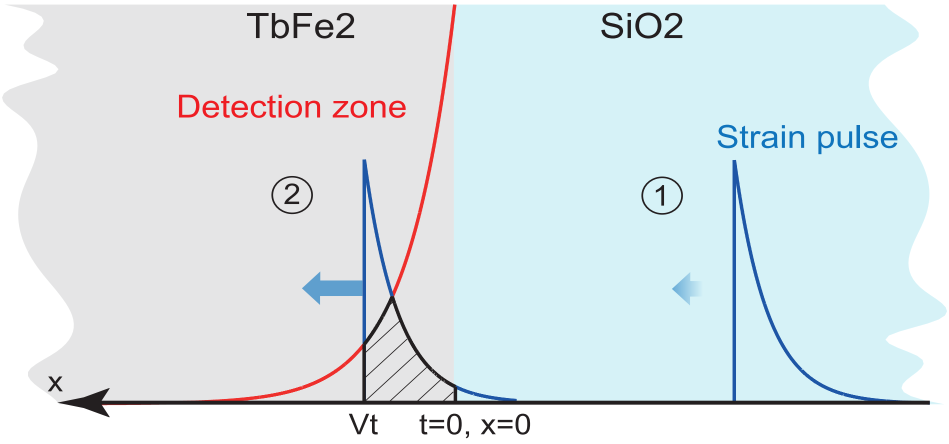

Fig. 2.30: Detection of the acoustic pulses in the skin depth of the Terfenol film.

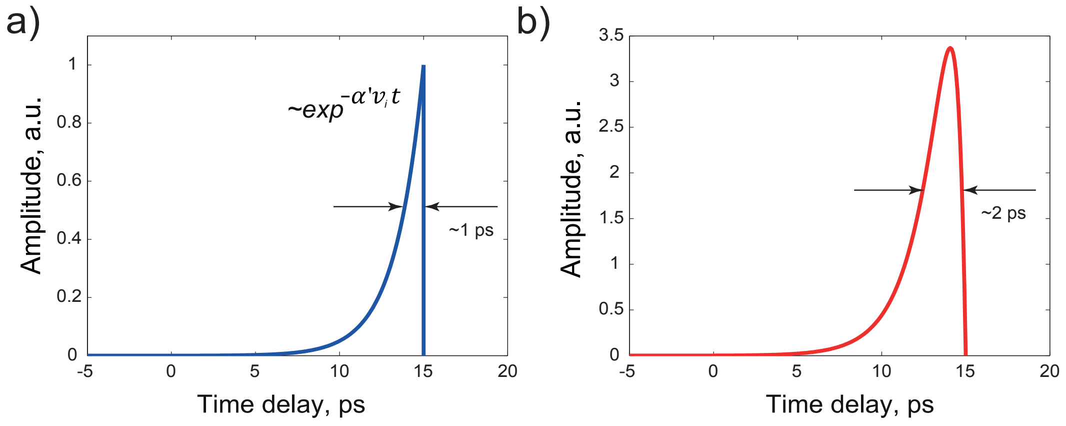

Fig. 2.31: a) Simulations of the acoustic strain time profile $\sim \exp^{-\alpha v_i t}$ and b) of the detected acoustic echo time profile.

following expression

$$R(t) \sim \int_0^{+\infty} \eta(t - \frac{x}{v_i}) \exp^{-\alpha x} dx, \tag{2.69}$$

where, $\eta(t - \frac{x}{v_i})$ is the acoustic strain and $\exp^{-\alpha x}$ is spatial profile of the optical penetration depth, i.e. simplified sensitivity function. Due to the spatial limitation of the optical detection area Eq. (2.69) is non-zero between $x = 0$ and $x = v_i t$. Assuming that the strain follows an exponent in the form $\exp^{-\alpha' v_i (t + \frac{x}{v_i})}$, it can be modified as

$$\begin{aligned} R(t) &\sim \int_0^{v_i t} \exp^{-\alpha' v_i (t+\frac{x}{v_i})} \exp^{-\alpha^* x} dx = \exp^{-\alpha' v_i t} \int_0^{v_i t} \exp^{-(\alpha'+\alpha^*)x} dx \\ &= \exp^{-\alpha' v_i t} \left| \frac{\exp^{-(\alpha'+\alpha^*)x}}{-2(\alpha'+\alpha^*)} \right|_0^{v_i t} = \exp^{-\alpha' v_i t} (\exp^{-(\alpha'+\alpha^*)v_i t} - 1) / -2(\alpha'+\alpha^*). \end{aligned} \tag{2.70}$$

The numerical simulation of Eq. (2.70) is described in Fig. 2.31. The optical detection of the acoustic strain with ~ 1 ps time duration in the skin depth of Terfenol leads to the broadening of its time profile up to ~ 2 ps, see Fig. 2.31 (b).

The sensitivity function presented in [48] describes the change in reflectivity correct to the first order in strain. In the present case, the acoustic echoes are detected via polarization dependent measurements. Hence, unlike [48], detection is magneto-optical rather than photo-elastic. In magneto-optical detection there are several sensitivity functions, that can be found following [34]. We can assume that the physical content of the sensitivity function is identical with [48], in the sense that the acoustic waves are detected in the optical skin depth of the magnetic layer. It is hard to estimate the real sensitivity function of Terfenol due to the indeterminate position of its magnetization and lack of data about its optical and magneto-optical properties. However, since the time duration of the acoustic pulse is relatively short, the sensitivity function doesn't play the crucial role in determination of the detected echo shape. The reconstruction model, presented in this section gives an idea about real time constants of the strain pulses.

The optical excitation of the 300 nm thick $TbFe_2$ film results in the generation of longitudinal and shear strain waves, that propagate in the attached 1000 nm of SiO_2. The propagation of the strain through 2 μm of dielectric layer causes spatial and temporal broadening of its profile. High frequencies will be more attenuated compared to lower components of the frequency spectrum, this leads to the increase of the rise front time duration. Acoustic waves are detected as echoes in the differential signal $+H-(-H)$ with subtracted background, as it is presented in Fig. 2.24. The first longitudinal acoustic echo is depicted in Fig. 2.32 (a). Fig. 2.32 (b) gives a graphical representation of Terfenol simplified sensitivity function $\exp(-\alpha x)$, see Eq. (2.69). The parameters used in its determination are $k = 3.3545$ at the probe wavelength of $\lambda = 800$ nm [49]. Fig. 2.32 (c) shows the temporal profile of the first laser-induced longitudinal acoustic pulse (1L) in the 300 nm thick $TbFe_2$ film that we use in the model that assumes a linear rising front to account for the laser demagnetization, followed by a sharp decay. The time duration of the acoustic pulse in the model measured at FWHM is equal to $\sim 8.0 \pm 0.1$ ps. The temporal profile of the unipolar laser-induced longitudinal acoustic pulse is presented in Fig. 2.32 (c). Pulse shape was chosen so that its convolution with sensitivity function of Terfenol best describes the measured acoustical echo temporal profile. In Fig. 2.32 (d) differential signal $+H-(-H)$ with subtracted background (blue solid line) is superimposed with the convolution of two functions presented in Fig. 2.32 (b) and Fig. 2.32 (c).

The same analysis was performed to reveal the temporal profile of the first shear pulse (1S). It is depicted in Fig. 2.33 (a). Fig. 2.33 (b) gives a graphical representation of the Terfenol sensitivity function $\exp(-\alpha x)$, which is identical to the one used for the reconstruction of the longitudinal pulse. The temporal profile of the unipolar laser-induced shear strain, used in our model is presented in Fig. 2.33 (c)[6]. Its time duration measured at FWHM is equal to $\sim 8.0 \pm 0.1$ ps. Complex Fourier transform has been performed in order to reveal the frequency spectrum of the pulse, see the inset. In Fig. 2.33 (d) differential signal $+H-(-H)$ with subtracted background (blue solid line) is superimposed with the convolution of two functions, presented in Fig. 2.33 (b) and Fig. 2.33 (c).

---

[6] In practice peak will have smoother shape at the maximal amplitude values.

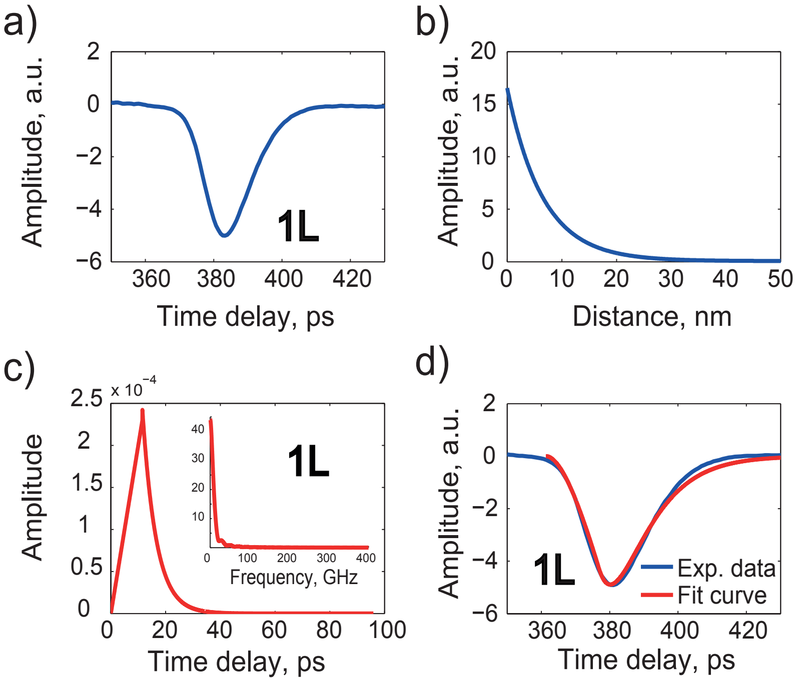

Fig. 2.32: Temporal profiles of the a) longitudinal acoustic echo in the 300 nm thick $TbFe_2$ film and propagated through the 1000 nm of SiO_2, see Fig. 2.24, b) Terfenol sensitivity function, c) temporal profile of the unipolar laser-induced longitudinal acoustic pulse, used in the model. d) Differential signal $+H-(-H)$ with subtracted background (blue solid line) is superposed with the convolution (c) (red solid line).

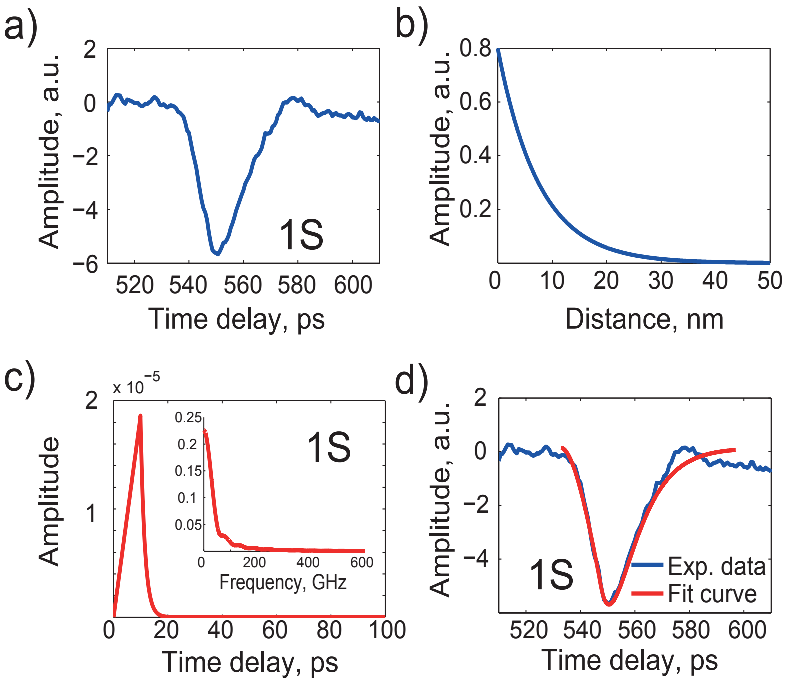

Fig. 2.33: Temporal profiles of the a) shear acoustic echo in the 300 nm thick $TbFe_2$ film and propagated through the 1000 nm of SiO_2, see Fig. 2.24, b) Terfenol sensitivity function, c) temporal profile of the unipolar laser-induced shear acoustic pulse, used in the model. d) Differential signal $+H-(-H)$ with subtracted background (blue solid line) is superposed with the convolution (c) (red solid line).

Magneto-optical detection of the acoustic pulses can be presented as a reaction of magnetization on arrival of the strain acoustic pulses. Equations of magnetic perturbation from the acoustic strains in the (x', y', z') coordinate system can be expressed as in supplementary material of [60]

$$\begin{aligned}\frac{dm_{x'}}{dt} &= \frac{\gamma_L}{2M_s}[2K_1(3m_{x'}^2 + m_{y'}^2 - 2m_{z'}^2)m_{y'}m_{z'} + K_2(m_{x'}^2 - m_{y'}^2)(m_{x'}^2 - m_{y'}^2 + 2m_{z'}^2)m_{y'}m_{z'} \\ &+ b_1(4\varepsilon_{x^*y^*}m_{x'} - 2(\varepsilon_{x^*x^*} + \varepsilon_{y^*y^*} - 2\varepsilon_{z^*z^*})m_{y'})m_{z'} \\ &+ b_2(\varepsilon_{y^*z^*}m_{x'}m_{y'} - 2\varepsilon_{x^*z^*}m_{y'}^2 - \varepsilon_{x^*x^*}m_{y'}m_{z'} + 2\varepsilon_{x^*z^*}m_{z'}^2)],\end{aligned} \tag{2.71}$$

$$\begin{aligned}\frac{dm_{y'}}{dt} &= -\frac{\gamma_L}{2M_s}[2K_1(m_{x'}^2 + 3m_{y'}^2 - 2m_{z'}^2)m_{x'}m_{z'} + K_2(m_{x'}^2 - m_{y'}^2)(m_{x'}^2 - m_{y'}^2 - 2m_{z'}^2)m_{x'}m_{z'} \\ &+ 2b_1(\varepsilon_{x^*x^*}m_{x'} + \varepsilon_{y^*y^*}m_{x'} - 2(\varepsilon_{z^*z^*}m_{x'} + \varepsilon_{x^*y^*}m_{y'}))m_{z'} \\ &+ b_2(2\varepsilon_{y^*z^*}m_{x'}^2 - 2\varepsilon_{y^*z^*}m_{y'}^2 + \varepsilon_{x^*x^*}m_{x'}m_{z'} - \varepsilon_{y^*y^*}m_{x'}m_{z'} - 2\varepsilon_{x^*z^*}m_{y'}m_{x'})],\end{aligned} \tag{2.72}$$

$$\begin{aligned}\frac{dm_{z'}}{dt} &= -\frac{\gamma_L}{M_s}[2K_1(m_{y'}^2 - m_{x'}^2)m_{x'}m_{y'} + 2K_2(m_{y'}^2 - m_{x'}^2)m_{x'}m_{y'}m_{z'}^2 - 2b_1(\varepsilon_{x^*y^*}(m_{x'}^2 - m_{y'}^2) \\ &+ b_2(\varepsilon_{x^*x^*}m_{x'}m_{y'} - \varepsilon_{y^*y^*}m_{x'}m_{y'} - \varepsilon_{x^*z^*}m_{x'}m_{z'} - \varepsilon_{y^*z^*}m_{y'}m_{z'}) - M_s\mu_0 m_{z'}m_{x'}],\end{aligned} \tag{2.73}$$

where $\gamma_L = \gamma/(1+\alpha^2)$, $m_{x'}$, $m_{y'}$, $m_{z'}$ in the right hand side of this dynamical equations are the initial magnetization direction cosines. Only the waves propagating along the normal to the surface are considered i.e. $\varepsilon_{y^*y^*} = \varepsilon_{z^*z^*} = \varepsilon_{y^*z^*} = 0$, that allows some simplifications in Eq. (2.71) - Eq. (2.73):

$$\begin{aligned}\frac{dm_{x'}}{dt} &= \frac{\gamma_L}{2M_s}[-2b_1\varepsilon_{x^*x^*}m_{y'}m_{z'} - b_2\varepsilon_{x^*x^*}m_{y'}m_{z'} + 4b_1\varepsilon_{x^*y^*}m_{x'}m_{z'} \\ &- 2b_2\varepsilon_{x^*z^*}m_{y'}^2 + 2b_2\varepsilon_{x^*z^*}m_{z'}^2],\end{aligned} \tag{2.74}$$

$$\frac{dm_{y'}}{dt} = -\frac{\gamma_L}{2M_s}[2b_1\varepsilon_{x^*x^*}m_{x'} + 4b_1\varepsilon_{x^*y^*}m_{y'}m_{z'} - 2b_2\varepsilon_{x^*z^*}m_{y'}m_{x'}], \tag{2.75}$$

$$\frac{dm_{z'}}{dt} = \frac{\gamma_L}{M_s}[b_2\varepsilon_{x^*x^*}m_{x'}m_{y'} - 2b_1\varepsilon_{x^*y^*}(m_{y'}^2 - m_{z'}^2) - b_2\varepsilon_{x^*z^*}m_{x'}m_{z'}]. \tag{2.76}$$

The probe beam normally incident to the surface is sensitive to the $m_{x'}$ component of $\overrightarrow{M}$. Oblique incidence provides an access to the detection of in-plane magnetization $(m_{y'},\ m_{z'})$. Detection of laser-induced dynamics in transversal MOKE configuration

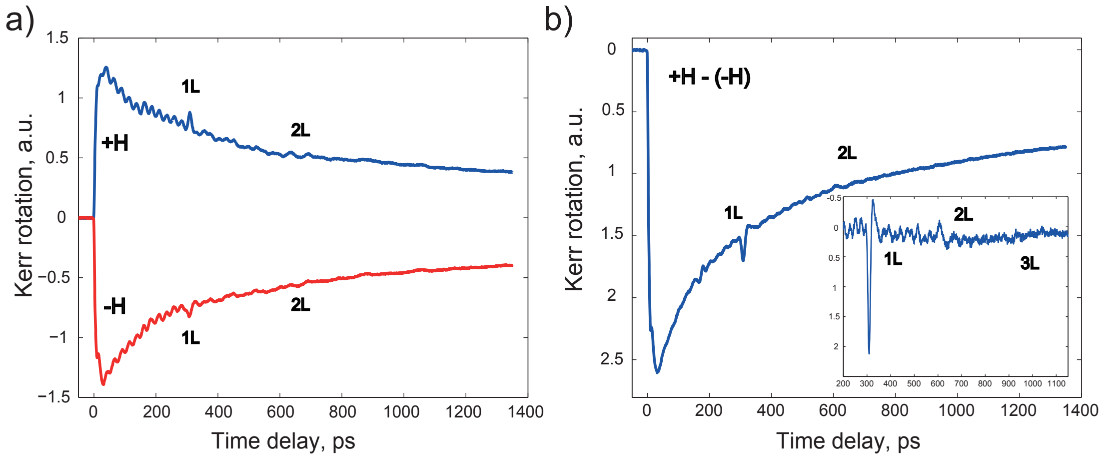

Fig. 2.34: a) Transient time resolved pump-probe MOKE signals recorded in a 300 nm $TbFe_2/775$ nm SiO_2 multi-layer sample of in-plane static magnetization at two out-of-plane magnetic field orientations $\pm H$. b) Differential signal $+H-(-H)$ with subtracted background (the inset) reveals only the presence of longitudinal acoustic waves generated in the 300 nm Terfenol layer. Probe of 400 nm wavelength is normal incident to the surface.

with different probe polarization (s, p) allow to distinguish only one particular in-plane component from the left part of Eq. (2.75) and Eq. (2.76). The time-resolved Kerr signals obtained with normally incident probe show mainly the detection of longitudinal acoustic waves only, see Fig 2.34. Thus the contribution of the longitudinal strain to the variation of $dm_{x'}/dt$ is bigger than that of the transversal pulse. Shear detection sensitivity increases with the angle of incidence of the probe with respect to the normal [41]. Hence, arrival of the shear strain to the Terfenol alters mostly the in-plane projections of the $\overrightarrow{M}$.

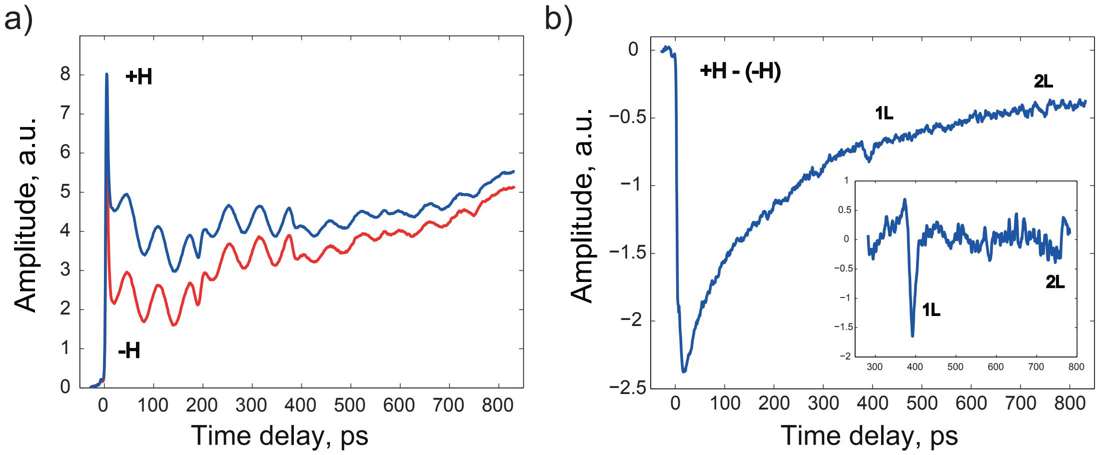

Fig. 2.35: a) Transient time resolved reflectivity signals recorded in a 300 nm $TbFe_2/1000$ nm SiO_2 multi-layer sample of in-plane static magnetization at two out-of-plane magnetic field orientations $\pm H$. b) Differential signal $+H-(-H)$ with subtracted background (the inset). P-polarized probe beam with 800 nm wavelength is obliquely incident to the surface. The inset shows the detection of longitudinal echoes.

Fig. 2.35 presents the time resolved differential reflectivity recorded at $\pm H$ in a 300 nm $TbFe_2$/1000 nm SiO_2 multi-layer sample. In the current case, p-polarized probe monitors the change of $\frac{dm_{y'}}{dt}$ (projection of $\overrightarrow{M}$ on the y experimental axis). Detection of only longitudinal echoes evidences that shear strain $\varepsilon_{x^*y^*}$, associated with low magneto-elastic coefficient b_1 in Eq. (2.75) doesn't have a significant influence to the $\frac{dm_{y'}}{dt}$ evolution. Therefore, the measurements of the shear echoes should be performed in longitudinal MOKE configuration.

Since the experimental schemes of MOKE (magneto-optic detection) and depolarized Brillouin scattering (photo-elastic detection) are identical, it is problematic to distinguish and optimize the proper detection mechanism. Moreover, the final experimental curves are represented by a difference of two time-resolved signal detected with two opposite orientations of the magnetic field ±H (in order to filter a non-magnetic impact to the signal). In practice it means that the sign of some magnetoelastic strains will be changed during the magnetic field reversal, following direction of the applied field. Furthermore, one has to be careful considering a differential signal (+H - (-)H), because if the strain doesn't change its sign at ±H, it is not detected by photo-elastic effect. Unlike longitudinal pulse, shear strains change their signs during the generation (see, expressions Eq. (2.36) - Eq. (2.38)), hence, they can be detected by the photo-elastic effect at oblique incidence of the probe. If the strain preserves its sign during the reversal of the magnetic filed ±H, it can be detected by magneto-optic detection. Tab. 2.2 summaries data about the detection mechanisms, following Eq. (2.71) - Eq. (2.73).

	Magneto-optic detection	**Photo-elastic detection**
$\varepsilon_{x^*x^*}$ **(Longitudinal)**	YES	NO
$\varepsilon_{x^*y^*}$ **(Shear)**	YES	YES
$\varepsilon_{x^*z^*}$ **(Shear)**	NO	YES

Table 2.6: Detection of the magneto-elastic strains.

Magnetostrictive anisotropy of Terfenol films

The theoretical analysis of the build-in static strain amplitudes has emphasized the crucial importance of the initial magnetization orientation with respect to the crystallographic axes, see Eq. (2.37) and Eq. (2.38). The amplitude of the shear strains generated through demagnetostriction reaches its maxima when $\overrightarrow{M}$ is tilted at $\theta = 45$ degrees out of its initial position. In order to check this theoretical result experimentally, we have performed several measurements at different angles of the applied external magnetic field. Fig. 2.36 shows the sample and magnetic field geometry used in the experiment.

MOKE data were recorded with a static magnetic field of H_{ex} =7 kOe applied along the plane that contains the normal to the surface and the crystallographic orientation $[1\bar{1}0]$. Each pair of MOKE data were recorded for different pairs of ξ angles by discrete steps of 45 degrees. The differential time-resolved MOKE signals were calculated for each pair of ξ angles that correspond to two opposite orientations of the magnetic field vector $\pm\overrightarrow{H}$, i.e. ξ and ξ + 180 degrees. The differential MOKE data obtained with a 300 nm Terfenol film, covered with 775 nm thick SiO_2, reveal several acoustic echoes of longitudinal or shear acoustic polarization on top of a demagnetization background. Fig. 2.37 show an increase of the shear echo amplitude from 0 % to 19 %, which follows the reorientation of $\overrightarrow{M}$. Indeed, it is relevant with the analytical model of Eq. (2.37) and Eq. (2.38). Since the measurements of the echo amplitudes can be disturbed by experimental artifacts, such as beam pointing stability during the magnetic field reorientation, the ratio of the shear A_S and longitudinal A_L echoes amplitudes is utilized in Tab. 2.7 in order to weight the generation efficiency at different ξ orientations. A_S/A_L is insensitive to optical artifacts.

If the magnetization remains in the plane of the film or aligned along its normal, one of the direction cosines $m_{x'}$, $m_{y'}$, $m_{z'}$ will be equal to 0, which results in the generation of longitudinal strain pulses only as evidenced in Fig. 2.37 (c). On the contrary, the excitation of the shear strain occurs if the magnetization is tilted out-of-plane of the surface. However, there is no obvious variation in A_S/A_L ratio when H is tilted from 0 to 45 degrees, which is expected from the theoretical model. In fact, the applied magnetic field is probably not strong enough to tilt substantially $\overrightarrow{M}$ at 45 degrees out-of-plane. The applied magnetic field of 700 mT slightly tilts the magnetization out-of-plane without a strong difference between 0 and 45 degrees. The magnitude of the shear generation could be enhanced by application of stronger magnetic fields.

The strong magnetocrystalline anisotropy of the thick $TbFe_2$ films ($K_1 = -760 \cdot$

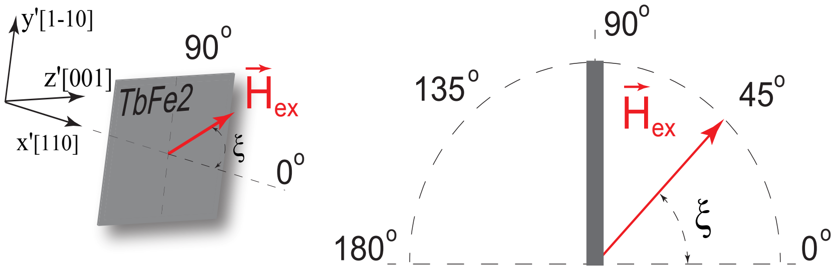

Fig. 2.36: Geometry of the sample orientation and magnetic field orientation.

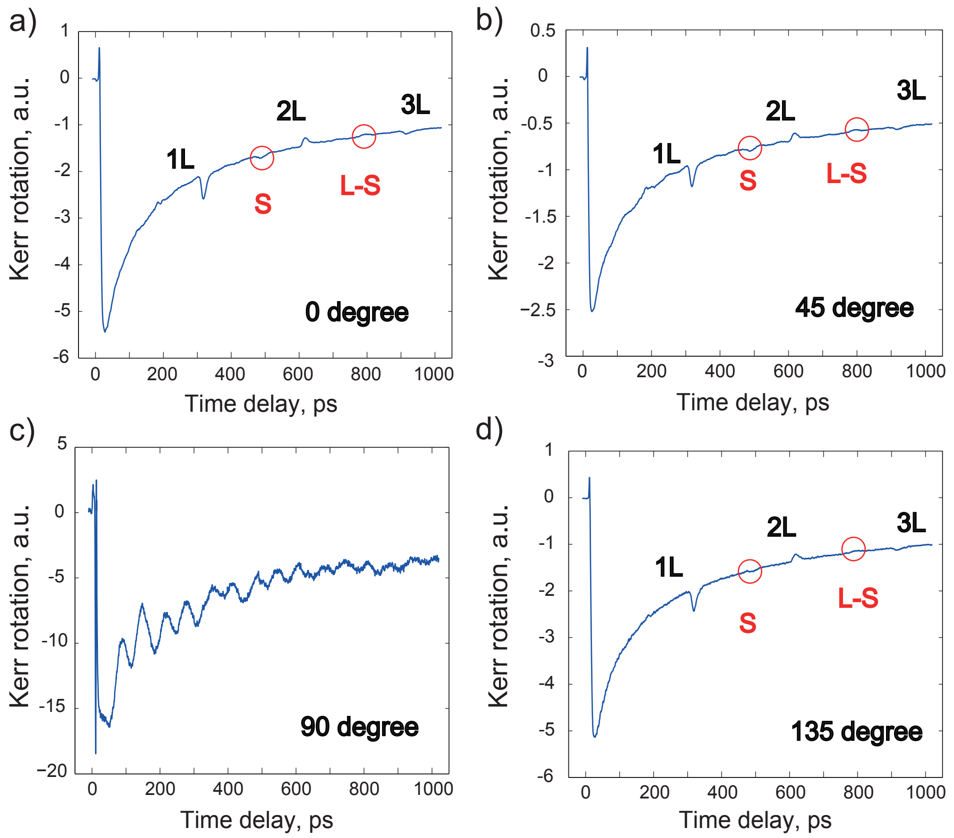

Fig. 2.37: Differential time resolved MOKE data recorded at different applied magnetic field orientations along a) the normal of the sample surface $\xi = 0 \pm 180$ degrees, b) tilted at $\xi = 45 \pm 180$ degrees, c) in plane of the sample $\xi = 90 \pm 180$ degrees, d) tilted at $\xi = 135 \pm 180$ degrees.

10^{-4} Pa) [10] was confirmed by our measurements of the static MOKE, as shown in Fig. 2.5. For thin films with in-plane magnetization, the magnetic orientations [001], $[1\bar{1}0]$ are defined as magnetically hard and easy axes. In case of out-of-plane magnetized thin films, static MOKE measurements have revealed $[11\bar{2}]$ and $[1\bar{1}0]$ directions as easy and hard axes, respectively. The strong magnetocrystalline anisotropy is in fact connected to the magnetostrictive anisotropy. In such samples with huge magnetostrictive anisotropy for which $\lambda_{111} \gg \lambda_{100}$ (see Tab. 2.1), the release of the shear strains along the crystallographic axis with stronger magnetostrictive constant should increase the efficiency of shear excitation due to the rhomboidal lattice distortion along the [111] direction (see Fig. 2.1). We have performed experiments to reveal the magnetostrictive anisotropy by varying the in-plane orientation ϕ (defined in Fig. 2.10) of the $TbFe_2$

Tilt angle, deg	0	45	90	135
A_S/A_L, %	19	19	−/−	12

Table 2.7: Ratio of the longitudinal to shear echo amplitudes as a function of the magnetic field orientation.

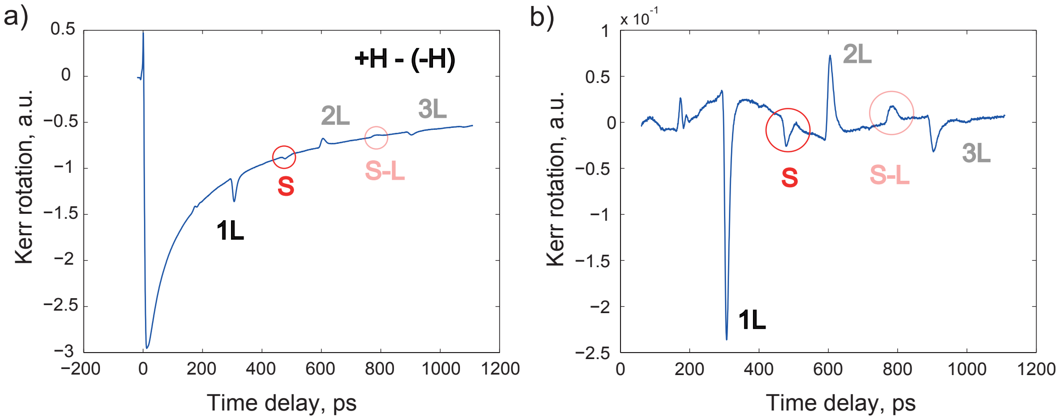

Fig. 2.38: Time resolved variation of the MOKE signal recorded with a 300 nm $TbFe_2$ sample covered with a 775 nm thick SiO_2 layer from two orthogonally applied magnetic field. a) Differential signal $+H-(-H)$ and b) subtracted baseline.

crystal with respect to the probe plane of incidence. Time-resolved MOKE dynamics of in-plane magnetized 300 nm Terfenol films, covered with a 775 nm thick SiO_2 layer, were monitored at different in-plane crystallographic orientations ϕ. Fig. 2.38 (a) presents the differential MOKE signal obtained for two applied magnetic fields $+H-(-H)$ at $\phi = 0$ degree and Fig. 2.38 (b) emphasizes the acoustic echoes. A set of pump-probe differential MOKE experiments were performed at different in-plane crystallographic orientations ϕ and magnetic field orientations ξ. For each data, we have extracted the ratio of the detected shear (S) and longitudinal acoustic (1L) echoes. In Tab. 2.8, the columns [1-10], [001], [1-11] indicate the crystallographic axis perpendicular to the optical plane of incidence, while the left column denotes the magnetic field orientation ξ. The amplitude ratios A_S/A_L were calculated in order to minimize the experimental artifacts. The [1-11] direction is expected to coincide with the axis of strong magnetostriction of Terfenol ($\lambda_{111} = 2460 \cdot 10^{-6} \gg \lambda_{100} = 300 \cdot 10^{-6}$), consequently, the shear strains released after the laser demagnetization of the film, must have the highest amplitudes. Indeed, at some field orientation of $\xi = 45$ degrees, Tab. 2.8 shows that the ratio of amplitudes is the highest, but there is no clear difference among the data. Unfortunately, the laser-induced excitation of the picosecond shear strain waves in Terfenol films does not evidence the strong magnetostrictive anisotropy. This is probably due to the fact that the static magnetic field is not strong enough to force the magnetization along different crystallographic orientations in our experiment.

	[1-10] $\phi = 0$ deg	**[001]** $\phi = 90$ deg	**[1-11]** $\phi = 45$ deg
$\xi = 90$ deg (H along the normal)	11 %	12 %	8.4 %
$\xi = 45$ deg (H along the diagonal)	10 %	8.8 %	14 %
$\xi = 135$ deg (H along the diagonal)	8 %	8.8 %	12 %

Table 2.8: Ratio of the first shear and longitudinal (A_S/A_L) echoes amplitudes as a function of the initially in-plane magnetized crystal orientation ϕ and of the magnetic field orientation ξ.

2.3 Magnetostrictive mode conversion in Terfenol thin films

As evidenced in the experimental results that has revealed the so called L-S shear acoustic pulses, see for example Fig. 2.38 at 800 ps time delay, the injection of picosecond longitudinal strain pulses in magnetostrictive Terfenol films lead to the partial conversion of the longitudinal strain pulse into a shear strain pulse upon reflection at the interface. This mode conversion phenomenon is a surface effect of magnetostrictive origin, it could be an alternative approach for the excitation of shear acoustic waves in Terfenol. In fact the longitudinal strain pulse modifies the magnetic anisotropy field and tilts H_{eff} that causes the reorientation of $\overrightarrow{M}$, which is no longer aligned along H_{eff}. In the Landau-Lifshitz model of Eq. (1.3), the direction and the magnitude of H_{eff} are determined by the free energy density of the film F, which includes the magneto-elastic energy density term F_{me}, see Eq. (2.79) and Eq. (2.80). It provides a direct coupling of the acoustic strain and orientation of the magnetization of the film. Since initially $\overrightarrow{M}$ is tilted out-of-plane of the sample at some degree, change of of its orientation is coupled to the generation of shear wave, as in the demagnetostriction process described in the previous section Sec. 2.1. In this section, we present the analytical model describing the magnetization and magnetostrictive response following the injection of a longitudinal strain pulse in a Terfenol layer.

The inverse magnetostriction mechanism for shear acoustic mode conversion in the hybrid Terfenol sample is sketched in Fig. 2.39. The longitudinal acoustic strain $\varepsilon_L(x,t)$, initially laser generated at the ferromagnetic layer, is injected back after its round trip in the acoustic delay line in the Terfenol layer where it modifies the free energy density F of Terfenol. It results in the excitation from mode-conversion at the interface of a shear strain $\varepsilon_{L-S}(x,t)$ transmitted in the SiO_2 layer. This peculiar inverse magnetostriction mechanism is a route for inter-mode acoustic conversion in Terfenol hybrid sample and an alternative pathway for ultrafast shear acoustic waves generation. In the following, the analytical theory and numerical simulations were performed in order to determine

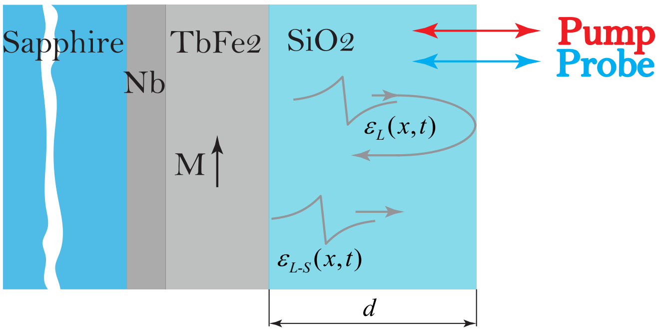

Fig. 2.39: Shear wave generation by acoustic mode conversion process in $TbFe_2$ films. The shape of the acoustic strains is arbitrary.

the efficiency of this mode conversion mechanism.

The magnetization of magnetic and magnetostrictive materials can be manipulated by acoustic pulses at picosecond timescale (see Sec. 1.3). This inverse magnetostriction effect is described by the Landau-Lifshitz equation, which predicts the rotation of $\overrightarrow{M}$ in response to the acoustic perturbation.

$$\frac{\partial\overrightarrow{m}}{\partial t} = -\gamma\mu_0\overrightarrow{m} \times \overrightarrow{H}_{eff}, \tag{2.77}$$

where γ, μ_0 are the gyromagnetic ratio and magnetic permeability of vacuum, respectively. $\overrightarrow{m}$ is the unit magnetization vector of the $TbFe_2$ layer, $\overrightarrow{H}_{eff}$ is the effective magnetic field of Terfenol. The projections on the coordinate axes of Eq. (2.77) can be expressed as

$$\begin{gathered}\frac{\partial m_{x'}}{\partial t} = -\gamma\mu_0(m_{y'}\overrightarrow{H}_{effz'} - m_{z'}\overrightarrow{H}_{effy'}),\\ \frac{\partial m_{y'}}{\partial t} = -\gamma\mu_0(m_{z'}\overrightarrow{H}_{effx'} - m_{x'}\overrightarrow{H}_{effz'}),\\ \frac{\partial m_{z'}}{\partial t} = -\gamma\mu_0(m_{x'}\overrightarrow{H}_{effy'} - m_{y'}\overrightarrow{H}_{effx'}).\end{gathered} \tag{2.78}$$

The effective magnetic field $\overrightarrow{H}_{eff}$ is equal to

$$\overrightarrow{H}_{eff} = -\frac{1}{\mu_0 M_0}\frac{\partial F}{\partial m_i}, \tag{2.79}$$

where M_0, F are the saturation of magnetization and the free energy density of Terfenol, respectively. The free energy density can be written in the form

$$F = F_m + F_{me} + F_e, \tag{2.80}$$

where F_m, F_{me}, F_e are magnetic, magneto-elastic and elastic energy densities of the ferromagnetic film. F_e will be omitted in the further considerations, since it gives a zero contribution into expression Eq. (2.79)

$$F_m \quad = \quad K(m_x^2 m_y^2 + m_y^2 m_z^2 + m_x^2 m_z^2) - \mu_0 M_0 \overrightarrow{H} \overrightarrow{m'} + \frac{\mu_0}{2}(M_0 m_{x'})^2, \tag{2.81}$$

where M is the magnetic anisotropy constant, $\overrightarrow{H}$ is the external DC magnetic field. The first term of Eq. (2.81) corresponds to the energy of magnetic anisotropy in the (x, y, z) system of coordinates. Second and third therm are Zeeman and dipole-dipole energies, respectively. Transition from the arbitrary coordinate system (x, y, z) to the experimental system (x', y', z') take the form

$$\begin{pmatrix} m_x \\ m_y \\ m_z \end{pmatrix} = \begin{pmatrix} \frac{1}{\sqrt{2}}\cos\xi & \frac{1}{2}\sin\xi & 0 \\ -\sin\xi & \cos\xi & 0 \\ 0 & 0 & 1 \end{pmatrix} \begin{pmatrix} m_{x'} \\ m_{y'} \\ m_{z'} \end{pmatrix} \tag{2.82}$$

$$\begin{gathered} m_x = \cos\xi m_{x'} + \sin\xi m_{y'}, \\ m_y = -\sin\xi m_{x'} + \cos\xi m_{y'}, \\ m_z = m_{z'}. \end{gathered} \tag{2.83}$$

Thus, if $\xi = \pi/4$, the energy of the magnetic anisotropy F_a in Eq. (2.81) should be modified accordingly, we obtain

$$\begin{aligned} F_a = K(m_x^2 m_y^2 + m_y^2 m_z^2 + m_x^2 m_z^2) = K((\frac{\sqrt{2}}{2}m_{x'} - \frac{\sqrt{2}}{2}m_{y'})^2 \times (\frac{\sqrt{2}}{2}m_{x'} + \frac{\sqrt{2}}{2}m_{y'})^2 \\ + (\frac{\sqrt{2}}{2}m_{x'} - \frac{\sqrt{2}}{2}m_{y'})^2 m_{z'}^2 + (\frac{\sqrt{2}}{2}m_{x'} - \frac{\sqrt{2}}{2}m_{y'})^2 m_{z'}^2) \\ = K(\frac{1}{4}(m_{x'}^2 - m_{y'}^2)^2 + m_{x'}^2 m_{z'}^2 + m_{y'}^2 m_{z'}^2). \end{aligned} \tag{2.84}$$

Substitution of Eq. (2.84) into the expression of the magnetic energy density of Eq. (2.81) results in

$$F_m = K(\frac{1}{4}(m_{x'}^2 - m_{y'}^2)^2 + m_{x'}^2 m_{z'}^2 + m_{y'}^2 m_{z'}^2) - \mu_0 M_0 \overrightarrow{H} \overrightarrow{m'} + \frac{\mu_0}{2}(M_0 m_{x'})^2. \tag{2.85}$$

Eq. (2.85) describes the final expression of the magnetic energy for the in-plane magnetized Terfenol film. Now, since all contributions to the free energy density F are determined, the effective magnetic field of Eq. (2.79) can be estimated (F_e elastic energy density has a zero contribution to H_{eff}, so its impact will be neglected). But first, the direction of the external field should be defined.

Fig. 2.40 depicts the orientation of the applied DC magnetic field with respect to the (x', y', z') axes. ξ is a polar angle between $\overrightarrow{H}$ and the surface of the film. ψ is an azimuthal angle between the projection of $\overrightarrow{H}$ on $y'z'$ plane and the y' axis.

The magneto-elastic energy density F_{me} was described in the previous section (see Sec. 2.1) and have form of Eq. (2.8). Substitution of the expression of the magneto-elastic and magnetic energy densities of Terfenol (see Eq. (2.8) and Eq. (2.85), respectively) into Eq. (2.79) with projection on the x', y', z' axes results in

$$\begin{aligned} H_{effx'} &= -\frac{K}{\mu_0 M_0}(m_{x'}^3 - m_{x'}m_{y'}^2 + 2m_{x'}m_{z'}^2) + Hsin\xi - M_0 m_{x'} \\ &- \frac{b_1}{\mu_0 M_0}(m_{x'}\varepsilon_{x'x'} + 2m_{y'}\varepsilon_{x'y'}) - \frac{b_2}{\mu_0 M_0}(m_{x'}\varepsilon_{x'x'} + 2m_{z'}\varepsilon_{x'z'}), \end{aligned} \tag{2.86}$$

$$\begin{aligned} H_{effy'} &= -\frac{K}{\mu_0 M_0}(m_{y'}^3 - m_{y'}m_{x'}^2 + 2m_{y'}m_{z'}^2) + Hcos\xi cos\psi \\ &- \frac{b_1}{\mu_0 M_0}(m_{y'}\varepsilon_{x'x'} + 2m_{x'}\varepsilon_{x'y'}) - \frac{b_2}{\mu_0 M_0}m_{y'}\varepsilon_{x'x'}, \end{aligned} \tag{2.87}$$

$$H_{effz'} = -\frac{2K}{\mu_0 M_0}(m_{x'}^2 + m_{y'}^2)m_{z'} + Hcos\xi sin\psi - \frac{2b_2}{\mu_0 M_0}m_{x'}\varepsilon_{x'z'}. \tag{2.88}$$

The last two terms of Eq. (2.86) and Eq. (2.87) and the last term in Eq. (2.88) represent the contribution of the magneto-elastic energy density to the effective field H_{eff}

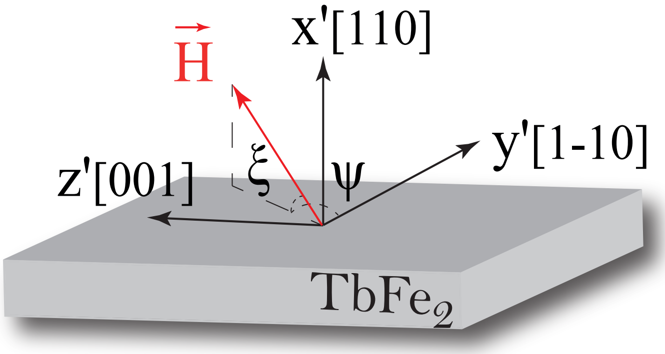

Fig. 2.40: Orientation of the external magnetic field H with respect to the crystallographic directions of the $TbFe_2$ film.

and directly couple strain and magnetization of Terfenol. Primarily, only the first longitudinal strain pulse $\varepsilon_{x^*x^*}$[8] incident on the ferromagnetic film is considered. Further, excitation of the shear strain waves is considered in reaction to the reorientation of $\overrightarrow{M}$. The magnetization projection on the experimental coordinate system can be assumed to follow

$$m_i = m_i^0 + m_{i0} \cdot \exp(j(\omega t - k_l x')), \tag{2.89}$$

where $i = x',\ y',\ z',\ k_l$ is the acoustic wavevector of the longitudinal wave and m_i is the perturbation of the magnetization induced by the acoustic pulse. The acoustic displacement $u_{x'}$ along the normal of the sample x' is expressed in a similar way

$$u_{x'} = u_{x'0} \cdot \exp(j(\omega t - k_l x')). \tag{2.90}$$

Eq. (2.90) corresponds to the longitudinal wave (1L) incident on the Terfenol film. Eq. (2.89) and Eq. (2.90) are substituted into the system of Eq. (2.78). The transformed system will have the form

$$A \cdot \overrightarrow{m}_{i0} = \overrightarrow{U}, \tag{2.91}$$

where A is the matrix, $\overrightarrow{m}_{i0}$ is the unit magnetization vector induced by the acoustic wave.

$$\overrightarrow{m}_{i0} = \begin{pmatrix} m_{x'0} \\ m_{y'0} \\ m_{z'0} \end{pmatrix}, \tag{2.92}$$

$$\overrightarrow{U} = \begin{pmatrix} U_1 \\ U_2 \\ U_3 \end{pmatrix}, \tag{2.93}$$

$$A = \begin{pmatrix} A_{11} & A_{12} & A_{13} \\ A_{21} & A_{22} & A_{23} \\ A_{31} & A_{32} & A_{33} \end{pmatrix}. \tag{2.94}$$

The elements of the vector $\overrightarrow{U}$ and matrix A are

$$U_1 = -jk_l \frac{\gamma m_{z'}^0 m_{y'}^0}{M_0}(b_1 - b_2) u_{x'0},$$

---

[8] Sign * means the longitudinal strain pulse propagating in the SiO_2 layer towards the $TbFe_2$ film.

$$U_2 = -jk_l \frac{\gamma m^0_{x'} m^0_{z'}}{M_0}(b_1 - b_2) u_{x'0},$$

$$U_3 = -jk_l \frac{2\gamma b_2 m^0_{y'} m^0_{x'}}{M_0} u_{x'0},$$

$$A_{11} = -j\omega \frac{6K\gamma}{M_0} m^0_{x'} m^0_{y'} m^0_{z'},$$

$$A_{12} = \gamma\mu_0 (\frac{K}{\mu_0 M_0} m^0_{z'} (3m^{o2}_{x'} - 2m^{o2}_{z'} + 3m^{o2}_{y'}) - H\cos\xi\sin\psi),$$

$$A_{13} = \gamma\mu_0 (\frac{K}{\mu_0 M_0} m^0_{y'} (3m^{o2}_{x'} + m^{o2}_{y'} - 6m^{o2}_{z'}) + H\cos\xi\cos\psi),$$

$$A_{21} = \gamma\mu_0 (\frac{K}{\mu_0 M_0} m^0_{z'} (-3m^{o2}_{x'} - 3m^{o2}_{y'} + 2m^{o2}_{z'}) + m_{z'} M_0 + H\cos\xi\cos\psi),$$

$$A_{22} = -j\omega - \gamma \frac{6K}{M_0} m^0_{x'} m^0_{y'} m^0_{z'},$$

$$A_{23} = \gamma\mu_0 (\frac{K m^o_{x'}}{\mu_0 M_0} (-m^{o2}_{x'} - 3m^{o2}_{y'} + 6m^{o2}_{z'}) - H\sin\xi + m^o_{x'} M_0),$$

$$A_{31} = \gamma\mu_0 (\frac{2K}{\mu_0 M_0} m^o_{y'} (m^{o2}_{y'} - 3m^{o2}_{x'}) - H\cos\xi\cos\psi - m^o_{y'} M_0),$$

$$A_{32} = \gamma\mu_0 (\frac{2K}{\mu_0 M_0} m^o_{x'} (3m^{o2}_{y'} - m^{o2}_{x'}) + H\sin\xi - m^o_{x'} M_0),$$

$$A_{11} = -j\omega.$$

The coefficients U_i depend on the direction cosines of magnetization $m^o_{x'}$, $m^o_{y'}$, $m^o_{z'}$ and on the magnetoelastic constants b_1, b_2 of the Terfenol film. The coefficients A_{ij} depend on the direction cosines of magnetization but also on the orientation of the external field H with respect to the axes of the film, via the ξ, ψ angles. Two special cases are considered in order to simplify the calculations: the external magnetic field is tilted out-of-plane of the sample in (i) $x'y'$ plane, thus, $m^o_{z'} = 0$, $\psi = 0$ and in the (ii) $x'z'$ plane, thus, $m^o_{y'} = 0, \psi = \pi/2$ (see Fig. 2.40).

In the first case, where $\overrightarrow{H}$ points in the arbitrary direction between x' [110] out-of-plane and y' $[1-10]$ in-plane axes, the coefficients U_i, A_{ij} are equal to

$$U_1 = 0, \quad U_2 = 0, \quad U_3 = -jk_l \frac{2\gamma b_2 m^o_{y'} m^o_{x'}}{M_0} U_{x'o}.$$

$$A_{11} = -j\omega, \quad A_{12} = 0,$$

$$A_{13} = \gamma\mu_0\left(\frac{K}{\mu_0 M_0} m^0_{y'}(3m^{o2}_{x'} + m^{o2}_{y'}) + H\cos\xi\right),$$

$$A_{21} = 0, \quad A_{12} = -j\omega,$$

$$A_{23} = \gamma\mu_0\left(-\frac{K m^o_{x'}}{\mu_0 M_0}(m^{o2}_{x'} + 3m^{o2}_{y'}) - H\sin\xi + m^o_{x'} M_0\right),$$

$$A_{31} = \gamma\mu_0\left(\frac{2K}{\mu_0 M_0} m^o_{y'}(m^{o2}_{y'} - 3m^{o2}_{x'}) - H\cos\xi - m^o_{y'} M_0\right).$$

The coefficients A_{32}, A_{33} are not modified. In the second particular case, where $\overrightarrow{H}$ points in the arbitrary direction between x' [110] out-of-plane and z' [001] in-plane axes with $m^o_{y'} = 0, \psi = \pi/2$, the coefficients U_i, A_{ij} are equal to

$$U_1 = 0, \quad U_2 = jk_l \frac{\gamma b_2 m^o_{x'} m^o_{z'}}{M_0}(b_1 + b_2) U_{x'o}, \quad U_3 = 0.$$

$$A_{11} = -j\omega, \quad A_{13} = 0,$$

$$A_{12} = \gamma\mu_0\left(\frac{K}{\mu_0 M_0} m^0_{z'}(3m^{o2}_{x'} - 2m^{o2}_{z'}) - H\cos\xi\right),$$

$$A_{22} = -j\omega,$$

$$A_{21} = \gamma\mu_0\left(\frac{K}{\mu_0 M_0} m^o_{z'}(-3m^{o2}_{x'} + 2m^{o2}_{z'}) + H\cos\xi + m^o_{z'} M_0\right),$$

$$A_{23} = \gamma\mu_0\left(\frac{K}{\mu_0 M_0} m^o_{x'}(-m^{o2}_{x'} + 6m^{o2}_{z'}) - H\sin\xi + m^o_{x'} M_0\right),$$

$$A_{31} = 0, \quad A_{33} = -j\omega,$$

$$A_{32} = \gamma\mu_0\left(-\frac{2K}{\mu_0 M_0} m^{o3}_{x'} + H\sin\xi - m^o_{x'} M_0\right).$$

The perturbed magnetization vector $m_{x'o}$, $m_{y'o}$, $m_{z'o}$ can be found utilising the Cramer's rule (for the first particular case of $m^o_{z'} = 0$, $\psi = 0$). The solutions of Eq. (2.91) will take the form

$$m_{io} = \frac{\Delta_i}{\Delta}, \tag{2.95}$$

where Δ is the Cramer's determinant of the matrix A and Δ_i is the determinant of the matrix obtained by replacing the i column of the matrix A by the vector $\overrightarrow{U}$. The

Cramer's determinant is equal to

$$\Delta = \begin{vmatrix} -j\omega & 0 & A_{13} \\ 0 & -j\omega & A_{23} \\ A_{31} & A_{32} & -j\omega \end{vmatrix} = j\omega(\omega^2 + A_{23}A_{32}) + j\omega A_{13}A_{31}, \tag{2.96}$$

we introduced a coefficient ω_f to express the determinant in a more compact with

$$\omega_f^2 = -A_{23}A_{32} - A_{13}A_{31}. \tag{2.97}$$

This coefficient is related to the magnetization precession. By taking to account Eq. (2.97), the Cramer's determinant can be expressed as

$$\Delta = j\omega(\omega^2 - \omega_f^2). \tag{2.98}$$

The determinants Δ_1, Δ_2, Δ_3 results in

$$\Delta_1 = \begin{vmatrix} 0 & 0 & A_{13} \\ 0 & -j\omega & A_{23} \\ U_3 & A_{32} & -j\omega \end{vmatrix} = A_{13}j\omega U_3 = \omega A_{13}U_3^1 u_{x'o}, \tag{2.99}$$

where

$$U_3^1 = \frac{2\gamma k_l b_2 m_{y'}^o m_{x'}^o}{M_0}. \tag{2.100}$$

$$\Delta_2 = \begin{vmatrix} -j\omega & 0 & A_{13} \\ 0 & 0 & A_{23} \\ A_{31} & U_3 & -j\omega \end{vmatrix} = A_{23}j\omega U_3 = \omega A_{23}U_3^1 u_{x'o}, \tag{2.101}$$

$$\Delta_3 = \begin{vmatrix} -j\omega & 0 & 0 \\ 0 & -j\omega & 0 \\ A_{31} & A_{32} & U_3 \end{vmatrix} = -\omega^2 U_3 = j\omega^2 U_3^1 u_{x'o}. \tag{2.102}$$

The Cramer's determinant Δ of the matrix A and the determinants Δ_i allow to calculate the m_{io}, which are equal to

$$m_{x'o} = \frac{\Delta_1}{\Delta} = \frac{A_{13}U_3^1}{j(\omega^2 - \omega_f^2)} u_{x'o}, \tag{2.103}$$

$$m_{y'o} = \frac{\Delta_2}{\Delta} = \frac{A_{23}U_3^1}{j(\omega^2 - \omega_f^2)} u_{x'o}, \tag{2.104}$$

$$m_{z'o} = \frac{\Delta_3}{\Delta} = \frac{\omega U_3^1}{\omega^2 - \omega_f^2} u_{x'o}. \tag{2.105}$$

Eq. (2.103) - Eq. (2.105) denote the expressions of the perturbed unit magnetization vector in projection on the experimental coordinate axes. The boundary conditions, which take into account the continuity of the normal components of the mechanical stress at the Terfenol/fused silica interface, are

$$\sigma_{x'x'}\Big|_{x'=0} = \sigma_{x^*x^*}\Big|_{x^*=0}, \quad \sigma_{x'y'}\Big|_{x'=0} = -\sigma_{x^*y^*}\Big|_{x^*=0}, \quad \sigma_{x'z'}\Big|_{x'=0} = \sigma_{x^*z^*}\Big|_{x^*=0}. \tag{2.106}$$

$$u_{x'}\Big|_{x'=0} = -u_{x^*}\Big|_{x^*=0}, \quad u_{y'}\Big|_{x'=0} = u_{y^*}\Big|_{x^*=0}, \quad u_{z'}\Big|_{x'=0} = -u_{z^*}\Big|_{x^*=0}. \tag{2.107}$$

Eq. (2.106) can be expressed using the parameters of the $TbFe_2$ and SiO_2 films and from Eq. (2.52) in the form

$$c_l \frac{\partial u_{x'}}{\partial x'} + \frac{1}{2}(b_1(m_{x'}^2 + m_{y'}^2) + b_2(m_{x'}^2 - m_{y'}^2))\Big|_{x'=0} = c_{11}^* \frac{\partial u_{x*}}{\partial x*}\Big|_{x^*=0}, \tag{2.108}$$

$$c_{t1} \frac{\partial u_{y'}}{\partial x'} + b_1 m_{x'} m_{y'}\Big|_{x'=0} = -c_{44}^* \frac{\partial u_{y*}}{\partial x*}\Big|_{x^*=0}, \tag{2.109}$$

$$c_{t2} \frac{\partial u_{z'}}{\partial x'} + b_2 m_{x'} m_{z'}\Big|_{x'=0} = c_{44}^* \frac{\partial u_{z*}}{\partial x*}\Big|_{x^*=0}. \tag{2.110}$$

The displacements $u_{y'}$, $u_{z'}$, u_{x*}, u_{y*}, u_{z*} can be expressed by taking into account the incident and reflected waves at the Terfenol/fused silica interface, for the longitudinal displacement u_{x*}. The two media are depicted as a half spaces separated by the interface, see Fig. 2.41, u_{x*}^-, u_{x*}^+[9] denote the incident and reflected longitudinal displacements in SiO_2. u_{x*}^- is, thus, the initial longitudinal acoustic wave that is injected in Terfenol and entails mode conversion. It is partially transmitted to the $TbFe_2$ layer and is denoted as $u_{x'}$ in the ferromagnetic film.

Ultimately, the analytical expressions of the surface acoustic displacements take the form

$$u_{y'} = u_{y'o} exp(j(\omega t - k_{t1}x')), \tag{2.111}$$

$$u_{z'} = u_{z'o} exp(j(\omega t - k_{t2}x')). \tag{2.112}$$

---

[9] Sign "-" at u_{x*}^- is referred to the laser generation of the longitudinal strain displacement in $TbFe_2$, which is then reflected from the free interface of the SiO_2 layer and propagates along the negative direction of the x axis.

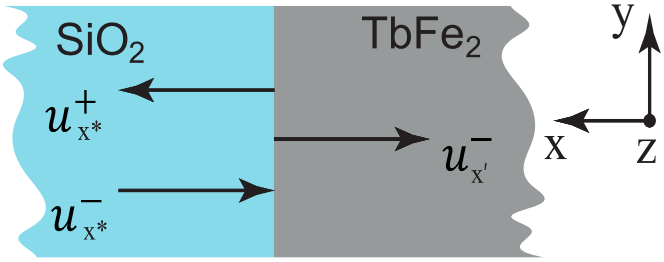

Fig. 2.41: Incident and reflected strain waves at the $SiO_2/TbFe_2$ interface along the x direction.

$$u_{x*} = u^+_{x*o} exp(j(\omega t - k_1^* x*)) + u^-_{x*o} \exp(j(\omega t + k_1^* x*)), \tag{2.113}$$

$$u_{y*} = u_{y*o} \exp(j(\omega t - k_2^* x*)), \tag{2.114}$$

$$u_{z*} = u_{y*o} \exp(j(\omega t - k_2^* x*)). \tag{2.115}$$

Eq. (2.113) describes an analytical expressions of the incident u^-_{x*o} and reflected u^+_{x*o} acoustic displacement at the $TbFe_2/SiO_2$ interface. It can be rewritten in the compact form

$$u_{x*} = u^+_{x*o} + u^-_{x*o}, \tag{2.116}$$

where u^-_{x*o}, u^+_{x*o} are the incident and reflected amplitudes components, respectively. The displacements of Eq. (2.108) - Eq. (2.110) can be expressed using Eq. (2.111) - Eq. (2.115). It allows to express the imaginary part of Eq. (2.108) - Eq. (2.110) in the first order, relatively to the m_{io} components

$$-jk_l c_l u_{x'o} + \frac{1}{2}(b_1(2m^0_{x'} m_{x'o} + 2m^0_{y'} m_{y'o}) + b_2(2m^0_{x'} m_{x'o} - 2m^0_{y'} m_{y'o})) = -jk_1^* c_{11}^* (u^+_{x*o} - u^-_{x*o}), \tag{2.117}$$

$$- \quad jk_{t1} c_{t1} u_{y'o} + b_1(m^0_{x'} m_{y'o} + m^0_{y'} m_{x'o}) = c^*_{44}(-jk_2^*) u_{y*o}, \tag{2.118}$$

$$- \quad jk_{t2} c_{t2} u_{z'o} + b_2(m^0_{x'} m_{z'o} + m^0_{z'} m_{x'o}) = c^*_{44}(-jk_2^*) u_{z*o}. \tag{2.119}$$

Taking into account $m^o_{z'} = 0, \psi = 0$, Eq. (2.117) - Eq. (2.119) follows

$$jk_l c_l u_{x'o} - (b_1 + b_2) m^0_{x'} m_{x'o} - (b_1 - b_2) m^0_{y'} m_{y'o} = jk_1^* c_{11}^* (u^+_{x*o} - u^-_{x*o}), \tag{2.120}$$

$$jk_{t1}c_{t1}u_{y'o} - b_1(m^0_{x'}m_{y'o} + m^0_{y'}m_{x'o}) = jk_2^* c_{44}^* u_{y*o}, \tag{2.121}$$

$$jk_{t2}c_{t2}u_{z'o} - b_2 m^0_{x'}m_{z'o} = jk_2^* c_{44}^* u_{z*o}. \tag{2.122}$$

The amplitude of the displacement $u_{x'o}$, transmitted into the $TbFe_2$ layer can be determined using the boundary condition Eq. (2.107)

$$\begin{cases} u_{x'o} = -(u^+_{x*o} + u^-_{x*o}), \\ jk_l c_l u_{x'o} - (b_1 + b_2)m^0_{x'}m_{x'o} - (b_1 - b_2)m^0_{y'}m_{y'o} = jk_1^* c_{11}^*(u^+_{x*o} - u^-_{x*o}). \end{cases} \tag{2.123}$$

The amplitude of the longitudinal displacement $u^+_{x'o}$, reflected from the $TbFe_2/SiO_2$ interface can be found from Eq. (2.123)

$$u^+_{x*o} = -(u_{x'o} + u^-_{x*o}). \tag{2.124}$$

Next it is substituted in Eq. (2.120)

$$\begin{aligned} Im &= jk_l c_l u_{x'o} - (b_1 + b_2)m^0_{x'}m_{x'o} - (b_1 - b_2)m^0_{y'}m_{y'o} \\ &= jk_1^* c_{11}^*(-u_{x'o} - 2u^-_{x*o}). \end{aligned} \tag{2.125}$$

The displacement $u_{x'o}$ can be obtained from Eq. (2.125) by taking into account Eq. (2.103) and Eq. (2.104)

$$u_{x'o}(jk_l c_l + jk_1^* c_{11}^*) - (b_1 + b_2)m^0_{x'}m_{x'o} - (b_1 - b_2)m^0_{y'}m_{y'o} = -2jk_1^* c_{11}^* u^-_{x*o},$$

$$u_{x'o}j(k_l c_l + k_1^* c_{11}^*) - (b_1 + b_2)m^0_{x'}\frac{A_{13}U_3^1}{j(\omega^2 - \omega_f^2)}u_{x'o} - (b_1 - b_2)m^0_{y'}\frac{A_{23}U_3^1}{j(\omega^2 - \omega_f^2)}u_{x'o} = -2jk_1^* c_{11}^* u^-_{x*o},$$

$$u_{x'o}\frac{[(k_l c_l + k_1^* c_{11}^*)(\omega^2 - \omega_f^2) + U_3^1((b_1 + b_2)m^0_{x'}A_{13}) + (b_1 - b_2)m^0_{y'}A_{23})]}{j(\omega^2 - \omega_f^2)} = -2jk_1^* c_{11}^* u^-_{x*o},$$

$$u_{x'o} = -\frac{2k_1^* c_{11}^*(\omega^2 - \omega_f^2)u^-_{x'o}}{(k_l c_l + k_1^* c_{11}^*)(\omega^2 - \omega_f^2) + U_3^1[(b_1 + b_2)m^0_{x'}A_{13}) + (b_1 - b_2)m^0_{y'}A_{23}]}. \tag{2.126}$$

Replacement of the wave vector $k_l = \omega/\upsilon_l$, $k_1^* = \omega/\upsilon_1^*$ and by introducing $E = U_3^1[(b_1 +$

$b_2)m^o_{x'}A_{13} + (b_1 - b_2)m^o_{y'}A_{23}]$ in Eq. (2.126), allow to express it in a more compact form

$$u_{x'o} = \frac{-2c_{11}(\omega^2 - \omega_f^2)u^-_{x^*o}}{\upsilon_1^*(c_l/\upsilon_l + c_{11}^*/\upsilon_1^*)(\omega^2 - \omega_f^2) + E/\omega}. \tag{2.127}$$

To find the shear displacements u_{y^*o} and u_{z^*o} we transform Eq. (2.121) and Eq. (2.122) by taking into account the boundary conditions, presented in Eq. (2.107). We can rewrite Eq. (2.121) and Eq. (2.122) in the form

$$jk_{t1}c_{t1}u_{y'o} - b_1(m^0_{x'}m_{y'o} + m^0_{y'}m_{x'o}) = -jk_2^*c_{44}^*u_{y*o}, \tag{2.128}$$

$$-jk_{t2}c_{t2}u_{z'o} - b_2m^0_{x'}m_{z'o} = jk_2^*c_{44}^*u_{z*o}. \tag{2.129}$$

Ultimately, the shear displacements in the SiO_2 layer u_{y^*o} and u_{z^*o} are deduced

$$u_{y^*o} = \frac{b_1(m^0_{x'}m_{y'o} + m^0_{y'}m_{x'o})}{j(k_{t1}c_{t1} + k_2^*c_{44}^*)}, \tag{2.130}$$

$$u_{z^*o} = -\frac{b_2m^0_{x'}m_{z'o}}{j(k_{t2}c_{t2} + k_2^*c_{44}^*)}. \tag{2.131}$$

The unit magnetization vector $m_{i'o}$ in Eq. (2.130) and Eq. (2.131) is expressed in Eq. (2.103) - Eq. (2.105). It results in

$$u_{y^*o} = \frac{b_1(m^0_{x'}A_{23} + m^0_{y'}A_{13})U_3^1}{(k_{t1}c_{t1} + k_2^*c_{44}^*)(\omega^2 - \omega_f^2)}u_{x'o}, \tag{2.132}$$

$$u_{z^*o} = -\frac{b_2m^0_{x'}\omega U_3^1}{j(k_{t2}c_{t2} + k_2^*c_{44}^*)(\omega^2 - \omega_f^2)}u_{x'o}. \tag{2.133}$$

Eq. (2.132) and Eq. (2.133) couples an incident longitudinal displacement $u_{x'o}$ with emitted shear displacements u_{y^*o} and u_{z^*o}. Substitution of $u_{x'o}$ from Eq. (2.127) with $k_{t1} = \omega/\upsilon_{t1}$, $k_{t2}^* = \omega/\upsilon_{t2}^*$, $k_2^* = \omega/\upsilon_2^*$ into Eq. (2.132) and Eq. (2.133) allows to determine two acoustically-induced shear surface displacements,

$$u_{y^*o} = \frac{2b_1(m^0_{x'}A_{23} + m^0_{y'}A_{13})U_3^1c_{11}^*u^-_{x^*o}}{\omega(c_{t1}/\upsilon_{t1} + c_{44}^*/\upsilon_2^*)[\upsilon_1^*(c_l/\upsilon_l + c_{11}^*/\upsilon_1^*)(\omega^2 - \omega_f^2) + E/\omega]}, \tag{2.134}$$

$$u_{z^*o} = -\frac{2b_2m^0_{x'}U_3^1c_{11}^*u^-_{x^*o}}{j(c_{t2}/\upsilon_{t2} + c_{44}^*/\upsilon_2^*)[\upsilon_1^*(c_l/\upsilon_l + c_{11}^*/\upsilon_1^*)(\omega^2 - \omega_f^2) + E/\omega]}. \tag{2.135}$$

Equations Eq. (2.134) and Eq. (2.135) establish the relationship between the shear strain components of the displacements u_{y^*o}, u_{z^*o} and the incident longitudinal wave $u^-_{x^*o}$. It means that the shear strain waves can be excited via acoustic mode conversion of the longitudinal pulse at the interface of Terfenol/dielectric and vice a versa. The expression describing the propagation of the longitudinal strain wave in the SiO_2 medium was derived in Sec. 2.1.3. The problem can be simplified by assuming a stepwise temperature rise at $\Delta t = 0$, that leads to a longitudinal component of the displacement $u^-_{x^*o}$, described by the relation

$$u^-_{x^*o}(t) = A_0(1 - exp(-\upsilon_l \alpha t))H(t), \tag{2.136}$$

where A_0 is the amplitude of the injected acoustic strain, $H(t)$ is the Heaviside function. Since the displacements in Eq. (2.134) and Eq. (2.135) are presented in the frequency domain, a Fourier transform of Eq. (2.136) should be performed. It has the form

$$u^-_{x^*o}(\omega) = \int_{-\infty}^{+\infty} u^-_{x^*o}(t) exp(j\omega t)dt. \tag{2.137}$$

Substitution of the displacement $u^-_{x^*o}(t)$ from Eq. (2.136) into the Fourier transform Eq. (2.137) gives

$$u^-_{x^*o}(\omega) = A_0[\frac{1}{j\omega - \upsilon_l \alpha} - \frac{1}{j\omega}]. \tag{2.138}$$

The second term $1/j\omega$, that corresponds to the static strain, will be neglected in the further analysis. The time dependence of u_{y^*o}, u_{z^*o} can be obtained by an inverse Fourier transform of the Eq. (2.134) and Eq. (2.135), respectively. To do this, first, Eq. (2.134) and Eq. (2.135) should be expressed taking into account the dependence of the coefficients E, U^1_3 on the frequency ω,

$$u_{y^*o} = \frac{D_1 u^-_{x^*o}}{D_2(\omega^2 - \omega_f^2) + E^*}, \tag{2.139}$$

$$u_{z^*o} = \frac{D_3 u^-_{x^*o} \omega}{j(D_2(\omega^2 - \omega_f^2) + E^*)}, \tag{2.140}$$

where the parameters D_1 - D_3 are equal to

$$D_1 = \frac{2b_1(m^o_{x'} A_{23} + m^o_{y'} A_{13}) c^*_{11} U^*_3}{c_{t1}/\upsilon_{t1} + c^*_{44}/\upsilon^*_2}, \tag{2.141}$$

$$D_2 = \upsilon^*_1(c_l/\upsilon_l + c^*_{11}/\upsilon^*_1), \tag{2.142}$$

$$D_3 = -\frac{2b_1 m^o_{x'} U^*_3 c^*_{11}}{c_{t2}/\upsilon_{t2} + c^*_{44}/\upsilon^*_2}, \tag{2.143}$$

$$U_3^* = \frac{2\gamma b_2 m_{x'}^o m_{y'}^o}{\upsilon_l M_o}. \tag{2.144}$$

The longitudinal displacement in the frequency domain of Eq. (2.138) is substituted in Eq. (2.139), Eq. (2.140), that results in

$$u_{y^*o} = A_0 \cdot \frac{D_1}{(D_2(\omega^2 - \omega_f^2) + E^*)(j\omega - \upsilon_l \alpha)}, \tag{2.145}$$

$$u_{z^*o} = A_0 \cdot \frac{D_3 \omega}{j(D_2(\omega^2 - \omega_f^2) + E^*)(j\omega - \upsilon_l \alpha)}. \tag{2.146}$$

The inverse Fourier transforms of u_{y^*o} and u_{z^*o} are defined as follows

$$u_{y^*o}(t) = \frac{1}{2\pi}\int_{-\infty}^{+\infty} u_{y^*o}(\omega)\exp(-j\omega t)d\omega, \tag{2.147}$$

$$u_{z^*o}(t) = \frac{1}{2\pi}\int_{-\infty}^{+\infty} u_{z^*o}(\omega)\exp(-j\omega t)d\omega. \tag{2.148}$$

The inverse Fourier transform of Eq. (2.145) and Eq. (2.146), respectively, will take the form

$$u_{y^*o}(t) = \frac{1}{2\pi}A_0 D_1 \int_{-\infty}^{+\infty} \frac{\exp(-j\omega t)d\omega}{(D_2(\omega^2 - \omega_f^2) + E^*)(j\omega - \upsilon_l \alpha)}, \tag{2.149}$$

$$u_{z^*o}(t) = \frac{1}{2\pi}A_0 D_3 \int_{-\infty}^{+\infty} \frac{\omega \exp(-j\omega t)d\omega}{(D_2(\omega^2 - \omega_f^2) + E^*)(j\omega - \upsilon_l \alpha)}. \tag{2.150}$$

Integration of the rational functions in the complex plane requires utilization of the method of residues. It is a powerful tool to calculate the integrals of complex rational functions. The integration path forms a closed curve surrounding the poles of the function. Zeroes of the denominators (poles of the function) are imaginary and real numbers. In order to determine the poles, finding the solutions of the following equation is required

$$(D_2(\omega^2 - \omega_f^2) + E^*)(j\omega - \upsilon_l \alpha) = 0. \tag{2.151}$$

Replacement of ω_f^2 with ω_f^{*2} permits to disregard the E^* term by assuming,

$$\omega_f^{*2} = \omega_f^2 - \frac{E^*}{D_2}. \tag{2.152}$$

Consequently, a simplified form of Eq. (2.151) is

$$(\omega^2 - \omega_f^{*2})(j\omega - \upsilon_l \alpha) = 0. \tag{2.153}$$

It is straightforward to note that the poles of the function are $\omega = \pm\sqrt{\omega_f^{*2}}$ and $\omega =$

$-j\upsilon_l\alpha$. There are two poles on the real axis and one on the imaginary axis, as it is displayed on Fig. 2.42.

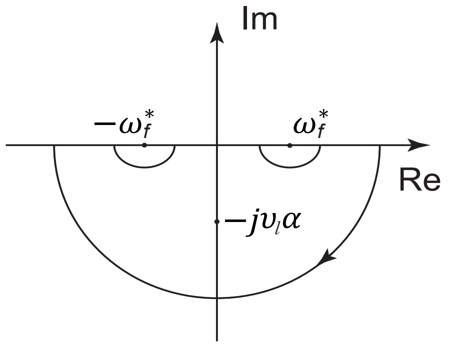

Fig. 2.42: Integration circuit in the complex plane.

Two possible cases are assumed: (i) if $\omega_f^{*2} > 0$ then the solution with poles $\omega = \pm\sqrt{\omega_f^{*2}}$ will take form of oscillations. (ii) If $\omega_f^{*2} < 0$, then the solution will take form of the hyperbolic functions. Hence, only the case where $\omega_f^{*2} > 0$ will be considered as more physical. Integration of the integral presented in Eq. (2.149) will have the form

$$\begin{aligned}
&\int_{-\infty}^{+\infty} \frac{\exp(-j\omega t)d\omega}{(D_2(\omega^2-\omega_f^2)+E^*)(j\omega-\upsilon_l\alpha)} = \frac{1}{D_2}\int_{-\infty}^{+\infty} \frac{\exp(-j\omega t)d\omega}{(\omega^2-\omega_f^2)+E^*)(j\omega-\upsilon_l\alpha)} = \\
&\frac{1}{D_2}(-j\pi[\frac{\exp(-j(-\omega^{)}_f * t)}{2(-\omega_f^*)(j(-\omega_f^*)-\upsilon_l\alpha)} + \frac{\exp(-j\omega_f^* t)}{2\omega_f^*(j\omega_f^*-\upsilon_l\alpha)}] - 2j\pi\frac{\exp(-\alpha\upsilon_l t)}{(j(\alpha\upsilon_l)^2-\omega_f^{*2})}) = \\
&\frac{1}{D_2}[2\pi\frac{\exp(-\alpha\upsilon_l t)}{(\upsilon_l\alpha)^2+\omega_f^{*2}} - j\pi(\frac{\exp(j\omega_f^* t)}{2\omega_f^*(j\omega_f^*+\upsilon_l\alpha)} + \frac{\exp(-j\omega_f^* t)}{2\omega_f^*(j\omega_f^*-\upsilon_l\alpha)})] = \frac{1}{D_2}[2\pi\frac{\exp(-\alpha\upsilon_l t)}{(\upsilon_l\alpha)^2+\omega_f^{*2}} + \\
&\pi(\frac{\exp(j\omega_f^* t)-\exp(-j\omega_f^* t)}{2j}\frac{\alpha\upsilon_l}{\omega_f^*(\omega_f^{*2}+(\alpha\upsilon_l)^2)} - \frac{\exp(j\omega_f^* t)-\exp(-j\omega_f^* t)}{2}\frac{1}{\omega_f^*+(\upsilon_l\alpha)^2}] = \\
&\frac{1}{D_2}[2\pi\frac{\exp(-\alpha\upsilon_l t)-\frac{1}{2}\cos(\omega_f^* t)}{(\upsilon_l\alpha)^2+\omega_f^{*2}} + \pi\frac{\upsilon_l\alpha}{\omega_f^*((\upsilon_l\alpha)^2+\omega_f^{*2})}\sin(\omega_f^* t)]. \qquad (2.154)
\end{aligned}$$

In fact, this integral represents the propagative term of the shear displacement. Its full expression is found by substitution of Eq. (2.154) into Eq. (2.149)

$$u_{y^*o}(t) = A_0\frac{D_1}{D_2}[\frac{\exp(-\alpha\upsilon_l t)-\frac{1}{2}\cos(\omega_f^* t)}{(\upsilon_l\alpha)^2+\omega_f^{*2}} + \frac{\upsilon_l\alpha\sin(\omega_f^* t)}{2\omega_f^*((\upsilon_l\alpha)^2+\omega_f^{*2})}]. \qquad (2.155)$$

The integral in Eq. (2.150) was calculated in a similar way

$$
\begin{aligned}
&\int_{-\infty}^{+\infty} \frac{\omega \exp(-j\omega t) d\omega}{(D_2(\omega^2 - \omega_f^2) + E^*)(j\omega - \upsilon_l \alpha)} = \frac{1}{D_2} \int_{-\infty}^{+\infty} \frac{\omega \exp(-j\omega t) d\omega}{(\omega^2 - \omega_f^2)(j\omega - \upsilon_l \alpha)} = \\
&\frac{1}{D_2}(-j\pi[\frac{-\omega_f^* \exp(j\omega_f^* t)}{2\omega_f^*(j\omega_f^* + \upsilon_l \alpha)} + \frac{\omega_f^* \exp(-j\omega_f^* t)}{2\omega_f^*(j\omega_f^* - \upsilon_l \alpha)}] - 2j\pi \frac{(-j\alpha\upsilon_l)\exp(-\alpha\upsilon_l t)}{j(-(\alpha\upsilon_l)^2 - \omega_f^{*2})}) = \\
&\frac{1}{D_2}[-2\pi \frac{\upsilon_l \exp(-\alpha\upsilon_l t)}{(\upsilon_l\alpha)^2 + \omega_f^{*2}} + j\pi(\frac{\exp(j\omega_f^* t)}{2(j\omega_f^* + \upsilon_l\alpha)} - \frac{\exp(-j\omega_f^* t)}{2(j\omega_f^* - \upsilon_l\alpha)})] = \\
&\frac{1}{D_2}[-2\pi \frac{\upsilon_l\alpha \exp(-\alpha\upsilon_l t)}{(\upsilon_l\alpha)^2 + \omega_f^{*2}} + j\pi(\frac{\sin(\omega_f^* t)\omega_f^* + \upsilon_l\alpha\cos(\omega_f^* t)}{(\upsilon_l\alpha)^2 + \omega_f^{*2}}) = \\
&\frac{1}{D_2}[-2\pi \frac{\upsilon_l\alpha(\exp(-\alpha\upsilon_l t) - \frac{1}{2}\cos(\omega_f^* t))}{(\upsilon_l\alpha)^2 + \omega_f^{*2}} + j\pi \frac{\omega_f^* \sin(\omega_f^* t)}{(\upsilon_l\alpha)^2 + \omega_f^{*2})}]. \qquad (2.156)
\end{aligned}
$$

Substitution of Eq. (2.156) into Eq. (2.150) results in

$$
u_{z^*o}(t) = A_0 \frac{D_3}{D_2} \cdot [-\frac{\alpha\upsilon_l \exp(-\alpha\upsilon_l t) - \frac{1}{2}\cos(\omega_f^* t)}{(\upsilon_l\alpha)^2 + \omega_f^{*2}} + \frac{\omega_f^* \sin(\omega_f^* t)}{2((\upsilon_l\alpha)^2 + \omega_f^{*2})}]. \qquad (2.157)
$$

where A_0 is the amplitude of the incident longitudinal acoustic displacement.

The displacements $u_{y^*o}(t)$ and $u_{z^*o}(t)$ expressed in Eq. (2.155) and Eq. (2.157), respectively, are valid at the fused silica/Terfenol interface $x^* = 0$. To find the analytical expression of the dynamical displacements away from the interface $x^* > 0$, the time should be introduced in Eq. (2.157) following the relation $\Delta t = t - x^*/\upsilon_2^*$, where υ_2^* is velocity of the shear strain in the SiO_2 layer. Ultimately, Eq. (2.155), Eq. (2.157) valid for $x^* > 0$, will be expressed as

$$
u_{y^*}(x^*, t) = A_0 \frac{D_1}{D_2} \cdot [\frac{\exp(-\alpha\upsilon_l(t - \frac{x^*}{\upsilon_2^*})) - \frac{1}{2}\cos(\omega_f^*(t - \frac{x^*}{\upsilon_2^*}))}{(\upsilon_l\alpha)^2 + \omega_f^{*2}} + \frac{\upsilon_l\alpha \sin(\omega_f^*(t - \frac{x^*}{\upsilon_2^*}))}{2\omega_f^*((\upsilon_l\alpha)^2 + \omega_f^{*2})}], \qquad (2.158)
$$

$$
u_{z^*}(x^*, t) = A_0 \frac{D_3}{D_2} \cdot [-\frac{\alpha\upsilon_l \exp(-\alpha\upsilon_l(t - \frac{x^*}{\upsilon_2^*})) - \frac{1}{2}\cos(\omega_f^*(t - \frac{x^*}{\upsilon_2^*}))}{(\upsilon_l\alpha)^2 + \omega_f^{*2}} + \frac{\omega_f^* \sin(\omega_f^*(t - \frac{x^*}{\upsilon_2^*}))}{2((\upsilon_l\alpha)^2 + \omega_f^{*2})}]. \qquad (2.159)
$$

Eq. (2.158) and Eq. (2.159) are the analytical expressions of the shear acoustic displacements. Subsequently, shear strains can be calculated with the help of the following expressions

$$
\varepsilon_{x^*y^*} = \frac{1}{2}\frac{\partial u_{y^*}}{\partial x^*}(x^*, t), \qquad (2.160)
$$

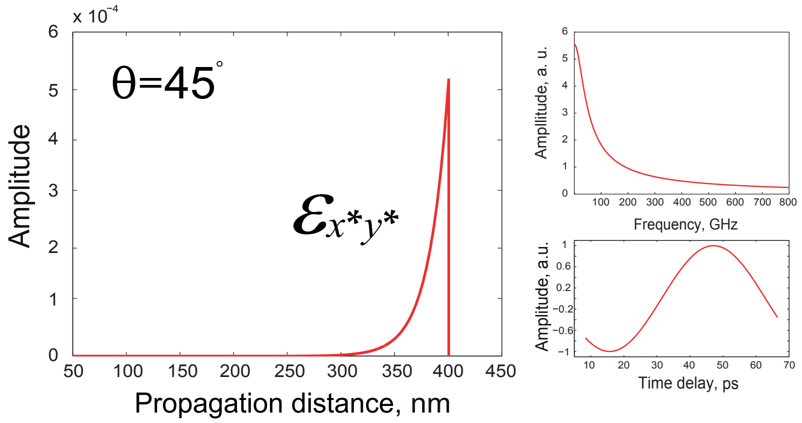

Fig. 2.43: $\varepsilon_{x'y'}$ shear strain spatial profile. Inset shows its frequency spectrum and oscillations during the first 70 ps.

$$\varepsilon_{x^*z^*} = \frac{1}{2}\frac{\partial u_{z^*}}{\partial x^*}(x^*, t). \tag{2.161}$$

The analytical expression of the shear strains generated by mode conversion in Terfenol and injected into the SiO_2 layer can be found from Eq. (2.158) and Eq. (2.159) and will have the form

$$\begin{aligned}
\varepsilon_{x^*y^*} &= A_0\frac{D_1}{2\upsilon_2^* D_2}\Big[\frac{\alpha\upsilon_l\exp(-\alpha\upsilon_l(t-\frac{x^*}{\upsilon_2^*})) - \frac{1}{2}\omega_f^*\sin(\omega_f^*(t-\frac{x^*}{\upsilon_2^*}))}{(\upsilon_l\alpha)^2+\omega_f^{*2}} - \frac{\upsilon_l\alpha\omega_f^*\cos(\omega_f^*(t-\frac{x^*}{\upsilon_2^*}))}{2\omega_f^*((\upsilon_l\alpha)^2+\omega_f^{*2})}\Big]\\
&= A_0\frac{D_1}{2\upsilon_2^* D_2}\Big[\frac{\alpha\upsilon_l\exp(-\alpha\upsilon_l(t-\frac{x^*}{\upsilon_2^*})) - \frac{1}{2}\omega_f^*\sin(\omega_f^*(t-\frac{x^*}{\upsilon_2^*}))}{(\upsilon_l\alpha)^2+\omega_f^{*2}} - \frac{\upsilon_l\alpha\cos(\omega_f^*(t-\frac{x^*}{\upsilon_2^*}))}{2((\upsilon_l\alpha)^2+\omega_f^{*2})}\Big]\\
&= A_0\frac{D_1}{2\upsilon_2^* D_2}\Big[\frac{\upsilon_l\alpha}{(\upsilon_l\alpha)^2+\omega_f^{*2}}\Big]\cdot\Big[\exp(-\alpha\upsilon_l(t-\frac{x^*}{\upsilon_2^*}))\\
&- \frac{1}{2\upsilon_l\alpha}\cos(\omega_f^*(t-\frac{x^*}{\upsilon_2^*})) - \frac{\omega_f^*}{2\upsilon_l\alpha}\sin(\omega_f^*(t-\frac{x^*}{\upsilon_2^*}))\Big],
\end{aligned} \tag{2.162}$$

$$\begin{aligned}
\varepsilon_{x^*z^*} &= -A_0\frac{D_3}{2\upsilon_2^* D_2}\Big[\frac{(\upsilon_l\alpha)^2}{(\upsilon_l\alpha)^2+\omega_f^{*2}}\Big]\cdot\Big[\exp(-\alpha\upsilon_l(t-\frac{x^*}{\upsilon_2^*}))\\
&- \frac{\omega_f^*}{2\upsilon_l\alpha}\sin(\omega_f^*(t-\frac{x^*}{\upsilon_2^*})) + \frac{\omega_f^{*2}}{2(\upsilon_l\alpha)^2}\cos(\omega_f^*(t-\frac{x^*}{\upsilon_2^*}))\Big],
\end{aligned} \tag{2.163}$$

where A_0 is the amplitude of the incident longitudinal acoustic displacement. $\upsilon_1^* = \sqrt{c_{11}^*/\rho^*}$ and $\upsilon_2^* = \sqrt{c_{44}^*/\rho^*}$ are the longitudinal and shear acoustic wave velocities in the SiO_2 film. D_1, D_2, D_3, ω_f^{*2} are parameters that depend on the direction cosines of the magnetization m_i. The parameter γ_1 is also defined by the direction cosines of the magnetization $m_{x'}$ and $m_{y'}$. It has a non-zero contribution to the amplitudes and is maximal if the magnetization is tilted at 90 degrees out-of-plane of the film.

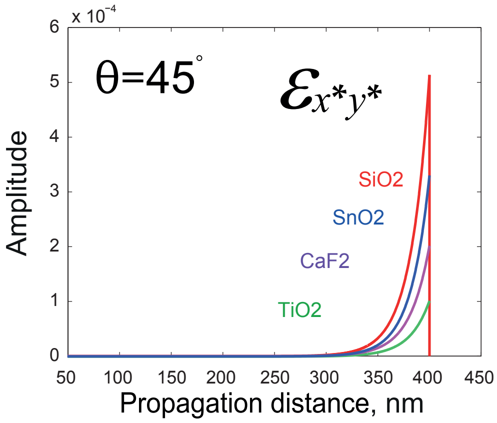

Fig. 2.44: $\varepsilon_{x'y'}$ shear strain amplitude as a function of acoustic delay line material.

Eq. (2.162) and Eq. (2.163) can be presented as the product of two factors. The first term denotes the amplitude of the strain, while the second is the propagative term (*exp* term). If the longitudinal acoustic pulse with an amplitude in order of 10^{-3} excite the ferromagnetic film, the shear wave with amplitude 10^{-4} emerges. Fig. 2.43 presents a simulation of the $\varepsilon_{x^*y^*}$ shear strain profile, excited by an incident longitudinal pulse. Initial out-of-plane tilt angle of magnetization was set to $\theta = \pi/4$. The frequency bandwidth of the pulse lies in order of several hundreds of GHz, see inset of Fig. 2.43. The low frequency oscillations (in order of tens of GHz) are associated to the $[-\frac{\omega_f^*}{2\upsilon_l\alpha}\sin(\omega_f^*(t-\frac{x^*}{\upsilon_2^*}))+\frac{\omega_f^{*2}}{2(\upsilon_l\alpha)^2}\cos(\omega_f^*(t-\frac{x^*}{\upsilon_2^*}))]$ term of Eq. (2.162) and contribute to the total frequency spectrum of the pulse.

Amplitudes of the excited shear strains upon mode conversion depend on the material properties of the transparent film as well. Fig. 2.44 depicts the $\varepsilon_{x^*y^*}$ shear strain spatial profile as a function of the attached material. It is found that the strain amplitude is 1.5, 2.5 and 3 times higher in the case of SiO_2 in comparison with SnO_2, CaF_2 and TiO_2 films, respectively. The reason for that is the acoustic impedance mismatch between the attached layers. The smaller acoustic reflection of the incident longitudinal wave at the interface leads to the more efficient mode conversion in Terfenol, i.e. higher amplitude of the L pulse transmitted through the interface causes more efficient excitation of the shear acoustic pulse. Indeed, coefficient of the longitudinal wave acoustic reflection for fused silica is equal to 27 %, 33 % for SnO_2, 65 % for CaF_2, 66 % for TiO_2. This estimates are confirmed by the detected 1L and 2L echoes propagated through 1000 nm thick acoustic delay line, see the amplitudes of the 1L and 2L echoes in Fig. 2.24. The measured ratio 2S/1L is equal to 28 %, which is in a good agreement with the calculated value.

In comparison with the laser-induced shear pulses, generated by demagnetostriction of Terfenol (see Eq. (2.61) and Eq. (2.62)), the expressions of the acoustically-induced shear waves (see Eq. (2.162) and Eq. (2.163)) reveal two additional oscillatory *sin* and *cos* terms, associated with the frequency ω_f^*. During the analysis it was suggested that its value is always positive $\omega_f^{*2} > 0$ and equal to

$$\begin{aligned}
\omega_f^{*2} &= \omega_f^2 - \frac{E^*}{D_2} = -A_{23}A_{32} - A_{13}A_{31} - \frac{U_3^1[(b_1 - b_2)m_{x'}^o A_{13} + (b_1 - b_2)m_{y'}^o A_{23}]}{\upsilon_1^*(c_l/\upsilon_l + c_{11}^*/\upsilon_1^*)} \\
&= -\gamma^2 M_0[(\frac{Km_{x'}^o}{\mu_0 M_0}(-m_{x'}^{o2} - 3m_{y'}^{o2} + 6m_{z'}^{o2}) - Hcos\xi + m_{x'}^o M_0) \\
&\times (\frac{2Km_{x'}^o}{\mu_0 M_0}(3m_{y'}^{o2} - m_{x'}^{o2}) + Hcos\xi - m_{x'}^o M_0) + (\frac{Km_{y'}^0}{\mu_0 M_0}(3m_{x'}^{o2} + m_{y'}^{o2} - 6m_{z'}^{o2}) - Hcos\xi cos\psi) \\
&\times (\frac{2K}{\mu_0 M_0} m_{y'}^o(m_{y'}^{o2} - 3m_{x'}^{o2}) - Hcos\xi cos\psi - m_{y'}^o M_0)] \\
&- \frac{2\gamma k_l b_2 m_{x'}^o m_{y'}^o[(b_1 - b_2)m_{x'}^o A_{13} + (b_1 - b_2)m_{y'}^o A_{23}]}{M_0 \upsilon_1^*(c_l/\upsilon_l + c_{11}^*/\upsilon_1^*)},
\end{aligned} \tag{2.164}$$

where γ, M_0 are the gyromagnetic ratio and the saturation magnetization. The frequency ω_f^* is defined by the direction cosines of magnetization $m_{x'}^o$, $m_{y'}^o$, $m_{z'}^o$ prior to the arrival of the longitudinal pulse at the ferromagnetic film, to the orientation of the external magnetic field H with respect to the plane of the film (values of polar ξ and azimuthal ψ angles). Thus, the longitudinal wave is coupled with the precession of the magnetization. Indeed, injection of planar strain waves into the magnetostrictive thin film induce precession of its magnetization vector [98], [57]. Dependence of the static strain amplitudes on the orientation of magnetization (see Eq. (2.36) - Eq. (2.38)) shows that coherent precession of magnetization will cause a time dependent modulation of the strains. This amplitudes variation can be considered as *circularly (elliptically)*

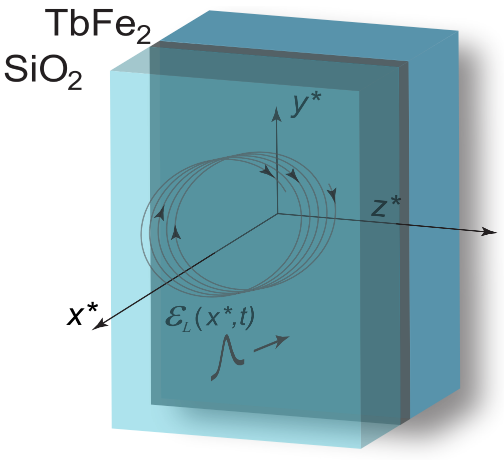

Fig. 2.45: Laser-induced generation of circularly polarized magneto-acoustic wave in the Terfenol.

polarized magneto-acoustic waves, i.e. two superposed plane waves of sinusoidal form lying in perpendicular planes (along y' and z' axes) and shifted in phase by $\pi/2$. This circularly polarized wave propagates in the ferromagnetic film (along the x' axis), as it is described in [92] and it will be partially transmitted into the attached dielectric layer (see Fig. 2.45). Its frequency ω (see inset of Fig. 2.43) will be associated with the frequency of magnetization precession ω_0 from $\omega = 2 \cdot \omega_0$.

The amplitudes of the acoustically-induced shear strains from mode conversion in Eq. (2.162) and Eq. (2.163) include the amplitude of the incident L strain pulse multiplied by some coefficient in the form

$$\varepsilon_{x'y'} = \frac{1}{2}\varepsilon_{x^*x^*} \cdot \frac{D_1}{D_2}[\frac{\upsilon_l}{\upsilon_2^*((\upsilon_l\alpha)^2 + \omega_f^{*2})}], \tag{2.165}$$

$$\varepsilon_{x'z'} = -\frac{1}{2}\varepsilon_{x^*x^*} \cdot \frac{D_3}{D_2}[\frac{\upsilon_l^2\alpha}{\upsilon_2^*((\upsilon_l\alpha)^2 + \omega_f^{*2})}]. \tag{2.166}$$

The terms $D_1/D_2 \cdot [1/\upsilon_2^*((\upsilon_l\alpha)^2+\omega_f^{*2})]$ and $D_3/D_2 \cdot$ $[\upsilon_l\alpha/\upsilon_2^*((\upsilon_l\alpha)^2+\omega_f^{*2})]$ are lower that 1 at all orientations of $\overrightarrow{M}$. Together with factor ± 0.5 it indicates that the amplitude of the acoustically-induced shear waves will be lower than the amplitude of the incident longitudinal wave. The efficiency of the acoustic mode conversion can be estimated by taking the amplitudes ratio of the incident longitudinal strain and the emitted shear strain,

$$\frac{\varepsilon_{x'y'}}{\varepsilon_{x^*x^*}} = \frac{D_1}{2D_2\upsilon_2^*((\upsilon_l\alpha)^2 + \omega_f^{*2})}, \tag{2.167}$$

$$\frac{\varepsilon_{x'z'}}{\varepsilon_{x^*x^*}} = \frac{D_3\upsilon_l\alpha}{2D_2\upsilon_2^*((\upsilon_l\alpha)^2 + \omega_f^{*2})}. \tag{2.168}$$

The ratios D_1/D_2 and D_3/D_2 in Eq. (2.167) and Eq. (2.168), respectively, take the form

$$\frac{D_1}{D_2} = \frac{4\gamma b_1 b_2 c_{11}^* m_{x'}^o m_{y'}^o (m_{x'}^o A_{23} + m_{y'}^o A_{13})}{\upsilon_l M_0(c_{t1}/\upsilon_{t1} + c_{44}^*/\upsilon_2^*)[\upsilon_1^*(c_l/\upsilon_l + c_{11}^*/\upsilon_1^*)]}, \tag{2.169}$$

$$\frac{D_3}{D_2} = -\frac{4\gamma b_1 b_2 m_{y'}^o c_{11}^* (m_{x'}^o)^2}{\upsilon_l M_0(c_{t2}/\upsilon_{t2} + c_{44}^*/\upsilon_2^*)[\upsilon_1^*(c_l/\upsilon_l + c_{11}^*/\upsilon_1^*)]}, \tag{2.170}$$

where $m_{x'}^o$, $m_{y'}^o$ are the direction cosines of magnetization in the experimental crystallographic axes. A_{13}, A_{23} coefficients depend on the gyromagnetic ratio γ, magnetic permeability of vacuum μ_0, saturation magnetization M_0, magnetic anisotropy constant K of Terfenol, $m_{x'}^o$, $m_{y'}^o$, $m_{z'}^o$ and on the orientation of the applied magnetic field H with

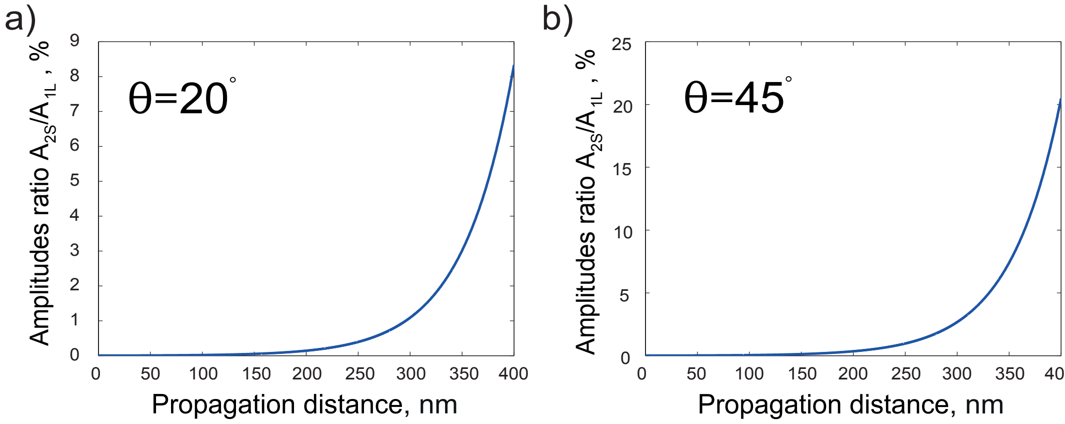

Fig. 2.46: Ratio of the emitted shear with the incident longitudinal strain amplitudes at $\Delta t \sim 100$ ps and for a tilt angle of magnetic field H=7 kOe equal to a) $\theta = 20$ deg, b) $\theta = 45$ deg.

respect to the plane of the film (values of polar ξ and azimuthal ψ angles),

$$A_{13} = \gamma\mu_0\left(\frac{Km^0_{y'}}{\mu_0 M_0}(3m^{o2}_{x'} + m^{o2}_{y'} - 6m^{o2}_{z'}) + Hcos\xi cos\psi\right), \tag{2.171}$$

$$A_{23} = \gamma\mu_0\left(\frac{Km^o_{x'}}{\mu_0 M_0}(-m^{o2}_{x'} + 3m^{o2}_{y'} + 6m^{o2}_{z'}) - Hcos\xi + m^o_{x'}M_0\right). \tag{2.172}$$

The contribution of ξ and ψ angles to the final amplitudes is small, so it can be neglected. On the contrary, $m^o_{x'}$, $m^o_{y'}$, $m^o_{z'}$ parameters play the main role in the determination of the amplitude of the acoustic strains. Analytical analysis of Eq. (2.167) and Eq. (2.168) shows that the ratio varies from 0.1 % up to 20 % and strongly depends on the initial orientation of magnetization and there is no shear waves generation if the magnetization remains in the plane of the film or tilted at $\theta = 90$ degrees out of its plane. The maximum value of the amplitudes ratio will be reached if $\overrightarrow{M}$ is tilted at $\theta = 45$ degrees out-of-plane of the film. Fig. 2.46 depicts the numerical simulations at the time delay between the pump and probe pulses set at $\Delta t = 100$ ps and at two tilt angles of magnetization (a) $\theta = 20$ degrees and (b) $\theta = 45$ degrees. The parameters used for the numerical analysis of the acoustic mode conversion efficiency in Terfenol films are listed in Tab. 2.3.

In fact, the same conditions apply as for the demagnetostriction mechanism: the initial magnetization vector needs to be tilted out of the film plane.

The final analytical expressions of the shear strains generated from mode conversion mechanism in the Terfenol film and propagating in the attached layer of fused silica are described in Eq. (2.162) and Eq. (2.163). They emphasize a strong coupling of elastic and spin subsystems in Terfenol and confirm that the inverse magnetostriction

Terfenol [74], [77], [78], [95]		**Fused silica** [74]	
Parameter, units	***Value***	***Parameter, units***	***Value***
Optical absorption coefficient α, m^{-1}	$5.26{\cdot}10^7$	Shear wave velocity υ_2^*, nm/ps	3.7
Shear wave velocity υ_{t1}, nm/ps	1.87	Longitudinal wave velocity υ_1^*, nm/ps	5.9
Shear wave velocity υ_{t2}, nm/ps	1.87	Elastic constant c_{11}^*, N/m^2	$75 \cdot 10^9$
Longitudinal wave velocity υ_l, nm/ps	4.17	Elastic constant c_{44}^*, N/m^2	$22.5 \cdot 10^9$
Elastic constant c_{t1}, N/m^2	$38.1 \cdot 10^9$	**General**	
Elastic constant c_{t2}, N/m^2	$48.4 \cdot 10^9$	Saturation magnetic field M_0, $kg/s^2{\cdot}A$	0.65
Elastic constant c_l, N/m^2	$117 \cdot 10^9$	External magnetic field H, $kg/s^2 \cdot A$	0.7
Magneto-elastic constant b_1, N/m^2	$-34.29 \cdot 10^6$	Gyromagnetic ratio γ, $rad/T \cdot s$	$1.76 \cdot 10^{11}$
Magneto-elastic constant b_2, N/m^2	$-359.4 \cdot 10^6$	Magnetic permeability μ_0, N/A^2	$4\pi \cdot 10^{-7}$
Magnetic anisotropy constant K, N/m^2	$-3.85 \cdot 10^6$		

Table 2.9: Simulation parameters of the mode conversion efficiency in Terfenol.

mechanism is responsible for the generation of 1L-S shear acoustic pulses. The arrival time of the 1L-S shear echoes on the measured signals confirms this experimentally.

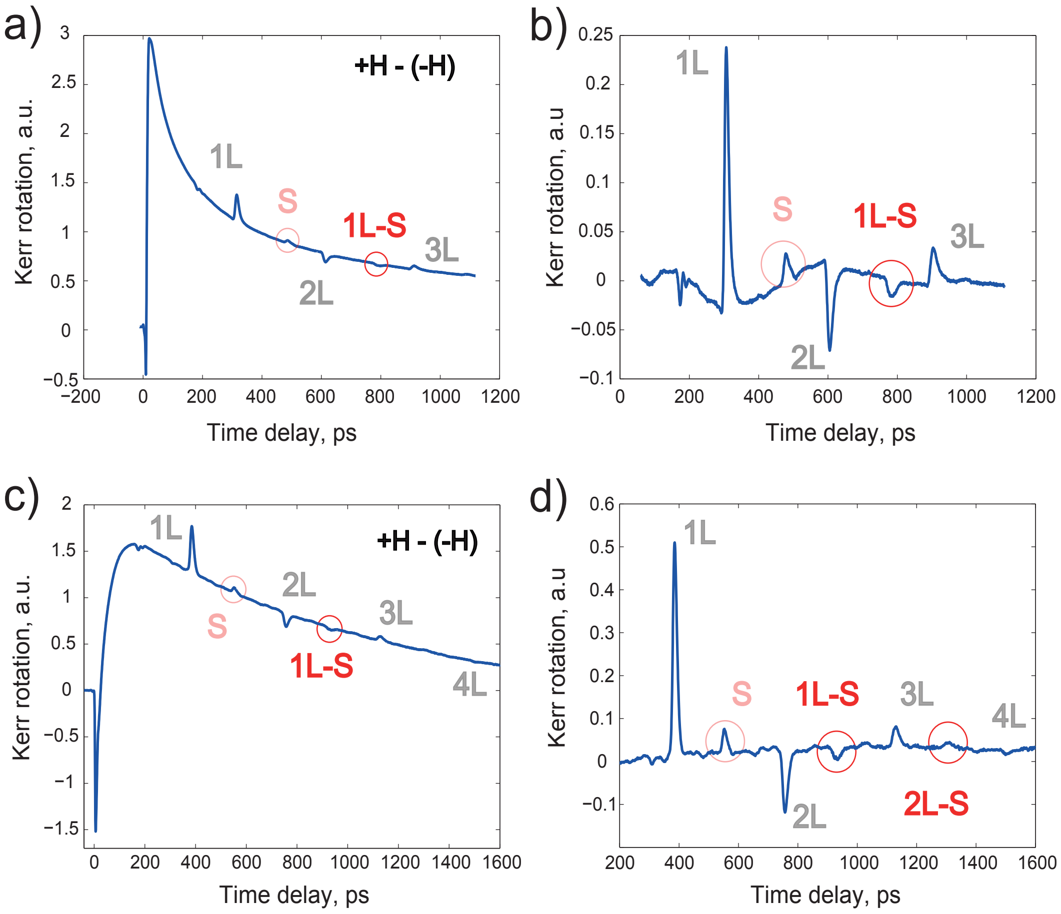

Fig. 2.47: Generation of the shear strain wave via the L-S acoustic mode conversion in a) 300 nm $TbFe_2$/775 nm SiO_2 and c) 300 nm $TbFe_2$/1000 nm SiO_2 samples.

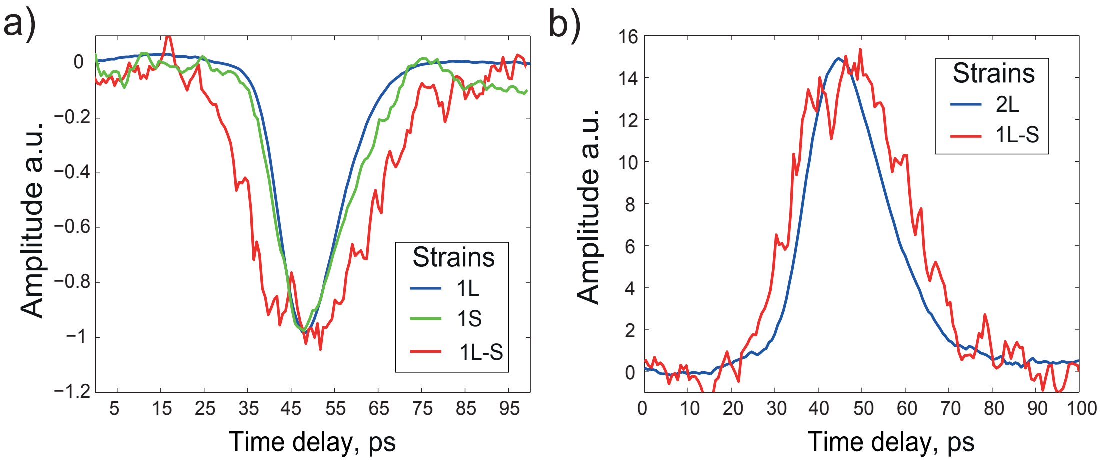

Fig. 2.48: a) Time profiles of the first longitudinal (1L) and the two shear (S and 1L-S) echoes, generated in a 300 nm thick $TbFe_2$ film and after propagation through 1000 nm of SiO_2 layer. b) The second longitudinal (2L) and the second shear 1L-S echoes time profiles.

Fig. 2.47 emphasizes the 1L-S detected shear echoes in hybrid sample of 300 nm $TbFe_2$/775 nm SiO_2 and in a 300 nm $TbFe_2$/1000 nm SiO_2 sample, centered at $\tau_{L-S} \sim$ 800 ps and $\tau_{L-S} \sim$ 900 ps, respectively. An echo centered at $\tau_{2L-S} \sim$ 1300 ps is generated by a mode conversion of the 2L strain pulse at the dielectric/ferromagnetic interface. Ratio of amplitude of the A_{2L-S}/A_{2L} and A_{L-S}/A_{1L} is equal to ∼1/15. Fig. 2.47 (a) and (c) shows the differential $-H + H$ signal of the magnetic origin, it reveals the generation/detection of two shear echoes S and 1L-S. Fig. 2.47 (b) and (d) depicts the same signal, starting from time delay of $\Delta t \geq 100$ ps, with subtracted slow remagnetization background.

The first longitudinal (1L) and the two shear (S and 1L-S) echoes time profiles, extracted from Fig. 2.47 (d) are depicted on Fig. 2.48 (a). The efficiency of mode conversion in this film is ∼5%. Increase of the out-of-plane magnetization tilt angle θ should enhance it up to ∼20% as in Fig. 2.46. Different time duration of the shear echoes (∼ 14 ps and ∼ 23 ps) is explained by the difference in the mechanisms of their excitation. 1S is excited by laser-induced demagnetostriction (its time profile matches the time profile of the similarly excited first longitudinal echo ∼ 14 ps), while 1L-S is generated by mode conversion of acoustic pulse and is broader due to acoustic attenuation. Fig. 2.48 (b) shows temporal profiles of the second longitudinal (2L) and the second shear 1L-S echoes. According to timescale of the detected echoes, shear strain is slightly more damped during the propagation in dielectric layer compared to longitudinal strain. Fig. 2.49 (a) shows the temporal profile of the 1L-S shear acoustic echo, excited by mode-conversion as a function of laser pump fluence. Evolution of 1L-S echo amplitude at its maximal value perfectly matches with evolution of the 1L echo amplitude, see Fig. 2.29 (a). It means that L-S excitation efficiency (mode-conversion efficiency) is linear with 1L strain amplitude. This result is relevant with numerical simulations presented in this section. Ratio of the amplitudes A_{L-S}/A_{1L} is about 1/15.

In summary, the excitation of highly magnetostrictive Terfenol films by normally incident picosecond longitudinal strain pulses leads to acoustic mode conversion and, consequently, to the generation of shear acoustic waves. The amplitude of these shear strains are strongly modulated by the out-of-plane tilt angle of the film magnetization, which is an essential condition for the efficient mode conversion in Terfenol films.

2.4 Conclusion

Ultrafast laser-induced demagnetization and coherent magnetization dynamics of $TbFe_2$ has been studied using time-resolved linear MOKE technique. The demagnetization timescale of the Terfenol films is influenced by the strong spin-lattice coupling of the RE Terbium and matches with the time duration of the excited acoustic pulses. It is dominated by the anisotropy of $4f$ states of the half-filled 4f shell of Tb and exceeds 1 ps. Hence, the role of acoustic phonons cannot be neglected during the demagnetization process in case of materials with strong magneto-elastic coupling, due to the significant contribution of the spin-lattice relaxation channel in the laser-induced demagnetization. Expected frequency bandwidth of the acoustic pulses is associated with the demagnetization timescale of the ferromagnetic layer $\tau_1 \sim 1.5$ ps (650 GHz). Ex-

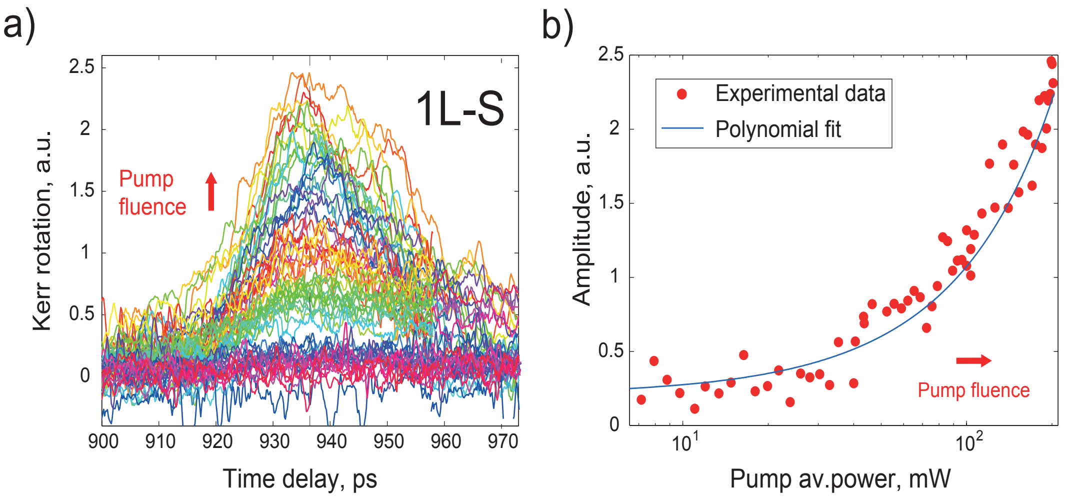

Fig. 2.49: a) Time-profile of the L-S shear acoustic echo of Fig. 2.47 (d) as a function of pump fluence. The insets show a maximal relative amplitudes change as a function of pump fluence. b) Maximal echo amplitude as a function of pump fluence. Solid line is a fit of 1L echo fluence-resolved amplitude, see Fig. 2.29 (a).

pressions of the build-in static strains of Terfenol films were derived by minimizing their free energy density F, which is assumed to be a sum of the elastic F_e and magneto-elastic F_{me} energies contributions. Numerical simulations of static strain amplitudes in monocrystalline and polycrystalline Terfenol films have been performed in order to determine an optimal experimental geometry. The phenomenological model of the demagnetostriction mechanism for shear waves generation is based on the fundamental principle of the dynamics of an elementary volume subjected into a stress gradient in a continuous medium has been developed. Measurements of time-resolved depolarized Brillouin scattering reveal the laser-induced excitation of picosecond shear waves via ultrafast demagnetostriction in Terfenol films and subsequent propagation of the strains in the attached SiO_2 layer. The frequency bandwidth of the generated strain pulses lies in the order of hundreds of GHz. Shear waves excitation efficiency depends on the out-of-plane tilt of the film magnetization $\overrightarrow{M}$. $\theta = \pi/4$ tilt is found to be an optimum angle for efficient shear waves excitation in the studied samples, while longitudinal strain is generated upon both laser-induced demagnetostriction and thermo-elastic mechanisms.

Furthermore, an inverse magnetostriction effect of Terfenol also causes excitation of picosecond shear waves. Injection of ultrasonic acoustic pulses into $TbFe_2$ thin films leads to the magneto-acoustic inter-mode conversion from longitudinal to shear and vice versa. Unlike other mechanisms of acoustic mode conversion, observed in non-magnetostrictive materials, it doesn't require utilization of sophisticated experimental techniques or crystals with ”broken axial symmetry” for the generation of GHz shear waves. However, application of the strong external magnetic field is required in order to increase the efficiency of the SW excitation. It can be increased by a careful selection of an acoustic transducer that could inject high amplitude longitudinal strain pulses in Terfenol film without any significant acoustic reflection. An analytical model, based on the Landau-Lifshitz equations, and numerical simulations were utilized to find an optimal experimental geometry for the magneto-acoustic mode conversion in monocrystalline Terfenol films.

Results presented in this chapter demonstrate the first experimental observation of picosecond shear acoustic waves, generated via laser-induced demagnetostriction mechanism. They can be extrapolated to other materials with strong magneto-elastic coupling to optically excite GHz shear waves. Prototype samples of Terfenol films, studied in this thesis, show an efficient generation of shear strain waves, despite of the requirement of strong magnetic field to control their magnetization. Magnetic fields exceeding 1 T are needed to increase the amplitudes of the excited shear waves.

Chapter 3

Summary and outlook

This chapter summaries all the results presented in this thesis. Upon laser excitation of Terfenol films, both picosecond longitudinal and shear strain pulses emerge, as result of direct magnetostriction effect. Their frequency bandwidth is associated with the demagnetization time scale of the ferromagnetic layer and lies in the order of hundreds of GHz. It is strongly influenced by the presence of rare-earth ions and consists of two steps: an initial demagnetization of $\tau_1 = 1.5$ ps occurs at non-equilibrium timescale before the equilibration of excited electrons and lattice and doesn't depend on the spin-lattice coupling. However, the characteristic time constant of the second step $\tau_2 = 40$ ps strongly depends on the material. It is linked with the coupling strength of the 4f magnetic moments of Tb and the lattice. The amplitude of the released acoustic pulses is determined by the static build-in strains, which depend on the orientation of the magnetization of the Terfenol film. For efficient excitation of shear acoustic waves, the out-of-plane tilt angle of magnetization should be equal to $\theta = \pi/4$. The generation of longitudinal acoustic waves occurs mainly from the thermo-elastic mechanism, so in this case, the orientation of the magnetization is not a crucial parameter. Acoustic echoes are detected after their propagation in the attached transparent acoustic delay line, with well known mechanical and optical properties. Laser-induced generation of picosecond shear strain waves and their subsequent propagation in the attached transparent SiO_2 layer demonstrates that strongly magnetostrictive materials can be a source of GHz shear acoustic waves in a simple picosecond ultrasonics geometry.

3.1 Demagnetostriction and inverse magnetostriction in Terfenol thin films

Laser induced magneto-elastic generation of picosecond shear acoustic pulses in highly magnetostrictive Terfenol films has been studied using linear time-resolved optical spectroscopy techniques. Experimental results highlight several laser-induced effects occurring in highly magnetostrictive ferromagnetic films.

1. Laser-induced demagnetostriction of Terfenol film leads to the generation of longitudinal and shear acoustic strains with up to 1 THz frequency bandwidth. The amplitudes of the pulses depend on the orientation of the film magnetization. They reach their maximum values when $\overrightarrow{M}$ is tilted at 45 degrees out-of-plane of the film. A magnetic field of about 2 T would be required to tilt sufficiently the magnetization of Terfenol, to reach the maximum shear wave generation efficiency.

2. Injection of the ultrashort longitudinal strain pulses into Terfenol films causes acoustic mode conversion, which occurs at the interface. It is another mechanism of picosecond shear waves excitation in Terfenol from inverse magnetostriciton.

Each effect can be discussed separately from each other, their theoretical analysis led to a self-consistent model, which describes the coupling of the magnetic and elastic subsystems in Terfenol thin films and confirms magneto-elastic mechanisms of GHz shear strain waves generation in materials with strong magneto-elastic coupling. This model can be applied to other magnetic materials with weaker coupling with lower saturation fields. The analytical description will be similar to that given in this thesis, taking into account their crystal symmetries.

Influence of Terfenol thickness on the shear waves generation efficiency

$TbFe_2$ samples with different thickness were investigated in order to optimize different parameters of the films that can affect the ultrasonic measurements: roughness, island effects, etc. Terfenol films of 30 nm, 50 nm, 100 nm, 150 nm, 300 nm and 500 nm were fabricated in order to compare the efficiency of the shear waves excitation as a function of $TbFe_2$ thickness. The experimental results are summarized in the Tab. 3.1.

Magnetic anisotropy of thick films is more important than that of the thin ones. The optical penetration depth of pump pulse in Terfenol at $\lambda = 800$ nm is equal to $\delta = \lambda/4\pi k = 19$ nm, thus the laser absorption is more or less homogeneous only in thin films (10-30 nm). It leads to the uniform demagnetization of the film, which

	$TbFe_2$ **(10-30 nm)**	$TbFe_2$ **(50-500 nm)**
Demagnetization	uniform	not uniform
In-plane magnetization anisotropy	low	strong
Roughness	high	low

Table 3.1: Summary of sample properties with different Terfenol thickness.

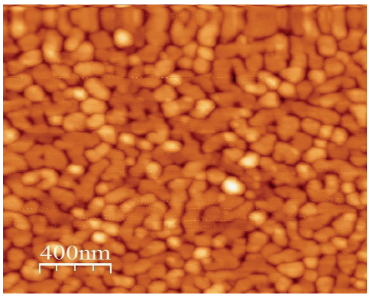

Fig. 3.1: AFM image of the 50 nm thick Terfenol film surface. The Terfenol growth of thin films is of island type.

is a preferential situation for the shear waves excitation, since the surrounding non-demagnetized regions don't influence demagnetized film volume.

The magnetic anisotropy of thick films is more important than that of thin films. Thick films have similar properties than bulk Terfenol crystals, on the contrary to thin films. However, since the optical penetration depth of the pump pulse in Terfenol at $\lambda = 800$ nm is equal to $\delta = \lambda/4\pi k = 19$ nm, the laser absorption is more or less homogeneous only in thin films (10-30 nm). The disadvantage of thick films is that the demagnetization of the film is not uniform, which is not a preferential situation for the shear waves excitation, since the surrounding non-demagnetized regions influence the demagnetization of the laser heated region.

Ideally, the roughness of the Terfenol surface should be less than 1 nm to prevent acoustic attenuation and diffusion across the interface. The generation of shear acoustic pulses was observed only in thick (150 nm, 300 nm, 500 nm) films with minimized roughness compared to thin films in the range 10-30 nm. The surface quality of thinner films with structural inhomogeneity and/or big roughness, which is about 4 nm[1], see Fig. 3.1, prevent efficient excitation of shear acoustic waves. Hence, all qualitative and quantitative studies, presented in this thesis, were performed on samples with thick Terfenol layers of thickness greater than 150 nm.

3.2 Terfenol thin films as shear waves transducers

Generation of shear strain waves in Terfenol thin films through demagnetostriction and mode conversion mechanisms was shown theoretically and confirmed experimentally in Chapter 2. Based on these results, time-resolved picosecond ultrasonics experiments were performed in order to demonstrate a possible application for Terfenol films as GHz

---

[1] AFM measurements were performed at IJL after deposition of the ferromagnetic films.

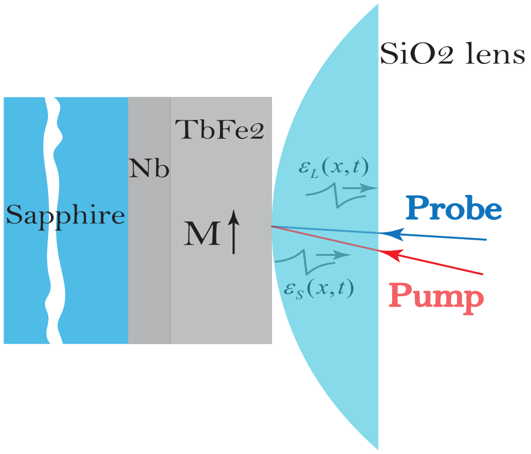

Fig. 3.2: Experimental pump-probe geometry with a lens of arbitrary radius. The liquid is squeezed in between the Terfenol sample and the lens.

shear acoustic wave transducers. Fig. 3.2 displays the experimental pump-probe geometry to utilize shear strain waves generated in Terfenol thin films for the measurement of the viscoelastic properties of liquids at GHz-THz frequencies.

A plano-convex lens made of fused silica was used to squeeze liquid glycerol in between a 300 nm thick Terfenol film and the curved lens surface, as depicted in Fig. 3.2. The thickness of the lens is much greater than that of the ferromagnetic layer and can be considered as semi-infinite. Since the mechanical and optical properties of the SiO_2 lens are well known, it is used as a propagation and detection medium for the acoustic waves. The sample was excited with an intense pump pulse of 150 fs duration at $\lambda = 800$ nm central wavelength. The spot size was $\sim 100\ \mu m$ that is two times larger than the probe spot. Ten times weaker time-delayed second harmonic probe pulse ($\lambda = 400$ nm) was used to monitor time-resolved dynamics of the sample. The angle of incidence of the pump pulse was ~70 degrees. The time-resolved response of the sample was detected through Brillouin scattering with time-delayed probe pulses. Its angle of incidence was 45 degrees with respect to the normal of the surface. Fig. 3.3 shows an example of the experimental signal.

Upon ultrafast laser excitation at $\Delta t = 0$ time delay, coherent oscillations of acoustic nature are clearly visible couple of nanoseconds on top of a slow thermal background, see Fig. 3.3. To determine the frequency content of the oscillations, we have performed Fast Fourier transform of the signal. Inset of Fig. 3.3 shows the presence of two acoustic modes, propagating in the bulk of the lens: stronger and weaker at 42.5 GHz and 23.5 GHz, that correspond to longitudinal and shear strain waves with v_l, v_s sound velocities, respectively. The detected Brillouin frequencies are related to the

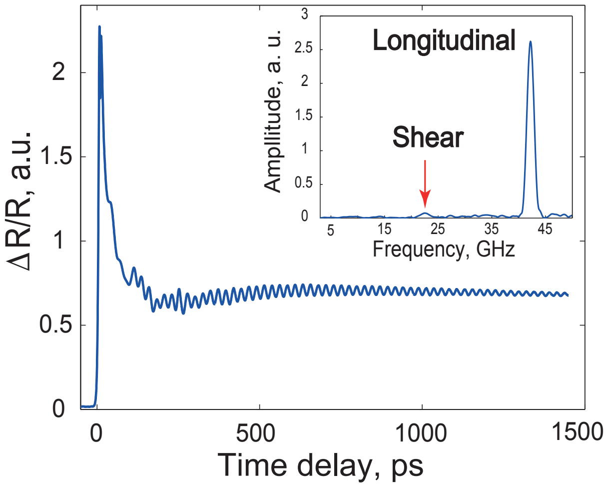

Fig. 3.3: Time resolved depolarized Brillouin scattering signal recorded at room temperature. The frequency spectrum shown in inset reveals the photo-excitation of GHz longitudinal and shear coherent acoustic waves.

probe wavelength λ, the longitudinal υ_l or shear υ_s sound velocities, the SiO_2 refractive index n and to the back-scattering angle θ through

$$\nu = 2\, n\upsilon \cos\theta/\lambda. \tag{3.1}$$

The experimental results presented in Fig. 3.3 confirm the applicability of Terfenol thin films as shear acoustic waves transducers. Terfenol can be utilized to investigate the mechanical properties of different materials at high frequencies, such as liquids squeezed up to several molecular layers between the ferromagnetic film and a lens. With a such device, bulk and shear elastic modulus of liquids at GHz frequencies can be determined [99],[100]. Moreover, the efficiency of the shear acoustic wave generation can be increased by applying a strong out-of-plane magnetic fields in order to tilt the Terfenol magnetization from its initial quasi in-plane orientation Sec. 2.1.2.

3.3 Other magnetostrictive materials

Magnetostrictive thin films

Terfenol-D ($Tb_xDy_{1-x}Fe_2$).

Highly magnetostrictive ternary compound Terfenol-D ($\lambda_{[111]} = +1620 \cdot 10^{-6}$) with cubic structure and epitaxially grown in the (110) direction on a lattice-mismatched sapphire substrate induces built-in static strains, similar to that of Terfenol films [60]. Laser induced magnetoelastic excitation of the shear strains is expected to be as efficient as it is in Terfenol films. However, similarly with Terfenol, the high saturation magnetization ($\mu_0 M_s \sim 1$ T) of the alloy makes the control over its magnetization a difficult task.

Galfenol ($Fe_{100-x}Ga_x$).

Magnetostriction of pure Fe is very low ($\lambda_{[100]} = +19 \times 10^{-6}$) [72], however when some fraction of Iron atoms is replaced by non-magnetic atoms of Gallium, the resulting magnetostrictive coefficient $\frac{3}{2}\lambda_{[100]}$ increases up to 12 times ($+400 \cdot 10^{-6}$) [101]. In adition, the saturation magnetization of the component remains relatively low ~0.1 T [102], with a Curie temperature of $T_c = 973$ K. There is a general consensus that the strong magnetostrictive response of Galfenol results from the Ga-induced tetragonal distortion in the atomic arrangement. Galfenol thin films already have been used in studies related to ultrafast inverse magnetostriction [103]. Epitaxially grown single crystal Galfenol thin films with very smooth surface (roughness lower than 1 nm) can be utilized to study the excitation of picosecond shear waves by laser-induced demagnetostriction. In this case an analytical analysis of the strain generation will be similar to that given in this thesis due to bcc-like crystal structure of the alloy. The main advantages of Galfenol compound are its high magnetostriction at low saturation field and potentially high quality of the film surfaces.

Nanostructured multi-layer films.

Magnetically-induced variation of the Rayleigh and shear horizontal waves velocity in 200 nm thick $20\times TbCo_2(5\text{ nm})/FeCo(5\text{ nm})$ nanostructured uni-axial thin films was recently studied theoretically and experimentally [104]. The variations of the elastic properties in the optimized magnetostrictive film with cubic symmetry can be higher than 20%. At the same time, the saturation magnetization of the supperlattice is about ~0.2 T. It is assumed, that optical excitation of such multi-layer films will lead to the generation of picosecond shear acoustic waves via ultrafast demagnetostriction mechanism.

Spin-crossover molecular crystals

Laser-induced coherent lattice dynamics of $Fe^{II}(phen)_2(NCS)_2$ and $Fe(PM-AzA)_2(NCS)_2$ crystals are studied in Appendix A. These molecular crystals are characterized by a temperature-guided spin phase (PT) transition, causing their structural reorganization, in particular, an elongation of the Fe-ligand distance. Due to the collective effect occurring between the molecules of the crystal, the laser excitation leads to the generation of coherent acoustic phonons, which is affected by the phase transition. Hence, it is possible to monitor the temperature-induced PT via picosecond ultrasonics measurements. Moreover, in order to reveal non-thermal laser-induced generation mechanisms of picosecond acoustic phonons in these crystals, we have performed temperature-resolved pump-probe measurements. The evolution of the optical and mechanical properties of $Fe(PM-AzA)_2(NCS)_2$ molecular crystals were monitored across the spin phase transition. Significant modification of the phase of coherent Brillouin oscillations highlights a profound change in the laser-induced non-thermal mechanism of acoustic phonons excitation. These type of materials can be an alternative source of GHz coherent longitudinal and, due to their structural anisotropy, shear acoustic waves.

3.4 Conclusion

Future studies could be dedicated to (i) the investigation of direct magnetostriction mechanism of picosecond shear waves generation in materials with lower coercive fields compared to Terfenol, to pull $\overrightarrow{M}$ more easily towards $\pi/4$ and (ii) inverse magnetostriction effect in highly magnetostrictive materials, which is a promising approach in the view of ultrafast magnetic recording.

General conclusion

The present thesis is focused on the study of ultrafast shear acoustic waves excitation via laser-induced demagnetization of highly magnetostrictive Terfenol films. It has been experimentally studied using time-resolved linear optical spectroscopy techniques, in particular MOKE and Brillouin scattering. We have found a quantitative agreement between the experimental results and the developed analytical model.

The elastic properties of Terfenol thin films greatly depend on the magnetic state and on the direction of an applied magnetic field due to the strong coupling of its elastic and magnetic subsystems. Irradiation of highly magnetostrictive films with femtosecond laser pulses leads to the release of their built-in strains, i.e. *demagnetostriction* - laser-induced generation of the picosecond acoustic pulses. We derived the expressions of the built-in static strains in case of in-plane and out-of-plane magnetized Terfenol films. Numerical simulations of the static strain amplitudes in monocrystalline and polycrystalline Terfenol films have been performed in order to determine the optimal experimental geometry. The excitation efficiency of the shear strains depends on the tilt of the film magnetization $\overrightarrow{M}$ out-of its initial orientation. An out-of-plane tilt angle $\theta = \pi/4$ is found to be an optimal angle for efficient shear acoustic wave excitation in the studied samples, while longitudinal acoustic strains are excited upon both laser-induced demagnetostriction and thermo-elastic generation mechanisms. Laser-mediated direct magnetostriction in Terfenol leads to the excitation of longitudinal and shear acoustic pulses, which propagate in the attached SiO_2 layer. The frequency bandwidth of the excited strains is associated with the ferromagnetic film demagnetization timescale. Like other rare-earth based alloys, Terfenol shows a relatively slow drop of the remanent magnetization, which lies in order of $\tau_1 \sim 1.5$ ps. The frequency bandwidth of the generated strain pulses lies in the order of hundreds of GHz.

Injection of ultrafast longitudinal acoustic pulses into highly magnetostrictive Terfenol films leads to acoustic mode conversion mediated by inverse magnetostriction. This phenomenon is considered as a surface effect, and represents an alternative approach for the excitation of shear acoustic waves in Terfenol. When ultrafast longitudinal strain pulses reaches the ferromagnetic layer, they modify the magnetic anisotropy field and tilts H_{eff}, that causes the reorientation of $\overrightarrow{M}$, which is no longer aligned with H_{eff}. The direction and value of H_{eff} are determined by the free energy density of the film F, which includes the magneto-elastic energy density term F_{me}. It provides a direct coupling of the strain and orientation of the film magnetization. Consequently, the developed analytical model of acoustic mode conversion in Terfenol, based on the Landau-Lifshitz equation, describes the response of its magnetization on the acoustic excitation. The efficiency of the acoustic mode conversion from longitudinal to shear pulse in Terfenol films depends on the orientation of its magnetization and on the acoustic properties of the attached transparent layer. Eventually, it can be optimized and reach up to 20 % efficiency.

The most important factor that modulate the efficiency of the shear acoustic waves excitation in Terfenol is the out-of-plane tilt of the film magnetization. Results, presented in this thesis, demonstrate the first experimental observation of picosecond shear acoustic waves, generated via laser-induced magneto-elastic mechanism (demagnetostriction) and via magnetostrictive mode conversion. These results can be applied to study the magneto-elastic coupling of other materials to optically excite GHz shear acoustic waves. These type of samples can be utilized as ultrasonic shear acoustic waves transducers to probe the mechanical properties of attached media in the entire Brillouin zone and in the frequency range of several hundreds of GHz. Moreover, they can be considered as an alternative approach for ultrafast magnetic data recording with longitudinal and shear picosecond acoustic waves.

Appendix A

Spin-crossover molecular systems

Study of spin crossover (SCO) molecular crystals by means of picosecond ultrasonics is presented. SCO phenomenon is often referred to spin transition effect. It occurs in metal complexes whose spin state can be modified by the variation of external conditions: temperature [105], pressure, laser-excitation [106], etc. While such systems have been already studied with different techniques [105, 107, 108, 109], there is a shortage of information about the interplay between magnetization, crystal deformation and excitation of coherent acoustic phonons, which clearly deserves further experimental investigations.

All-optical non-thermal generation of GHz longitudinal and shear coherent acoustic waves in $Fe^{II}(phen)_2(NCS)_2$ and $Fe(PM-AzA)_2(NCS)_2$ molecular crystals is reported. The detection occurs via the ultrafast Brillouin spectroscopy technique. The crystals are composed of interacting molecules with central element (Fe) and its environment, that gives rise to collective transformations: laser-induced ferroelectric structural ordering [110], metal-insulator transitions [111], reversible spin state change [112]. The molecules possesses highly asymmetric structures, thus, have directional intermolecular forces of different nature acting on the crystal [113], that leads to anisotropy of its optical and/or mechanical properties, which is generally hard to study. However, temperature-guided evolution of the optical and mechanical properties of a $Fe(PM-AzA)_2(NCS)_2$ prototype crystal can be monitored by time-resolved Brillouin spectroscopy.

Spin-crossover effect and the ligand field

Fe^{2+}, Fe^{3+} and Co^{2+} ions play the main role in molecular crystals, where spin crossover switching has been observed. Spin-crossover phenomenon is described by the considerations of the ligand field theory. In the case of a transition metal systems with 5 electrons in the d-shell that has an octahedral environment, the theory predicts a splitting of the d orbitals with t_{2g} and e_g levels and two possible electronic ground states. Hence the effect of spin-crossover transitions can be considered as a distribution of the electrons between $LS \rightleftarrows HS$ states. In LS state electrons populate only the t_{2g} bonding orbitals. Unlikely, the high spin state electrons populate both t_{2g} and antibonding orbitals obeying the Hund's rules. Change of the population of e_g, which is facing the ligand, and opposing change of t_{2g}, affecting electron back-donation from metal ion to vacant π^* ligand orbital, modifies metal-ligand distance, consequently originating structural reorganization of the molecule. Switching from LS to HS state in Fe^{II} and Fe^{III} compounds elongates the Fe-ligand distance, inversely, going from the HS to LS shrinks it. Typical $Fe - N$ distance R in Fe^{II} compounds is ~ 2 Å and varies on ~ 0.1 Å under spin state transition [105].

In ligand field theory $\mathit{\Delta} l$ depends inversely on the fifth power on metal-ligand distance l, thus each molecule experiences a change in ligand field strength under spin state evolution, $\mathit{\Delta}_{LS} = 1.6\mathit{\Delta}_{HS}$ [114]. Hence, modification of the metal-ligand distance Δl of a single molecule leads to the change of its potential energy density ΔE, which causes a change of the material properties. SCO effect has a molecular origin, but since one crystal consists of numerous molecules, its properties and their evolution through the spin-state transition, depend on the interacting forces between them. Existence of the intermolecular interaction in a crystal causes the cooperative effect, which determines the abruptness of the spin-crossover hysteresis (see [105]). It means that materials with strong cooperative effect has sharper hysteresis (χ_M or n_{HS}) across the transition. Molar fraction of HS state molecules can be calculated following the expression

$$n_{HS} = \frac{\chi_M T - (\chi_M T)_{LS}}{(\chi_M T)_{HS} - (\chi_M T)_{LS}},$$

where T and χ_M are the absolute temperature and molar magnetic susceptibility, respectively. In the *"lattice expansion and elastic interaction model"*, the difference in volume between LS and HS states is assumed to cause a long-range elastic deformation, which leads to the cooperative spin-transition mechanism [114]. Thus, switching of the spin state of SCO material strongly modifies its shape and volume. Photoexcited coherent acoustic phonons allow to monitor their properties during transition of the spin state by a non-contact all-optical method.

Coherent lattice dynamics of the spin-crossover molecular crystals

Coherent lattice dynamics of $Fe^{II}(phen)_2(NCS)_2$ and $Fe(PM - AzA)_2(NCS)_2$ spin-crossover molecular complexes is studied by means of ultrafast pump-probe technique. The possibility of light excitation of coherent acoustic phonons in a variety of materials is known for a long time [5, 115], however, at the contrary to longitudinal acoustic waves, the photoexcitation of shear waves is always a challenging task (Sec. 1.2.1). The following results reveal the photoexcitation of shear acoustic waves in a simple manner and shed light on the interplay between molecular magnetization and elastic parameters in a spin-crossover compound as well as on the fundamental aspects of microscopic structural evolution under phase transition that occurs at temperature step-like change and probed with transient laser pump-probe reflectivity measurements.

Optical switching of the molecular magnetic phase between low-spin and high-spin states in d^4-d^7 transition metals complexes [116] triggered new perspectives in the future applications of spin-crossover compounds. For example, in optically controlled memories or molecular switching devices [117]. This phenomenon originates from the existence of two configurations for the metallic ion characterized by different spin states. The term "spin crossover" is commonly applied for metal complexes, mainly based on iron, cobalt, nickel and manganese. In the field of photo-induced phase transitions with molecular crystals, the role of coherent optical phonons has been long under scrutiny, whereas that of acoustic phonons and lattice deformations, has not benefited from the same surge of effort. It is of great importance from the fundamental point of view, as well as for the control of non-volatile information and energy storage, to further explore the acoustic phonons pathway for the persistence of the photo-induced states. A promising approach is the stabilization of non-equilibrium macroscopic states from coherent crystal deformation and propagating acoustic waves coupled to the order parameter field.

Photogeneration and detection of high frequency acoustic phonons in $[Fe^{II}(phen)_2(NCS)_2]$ (phen=1,10-phenanthroline) and $[Fe(PM{-}AzA)_2(NCS)_2]$ (cis-bis(thiocyanato) bis [(N-2'-pyridylmethylene) - 4 - (phenylazo)aniline]) prototypical spin-crossover compound is reported. These crystals are among the most studied $Fe^{II}SCO$ systems due to the significant structural changes during the phase transition [118], [119]. Time-resolved Brillouin spectroscopy reveals excitation of coherent longitudinal and shear picosecond acoustic phonons in both compounds. A non-thermal mechanism of the stain waves generation is modified by the temperature-guided spin phase transition. Moreover, strain spectroscopic ellipsometry measurements unfold both real and imaginary parts of AzA crystal refractive index along a, b, c crystal axis at 400 nm and 800 nm wavelength.

The $Fe^{II}(phen)_2(NCS)_2$ SCO complex consists of neutral $Fe^{II}(phen)_2(NCS)_2$ molecules within the orthorhombic $P_{bcn}; Z = 4$ cell. In the single $[Fe^{II}(phen)_2(NCS)_2]$ molecule, the Fe^{II} is surrounded by four N atoms belonging to $1,10-phenanthrolines$

and two N atoms of NCS^- groups. The compound shows a thermally induced phase transition from the LS phase to the HS phase at $T = 176K$, that is accompanied by a volume expansion, reflecting the elongation of $Fe - N$ bond distances by $0.10 - 0.20$ Å [120]. The $Fe(PM - AzA)_2(NCS)_2$ (AzA) molecular crystal belongs to the monoclinic space group $P2_{1/c}$ with one molecule as asymmetric unit and not coplanar phenyl rings. The experiments were performed on a parallelepipedic $2 \times 0.5 \times 0.5$ mm^3 single crystal, with a smooth, black colour and macroscopic surfaces [107]. An SEM image of the typical AzA single crystal is given on Fig. A 1 in order to provide an insight of the topography of its surfaces.

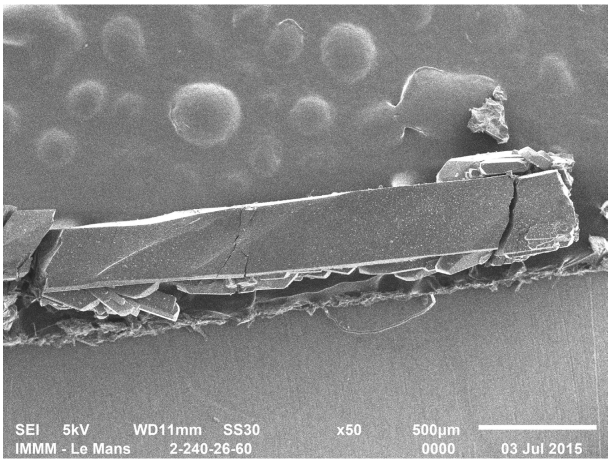

Fig. A 1: Image of a AzA spin-crossover molecular crystal taken by scanning electron microscope (SEM). The electron beam with energy of 5 keV was focused on the sample, zoom in is x50, scale bar is 500 μm.

The top plane depicts the [110] crystallographic plane of the crystal and was usually used as the reference surface for the pump-probe measurements. Due to the large optical density of the crystals, the pump-probe reflectivity measurements were performed at their front side (see Fig A. 2). A femtosecond Ti-Sapphire Coherent RegA 9000 regenerative amplifier was a source of the pump and probe pulses. It is operating at the central wavelength of 800 nm at a repetition rate of 250 kHz. The 400 nm pump pulses of 160 fs time duration were focused on the [110] surface of the crystal with a Gaussian spatial profile of FWHM ∼150 μm. The time delayed 800 nm probe of tenfold much weaker energy, was tightly focused on ∼100 μm spot, at 30 degree oblique incidence on the [110] surface normal of the crystal and spatially overlapped with the pump spot. The reflected probe beam was directed to a balanced photodiode to measure the transient differential reflectivity $\Delta R(t)$ as a function of time delay between pump and probe beams. Upon absorption of the 400 nm pump pulse over the optical skin depth of the crystal, the light energy is partially converted into mechanical that drives the excitation of bipolar acoustic pulses propagating away from the free interface Fig. A 2. Then the time delayed probe pulse is inelastically scattered by this acoustic pulses travelling into a crystal, hence interferometric Brillouin scattering oscillations are measured. A precise temperature control was achieved by use of a continuous flow cryostat.

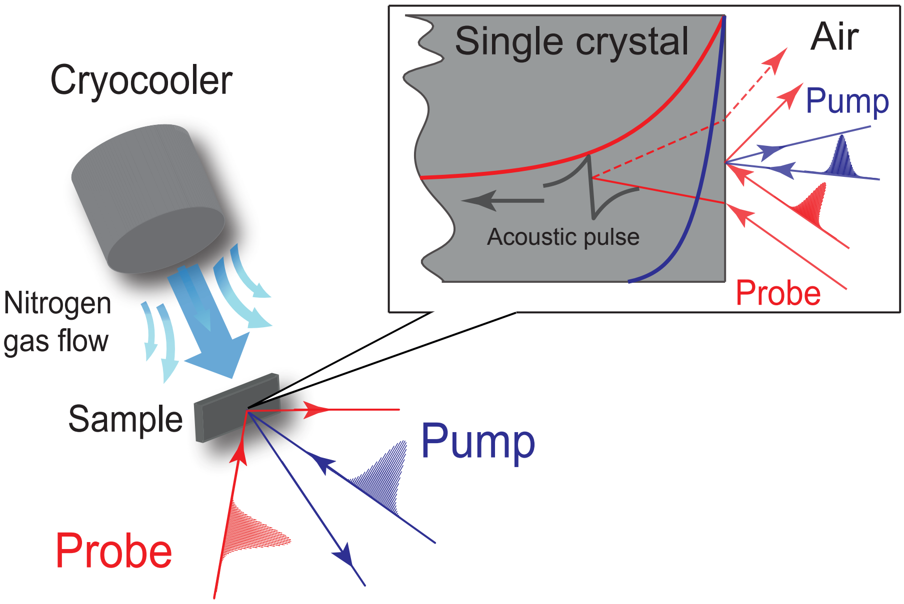

Fig. A 2: Sketch of the experimental set-up. A laser pump pulse photoexcites the molecular crystal sample, which is situated under continuous nitrogen flow for temperature control. Propagation of the photoexcited bipolar acoustic pulse is detected by a time-delayed optical probe pulse.

Coherent acoustic phonons in $[Fe^{II}(phen)_2(NCS)_2]$

Experiments were performed at room temperature, where the sample possesses 100% of paramagnetic HS state ($S = 2, t_{2g^4}e_{g^2}$). Fig. A 3 shows the generation of coherent acoustic phonons in the spin-crossover molecular crystal $[Fe^{II}(phen)_2(NCS)_2]$ (FePhen) (a). On Fig. A 3 (b) they are detected with help of the time resolved reflectivity $\Delta R/R$ measurement unfolding Brillouin scattering oscillations. The inset reveals the Brillouin frequency spectrum of the measured transient reflectivity during the first ns after the excitation.

As in any Brillouin scattering process, the frequencies ν_l, ν_s of these oscillations are related to the ultrasound velocities υ_l, υ_s in the material (probe light is scattered on propagating acoustic strain), to the probe wavelength λ, refractive index n of the medium and to the back-scattering angle θ through the expression

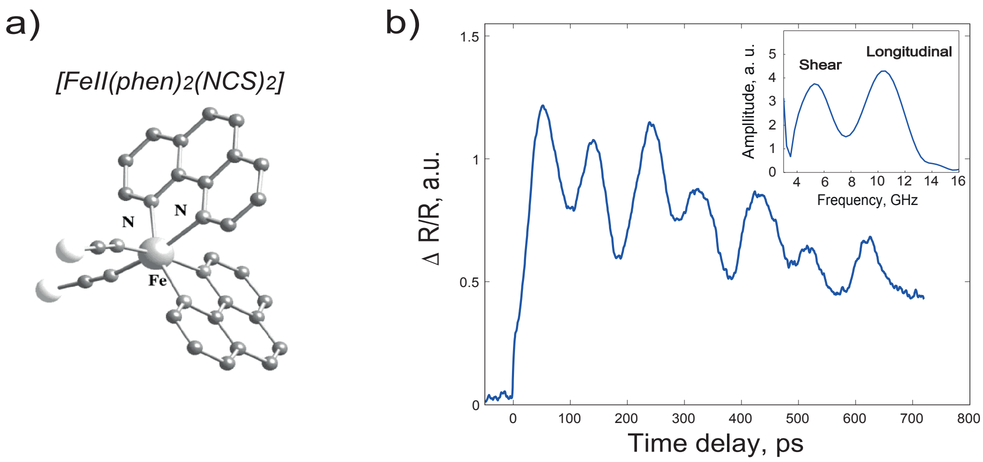

Fig. A 3: (a) Structure of the $[Fe^{II}(phen)_2(NCS)_2]$ compound. (b) Laser-induced Brillouin scattering oscillations in a crystal recorded at 280 K. The inset shows the frequency spectrum of the signal.

$$\nu = 2\ n\ v \cos\theta/\lambda. \tag{A1}$$

Since the ultrasonic velocities v_l, v_s of longitudinal and shear acoustic phonons are different, the corresponding Brillouin frequencies can be distinguished from each other in the frequency spectrum. Two peaks centred at ~5.5 GHz and ~11.3 GHz correspond to the shear and longitudinal modes, respectively. When laser pulse illuminates the crystal, it partially transfers its optical energy to the local rise of the lattice temperature ΔT. That leads to its subsequent expansion and generation of the elastic strains, which propagate in the bulk and significantly modulates optical reflectivity of the crystal. Due to the strong mechanical anisotropy of the crystal both acoustic modes are generated.

Coherent acoustic phonons in $[Fe(PM - AzA)_2(NCS)_2]$

The same type of pump-probe experiment were performed to study the generation of acoustic phonons in $Fe(PM - AzA)_2(NCS)_2$ single crystals (Fig. A 4 (a) at the room temperature. Fig. A 4 (b) shows the activation of the coherent picosecond strain waves, which are detected using transient reflectivity signal $\Delta R/R$. Oscillations are damped after Δt ~750 ps, the inset shows the Brillouin frequency spectrum of the measured reflectivity signal during the first 800 ps. Oscillations expected at ~5.5 GHz and ~11.3 GHz correspond to longitudinal and shear phonons. Detection of the longitudinal acoustic waves can be performed with the help of interferometric, deflectometric or reflectometric techniques. The reflectometric detection technique is sensitive to any

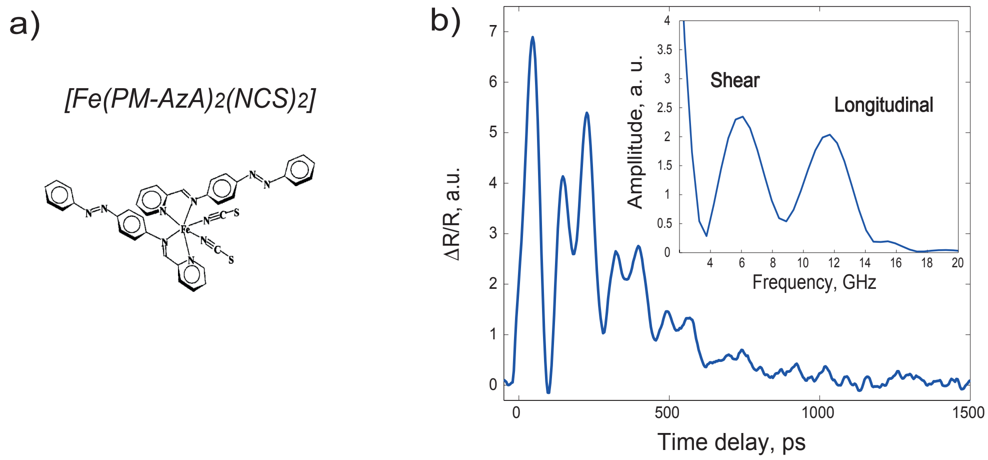

Fig. A 4: a) Structure of the $[Fe(PM-AzA)_2(NCS)_2]$ compound. b) Example of a transient reflectivity signal recorded at 280 K. The inset shows the frequency spectrum of the signal.

phenomenon that modifies the optical properties of the material such as pressure or change in density following the longitudinal acoustic phonons. In general shear acoustic waves do not modify the density of the isotropic materials, the reflectometric detection technique, which measures the change of the probe intensity is not sensitive to shear acoustic phonons. The alternative approach is to measure the rotation of the probe beam polarization, which is caused by shear phonons only, rather than reflectometry. In the case of AzA, which is a highly anisotropic crystal, the well-established rules for the detection of shear acoustic phonons in isotropic materials are still relevant. Fig. A 5 compares the experimental curves, detected by reflectometry and depolarized Brillouin scattering detection techniques. The frequency spectrum, shown on Fig. A 5 (b) and Fig. A 5 (d), evidences the enhancement of the detected shear amplitude in case of depolarized Brillouin scattering, which agrees well with the general rules for shear acoustic detection.

Fig. A 5 (a) shows an example of the experimental result obtained in depolarized detection configuration, Fig. A 5 (c) depicts the transient reflectivity experimental curve recorded from the same crystal. Frequency spectrum of both signals is highlighted on Fig. A 5 (b) and (d), respectively. Higher frequency oscillations of ∼11.3 GHz are longitudinal phonons, shear nature of lower frequency coherent oscillations of ∼5.5 GHz is confirmed by depolarized detection technique. It is clear that this technique is more sensible for the detection of shear waves due to the higher longitudinal/shear frequency amplitude ratio A_L/A_S, 0.83 to 2.21 in depolarized and reflectivity detection configuration respectively.

Longitudinal and shear acoustic phonons can be laser-excited in the mechanically

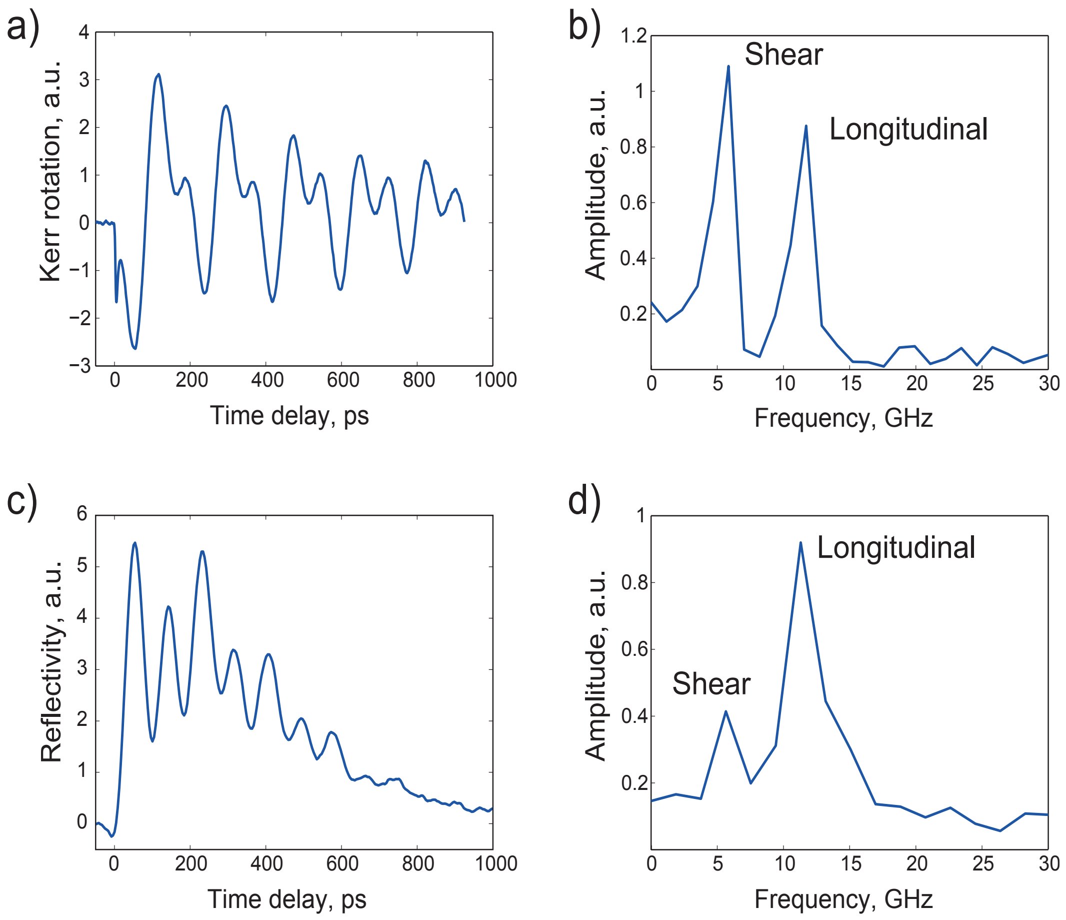

Fig. A 5: Kerr signal amplitude (a) and its frequency spectrum (b). Derivative of the transient reflectivity signal (c) and its frequency spectrum (d) measered at room temperature on $[Fe(PM-AzA)_2(NCS)_2]$ compound.

anisotropic SCO molecular crystals. They can be detected with the transient reflectivity and/or depolarized Brillouin scattering techniques. However, the polarization dependent measurements are more preferential for shear wave detection rather than the measurement of $\Delta R/R$. Variation of the shear acoustic wave sensitivity between reflectometry and depolarized Brillouin scattering techniques is a confirmation of the acoustic nature of the observed oscillations. Measurement of depolarized Brillouin scattering will be utilized for further phase-dependent experiments.

Evolution of the mechanical properties across the phase transition

The evolution of the mechanical properties of $Fe(PM-AzA)_2(NCS)_2$ crystal across the temperature-guided phase transition was studied using time-dependent depolarized Brillouin scattering technique. Since the material experiences a strong shape modification during the electronic transition from one spin state to another, propagation of the acoustic phonons will be detected differently upon the change of refractive index.

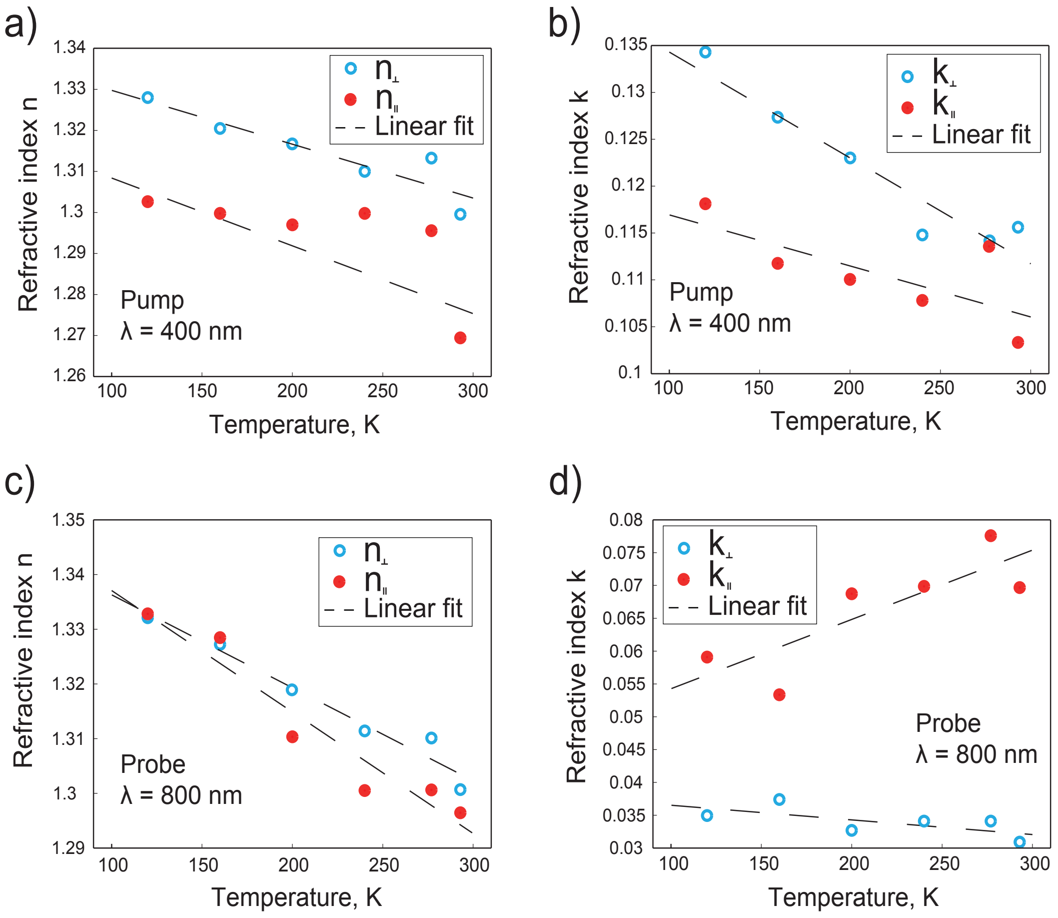

Fig. A 6: Temperature dependencies of the (a) Real n and (b) imaginary k parts of the refractive index of AzA molecular crystals at 400 nm pump wavelength. (c) Real n and (d) imaginary k parts of the refractive index of AzA molecular crystals at 800 nm probe wavelength. The data were obtained at different crystal temperatures across the spin crossover temperature and for two different polarizations parallel $\|$ or perpendicular $\perp$ to the optical plane of incidence.

The expression $\nu = 2\ n\ v \cos\theta/\lambda$ shows a coupling of the real part of the refraction index n with the frequency of the ultrasonic pulses. The modification of the optical absorption, related to the imaginary part of n, leads to the modulation of the amplitude. Hence, temperature-resolved white light optical ellipsometry were conducted to disclose temperature and wavelength dependencies of the complex refractive index of $Fe(PM-AzA)_2(NCS)_2$ crystal.

The extracted refractive index at 400 nm and 800 nm pump and probe wavelengths is displayed on Fig. A 6. The ellipsometry measurements were performed at five different orientations of the crystals, the temperature control was achieved using a continuous flow cryostat.

The calculations of the real n and imaginary k part of the optical index in the Mueller matrix were performed using the analytical 4×4 matrix algorithm from Schubert [121], derived from the 4×4 matrix formalism of Berreman [122]. The conventions

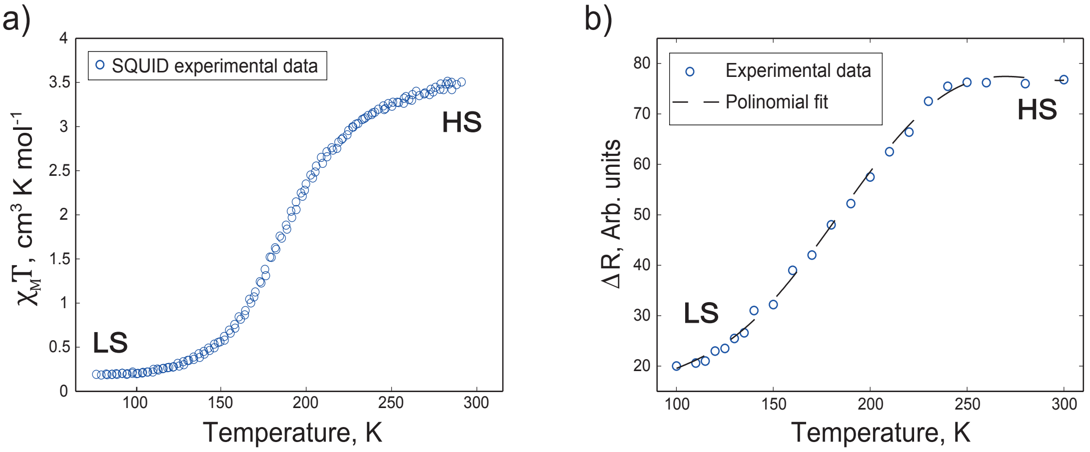

Fig. A 7: a) Smooth thermal spin-crossover transition characterized by the magnetic susceptibility, recorded across the LS to HS transition temperature of AzA molecular crystal [105]. b) Modification of the crystal reflectivity, measured at 800 nm, follows LS to HS transition.

$\parallel$ and $\perp$ used as a subscript for the indexes notations on Fig. A 6, refer to the probe polarization either parallel $\parallel$ or perpendicular $\perp$ to the plane of its incidence, which contains the c axis of the AzA crystal.

A slight decrease of the real part n of the index of refraction at increasing temperatures is consistent with the fact that the material density decreases at higher temperature. The imaginary part k of the refractive index, doesn't show a strong modification at different temperatures. One can notice a strong discrepancy between 400 nm and 800 nm wavelengths which emphasizes that AzA can be considered as opaque at the pump wavelength and semi-transparent at the probe wavelength. So the complex refractive index does not change significantly with temperature see Fig. A 6. Moreover, one can notice a difference in the refraction index for parallel $\parallel$ or perpendicular $\perp$ light polarizations that is related to the optical anisotropy of the compound. This study will be used for the subsequent determination of the generation mechanism, which dominates the excitation of acoustic phonons.

Thermal spin-crossover transition of AzA molecular crystal with a spin crossover temperature of $T_{1/2}$ ~180 K can be monitored experimentally from the measurement of the magnetic susceptibility χ_M and the product $\chi_M T$ [105] by SQUID magnetometry, which gives direct information on the spin state (see Fig. A 7 (a). The experiments have been conducted at different temperatures ranging from 50 K, where AzA spin states are almost 100 % diamagneticaly low spin (LS), up to 293 K, where crystal possess 100 % paramagnetic high-spin states (HS). Temperature step changes of 10 K were performed with a short working distance (~ 1 mm) continuous nitrogen flow cryostat. The crystal

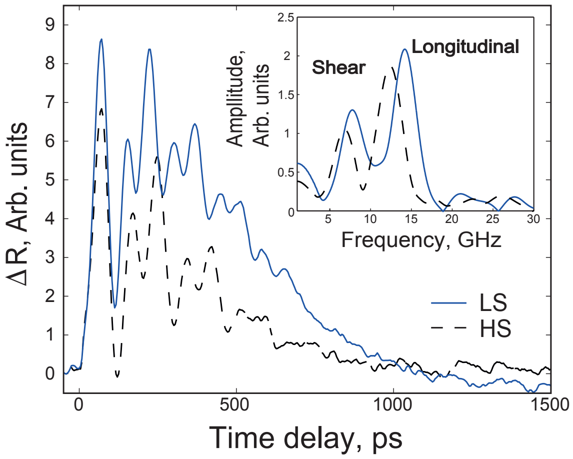

Fig. A 8: Transient reflectivity signals recorded in the LS and HS states. The frequency spectrum of the LS and HS Brillouin oscillations, presented in the inset, shows the photoexcitation of both longitudinal and shear acoustic phonons.

undergoes wide transition with a very small hysteresis of 6 K: $T_c(\downarrow)$ = 186 K, $T_c(\uparrow)$ = 192 K, which was previously reported in [123]. Fig. A 7 (b) shows the same kind of behaviour on the static measurement of reflectivity change at 800 nm wavelength. It confirms the modulation of the complex index of refraction across the temperature-guided LS to HS transition. It confirms that the optical response at 800 nm is sensitive to the structural reorganization of the crystal and gives a complementary signature of the SCO effect.

Measurements of time-resolved transient reflectivity of AzA were performed in between 300 K and 100 K, where the crystal possesses quasi-pure high and low spin states. The optical excitation of the both longitudinal and shear acoustic strain waves with different ultrasonic velocities υ_l, υ_s leads to the two distinct Brillouin frequencies.

Fig. A 8 shows an example of such time domain Brillouin scattering light modulation recorded at different temperatures. The periodic oscillations of 6 GHz and 12 GHz (see the inset) are detected right after pump excitation at zero time delay [124]. The shear acoustic nature of the 6 GHz frequency has been previously confirmed by depolarized Brillouin scattering measurements. For each recorded time domain Brillouin scattering signal in the $100 - 300\ K$ temperature range, the change of reflectivity has been numerically fitted in the form of a damped sinusoidal function

$$\Delta R \sim A \cdot \exp(-t/\tau)\sin(2\pi\nu t + \phi). \tag{A2}$$

The frequency ν, the damping time τ, the amplitude A, and the phase ϕ for each

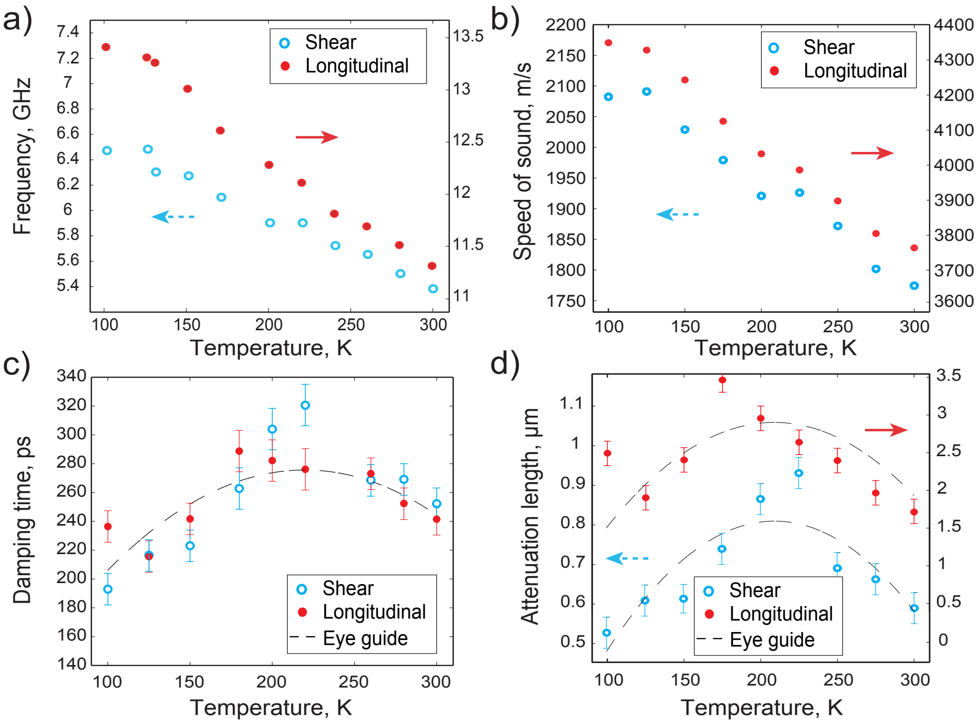

Fig. A 9: Time domain Brillouin scattering results obtained for vertically polarized pump and probe beams versus crystal temperature. Brillouin frequency (a), related speeds of sound (b), relaxation time (c), and attenuation length (d) of the acoustic modes.

longitudinal and shear acoustic mode were extracted from the fit within a given time delay t.

The extracted frequency and the damping coefficient of the measured Brillouin oscillations are depicted in Fig. A 9 (a) and (c), respectively. The temperature evolution of the AzA refraction index led to the calculated acoustic speed Fig. A 9 (b) and acoustic attenuation length Fig. A 9 (d) of the longitudinal and shear acoustic modes across $T_{1/2}$. The huge $\sim$ 15 % Brillouin frequency decrease for both acoustic modes, governed by Eq. (A1), is consistent with the expected temperature modification of both real part of the refractive index and the acoustic speed which should decrease with decrease of the material density at higher temperature. Based on the ellipsometric results shown in Fig. A 6, which confirm a slight variation of the optical index of refraction only of a few percent at different temperatures. The huge 15 % change in Brillouin frequency is caused by a pronounced change in both longitudinal and shear acoustic speed. According to Eq. (A1) and the measured real part $n_{\perp}$ of the index of refraction at the probe wavelength for vertically polarized light on Fig. A 6, we have calculated the change in Brillouin frequency to extract the variation in longitudinal and shear acoustic velocities with temperature. The results displayed in Fig. A 9 (b) confirm the substantial change in the acoustic speed, in the range of 10 %, which emphasizes the giant change in mechanical properties of the material across the spin crossover temperature. This intrinsic softening of the material at increasing temperature across $T_{1/2}$ is coupled to a substantial isostructural modification of the lattice parameters, such as the unit cell volume which is reduced by a large amount of ~ 3 % [105, 125]. As a comparison with highly magnetostrictives ferromagnetic compounds such as Terfenol [60] which is the foremost highest magnetostrictive alloy with a change of the unit cell volume by an amount of 0.1 % upon modification of the magnetization vector, the change in AzA lattice parameters in the order of few percent reveals the strong spin-lattice coupling in these atypical materials. The pronounced spin-lattice coupling in such compounds surely influence the coherent phonon generation. However, in our case of weak laser pump energy per pulse at 400 nm wavelength, we believe that the laser mediated LS → HS switching, which could elongate the $Fe - N$ bond within 160 fs, is not as efficient at this particular wavelength than at 800 nm laser pump wavelength.

The evolution of the damping coefficients with the temperature change is displayed in Fig. A 9 (c). It is related to the imaginary part of the refractive index $\mathrm{k}_\perp$ at the probe wavelength and to the intrinsic acoustic attenuation. Damping of the Brillouin oscillations in Fig. A 9 (c) exhibits a maximum at the spin-crossover temperature $T_{1/2}$, at the contrary to the imaginary part $k_\perp$ of the optical index at the probe wavelength that evolves smoothly across $T_{1/2}$, see Fig. A 6 (d). It means that the damping is mainly of acoustic contribution. It is associated with an expression $f(t) = \sin(\omega t)\exp(-\Gamma t) = \sin(\omega t)\exp(-\beta t)\exp(-\alpha \upsilon t)$, where Γ is an experimentally measured lifetime of the phonons. A change of the lifetime can occur for two reasons: change of β, which represents the anharmonicity of the lattice (phonon-phonon collision) or modification of the penetration depth of the probe beam into the crystal, which is governed by the term $\alpha = 4\pi k_\perp/\lambda$. From the measured $k_\perp$ at the probe wavelength, we have processed the measured damping of the Brillouin oscillations τ, in order to extract the acoustic attenuation length Γ from the straightforward calculation

$$1/\Gamma = 1/\upsilon\tau - 1/\xi, \tag{A3}$$

where υ is the longitudinal or shear acoustic speed and $\xi = \lambda/4\pi k_\perp$ is the optical penetration depth. The result of the calculation of the acoustic attenuation length for both acoustic modes, longitudinal and shear, is displayed on Fig. A 9 (d). The remarkable minimum damping measured in Fig. A 9 (c) is confirmed to be an exacerbation of the acoustic attenuation across the spin-phase crossover transition. However, the phenomenon is reverse from the well-known structural α-relaxation which has been evidenced in glass forming liquids across the T_g glass transition temperature [126]. The acoustic wave propagates at longer distances at the spin-crossover temperature which indicates that the structural modification of the lattice and the statistical growth or disappearance of the LS/HS states does not perturb the acoustic phonons propagation, vice versa, the acoustic phonons propagation is facilitated during the spin crossover transition.

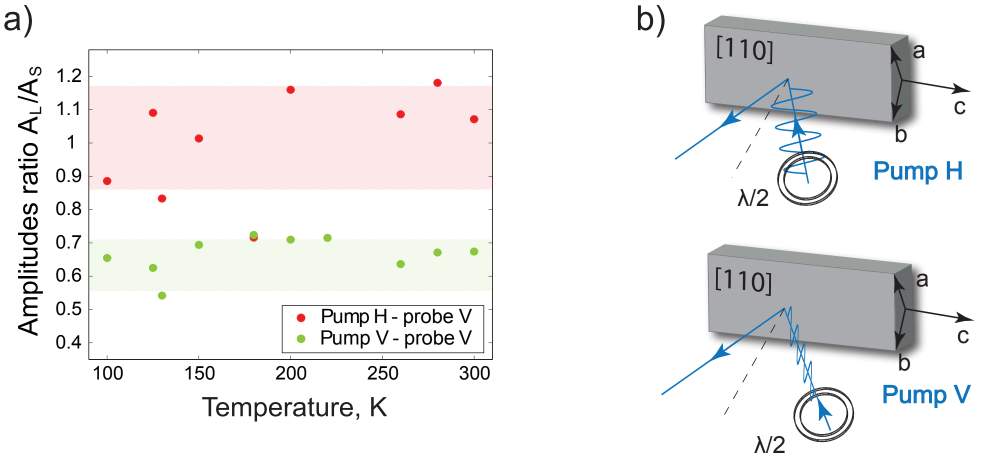

Fig. A 10: (a) Ratio between the longitudinal and shear Brillouin amplitudes for different pump polarizations. Red dots correspond to horizontally polarized pump, green to vertically polarized pump, as sketched in (b).

Several mechanisms are involved in the laser-driven lattice motion of the AzA crystal: (i) thermoelastic mechanism which is linked to the transient thermal dilation of the lattice following the temperature rise due to pump laser absorption, and two non-thermal mechanisms, (ii) the spin-lattice coupling mechanism and (iii) the deformation potential mechanism [6]. The temperature evolution of the Brillouin amplitudes and Brillouin phases at two different pump polarizations (horizontal (H) and vertical (V) polarizations) displayed in Fig. A 10 gather crucial information on the photoacoustic excitation process. The fact that the optical index of refraction (see Fig. A 6) do not vary significantly with temperature warrant that the measured Brillouin amplitude and phase is mainly sensitive to the excitation mechanisms and not to the detection process through a modification of the acousto-optic coefficients with temperature. Since the measurement of the Brillouin amplitude can suffer from experimental artifacts, such as beam pointing stability during sample heating or cooling, we have chosen to further process the longitudinal A_L and shear A_S Brillouin amplitudes data by taking the ratio of both amplitudes, defined as A_L/A_S, not biased by optical artefacts. This simple procedure highlights a discrepancy in Fig. A 10 (a) between H and V pump polarizations which can't be assigned to the thermoelastic mechanism. In fact, as indicated by the difference in optical absorption coefficients $k_\perp$ and $k_\parallel$ at the pump wavelength (see Fig. A 6), the laser induced temperature rise in such anisotropic crystals depends on the pump polarization. However, taking the ratio of both amplitudes modes is a proper way to conveniently remove the temperature rise contribution in the thermoelastic process of the acoustic excitation, which is identical for either longitudinal or shear acoustic modes. Therefore the gap between the amplitude ratio in Fig. A 10 (a) with H or V polarizations is assigned to a non-thermal mechanism, either spin-lattice coupling or deformation potential mechanism. One possible explanation of the observed amplitude jump would be the anisotropy in deformation potential mechanism. The latter should be considered as tensorial in such crystal with different diagonal and non-diagonal coefficients referring to preferential electronic excitations of the ligands by horizontally or vertically polarized pump pulses, with some similarities with [127] that demonstrates the wide range of electronic excitations of organic molecules that can drive coherent lattice phonon excitation. In addition to the electron deformation potential mechanism, we can't neglect the spin-lattice coupling anisotropy which is known to be highly sensitive to the pump polarization [36], [128].

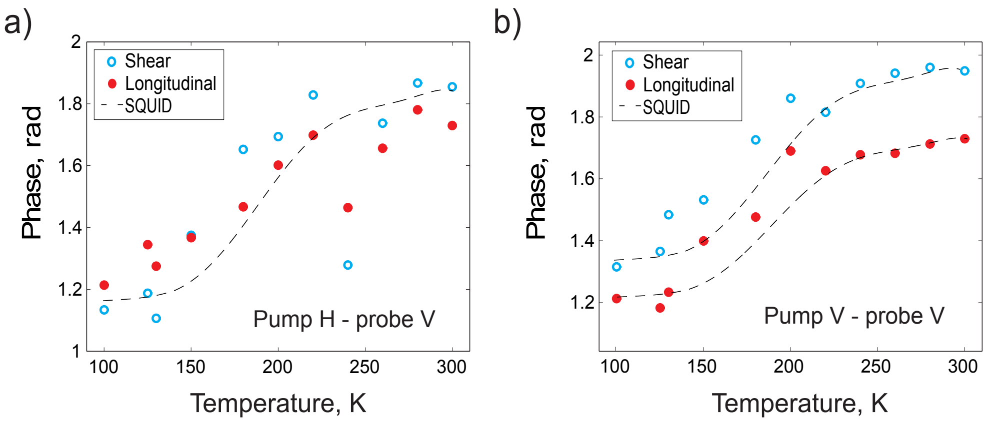

Fig. A 11: Extracted time domain Brillouin phase for horizontally (a) and vertically (b) polarized pump beams of both longitudinal and shear acoustic modes in AzA compound at different crystal temperatures. The SQUID curve matches the Brillouin phase evolution across $T_{1/2}$.

Another striking feature of an interplay of several photoacoustic mechanisms is revealed by the Brillouin phase change in Fig. A 11 (a) and Fig. A 11 (b) with H or V pump polarizations. Once again, if we assume that the slight change with temperature of the optical refraction index is irrelevant for the interpretation of our experimental observations, the substantial phase jump in the range of 0.6 radians of both longitudinal and shear Brillouin signals across the spin-crossover transition highlights a profound change in the laser-induced mechanism for acoustic phonons excitation. Based on [129], the phase change, which matches the evolution of the magnetic susceptibility of Fig. A 7 (a), can be attributed as a change in the acoustic excitation process through the contribution of the spin-lattice mechanism that vanishes once the compound reaches 100% HS spin state where the laser-induced evanescence of the spin-lattice coupling. However, as stated previously, the ultrafast release of the spin-lattice coupling is probably not the most efficient at this pump wavelength and energy. Therefore, we can't rule out the deformation potential mechanism as a relevant mechanism in the process of laser excitation of coherent acoustic phonons in AzA. The observation of a phase jump of about 0.2 radians in Fig. A 11 (b) between longitudinal and shear excitation points to a non-thermal mechanism of acoustic excitation sensitive to the pump polarization, see Fig. A 11 (a).

Temperature-resolved Brillouin phase of the bipolar acoustic pulse, generated by a thermo-elastic mechanism and travelling in the AzA compound was extracted from the numerical simulation. It is based on the model of the bi-polar acoustic pulse propagation in a semi-infinite medium. In our experiments a time-delayed probe beam with 800 nm wavelength monitors the transient change of reflectivity of the crystal. It occurs due to the strain propagating in material, that changes its complex refraction index [48].

$$\Delta n(z,t) = (\frac{\partial n}{\partial \eta} + i \cdot \frac{\partial k}{\partial \eta})\eta_{33}(z,t), \tag{A4}$$

where n and k are the real and imaginary part of the complex index of refraction. The temperature-induced change of the complex index of refraction of AzA molecular crystal doesn't lead to the significant change of the Brillouin phase, see Fig. A 12. Thus, the deformation field can not be simply described by an optical absorption. Another type of dynamic comes into play: structural relaxation, heat diffusion, etc. Hence, this is

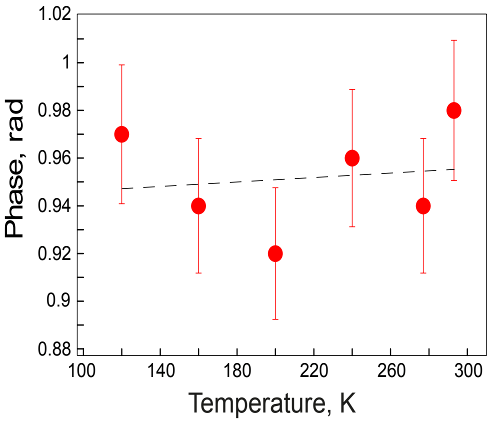

Fig. A 12: Simulation of the temperature-dependent time domain Brillouin phase of the acoustic pulse, propagating in AzA compound. Dots are the simulated phase, dashed line is a linear fit.

a confirmation of the assumption, that the process of generation of acoustic phonons changes during the temperature-guided phase transition. More likely, an efficiency of the one of the process of excitation increases due to the structural reorganization of crystal, which gives rise to the change of the Brillouin phase. From the other hand, change of the imaginary part of refractive index $\partial k/\partial \eta$ in Eq. (A4), which is related to the change of absorption coefficient, can also contribute to the modulation of the phase. This can be a signature of the detection modulation.

In summary, two photoexcited spin-crossover molecular crystals were investigated by time-resolved optical pump-probe technique. Our experimental results can invoke that most probably two non-thermal mechanisms of equivalent efficiency are involved together in the complex photoacoustic excitation process in AzA molecular crystals, with different efficiencies (amplitudes) and characteristic times (phases). Due to their structural anisotropy, such crystals may be used as efficient GHz shear waves transducers. In light of further research in the field of magnetic storage devices, investigation of spin-lattice coupling of the studied materials can be used as an interesting alternative to the present prototypes. Variable compositions of molecular crystals allow to tune their properties, it can be applied for creation of shear acoustic waves transducers with higher frequency bandwidth. Besides that, investigation of thin films based on molecular crystals may give rise to new unexpected effects.

The optical excitation of spin-crossover $[Fe^{II}(phen)_2(NCS)_2]$, $[Fe(PM-AzA)_2(NCS)_2]$ molecular crystals leads to the inelastic Brillouin scattering of the probe light from the generated acoustic strains, propagating in the bulk. Experimental results evidence a non-thermal excitation of GHz acoustic phonons in $[Fe(PM-AzA)_2(NCS)_2]$ across the temperature-guided spin-crossover phase transition, which could have spin-lattice and/or deformation potential origin. Furthermore, our results highlight the versatile and efficient generation of ultrashort shear acoustic phonons for future investigations of viscoelastic properties of materials such as liquids [130], glasses [99, 100], mixed multiferroics, correlated electron systems and magnetic materials. Other types of anisotropic molecular crystals can be utilized for further study in the field of picosecond ultrasonics. Indeed, knowledge of the spin-elastic coupling in spin-crossover molecular crystals will be crucial for the design of multifunctional molecular devices. Preliminary results of time-resolved Brillouin scattering in $[Fe^{II}(phen)_2(NCS)_2]$ (FePhen) crystal prove their suitability for picosecond ultrasonic studies by photoexcited gigahertz acoustic phonons. Moreover, fabrication of thin films, based on molecular crystals [131], [132] leads to the elaboration of potentially more efficient GHz shear waves transducers.

Appendix B

Electron structure and magnetism of Terbium (Tb) and Iron (Fe)

The electron structure and magnetism of two elements, Terbium and Iron, are presented with an eye to provide a better understanding of the laser-induced ultrafast dynamics of their alloy. Relation between Tb and Fe electronic structure and their magnetism is given.

Terbium (Tb)

Terbium (Tb) is one of the *lanthanide* metals with atomic numbers of 57 through 71 (from lanthanum La to lutetium Lu). These elements, together with the chemically similar scandium (Sc) and yttrium (Y), are collectively named *the rare earth* elements. Its atomic weight is equal to 158.9254 g·mol^{-1}. Tb is a heavy lanthanide metal with $[Xe]6s^2 4f^9$ electron configuration. Where mostly f electrons (among 65 electrons of Tb atom) determine its magnetic properties due to their highly anisotropic electronic shell. 97 % of the magnetic moment of Tb is carried by 4f electrons, the other 3 % - by 5d conduction electrons. Spin-orbit interactions of Tb ions is much stronger than the crystalline electric field that makes it ferromagnetic [133]. The $4f$ electron cloud is not spherical (oblate in form), which results in great magnetostriction (see Fig. 2.2). An oblate distribution of electrons links a rocking of the atomic magnetic moment directly to the lattice vibrations and vice versa. With a half filled 4f shell Tb possesses a magnetic moment equal to 9.34 μ_b per atom [134]. 4f wave functions are strongly localized and have small overlap with the corresponding wave functions in neighboring atoms, hence, direct interaction between 4f moments is weak. So magnetic ordering of Tb is mainly caused by an indirect exchange interaction or RKKY interaction [135], which is typical for lanthanides [136]. Assuming an atomic origin of magnetism, the magnetic properties of the material are determined by a spin-orbit interaction in atom, thus, by the quantity $\overline{\mu} = -g_J \mu_B J$, where $-g_J$ is the Landé spectroscopic g-factor, μ_B is the Bohr magneton, J is a resultant total angular momentum. While the spin quantum number decreases with the fulfillment of 4f shell in lanthanide metals, the orbital quantum number increases [137]. Tb^{+3} total orbit and spin angular momentums

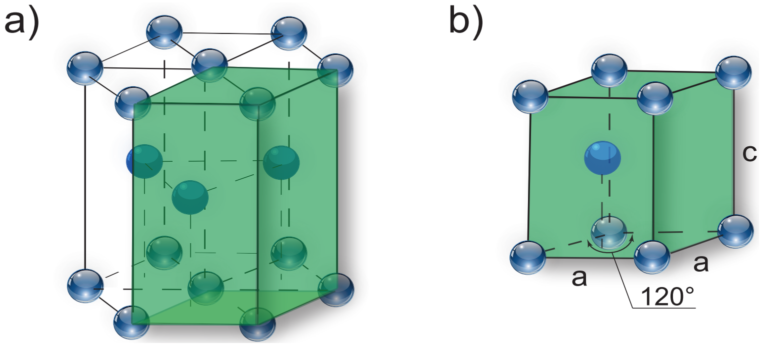

Fig. B 1: a) Hexagonal close packed (hcp) crystal structure of Terbium (atoms size is arbitrary) and b) its unit cell with lattice parameters.

are equal $\overline{L} = \overline{S} = 3$, thus, the resultant total angular momentum is $\overline{J} = 6$.

Terbium is ferromagnetic at low temperatures, but becomes antiferromagnetic at 221 K and has a Neel temperature of 229 K. In the antiferromagnetic state, spins have a helical arrangement, the vectors rotating about c axis with the twist angle between layers varying from 18.5 degrees at 221 K to 20.5 degrees at 229 K [138]. Fig. B 1 presents hcp crystal symmetry of Terbium with a=3.604 Å, c=5.698 Å [139] lattice parameters. Rare-earth Terbium was fused with 3d transition metals, Iron in particular, in order to increase its Curie temperature and, consequently, preserve the strong magnetostriction of alloy at room temperature.

Iron (Fe)

The highest magnetostriction at room temperature was found in an alloy of Terbium and Iron ($TbFe_2$). Iron (Fe) is a 3d ferromagnetic metal of the first *transition* series with atomic number of 26. It is a silver-grey metal (group VIII in the periodic table) and represents an example of allotropy in a metal. There are at least four allotropic forms of iron, known as α, γ, δ and ε as a function of pressure and temperature. Its electronic shell structure is $[Ar]3d^6 4s^2$ with atomic mass of 55.85 g·mol^{-1}. It has

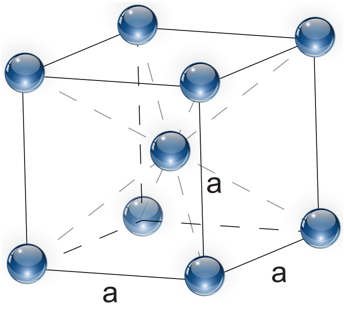

Fig. B 2: Body-centered cubic crystal structure of Iron (atoms size is arbitrary).

body-centered cubic (bcc) crystal symmetry Fig. B 2 with lattice parameters equal to $a = b = c = 286.65\ pm$ and $\alpha = \beta = \gamma = 90°$ [65].

Fe has spherical electron shells and does not show great magnetostriction on its own, but possesses a strong exchange interactions leading to high Curie temperature $T_C(Fe) = 700°$ C, so it remains ferromagnetic at room temperatures. Unlike rare-earth metals, the magnetism of Fe is defined by itinerant 3d electrons near the Fermi level. Fe^{+2} total orbit and spin angular momentums are equal $\overline{L} = \overline{S} = 2$, resulting in total angular momentum of $\overline{J} = 4$.

Appendix C

Fabrication of Terfenol films is a complex process. It is rare when the crystallographic axes of the deposited film coincide with the [100], [010], [001] axes of the elementary cubic cell. Therefore, the transformation of the right handed x, y, z coordinate system into the experimental one x', y', z' is required.

Transformation of the coordinate system

Fig. C 1 shows the Cartesian coordinate systems (x, y, z) and (x', y', z') adopted for the $TbFe_2$ layer. Following [91], the x' axis is set as normal to the surface of the film, while the y', z' axes lie in its plane. The x', y', z' directions coincide with the [110], [1$\bar{1}$0], [001] crystallographic axis, respectively. The (x, y, z) coordinate system can be obtained from the (x', y', z') by rotating a right-hand screw along the positive z direction at an angle ξ.

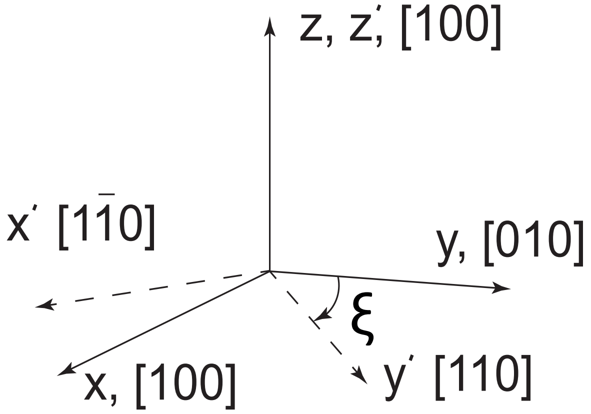

Fig. C 1: Transformation from a right handed x, y, z coordinate system that coincide with the crystallographic axes [100], [010], [001] into x', y', z' that coincide with [1$\bar{1}$0], [110], [001] directions, from a rotation around z axis with an angle ξ.

In case of an out-of-plane magnetized film, the magnetization coincide with the [111] crystallographic direction. Fig. C 2 describes the transformation of the coordinate system for an out-of-plane magnetized sample.

By analogy with the previous case, the crystallographic coordinate system (x', y', z') can be obtained from the initial (x, y, z) one by a rotation about z axis, using the right-hand rule, see Fig.C 2 (a). It sets the x', y' axes along the face diagonals of the initial

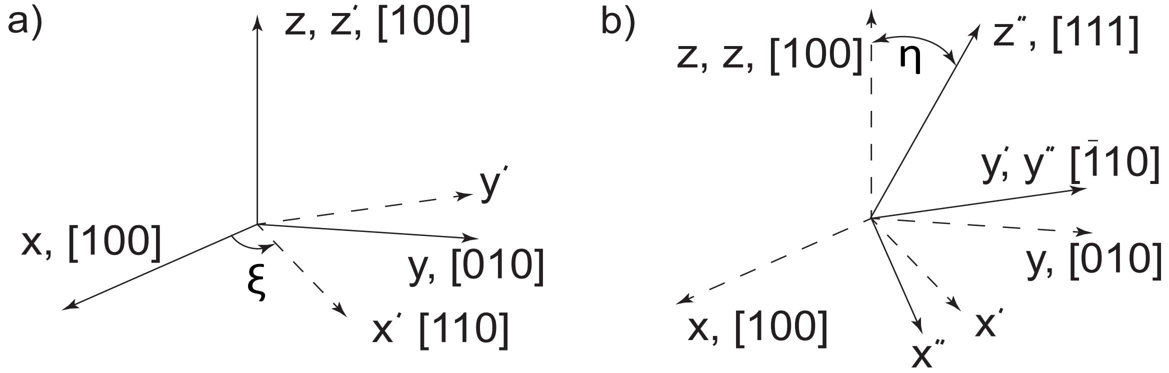

Fig. C 2: Transformation from right handed x, y, z coordinate system that coincide with crystallographic axes [100], [010], [001] to the experimental ones x', y', z' coupled with Terfenol film crystallographic directions [1$\bar{1}$0], [11$\bar{2}$], [111]. a) Clockwise rotation around z axis with an angle ξ, b) rotation around y' axis with an angle η.

cubic unit cell. Next, a clockwise rotation around y' axis with an angle η is required in order to bring the z' axis along the diagonal of the cube in Fig.C 2 (b), wherein $\eta = \cos^{-1}(1/\sqrt{3})$. Since the direction of propagation of the acoustic waves in the in-plane magnetized sample coincide with the x axis, a rotation about y'' on $\xi' = 90$ deg is required to set the x direction as normal to the surface of the out-of-plane magnetized film.

Thus, in case of both experimental geometries, the acoustic waves will propagate along the normal to the surface of the film, which coincide with x axis.

Appendix D

The experimental set-up depicted in Fig. D 1 for time-resolved MOKE and Brillouin spectroscopy has been built. It is based on the laser pump-probe technique, which utilizes an intense laser pulse to excite the sample and a weaker probe pulse to monitor its response. It allows to switch between one side pump-probe to back-pump front-probe schemes. Automatized magneto-optical measurements with different geometries and pump fluence-resolved measurements are possible due to the implementation of several motorized stages.

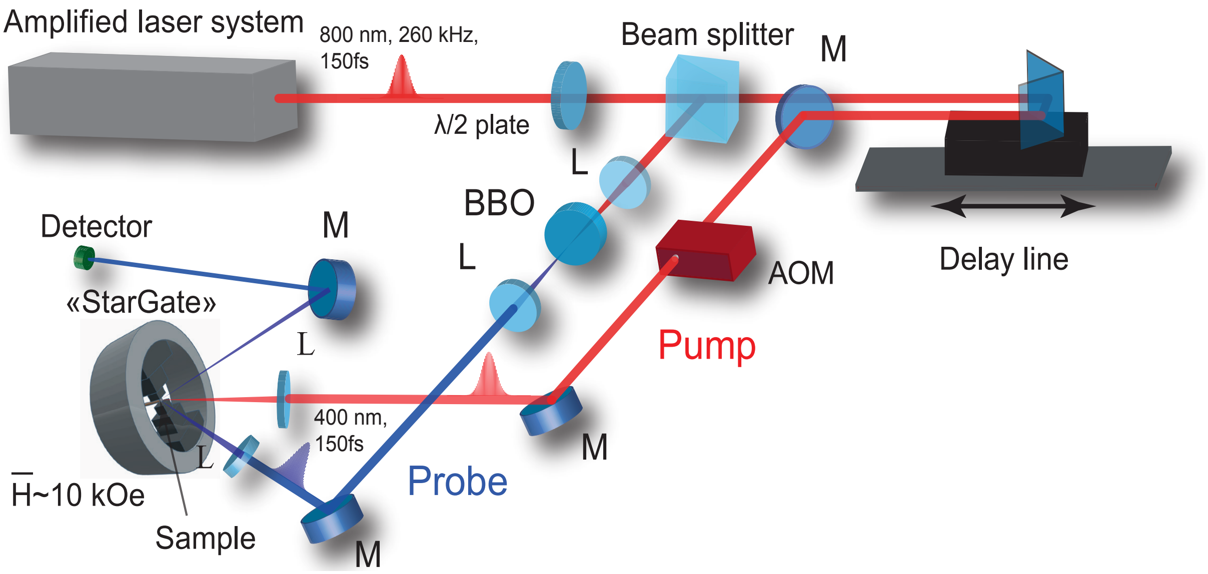

Fig. D 1: Experimental set-up. Abbreviations: M - mirror, L - lens, AOM - acousto-optic modulator.

Femtosecond laser system. A 800 nm femtosecond laser pump pulse excites the sample, while a femtosecond time-delayed 800 nm or 400 nm probe monitors the response of the material. In our experimental set-up the delay between pump and probe pulses allows to perform time-resolved ultrasonic experiments with a resolution of 150 fs. It is controlled by a mechanical delay line, that changes the length of the optical path of the pump beam. It is modulated by an acousto-optic modulator (AOM) at 50 kHz, which is synchronized with a lock-in amplifier. To produce 400 nm probe laser pulses, the fundamental beam passes through a nonlinear optical crystal made of Beta Barium Borate (BBO).

The key element of the experimental set-up for pump-probe spectroscopy experiments (Fig. D 1) is the amplified laser system (*laser system* in Fig. D 1). It is based on a *Coherent MIRA 900s* oscillator pumped by a continuous *Verdi 5W* pump diode laser. The gain medium of this laser is a titanium doped sapphire (Ti:Sapphire) crystal. The output of the system is injected in a *Coherent RegA 9000* femtosecond mode-locked Ti:Sapphire amplifier, pumped by a continuous *Verdi 12W* pump diode laser. The system generates 150 fs pulses with 6 μJ energy per pulse at a repetition rate of 250 kHz and at the fundamental wavelength of 800 nm. Typical diameters of pump and probe spot are 100 μm and 50 μm, respectively. Typical pump and probe fluences used during experiments are 5 mJ/cm^2 and 0.1-0.5 mJ/cm^2, respectively.

Acousto-optic modulator. To increase the signal-to-noise ratio (SNR), the intensity of the pump beam is modulated at a given frequency. In our set-up, the acousto-optic modulator is used to modulate the pump beam at 50 kHz. AOM is a device that deflects a normally incident laser beam at the Bragg's angle due to ultrasonic waves propagating in the AOM cell. It is much faster than typical mechanical choppers. When an electric current is applied to the piezoelectric transducer of the AOM modulator, it induces sound waves in the crystal (usually quartz or TeO_2). These moving periodic acoustic waves of expansion and compression change the index of refraction in the crystal and incoming laser light scatters on this periodic structure. The light deflection angle is the Bragg angle (θ_B) and is related to the refractive index n of the medium, the λ, Λ wavelengths of incident light and of the ultrasound as

$$\sin(\theta_B) = \frac{mn\lambda}{\Lambda}. \tag{D1}$$

The diffraction from a sinusoidal acoustic modulation signal results in $m = 0, \pm 1$ diffraction orders. The beam of $m = 0$ order is not diffracted, and the angle between $m = \pm 1$ orders is $2\theta_B$, which is about 3 degrees for 800 nm. A modulation frequency of 50 kHz of the standing acoustic waves in the AOM cell is used to implement synchronous detection with a Lock-In amplifier. In an ideal case, the modulation rate is 100%, in practice, the intensity, diffracted into a zero order can be varied between 15% to 95% of the input light intensity. At the same time the intensity of the first order can be varied between 0% and 95%.

Delay line. The optical delay line allows to perform computer-controlled variation of the optical path length with a required time step. It includes a linear DC servo stage which ensures precise and fast motion, a hollow retroreflector and a controller. The time delay τ_d between the probe and the modulated pump beam is performed by moving the retroreflector along the stage. The delay line provides a 30 cm total spatial delay. The optical path of one of the beams is fixed, while the second one is modified by the delay line. If the retroreflector is moved of a distance l, the optical path of the corresponding beam will change of $2l$, hence, the time delay will be equal to $\tau = 2l/c$. In total, the delay line of 30 cm length, provides 2 ns time delay for time-resolved measurements.

Photodetector. The photodetector collects the photons reflected (or transmitted through) from the sample. A 8 mm gain balanced photoreceiver by *Newfocus* which operate at 400-1070 nm spectral range was used. The balanced detection is ensured by a pair of two silicon photodiodes. It detects the variation of the optical signals sent on the two photodiods.

Lock-In amplifier. It is a type of amplifier that can extract a signal from an extremely noisy background. The signal amplitudes presented in this work are in the order of $\sim 10^{-7} - 10^{-3}$, so the Lock-In amplifier was utilized. Depending on the dynamic reserve of the instrument, signals up to 1 million times smaller than noise components, potentially fairly close by in frequency, can still be reliably detected. Recovering signals at low signal-to-noise (SNR) ratios requires a strong, clean reference signal at the same frequency as the received signal. Hence, the lock-in measurements are performed with a reference frequency. In our set-up the pump beam intensity was modulated at a fixed frequency of 50 kHz, provided by the AOM. The lock-in filters and amplifies the signal from the photodetector at this reference frequency.

1 T DC magnetic field set-up Terfenol films have large coercitivity, so strong magnetic fields of about H = 10 kOe are required to manipulate its magnetization. Moreover, it has been shown that the efficiency of generation of the shear waves depend on the out-of-plane tilt of its magnetization, so even higher values of H are necessary in order to efficiently tilt the magnetization.

In general, in the laboratory conditions, such a strong magnetic field is produced by electromagnets. Such magnets have their advantages: they are easy to operate, we can vary the magnitude of the applied field and it is easy to change their polarity. However, they are not convenient for some lab applications: they are heavy, big dimensions, expensive and tend to produce wide magnetic fields which can interfere with the equipment close to it. Thus, it was necessary to find an acceptable alternative. Solution was found based on magnetic lenses, which are passive devices that (in analogy with optics) focus or concentrate the static magnetic field. They can be based on superconductor, or DC meta-materials, static magnets pyramids or cones to achieve a static magnetic field enhancement in a closed free space region. A perpendicular field superimposition produces higher magnetic fields on the axis, than the remanent field of the integral components separately. To a first approximation a field strength of the static magnet field decreases inversely with the distance from the surface of the active coil or the magnet. Hence, a conventional closed DC magnetic lens can be used to achieve an enhancement of the DC magnetic field in the free space region only at relatively short distances (∼ 1 cm). Electric and magnetic fields are decoupled in the case of static fields, so to describe the magnetic lens only the permeability is required. To simplify the problem, two dimensional case is considered: geometrical shape of its elements may vary between cones, cylinders, etc. In our case it is rectangular with height h and thickness (length along the center axis direction) d. The magnetic permeability of the lens can be expressed as:

$$\mu = \mu_c sech(g \cdot x),$$

where μ_c is the permeability of the lens, g determines the slope of gradual changes of the permeability in the x direction. Larger g means that the permeability decreases faster from the middle point to the edge of the lens, $sech(x)$ is the hyperbolic secant function.

Fig. D 2 presents our home-made *"Magnetic Stargate"* set-up (valorisation industrielle SATT du "Magnetic Stargate"), which is based on permanent nickel-plated

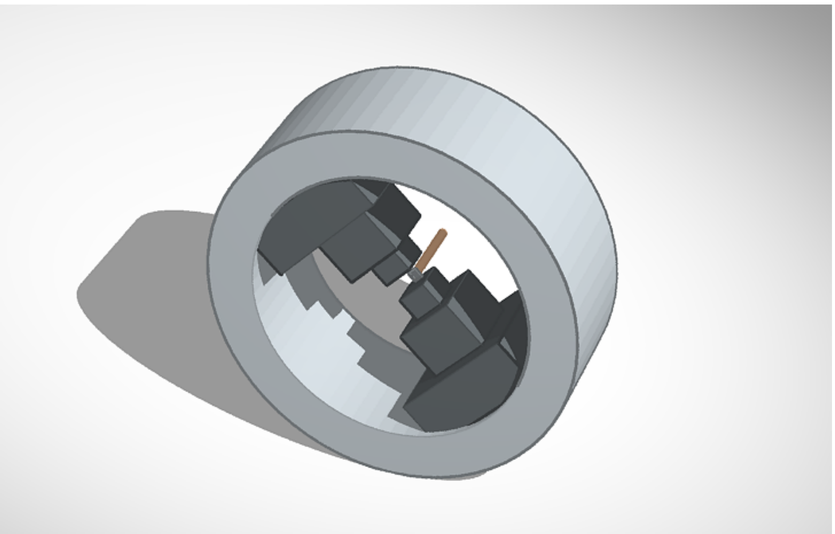

Fig. D 2: 1 T DC magnetic system.

neodymium magnet pyramids and cubes. It is the most widely used type of permanent magnets. It is made from an alloy of neodymium, iron and boron ($Nd_2Fe_{14}B$), their greater strength and durability (lose less than 1-2% of its magnetization in 10 years) allow the use of smaller and lighter magnets for a given application. Several pyramids can be installed (2, 4) to gain in the total field amplitude. Several pairs of magnetic lenses, comprising an adjustable amount of magnets, installed so that each set is aligned along one axis produce a greater magnetic field in the region between them. However, a resulting field in the center of the poles has a non-homogeneous pattern and varies from 700 mT closer to borders of the last magnets to 1 T in the middle. It can be characterized by a constant radial gradient (analytical function of the radial distance). The sample is fixed on the end of a non-magnetic rod. Often it is needed to reverse or modulate the magnetic field in-plane or out-of-plane of the sample. So, two magnetic lenses were installed on the ball-bearing frame, which allows to rotate the whole magnetic structure on 360 degrees, thereby to create a direction modulated magnetic field. It opens access to the field orientation dependent measurements. Ball-bearing frame is made of steal, thus, field lines are spreading inside of it, entering the wide end of the pyramid, which confines the field and guides it to the top of the magnetic lens.

To modulate the magnetic field direction in a controlled way, a common frame was connected with a rotation motor, which provides a field direction modulation at high frequency. The frequency range is variable, depending on the type of motor. Maximal modulation frequency of 20 Hz was achieved with available 12 W motor. Water cooling of the motor was added to ensure the stability of the modulation frequency. The set-up can be modified to apply out-of-plane field to the sample, which is necessary for the demagnetostriction experiments. One- and two-sides pump-probe experiment configurations can be performed with the set-up.

Higher frequency range of modulation can be reached by fixing the position of the magnetic field and rotating the sample. In this case sample is fixed on a motor axis, which is situated in between the static magnetic field. A modulation frequency of 125 Hz can be reached depending on the motor. However, this experimental geometry is not reliable due to the problems with the overlap of the beams during the high speed rotation.

Appendix E

The double modulation technique used for the shear waves detection in Terfenol film is reported in this section. Along this thesis, the non-magnetic part of the experimental signals measured by linear time-resolved MOKE was filtered by taking the difference of two magneto-optical signals, measured for opposite directions of the external magnetic field $+H - (-H)$. An alternative approach is based on the double modulation technique, which, in the general case, utilizes two reference frequencies to filter non-magnetic signal.

Double modulation technique for shear waves detection

The double-modulation (DM) sampling technique based on acousto-optic and mechanical modulations was utilized as an alternative experimental approach for ultrafast transient MOKE measurements. It combines an effect of high frequency acousto-optic modulation, which eliminates most of the low frequency noise, and low frequency mechanical modulation of the magnetic field, which filters a non-magnetic part of the signal. DM is a convenient technique for the detection of acoustic echoes in Terfenol hybrid samples. Its sensitivity is comparable to that of classical pump-probe scheme.

In the DM measurements the pump beam was modulated by an acousto-optic modulator at the frequency of $f_{mod1} = 50$ kHz in a form of a square wave. Mechanical low-frequency modulation of the magnetic field applied to the sample at a frequency of $f_{mod2} = 20$ Hz was achieved using a ball-bearing frame conjugated by a common base with the rotation engine (see Appendix D). The signal was optically detected by two balanced photodiodes, connected to the first high-frequency lock-in amplifier, which filters the signal at 50 kHz with a time constant of less than 1 ms. Signal from the first lock-in amplifier was processed by a second lock-in operating at the 2 f_{mod} mode frequency. Thereby, DM allows to detect only the magnetic response free from the low frequency noise.

Signals detected using depolarized Brillouin scattering technique are presented in Fig. E 1. After photoexcitation of the $TbFe_2$ layer of 300 nm thickness by a laser pump pulse, the acoustic waves are generated upon both thermoelastic transient heating and

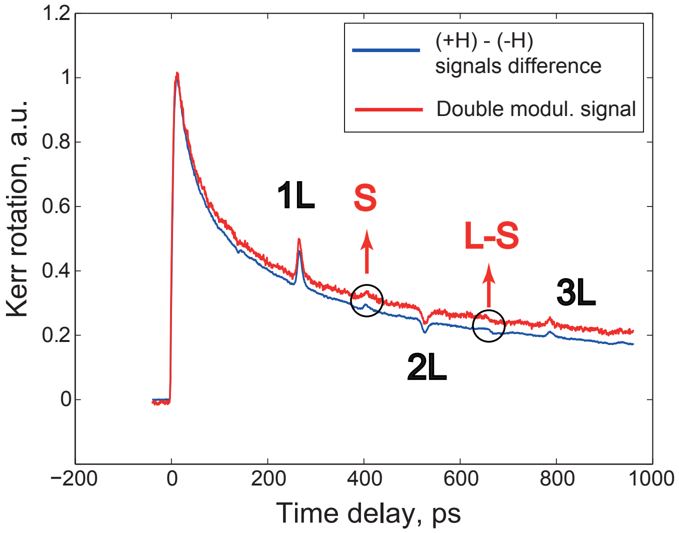

Fig. E 1: Time resolved (blue) differential MOKE signal and (red) double modulation signal show the same type of dynamics.

ultrafast release of magnetostriction mechanisms and launched in the surrounding SiO_2 (d = 775 nm) layer. These acoustic waves are detected by a time delayed probe pulse of 400 nm wavelength at an incident angle of 30 degrees with respect to the surface normal while propagating back and forth in the SiO_2. External magnetic field of 700 mT is applied along the normal of the sample surface. MOKE detection ensures filtering of the nonmagnetic components to the rotation of the probe polarization. Differential magneto-optical Kerr response (blue curve) reveals several acoustic echoes with L longitudinal or S shear acoustic polarization on top of the demagnetization background of the transient MOKE signal. The signal, detected by the double modulation technique (red curve), reveals the same response. It confirms that this type of detection is also suitable for magneto-acoustic experiments with Terfenol films. However, linear MOKE detection technique is preferable, in terms of signal to noise ratio. More scans of the experimental curves are required to obtain comparable signal to noise ratio via double modulation detection.

Bibliography

[1] Gordon E. Moore. Readings in computer architecture. chapter Cramming More Components Onto Integrated Circuits, pages 56–59. Morgan Kaufmann Publishers Inc., San Francisco, CA, USA, 2000. 1

[2] www.samsung.com. 1

[3] E. Beaurepaire et al. Ultrafast spin dynamics in ferromagnetic Nickel. *Phys. Rev. Lett. 76, p. 4250*, 1996. 2, 6, 7, 38

[4] Yong Xu, Marwan Deb, Grégory Malinowski, Michel Hehn, Weisheng Zhao, and Stéphane Mangin. Ultrafast magnetization manipulation using single femtosecond light and hot-electron pulses. *Advanced Materials*, 29(42):1703474–n/a, 2017. 1703474. 2

[5] C. Thomsen, J. Strait, Z. Vardeny, H. J. Maris, J. Tauc, and J. J. Hauser. Coherent phonon generation and detection by picosecond light pulses. *Phys. Rev. Lett.*, 53:989–992, Sep 1984. 2, 14, 16, 123

[6] T. Pezeril. Laser generation and detection of ultrafast shear acoustic waves in solids and liquids. *J. Opt. Laser Technol. 83, 177*, 2016. 2, 16, 17, 19, 134

[7] S. Legvold, J. Alstad, and J. Rhyne. Giant magnetostriction in Dysprosium and Holmium single crystals. *Phys. Rev. Lett.*, 10:509–511, Jun 1963. 3

[8] J. J. Rhyne and S. Legvold. Magnetostriction of Tb single crystals. *Phys. Rev.*, 138:A507–A514, Apr 1965. 3

[9] A.E. Clark, R.M. Bozorth, and B.F. Desavage. Anomalous thermal expansion and magnetostriction of single crystals of Dysprosium. *Physics Letters*, 5(2):100 – 102, 1963. 3

[10] A.E. Clark. *Magnetostrictive RFe2 intermetallic compounds.* Elsevier, Handbook on the Physics and Chemistry of Rare Earths, Vol. 2, Ch. 15 p. 231-258, 1979. 3, 22, 27, 30, 32, 33, 83, 161, 168

[11] K. H. J. Buschow and R. P. van Stapele. Magnetic properties of some cubic rare-earth-iron compounds of the type RFe2 and Rxy1-xFe2. *Journal of Applied Physics*, 41(10):4066–4069, 1970. 3, 31

[12] Daane A. H. Spedding F. H. *The Rare Earths.* Published by John Wiley & Sons, New York and London, 1961. 3

[13] V. Oderno. PhD thesis, INPL Ecole des Mines de Nancy, 1996. 3

[14] A. Mougin. *Nanosystemes magnetostrictifs de TRFe2(110) (TR=terre rare) : croissance, morphologie et proprietes magnetiques*. PhD thesis, Physique et chimie de la matiere et des materiaux Nancy 1, 1999. 3, 32

[15] Joachim Stör and Hans Christoph Siegmann. *Magnetism : from fundamentals to nanoscale dynamics*. Berlin, London : Springer, 2006. 6

[16] B. Koopmans. *Handbook of Magnetism and advanced magnetic materials Vol. 3, p. 1589-1613*. Wiley, 2007. 7

[17] B. Koopmans et al. Explaining the paradoxial diversity of ultrafast laser-induced demagnetization. *Nature Materials 9, 259*, 2010. 7, 8, 37, 38, 74

[18] T. Roth, A. J. Schellekens, S. Alebrand, O. Schmitt, D. Steil, B. Koopmans, M. Cinchetti, and M. Aeschlimann. Temperature dependence of laser-induced demagnetization in Ni: A key for identifying the underlying mechanism. *Phys. Rev. X*, 2, 2012. 7

[19] Ji-Wan Kim, Kyeong-Dong Lee, Jae-Woo Jeong, and Sung-Chul Shin. Ultrafast spin demagnetization by nonthermal electrons of TbFe alloy film. *Applied Physics Letters*, 94(19), 2009. 7

[20] J. Wang et al. Ultrafast quenching of ferromagnetism in InMnAs induced by intense laser irradiation. *Physical Review Letters*, 95(16), 2005. 7

[21] El'yashevich M.A. Imas Y.A. Pavlenko N.A. Anisimov S.I., Bonch-Bruevich A.M. and Romanov G.S. *Effect of powerful light fluxes on metals Vol. 36, p. 1273*. Zh. Teor. Fiz., 1966. 7

[22] Granovskii A. B. Agranat M. B., Ashitkov S. I. and Rukman G. I. *Interaction of picosecond laser pulses with the electron, spin, and phonon subsystems of Nickel Vol. Sov. Phys. JETP, p. 804*, volume 59. Zh. Eksp. Teor. Fiz., 1984. 7

[23] J.-Y. Bigot et al. Coherent ultrafast magnetism induced by femtosecond laser pulses. *Nature Physics 5, 515-520*, 2009. 8, 161

[24] Andrei Kirilyuk, Alexey V. Kimel, and Theo Rasing. Ultrafast optical manipulation of magnetic order. *Rev. Mod. Phys.*, 82:2731–2784, Sep 2010. 8, 9, 10

[25] D.A Garanin. Generalized equation of motion for a ferromagnet. *Physica A: Statistical Mechanics and its Applications*, 172(3):470 – 491, 1991. 10

[26] A. Vaterlaus, D. Guarisco, M. Lutz, M. Aeschlimann, M. Stampanoni, and F. Meier. Different spin and lattice temperatures observed by spin-polarized photoemission with picosecond laser pulses. *Journal of Applied Physics*, 67(9):5661–5663, 1990. 11

[27] A. Vaterlaus, T. Beutler, and F. Meier. Spin-lattice relaxation time of ferromagnetic Gadolinium determined with time-resolved spin-polarized photoemission. *Phys. Rev. Lett.*, 67:3314–3317, Dec 1991. 11

[28] D. J. Hilton, R. P. Prasankumar, S. A. Trugman, A. J. Taylor, and R. D. Averitt. On photo-induced phenomena in complex materials: Probing quasiparticle dynamics using infrared and far-infrared pulses. *Journal of the Physical Society of Japan*, 75(1):011006, 2006. 11

[29] et all Stamm, C. Femtosecond modification of electron localization and transfer of angular momentum in Nickel. *Nature Mater.*, 6:740–743, 2007. 11, 38

[30] Ru-Pin Pan, H. D. Wei, and Y. R. Shen. Optical second-harmonic generation from magnetized surfaces. *Phys. Rev. B*, 39:1229–1234, Jan 1989. 11

[31] J. Reif, J. C. Zink, C.-M. Schneider, and J. Kirschner. Effects of surface magnetism on optical second harmonic generation. *Phys. Rev. Lett.*, 67:2878–2881, Nov 1991. 11

[32] M. Faraday. *On the Magnetization of Light and the Illumination of Magnetic Lines of Force*. Experimental researches in electricity by Michael Faraday. Royal Society, 1846. 11

[33] John Kerr. On rotation of the plane of polarization by reflection from the pole of a magnet. *The London, Edinburgh, and Dublin Philosophical Magazine and Journal of Science*, 3(19):321–343, 1877. 11

[34] J. Zak, E.R. Moog, C. Liu, and S.D. Bader. Universal approach to magneto-optics. *Journal of Magnetism and Magnetic Materials*, 89(1):107 – 123, 1990. 11, 12, 76

[35] A. Hassdenteufel et al. Thermally assisted all-optical helicity dependent magnetic switching in amorphous Fe(100-x)Tb(x) alloy films. *Advanced Materials, Vol. 25, 22, 3122-3128*, 2013. 12

[36] S. Mangin et al. Engineered materials for all-optical helicity-dependent magnetic switching. *Nature materials, Vol. 13, 3, p. 286-292*, 2014. 12, 135

[37] Fundamentals of picosecond laser ultrasonics. *Ultrasonics*, 56(Supplement C):3 – 20, 2015. 14

[38] Pascal Ruello and Vitalyi E. Gusev. Physical mechanisms of coherent acoustic phonons generation by ultrafast laser action. *Ultrasonics*, 56:21 – 35, 2015. 14, 16

[39] T. Pezeril, P. Ruello, S. Gougeon, N. Chigarev, D. Mounier, J.-M. Breteau, P. Picart, and V. Gusev. Generation and detection of plane coherent shear picosecond acoustic pulses by lasers: Experiment and theory. *Phys. Rev. B*, 75:174307, May 2007. 14, 17, 59, 62, 68

[40] Sooheyong Lee, G. Jackson Williams, Maria I. Campana, Donald A. Walko, and Eric C. Landahl. Picosecond x-ray strain rosette reveals direct laser excitation of coherent transverse acoustic phonons. *Scientific Reports*, 6:1703474–n/a, 2016. 14

[41] O. Matsuda, O. B. Wright, D. H. Hurley, V. E. Gusev, and K. Shimizu. Coherent shear phonon generation and detection with ultrashort optical pulses. *Phys. Rev. Lett.*, 93:095501, Aug 2004. 14, 15, 19, 80

[42] V. Gusev and A. Karabutov. *Laser Optoacoustics.* New York : American Institute of Physics, 1993. 14

[43] C. Rossignol, J. M. Rampnoux, M. Perton, B. Audoin, and S. Dilhaire. Generation and detection of shear acoustic waves in metal submicrometric films with ultrashort laser pulses. *Phys. Rev. Lett.*, 94:166106, Apr 2005. 14

[44] Vitalyi Gusev. On generation of picosecond inhomogeneous shear strain fronts by laser-induced gratings. *Applied Physics Letters*, 94(16):164105, 2009. 15

[45] Mansour Kouyate, Thomas Pezeril, Denis Mounier, and Vitalyi Gusev. Generation of inhomogeneous plane shear acoustic modes by laser-induced thermoelastic gratings at the interface of transparent and opaque solids. *Journal of Applied Physics*, 110(12):123526, 2011. 15

[46] Keith A. Nelson. Stimulated Brillouin scattering and optical excitation of coherent shear waves. *Journal of Applied Physics*, 53(9):6060–6063, 1982. 15

[47] Sandlung L. *Proc. 3-rd int., Workshop on power transducers for sonics & ultrasonics.* Ed.Springer, 1992. 16

[48] C. Thomsen, H. T. Grahn, H. J. Maris, and J. Tauc. Surface generation and detection of phonons by picosecond light pulses. *Phys. Rev. B*, 34:4129–4138, 1986. 17, 75, 76, 136

[49] P. B. Johnson and R. W. Christy. Optical constants of transition metals: Ti, V, Cr, Mn, Fe, Co, Ni, and Pd. *Phys. Rev. B*, 9:5056–5070, Jun 1974. 18, 77

[50] K. J. Manke, A. A. Maznev, C. Klieber, V. Shalagatskyi, V. V. Temnov, D. Makarov, S.-H. Baek, C.-B. Eom, and K. A. Nelson. Measurement of shorter-than-skin-depth acoustic pulses in a metal film via transient reflectivity. *Applied Physics Letters*, 103(17):173104, 2013. 18

[51] D R Bauer, J I Brauman, , and R Pecora. Depolarized light scattering from liquids. *Annual Review of Physical Chemistry*, 27(1):443–463, 1976. 18

[52] Chang-Ki Min, David G. Cahill, and Steve Granick. Time-resolved ellipsometry for studies of heat transfer at liquid/solid and gas/solid interfaces. *Review of Scientific Instruments*, 81(7):074902, 2010. 18

[53] Nye J. F. *Physical Properties of Crystals.* Oxford University Press, Oxford, 1957. 19

[54] A. V. Scherbakov, A. S. Salasyuk, A. V. Akimov, X. Liu, M. Bombeck, C. Brüggemann, D. R. Yakovlev, V. F. Sapega, J. K. Furdyna, and M. Bayer. Coherent magnetization precession in ferromagnetic (Ga,Mn)As induced by picosecond acoustic pulses. *Phys. Rev. Lett.*, 105:117204, Sep 2010. 20, 21, 161

[55] L. Thevenard, E. Peronne, C. Gourdon, C. Testelin, M. Cubukcu, E. Charron, S. Vincent, A. Lemaître, and B. Perrin. Effect of picosecond strain pulses on thin layers of the ferromagnetic semiconductor (Ga,Mn)(As,P). *Phys. Rev. B*, 82:104422, Sep 2010. 21

[56] L. Thevenard, J.-Y. Duquesne, E. Peronne, H. J. von Bardeleben, H. Jaffres, S. Ruttala, J-M. George, A. Lemaître, and C. Gourdon. Irreversible magnetization switching using surface acoustic waves. *Phys. Rev. B*, 87:144402, Apr 2013. 21

[57] M. Bombeck, J. V. Jäger, A. V. Scherbakov, T. Linnik, D. R. Yakovlev, X. Liu, J. K. Furdyna, A. V. Akimov, and M. Bayer. Magnetization precession induced by quasitransverse picosecond strain pulses in (311) ferromagnetic (Ga,Mn)As. *Phys. Rev. B*, 87:060302, Feb 2013. 21, 103

[58] Ji-Wan Kim, Mircea Vomir, and Jean-Yves Bigot. Ultrafast magnetoacoustics in Nickel films. *Phys. Rev. Lett.*, 109:166601, Oct 2012. 21, 38

[59] T. L. Gilbert. A phenomenological theory of damping in ferromagnetic materials. *IEEE Transactions on Magnetics*, 40(6):3443–3449, Nov 2004. 21

[60] O. Kovalenko et al. New concept for magnetization switching by ultrafast acoustic pulses. *Phys. Rev. Lett. 110, 266602*, 2013. 21, 51, 79, 115, 133

[61] V. V. Temnov et all. Femtosecond nonlinear ultrasonics in gold probed with ultrashort surface plasmons. *Nature Communications*, 4(1468), 2013. 21

[62] J. Janušonis, C. L. Chang, P. H. M. van Loosdrecht, and R. I. Tobey. Frequency tunable surface magneto elastic waves. *Applied Physics Letters*, 106(18):181601, 2015. 21

[63] Eugene M. Chudnovsky and Reem Jaafar. Manipulating the magnetization of a nanomagnet with surface acoustic waves: Spin-rotation mechanism. *Phys. Rev. Applied*, 5:031002, Mar 2016. 21

[64] T Henighan, M Trigo, S Bonetti, P Granitzka, D Higley, Z Chen, MP Jiang, R Kukreja, A Gray, AH Reid, et al. Generation of high-frequency strain waves during femtosecond demagnetization of Fe/MgO films. *arXiv preprint arXiv:1509.03348*, 2015. 22

[65] E. F. Wassermann. Handbook of magnetic materials. *Elsevier Science, edited by K.H.J. Bushow and E.P. Wohlfarth, Vol. 5, Chap. 3*, 1990. 26, 140

[66] C. A. Feickert, J. Berman, J. Kamphaus, J. Trovillion, and R. Quattrone. A semi-quantitative analytic model for the magnetic response of a Terfenol-D impregnated composite specimen under tension. *Journal of Applied Physics*, 88(7):4265–4268, 2000. 27

[67] W. Heisenberg. Zur theorie des ferromagnetismus. *Zeitschrift für Physik*, 49(9):619–636, 1928. 27

[68] Pierre Weiss. L'hypothese du champ moléculaire et la propriété ferromagnétique. *J. Phys. Theor. Appl.*, 6(1):661–690, 1907. 27

[69] F. Robert et al. *Investigation of Terfenol-D for magnetostrictive tagging of fibre reinforced polymer composites.* US Army Corps of Engineers, ERDC, Construction Engineering Research Laboratory, 2000. 27

[70] J.P. Liu et al. On the 4f-3d exchange interaction in intermetallic compounds. *J. Magn. Magn. Mater. 132, p. 159*, 1994. 27

[71] Hansen, P. and Krishnan, R. Anisotropy and magnetostriction of 4d and 5d transition-metal ions in garnets and spinel ferrites. *J. Phys. Colloques*, 38:C1–147–C1–155, 1977. 31

[72] P. Hartemann. Effets et materiaux magnetostrictifs. *Technique de l'ingenieurs*, 4, Feb 1999. 31, 116

[73] C. T. Wang, B. M. Clemens, and R. L. White. Effects of substrate on the magnetic properties of epitaxial TbFe2(111) films. *IEEE Transactions on Magnetics*, 32(5):4752–4754, Sep 1996. 32

[74] G. Simmons and H. Wang. *Single Crystal Elastic Constants and Calculated Aggregate Properties: A Handbook*. MIT, Cambridge, MA. 32, 33, 106

[75] R. Brűckner. Properties and structure of vitreous silica. I. *Journal of Non-Crystalline Solids*, 5(2):123 – 175, 1970. 32

[76] Rei Kitamura, Laurent Pilon, and Miroslaw Jonasz. Optical constants of silica glass from extreme ultraviolet to far infrared at near room temperature. *Appl. Opt.*, 46(33):8118–8133, Nov 2007. 32

[77] L. Sandlund, M. Fahlander, T. Cedell, A. E. Clark, J. B. Restorff, and M. Wun-Fogle. Magnetostriction, elastic moduli, and coupling factors of composite Terfenol-D. *Journal of Applied Physics*, 75(10):5656–5658, 1994. 33, 106

[78] L. Garcia-Gancedo, S. C. Busbridge, P. Pernod, and V. Preobrazhensky. Magnetoacoustic properties of self-biased Terfenol-D 2-2 composites. *Journal of Applied Physics*, 101(9):09C514, 2007. 33, 106

[79] Michael de Podesta. *Understanding the Properties of Matter, 2nd edition*. Taylor-Francis, London. 33

[80] J. M. Winey, Y. M. Gupta, and D. E. Hare. R-axis sound speed and elastic properties of sapphire single crystals. *Journal of Applied Physics*, 90(6):3109–3111, 2001. 33

[81] M. Huth and C. P. Flynn. Magnetism and microstructure in epitaxial $\mathrm{TbFe_2}$(111) thin films. *Phys. Rev. B*, 58:11526–11533, Nov 1998. 35

[82] N Négre, M Goiran, S Jaren, C Meyer, R Barbaste, A.R Fert, and S Askénazy. Study of the magnetic anisotropy of a TbFe2 [111] thin film by MOKE. *Journal of Magnetism and Magnetic Materials*, 198:315 – 317, 1999. 35

[83] W. Hűbner and K. H. Bennemann. Simple theory for spin-lattice relaxation in metallic rare-earth ferromagnets. *Phys. Rev. B*, 53:3422–3427, Feb 1996. 37

[84] Marko Wietstruk. Hot-electron-driven enhancement of spin-lattice coupling in Gd and Tb $4f$ ferromagnets observed by femtosecond x-ray magnetic circular dichroism. *Phys. Rev. Lett.*, 106:127401, Mar 2011. 38

[85] A. Eschenlohr, M. Sultan, A. Melnikov, N. Bergeard, J. Wieczorek, T. Kachel, C. Stamm, and U. Bovensiepen. Role of spin-lattice coupling in the ultrafast demagnetization of $Gd_{1-x}Tb_x$ alloys. *Phys. Rev. B*, 89:214423, Jun 2014. 38

[86] A. R. Khorsand, M. Savoini, A. Kirilyuk, A. V. Kimel, A. Tsukamoto, A. Itoh, and Th. Rasing. Element-specific probing of ultrafast spin dynamics in multisublattice magnets with visible light. *Phys. Rev. Lett.*, 110:107205, Mar 2013. 38

[87] B.A. Auld. *Acoustic fields and waves in solids.* Wiley, V. 1, 1973. 41, 42

[88] S. Rinaldi et al. Magnetoelastic coupling in Tb0.3Dy0.7Fe2 measured ultrasonically. *Physics Letters A 61(7), p. 465-467*, 1977. 46, 47

[89] R.C. Le Craw R.L. Comstock. *Physical Acoustics.* W. P. Mason, Ed., Academic Press, N.Y., Vol. 3, Part B, Chap. 4, 1965. 46

[90] V.V. Lemanov. *Physics of magnetic dielectrics.* G.A. Smolensky, Nauka, Leningrad p. 299, 1974. 49

[91] C. de la Fuente et al. Magnetocrystalline anisotropy in a (110)(Tb0.27Dy0.73)Fe2 thin-film. *J. Phys.: Condens. Matter 16, p. 2959*, 2004. 51, 141

[92] Alexander G Gurevich and Gennadii A Melkov. *Magnetization oscillations and waves.* CRC press, 1996. 54, 104

[93] P. J. Grundy, D. G. Lord, and P. I. Williams. Magnetostriction in TbDyFe thin films. *Journal of Applied Physics*, 76(10):7003–7005, 1994. 57

[94] Rebecca M. Slayton, Keith A. Nelson, and A. A. Maznev. Transient grating measurements of film thickness in multilayer metal films. *Journal of Applied Physics*, 90(9):4392–4402, 2001. 57

[95] A.E. Clark, R. Abbundi, H.T. Savage, and O.D. McMasters. Magnetostriction of Rare-Earth-Fe2 laves phase compounds. *Physica B+C*, 86(Part 1):73 – 74, 1977. 61, 62, 106, 162

[96] A. Devos, R. Côte, G. Caruyer, and A. Lefèvre. A different way of performing picosecond ultrasonic measurements in thin transparent films based on laser-wavelength effects. *Applied Physics Letters*, 86(21):211903, 2005. 66

[97] H. N. Lin, R. J. Stoner, H. J. Maris, and J. Tauc. Phonon attenuation and velocity measurements in transparent materials by picosecond acoustic interferometry. *Journal of Applied Physics*, 69(7):3816–3822, 1991. 67

[98] T. L. Linnik, A. V. Scherbakov, D. R. Yakovlev, X. Liu, J. K. Furdyna, and M. Bayer. Theory of magnetization precession induced by a picosecond strain pulse in ferromagnetic semiconductor (Ga,Mn)As. *Phys. Rev. B*, 84:214432, Dec 2011. 103

[99] C. Klieber et al. Optical generation and detection of gigahertz-frequency longitudinal and shear acoustic waves in liquids: Theory and experiment. *J. Appl. Phys. 112, 013502*, 2012. 115, 137

[100] C. Klieber et al. Mechanical spectra of glass-forming liquids. II. Gigahertz-frequency longitudinal and shear acoustic dynamics in glycerol and DC704 studied by time-domain Brillouin scattering. *J. Chem. Phys. 138, 12A544*, 2013. 115, 137

[101] Wun-Fogle M. Restorff J. Clark, A. and T. Lograsso. Magnetostrictive properties of Galfenol alloys under compressive stress. *MATERIALS TRANSACTIONS*, 45(5):881 – 886, 2002. 116

[102] S. Fin, R. Tomasello, D. Bisero, M. Marangolo, M. Sacchi, H. Popescu, M. Eddrief, C. Hepburn, G. Finocchio, M. Carpentieri, A. Rettori, M. G. Pini, and S. Tacchi. In-plane rotation of magnetic stripe domains in $\mathrm{Fe}_{1-x}\mathrm{Ga}_x$ thin films. *Phys. Rev. B*, 92:224411, Dec 2015. 116

[103] J. V. Jäger, A. V. Scherbakov, T. L. Linnik, D. R. Yakovlev, M. Wang, P. Wadley, V. Holy, S. A. Cavill, A. V. Akimov, A. W. Rushforth, and M. Bayer. Picosecond inverse magnetostriction in Galfenol thin films. *Applied Physics Letters*, 103(3):032409, 2013. 116

[104] H. Zhou, A. Talbi, N. Tiercelin, and O. Bou Matar. Multilayer magnetostrictive structure based surface acoustic wave devices. *Applied Physics Letters*, 104(11):114101, 2014. 116

[105] P. Guionneau et al. Structural approach of the features of the spin crossover transition in Iron(II) compounds. *J. Mater. Chem.* 121, 122, 130, 133, 166

[106] M. Lorenc et al. Cascading photoinduced, elastic, and thermal switching of spin states triggered by a femtosecond laser pulse in an Fe(III) molecular crystal. *Phys. Rev. B*, 85:054302, 2012. 121

[107] A. Marino et al. Femtosecond optical pump-probe reflectivity studies of spin-state photo-switching in the spin-crossover molecular crystals [Fe(PM-AzA)2(NCS)2]. *Polyhedron*, 66(123), 2013. 121, 124

[108] Thierry Granier, Bernard Gallois, Jacques Gaultier, Jose Antonio Real, and Jacqueline Zarembowitch. High-pressure single-crystal x-ray diffraction study of two spin-crossover Iron(II) complexes: Fe(phen)2(NCS)2 and Fe(btz)2(NCS)2. *Inorganic Chemistry*, 32(23):5305–5312, 1993. 121

[109] J. A. Real et al. Comparative investigation of the spin-crossover compounds Fe(btz)2(NCS)2 and Fe(phen)2(NCS)2 (where btz= 2, 2'-bi-4, 5-dihydrothiazine and phen= 1, 10-phenanthroline). Magnetic properties and thermal dilatation behavior and crystal structure of Fe(btz)2(NCS)2 at 293 and 130 K. *Inorganic Chemistry*, 31(24):4972–4979, 1992. 121

[110] Eric Collet et al. Laser-induced ferroelectric structural order in an organic charge-transfer crystal. *Science*, 300(5619):612–615, 2003. 121

[111] Marina Servol et al. Local response to light excitation in the charge-ordered phase of $(\mathrm{EDO-TTF})_2\mathrm{SbF}_6$. *Phys. Rev. B*, 92:024304, Jul 2015. 121

[112] H. A. Goodwin P. Gutlich. *Spin Crossover in Transition Metal Compounds.* Springer, Ch. 1, 2004. 121

[113] Sunil Varughese, M. S. R. N. Kiran, Upadrasta Ramamurty, and Gautam R. Desiraju. Nanoindentation in crystal engineering: Quantifying mechanical properties of molecular crystals. *Angewandte Chemie International Edition*, 52(10):2701–2712, 2013. 121

[114] J-P. Sauvage. *Transition metals in supramolecular chemistry.* John Wiley & Sons, V. 21, 2008. 122

[115] Jean-François Létard, José Antonio Real, Nicolás Moliner, Ana B. Gaspar, Laurence Capes, Olivier Cador, and Olivier Kahn. Light induced excited pair spin state in an Iron(II) binuclear spin-crossover compound. *Journal of the American Chemical Society*, 121(45):10630–10631, 1999. 123

[116] A. Hauser et al. Cooperative phenomena and light-induced bistability in Iron(II) spin-crossover compounds. *Coord. Chem. Rev. 190, 471*, 1999. 123

[117] O Kahn and C Jay Martinez. Spin-transition polymers: from molecular materials toward memory devices. *Science*, 279(5347):44–48, 1998. 123

[118] J Laisney, A Tissot, G Molnar, L Rechignat, E Riviere, F Brisset, A Bousseksou, and M-L Boillot. Nanocrystals of Fe(phen)2(NCS)2 and the size-dependent spin-crossover characteristics. *Dalton Transactions*, 44(39):17302–17311, 2015. 123

[119] Edgar Koenig and K. Madeja. 5t2-1a1 equilibriums in some Iron(ii)-bis(1,10-phenanthroline) complexes. *Inorganic Chemistry*, 6(1):48–55, 1967. 123

[120] K. Kato, M. Takata, Y. Moritomo, A. Nakamoto, and N. Kojima. On-off optical switching of the magnetic and structural properties in a spin-crossover complex. *Applied Physics Letters*, 90(20):201902, 2007. 124

[121] M. Schubert. Polarization-dependent optical parameters of arbitrarily anisotropic homogeneous layered systems. *Phys. Rev. B 53, 4265*, 1996. 129

[122] D. W. Berreman. Optics in stratified and anisotropic media: 4x4-matrix formulation. *J. Opt. Soc. Am. 62, 502*, 1972. 129

[123] V. Ksenofontov, G. Levchenko, H. Spiering, and P. G˙Spin crossover behavior under pressure of Fe(pm-l)2(NCS)2 compounds with substituted 2'-pyridylmethylene 4-anilino ligands. *Chemical Physics Letters*, 294(6):545 – 553, 1998. 131

[124] T. Parpiiev, M. Servol, M. Lorenc, I. Chaban, R. Lefort, E. Collet, H. Cailleau, P. Ruello, N. Daro, G. Chastanet, and T. Pezeril. Ultrafast non-thermal laser excitation of gigahertz longitudinal and shear acoustic waves in spin-crossover molecular crystals [Fe(PM-AzA)2(NCS)2]. *Applied Physics Letters*, 111(15):151901, 2017. 131

[125] N. Klinduhov et al. Choice of dynamics in spin-crossover systems. *Phys. Rev. B 81, 094408*, 2010. 133

[126] Y. Yang et al. Impulsive stimulated light scattered from glass-forming liquids. ii. salol relaxation dynamics, nonergodicity parameter, and testing of mode coupling theory. *J. Chem. Phys. 103, 7732*, 1995. 134

[127] A. Rury et al. Intermolecular electron transfer from intramolecular excitation and coherent acoustic phonon generation in a hydrogen-bonded. *J. Chem Phys 144, 104701*, 2016. 135

[128] C. D. Stanciu, F. Hansteen, A. V. Kimel, A. Kirilyuk, A. Tsukamoto, A. Itoh, and Th. Rasing. All-optical magnetic recording with circularly polarized light. *Phys. Rev. Lett.*, 99:047601, Jul 2007. 135

[129] G. Vaudel et al. Laser generation of hypersound by a terahertz photo-dember electric field in a piezoelectric GaAs semiconductor. *Phys. Rev. B 90*, 2014. 135

[130] T. Pezeril et al. Structural heterogeneities at the origin of acoustic and transport anomalies in glycerol glass-former. *Phys. Rev. Lett. 102, 107402*, 2009. 137

[131] Masaki Matsuda and Hiroyuki Tajima. Thin film of a spin crossover complex [Fe(dpp)2](bf4)2. *Chemistry Letters*, 36(6):700–701, 2007. 137

[132] S. Shi, G. Schmerber, J. Arabski, J.-B. Beaufrand, D. J. Kim, S. Boukari, M. Bowen, N. T. Kemp, N. Viart, G. Rogez, E. Beaurepaire, H. Aubriet, J. Petersen, C. Becker, and D. Ruch. Study of molecular spin-crossover complex Fe(phen)2(NCS)2 thin films. *Applied Physics Letters*, 95(4):043303, 2009. 137

[133] P. Fulde. *Handbook on the Physics and Chemistry Rare Earth Vol. 2.* North-Holland. Inc., 1979. 138

[134] W Co Koehler. Magnetic properties of rare-earth metals and alloys. *Journal of Applied Physics*, 36(3):1078–1087, 1965. 138

[135] Melvin A Ruderman and Charles Kittel. Indirect exchange coupling of nuclear magnetic moments by conduction electrons. *Physical Review*, 96(1):99, 1954. 138

[136] J K Lang, Y Baer, and P A Cox. Study of the 4f and valence band density of states in rare-earth metals. II. Experiment and results. *Journal of Physics F: Metal Physics*, 11(1):121, 1981. 138

[137] B. Coqblin. *The electronic structure of rare-earth metals and alloys: the magnetic heavy rare-earths.* A Anouk. Academic Press, 1977. 138

[138] W.C. Koehler. Magnetic properties of rare-earth metals and alloys. *J. Appl. Phys., 36, 1078*, 1965. 139

[139] R Elliott. *Magnetic properties of rare earth metals.* Springer Science & Business Media, 1972. 139

List of Figures

List of Tables

UNIVERSITE
BRETAGNE
LOIRE

Le Mans
Université

Thèse de Doctorat

Tymur PARPIIEV

Magnéto-acoustique ultra-rapide dans les matériaux magnétostrictif

Résumé

Avec l'avènement du laser femtoseconde il est devenu possible de mesurer comment la démagnétisation femtoseconde peut permettre de sonder l'interaction d'échange dans les métaux ferromagnétiques. La démagnétisation induite par le laser d'un matériau avec un fort couplage magnéto-élastique amène à la relaxation de ses contraintes, générant ainsi des ondes acoustiques longitudinales et transversales.

Dans ce travail de thèse, la génération d'impulsions acoustiques picosecondes transversales par *le mécanisme de démagnétostriction* dans des matériaux fortement magnétostrictifs est traitée analytiquement et montrée expérimentalement dans le cas d'un alliage de Terfenol. En premier lieu, nous avons développé un modèle phénoménologique de magnétostriction directe dans un film monocristallin de Terfenol. Les expériences pompe-sonde linéaire MOKE résolues en temps montrent que la relaxation transitoire des contraintes magnéto-élastiques du film amène à l'excitation d'ondes GHz acoustiques longitudinales et transversales. Ces résultats sont la première observation expérimentale de l'excitation d'ondes acoustiques transversales picoseconde par mécanisme de démagnétostriction induit par laser.

En second lieu, nous avons analysé le processus d'interaction d'ondes acoustiques longitudinales générées optiquement avec l'aimantation d'un film mince de Terfenol. L'onde acoustique picoseconde produit un changement de magnétisation du film et induit la conversion de modes acoustiques. C'est une autre voie de génération d'ondes acoustiques transversales que nous avons mis en évidence. Par conséquent, il existe deux mécanismes de l'excitation des ondes transversales dans des matériaux à fort couplage magnéto-élastique: (i) démagnétostriction induite par laser et (ii) conversion de modes acoustiques. La gamme de fréquence des impulsions générées est liée à l'échelle de temps de démagnétisation, qui corresponds à quelques centaines de GHz - 1 THz. Les résultats expérimentaux et théoriques obtenus dans le cadre de cette thèse pourraient amener à des retombées applicatives importantes: spectroscopie Brillouin de matériaux à des fréquences GHz-THz impliquant des ondes acoustiques longitudinales mais aussi transverses, enregistrement magnétique à partir d'ondes acoustiques ultrarapides longitudinales et transverses.

Mots clés
Magnéto-acoustique ultrarapide, génération magnéto-élastique, magnétostriction directe / inverse, ondes picosecondes transversales.

Abstract

With the advent of femtosecond lasers it became possible to measure how femtosecond optical demagnetization can probe the exchange interaction in ferromagnetic metals. Laser-induced demagnetization of materials with strong magneto-elastic coupling should lead to the release of its build-in strains, thus to the generation of both longitudinal and shear acoustic waves.

In this thesis, generation of shear picosecond acoustic pulses in strongly magnetostrictive materials such as Terfenol is processed analytically and shown experimentally. In case of Terfenol with strong magneto-crystalline anisotropy, laser induced demagnetostriction is responsible for shear waves excitation. First, the phenomenological model of direct magnetostriction in a Terfenol monocrystalline film is developed. Transversal strain generation efficiency strongly depends on the orientation of the film magnetization. Time-resolved linear MOKE pump-probe experiments show that transient laser-induced release of the magnetoelastic strains in the films lead to the excitation of GHz longitudinal and shear acoustic waves. These results are the first experimental observation of picosecond shear acoustic wave excitation by laser-induced demagnetostriction mechanism.

Second, the interaction of an optically generated longitudinal acoustic wave with the magnetization of a Terfenol thin film is reported. Arrival of the ps strain wave alters a change of its magnetization and leads to the acoustic mode conversion. Which is another pathway of shear acoustic wave generation. This effect highlight a strong coupling of elastic and spin subsystems in Terfenol. Hence, there are two laser induced mechanisms of the shear wave excitation in materials with strong magneto elastic coupling: (i) transient demagnetostriction and (ii) acoustic mode conversion. The frequency bandwidth of the generated acoustic pulses matches the demagnetization timescale and lies in the range of several hundreds of GHz, close to 1 THz.
These experimental and theoretical results could have large impacts in several fields of applications: Brillouin spectroscopy at GHz-THz frequencies with both longitudinal and shear acoustic polarizations, magnetic recording with ultrafast longitudinal and shear acoustic waves.

Key Words
Ultrafast magneto-acoustics, magneto-elastic generation, direct / inverse magnetostriction, picosecond shear waves.

L'Université Bretagne Loire